THE UNIVERSITY OF CHICAGO

MAGNETISM OF INORGANIC-ORGANIC MOLECULAR MATERIALS FEATURING FIRST-ROW TRANSITION METALS

A DISSERTATION SUBMITTED TO

THE FACULTY OF THE DIVISION OF THE PHYSICAL SCIENCES

IN CANDIDACY FOR THE DEGREE OF

DOCTOR OF PHILOSOPHY

DEPARTMENT OF CHEMISTRY

BY

AIRI KAWAMURA

CHICAGO, ILLINOIS

JUNE 2020

Table of Contents

Abbreviations

χ	Molar magnetic susceptibility in cm^3/mol
T	Temperature in K or ° C
M	Magnetization, molar or per ion/unit, various units
H	Applied magnetic field in T or Oe
J	Magnetic coupling in cm^{-1}
S	Total spin, unitless
χ' / χ''	In-/Out-of-phase susceptibility in cm^3/mol
μ_{eff}	Effective magnetic moment in μ_B
g	Electron g-factor, unitless
D	Axial component of zero field splitting in cm^{-1}
E	Rhombic component of zero field splitting in cm^{-1}
δ	Mössbauer isomer shift in mm/s
ΔE_Q	Mössbauer quadrupole splitting in mm/s
τ	Magnetic relaxation time in s
Δ	Energy barrier, various units
μ_B	Bohr magneton, constant
ST/SCO	Spin transition/Spin crossover
HS/LS	High spin/Low spin
ZFS	Zero-field splitting
ZFC/FC	Zero field cooled/Field cooled
BDC	1,4-benzene dicarboxylate

pyz	Pyrazine
bipy	4,4’-bipyridine
N-ox	Aromatic N-oxide
PNO	Pyridine N-oxide
IQNO	Isoquinoline N-oxide
BPDC	4,4′-biphenyldicarboxylate
SNDC	4,8-disulfonyl-2,6-naphthalenedicarboxylate
DMF	N,N-Dimethylformamide
TPA	Tris(2-pyridylmethyl)amine
TTFtt	Tetrathiafulvalene-2,3,6,7-tetrathiolate
dmit	1,3Dithiole-2-thione-4,5-dithiolate
BAr^F_4	Tetrakis[3,5-bis(trifluoromethyl)phenyl]borate
THF	Tetrahydrofuran
MeOH	Methanol
DCM	Dichloromethane
NMR	Nuclear magnetic resonance
SXRD	Single crystal X-ray diffraction
XRPD	X-Ray powder diffraction
EPR	Electron paramagnetic resonance
DFT	Density functional theory

LIST OF MATERIALS

Chapter 2

1 – Fe(BDC)(pyz)

2 – Co(BDC)(pyz)

3 – Fe(BDC)(bipy)

4 – Co(BDC)(bipy)

Chapter 3

1 – Co(BDC)(PNO)

2 – Co(BPDC)(PNO)

3 – Co(BPDC)(IQNO)

Chapter 4

1 – $Cz^{tBu}(Pyr^{iPr})_2FeCl$

2 – $Cz^{tBu}(Pyr^{iPr})_2FeCl(THF)$

3 – $Cz^{tBu}(Pyr^{iPr})_2FeN_3$

Chapter 5

1 – $Fe_2(SNDC)(DMF)_5$

2 – $Co_2(SNDC)(DMF)_5$

Chapter 6

1 – $(FeTPA)_2TTFtt$

2 – $[(FeTPA)_2TTFtt][BAr^F{}_4]_2$

3 – Fe(TPA)(dmit)

4 – $[Fe(TPA)(dmit)][BAr^F{}_4]$

LIST OF TABLES

Chapter 2

Chapter 3

Chapter 6

LIST OF FIGURES

Chapter 2

Chapter 3

Chapter 4

Chapter 6

LIST OF EQUATIONS

Chapter 1

Chapter 2

Chapter 3

Chapter 4

ACKNOWLEDGEMENTS

Thank you to my advisor, Professor John S. Anderson. This research would not have been possible without his expertise and passion for chemistry. I also thank the other members of my defense committee; Professor Dmitri Talapin and Professor Wenbin Lin for their instruction and feedback in both my candidacy and defense committees.

I am grateful to my fellow lab members for their assistance over the years. I would like to specially thank Andrew McNeece and Dr. Ethan Hill for countless productive discussions and assistance. Thank you to Jiaze Xie whose foundational work was crucial on my final project (see: Chapter 6). Thank you to Kate Jesse who provided computational assistance. Thank you to Dr. Noah Horwitz for his helpful feedback. I would also like to thank the lab members in the Hopkins and Jordan labs who have provided guidance and assistance; especially Dr. Rebecca Black, Dr. Chris Hansen, and Dr. Erik Reinhart. Thank you to former undergraduates Moises Ballesteros and Rachel Conway for their excellent work and great attitudes.

This work would not have been possible without the collaborative effort of many talented scientists. A special thank you to Dr. Alexander S. Filatov, who has assisted in SXRD, XAS, XRPD, and SAXS as well as providing valuable feedback in multiple projects. Thank you to Arin R. Greenwood and Professor Giulia Galli for their great computational work (see: Chapter 2). Thank you to Professor Ie-Rang Jeon whose magnetic expertise was invaluable (see: Chapter 3). Thank you also to Jan-Niklas Boyn and Professor David A. Mazziotti whose computational work was instrumental to the studies in Chapter 6. Thank you also to Professor T. David Harris, Professor Danna Freedman, and their many graduate students, including Professor Joe Zadrozny, Dr. Majed Fataftah, Dr. David Zee, Dr. Audrey Gallagher, Dr. Jordan DeGayner, and Kelsey

Collins, who have shared a large amount of expertise as well as assisted with magnetic, conductivity, and Mössbauer measurements.

I am very grateful to my undergraduate advisor, Professor Susan M. Kauzlarich, whose early support and instruction was vital in my success. I am also extremely grateful to my graduate student mentor, Dr. Yufei Hu, who taught me many scientific skills and best practices that I took with me into my graduate career.

This work was made possible by numerous staff and support members, including Luigi Mazzenga, John Phillips, Melinda Moore, Laura Luburich, Mike Reedy, Vera Dragisich, and Laura Baker. Thank you to the various janitorial and facilities staff that kept GCIS functional.

Finally, a most heartfelt thank you to my friends and family. Thanks to Andrew P., Huw, Matt, Jon, Becca, TJ, Jean, John, Francesca, Pranav, Natalie, Dave, Steph, Chris, and everyone else in Chicago that I shared a drink and good memories with. Thanks to my parents who have always wanted me to be happy. Thank you Maroka and Sawato for always having my back, and always being down to have a good meal.

My thanks to Andrew most of all – who has been my constant source of happiness and support for these past five years – who I can never thank enough.

ABSTRACT

The work in this thesis covers a broad range of molecular materials with a variety of magnetic properties. The linking theme in this work is the inclusion of first-row transition metals—either Fe(II) or Co(II)—in their high-spin state coordinated by bridging organic ligands. The diversity of these transition metal centers in their coordination geometry, ligands, dimensionality, and coupling yield an assortment of materials from magnetic metal organic frameworks, to single chain magnets, to spin crossover molecules with cooperative organic diradical modulation.

Chapter 1 serves as an introduction and covers the background and basics of the field of molecular magnetism before briefly touching upon the current state of several fields within this broad area of research. Possible applications, current drawbacks, and the potential advantages over traditional magnetic materials are discussed.

Chapter 2 investigates novel metal-organic frameworks of the type M(BDC)(pyz) and M(BDC)(bipy) with M = Fe(II) and Co(II). These materials exhibit unique structures with high crystallinity and permanent porosity over 1,300 m^2/g. The diamagnetic ligands (i.e. aromatic heterocycles and carboxylates) which bridge the spin centers engender weak antiferromagnetic superexchange as investigated by dc magnetic measurements, and the importance of extended structure on magnetic behavior is highlighted. Our understanding of these materials was aided by computational work by our collaborators, Professor Giulia Galli and Arin Greenwood, as well as EXAFS and Mössbauer measurements by Dr. Alexander Filatov and Dr. Audrey Gallagher, respectively.

Chapter 3 discusses a new set of 2- and 3-dimensional coordination polymers of the MIL-53 family type. These coordination polymers feature chains of Co(II) and a bridging N-oxide, and

the slow magnetic relaxation observed by ac magnetic measurements suggests that these chains may feature spin canted antiferromagnetism. In particular, the material Co(BPDC)(IQNO) also has significant interchain ordering, leading to bulk (3D) magnetic ordering. Professor Ie-Rang Jeon was instrumental in both collecting some of the necessary magnetic data as well as its interpretation.

Chapter 4 describes the magnetic properties of a set of Fe(II) compounds with NNN-pincer ligands that were synthesized by our collaborators at Loyola University, Professor Wei-Tsung Lee and Adrianna Lugosan. While the two discrete complexes do not show remarkable magnetic behavior, the coordination polymer which utilizes EE-bound azide to bridge Fe(II) centers exhibits slow magnetic relaxation characteristic of a single chain magnet when investigated by ac magnetometry.

In Chapter 5, sulfur-based ligands are introduced in Fe(II) and Co(II) containing coordination polymers. Sulfur-based ligands were targeted in favor of more common oxygen and nitrogen containing ligands due to the superior energy matching of sulfur to first-row transition metals which should allow for improved electron delocalization and coupling. These materials are primarily investigated by SXRD and magnetometry.

Finally, in Chapter 6, the complex $(FeTPA)_2TTFtt$ is investigated. This complex contains the sulfur-based ligand TTFtt which is redox active at mild potentials and had been previously utilized and synthesized by Jiaze Xie. The doubly oxidized complex $[(FeTPA)_2TTFtt][BAr^F{}_4]_2$ features ligand centered oxidation yielding a largely closed shell, diamagnetic $TTFtt^{2-}$ core at room temperature. Upon cooling, however, the Fe(II) centers undergo spin transition from high-spin to low-spin. Simultaneously, there is a change in the electronic structure of the $TTFtt^{2-}$ unit to yield

significant open-shell, diradical character. These phenomena are investigated by a variety of experimental techniques, particularly SXRD, EPR, Mössbauer, dc magnetometry, NMR, and UV-Vis-NIR spectroscopy. Andrew McNeece and Dr. Ethan Hill were instrumental in acquiring and analyzing the SXRD and EPR data, respectively, and external collaborators Juan Mora and Kelsey Collins collected Mössbauer data. Understanding of these behaviors was dependent on key computational work carried out by Kate Jesse, Nik Boyn, and Professor David Mazziotti.

CHAPTER 1: INTRODUCTION TO MAGNETIC MATERIALS AND EXTENDED SOLIDS

1.1 History and Basics of Magnetism

Molecular magnetism emerged as a prominent field in the 20th century the field, aided by the groundbreaking work done by scientists such as J.H. Van Vleck, P.W. Anderson, J.B. Goodenough, J. Kanamori, and others. The fundamentals of molecular magnetism in this section are drawn heavily from the seminal work by Olivier Kahn in his book Molecular Magnetism.[1]

The primary way the magnetic properties of the materials in this thesis have been investigated and interpreted is by their molar magnetic susceptibility, χ [cm^3/mol or "emu"], where the definition of χ relies upon the experimentally determined magnetization (M, [cm^3 Oe/mol]) in a given applied magnetic field (H, [Oe]). In most cases, χ is defined as:

$$\mathrm{M} = H \times \chi \qquad \textbf{1.1}$$

It is clear why the susceptibility is so named, as it describes the characteristic of a material – in a specific state and at a specific temperature – that is how susceptible it is to being magnetized, where magnetization is simply the net alignment of electrons in a specific orientation. For materials containing first row transition metals, the magnitude of the susceptibility of paramagnetic materials is primarily related to the value of S (where S = ½ × # of unpaired electrons) and the temperature of the material. This is referred to a "spin only" treatment of the susceptibility. Angular momentum—introduced via spin-orbit coupling— for these lighter mass spin centers is typically a small adjustment to the spin only model, whereas for heavy atoms like rare-earths, spin-orbit coupling can be a major contributor to χ.

For paramagnetic materials (i.e. materials which have unpaired electrons residing on spin

centers, but negligible coupling between those spin centers) susceptibility is positive, meaning that electrons in parallel with an applied magnetic field are of a lower energy than electrons which are antiparallel with the field. Paramagnets therefore have magnetization in parallel with an applied field.

It must be noted here that pure electron spin is a quantum mechanical feature and has no intrinsic spatial component, so terms such as up/down, α/β, and +/- are interchangeable and based on convention. The removal of the degeneracy of these electron spin orientations in an applied field is known as Zeeman splitting. The energy of a spin center with a spin, *S*, due to an applied magnetic field is given by the Hamiltonian:

$$\hat{H} = g\,\mu_B\, H \cdot S \qquad \textbf{1.2}$$

To a lesser degree, paramagnetic materials – and indeed all materials – have a diamagnetic component of susceptibility which, unlike the paramagnetic susceptibility, is negative and in opposition to the applied field. The measured diamagnetic susceptibility of specific atoms—often referred to as Pascal's constants—are well known,[2] and these susceptibilities are corrected for throughout this thesis. Finally, a small temperature independent component of paramagnetic susceptibility may also be present in paramagnets, however this contribution is typically quite small.

The temperature of a sample dictates the susceptibility. As a general rule, the population of energy levels is determined—via Boltzmann distribution—by the available thermal energy available at a given temperature. As previously stated, paramagnets in an applied field will have different energies based on their orientation (e.g. parallel/antiparallel). The higher energy states are depopulated upon cooling, as less thermal energy is available (e.g. to "spin flip" the electron

into the higher energy state). For this reason, χ increases upon cooling for a paramagnet as there is less thermal energy available to excite electrons into an antiparallel state and the material is therefore more susceptible to magnetization (e.g. net parallel alignment) by the applied magnetic field. The χ multiplied by the temperature (T, [K]) versus temperature is used often throughout this thesis to evaluate materials in comparison to a hypothetical simple paramagnet which has a temperature independent χT. In a spin only approximation, this value is:

$$\chi T = (\frac{g^2}{8}) [S \times (S + 1)] \quad \textbf{1.3}$$

This approximation is especially useful at high temperatures (often room temperature for molecular magnetic materials such as those described in this thesis) where many non-paramagnetic materials can be treated as paramagnetic, because any magnetic coupling and/or single ion anisotropy are sufficiently weak.

As a note, the units most commonly used throughout this thesis are Gaussian-cgs, which are the conventional choice in the field and almost exclusively used over the SI unit system. Other "units" such as the Bohr magneton (μ_B) are also commonly used (e.g. as μ_B/ion for M) in the field and are occasionally used here. Conversion charts are readily available for those interested.

Beyond the more straightforward magnetism of diamagnetic or paramagnetic materials, more interesting behavior is observed with the inclusion of one or both of the following: single ion anisotropy or magnetic coupling. Single-ion anisotropy is a key phenomenon important for single molecule magnets,[3] but also plays a vital role in nearly all interesting magnetic materials. For transition metals, single ion anisotropy relies primarily upon spin-orbit coupling (SOC) which is the coupling between the spin of an electron and the angular momentum associated with the orbital it resides in. Because orbitals are anisotropic, SOC leads to certain directionalities (e.g. along some

bond axis) having lower energy, such that there is a preferred, "easy" axis (typically defined as a *z* axis) or plane along which the moments of unpaired electrons will orient preferentially. Relatedly, ions with an easy axis have a higher energy "hard" plane (*xy* plane) that acts as a barrier to spin flipping. The modulation of these energy levels (e.g. of different spatial orientations) such that they are no longer degenerate is known as zero-field splitting (ZFS), so called because the orientations are nondegenerate even in the absence of an applied magnetic field. Organic polyradicals, however, are typically composed of lightweight elements that have negligible SOC and therefore anisotropy observed in these cases is primarily due to electrostatic, dipolar coupling known as spin-spin coupling (SSC).[4] Regardless of the source, the axial component of ZFS is denoted as *D,* and the rhombic term is *E*. Both are defined by the Hamiltonian:

$$\hat{H} = D\,(\hat{S}_z^2 - \tfrac{1}{3}S(S+1)) + E\,(S_x^2 - S_y^2) \qquad \textbf{1.4}$$

Magnetic coupling (J, [cm^{-1}]) occurs when the orientation of one electron influences the orientation of another. The defining Hamiltonian of the magnetic coupling is given by:

$$\hat{H} = -\,J\,S_a S_b \qquad \textbf{1.5}$$

Here, the *a* and *b* designations differentiate spin centers which may have different *S*. It is important to note that a scaler multiplier of 2 is often included in this Hamiltonian. When comparing various reports of *J* in the literature, it is therefore very important to normalize for the same convention (i.e. with or without the 2 times multiplier). Throughout this thesis, the *J* values have been normalized to the convention without a 2 times multiplier. Ferromagnetic coupling is defined by a positive *J* and parallel alignment of electron spins between the spin centers. Antiferromagnetic coupling is therefore defined by a negative *J* and antiparallel alignment of electron spins.

Coupling can occur by many mechanisms. Among materials containing paramagnetic metal centers connected via diamagnetic organic ligands, superexchange is a commonly observed mechanism of magnetic coupling. In superexchange, a small admixture of the excited states of a bridging diamagnetic ligand allows for indirect magnetic coupling between the spin centers it connects. This effect is most prominent across short (e.g. one to three atom) bridges. The complexes in Chapters 2–5 exhibit coupling via superexchange and short atom bridges. From these we see that typical superexchange coupling is often on a scale of $<|5|$ cm^{-1} in magnitude. Superexchange, and particularly the *sign* of *J*, is heavily dependent on the geometry of the bridge of interest, and some simplistic rules for qualitative interpretation have been established for many decades thanks to the pioneering work of Goodenough, Kanamori and others.[5]

Alternatively, direct coupling (i.e. between two spin centers) is typically much stronger than an indirect method such as superexchange. The physical origins of direct exchange are rooted in quantum mechanics, and competitive forces such as delocalization by kinetic exchange and Pauli repulsion due to the antisymmetric exchange of electrons complicate a simplistic heuristic for qualitatively predicting direct coupling, although direct orbital overlap of the interacting electrons is necessary. Direct coupling of two organic based radicals is explored in Chapter 6.

Regardless of the mechanism of coupling, the most interesting magnetic phenomena are observed when coupling and anisotropy are combined. In one dimension, this yields single chain magnetism (SCM) and is observed in the materials in Chapter 3 and 4. In the systems therein, antiferromagnetic coupling between spin centers led to spin canted ferrimagnetism. Ferrimagnetism is a general term referring to any situation where an antiferromagnetic ground state does not yield zero magnetization. This is typically observed in two ways: coupling between

two spin centers of unequal *S* or the noncollinearity of the magnetic easy axes of spin centers resulting in a net magnetic moment. The latter case is called spin canted antiferromagnetism and is the type of ferrimagnetism observed in Chapter 3 and 4. SCMs, whether arising from spin canting or from ferromagnetic coupling, require anisotropy to exhibit their characteristic behavior: slow relaxation. This phenomenon was first theoretically proposed by Glauber in 1963,[6] but not shown experimentally until 2001 when Novak et al. published their work on chains of Co(II) and nitronyl nitroxide radicals.[7] Experimentally, slow relaxation is studied via ac magnetic measurements, where the applied field is oscillated between +*H* and -*H* at a given frequency. The phase (θ) shifted measured susceptibility is composed of a real, in-phase (χ′), and an imaginary, out-of-phase (χ′′) component, given by:

$$\chi' = \chi \times \cos(\theta) \quad \textbf{1.6}$$

$$\chi'' = \chi \times \sin(\theta) \quad \textbf{1.7}$$

To determine the time constants (τ_0) and energetic barriers to spin flipping (Δ) related to the material relaxation, the Arrhenius equation is used with the experimentally determined temperature dependent relaxation times (τ) of the material.

$$\tau = \tau_0 \exp(\Delta/k_B T) \quad \textbf{1.8}$$

These measurements are discussed in Chapters 3 and 4. Given a slow enough relaxation, pseudo-permanent (i.e. permanent on the time scale of measurements) magnetism can be observed. Permanent magnetism is characteristically exhibited by hysteretic magnetization versus applied field, and non-superimposable magnetization of a material that has been cooled with (FC) and without (ZFC) an applied field. These phenomena can be observed in Chapter 4.

Finally, the unique behavior of spin-crossover (SCO) or spin transition (ST) materials must be mentioned. For many first-row transition metals in an octahedral or pseudo-octahedral coordination geometry, the difference in energy between high-spin (HS) and low-spin (LS) is relatively small. With the modulation of an external stimuli, such as temperature, irradiation, or pressure, some of these materials have been observed to undergo ST between HS and LS states. This phenomenon was first reported by Cambi nearly a century ago,[8] and since then has been observed in a large number of first row transition metals — most commonly in iron. While SCO materials are often designed for large hysteretic effects for utility in molecular switch applications, we will see in Chapter 6 that the ST in materials can be coupled to secondary effects, such as modulation of diradical character of an organic ligand.

1.2 Current Advances and Future Applications

Molecular magnets have been touted for at least the last several decades as potential materials for cutting-edge applications in a wide and disparate range of areas from sensors and permanent magnets to qubits and spintronics. The eventual applications a material may be useful for depend intimately not only on the very specific magnetic behavior of that material, but are also profoundly dependent on other properties such as molecular structure, morphology, electrical conductivity, solubility, stability, and many others. The commonality in all of these materials is the basic argument in favor of molecular magnetic materials over more traditional magnetic materials. Traditional magnetic materials are typically fully inorganic, made of a limited number of constituent atoms, and often of very simple structure. While these materials have robust and important magnetic properties, such as permanent magnetism persisting at high temperatures, they are limited in the ways in which they can be modified or tuned for specific properties and applications. While traditional materials are largely limited to adjustment of proportions of

constituent elements, doping levels, or morphological features, molecular materials have a nearly limitless variety of alterations owing to their more complex coordination and the inclusion of organic ligands.

New work on SCMs is ongoing, utilizing a wide-ranging set of strategies to both increase uniaxial anisotropy and coupling strength. The very low temperatures at which magnetization becomes pseudo-permanent (i.e. the blocking temperature, T_B) remain a practical hurdle for SCMs, and the highest reported values are still under roughly 20 K. In recent work by Sutter and coworkers, superexchange over short cyanide bridges leads to ferromagnetic coupling between Cr(III) and Fe(II) on the order of $J \sim 2$ cm^{-1}. Despite the high energy barrier to spin flipping arising from large (for first row transition metals) uniaxial anisotropy of Fe(II) ($D \sim$ -16–20 cm^{-1}) , there is still no hysteresis observed above 5 K.[9] Many recent reports of SCMs show additional attractive features beyond slow relaxation. The semiquinoid chain compound reported by Harris *et al.* shows temperature dependent electron transfer between the Fe(II)-hydroquinone and Fe(III)-semiquinone radical forms. In the Fe(III)-semiquinone radical form, which exists below ca. 220 K, strong direct coupling between the Fe(III) and ligand radical yield significant antiferromagnetic coupling of J = -81 cm^{-1}. As a contrast to the previous case, however, the Fe(III) ions only engender a small degree of anisotropy, leading to negligible hysteresis above 1.8 K.[10] Similarly, Liu and coworkers have reported a chain material that undergoes electron transfer under irradiation to interconvert between the diamagnetic LS Co(III) and paramagnetic HS Co(II), thereby switching SCM behavior on and off.[11] Other approaches include the embedding of SCMs into metal-organic frameworks (MOFs) to combine the magnetic properties of SCMs with the physical properties of MOFs—notably permanent porosity and 3Dimensional structure—to both further tailor SCM behavior as well as create multifunctional materials.[12]

A commonly cited potential application for spin crossover materials is in information storage or processing, where the spin transition itself may one day be used as a binary digit. Materials that have secondary phenomenological effects, however, are also of increasing interest. Recently, ST has been used to modulate dielectric transitions,[13] fluorescence emissions,[14] SMM behavior,[15] and ligand acidity,[16] among other properties. In Chapter 6, an example will be given of cooperative Fe(II) spin transition and modulated coupling of an organic diradical.

Organic diradicals and polyradicals which are stable and isolable as more than short-lived transient species are rare. Rajca and coworkers have published work on numerous systems which are stable to at least 160 K and have triplet (i.e. ferromagnetically coupled) ground states. In these directly coupled systems, the organic radicals have strong coupling of at least several hundred wavenumbers.[17] Power *et al.* published an intriguing study of the modulation of the diradical coupling—which is directly related to the energy difference between the singlet and triplet energy states ($\Delta E(S\text{-}T)$). This study observed the temperature dependent phase transition between two conformations of a diradical which had markedly different coupling.[18] A similar transition is discussed in Chapter 6.

The work in this thesis spans a broad range of the areas mentioned. Specific attention has been paid to the choice of metal spin center and organic linker in these materials. The first row transition metals Fe(II) and Co(II) have been utilized because of the accessibility of their high-spin states (e.g. as compared to second row transition metals), their large *S* values (e.g. as compared to earlier and later transition metals), and their superior orbital overlap with ligands (e.g. as compared to rare earth ions). The choice of organic linker is more varied—spanning more traditional ligands like carboxylates and aromatic heterocycles to more bespoke sulfur based ligands. In general, rigid

linkers are featured, both for their ability to engender specific, ordered structures and for their ability to isolate metal nodes or chains, leading to porosity (Chapter 2) or interchain isolation necessary for SCM behavior (Chapter 3). The most interesting ligand-based properties are highlighted in Chapter 6, with the TTFtt ligand. Here, redox activity yields a magnetic diradical ligand, and metal-ligand interaction—likely facilitated by superior orbital matching of sulfur and iron—leading to cooperative metal/ligand spin transition.

1.3 References

1. Kahn, O., *Molecular magnetism*. VCH: New York, NY, 1993.

2. Bain, G. A.; Berry, J. F. *J. Chem.Ed.* **2008,** 85, 532.

3. (a) Glaser, T., *Chem. Commun.* **2011,** *47* (1), 116, (b) Bar, A. K.; Pichon, C.; Sutter, J.-P., *Coord. Chem. Rev.* **2016,** *308*, 346.

4. Tesler, J., *eMagRes*, **2017**, *6*: 207.

5. (a) Goodenough, J. B., *Phys. Rev.* **1955**, *100* (2), 564. (b) Kanamori, J., *J. Phys. Chem. Solids* **1959**, *10* (2), 87.

6. Glauber, R.J. *J. Math. Physics* **1963**, *4*, 294.

7. Caneschi, A.; Gatteschi, D.; Lalioti, N.; Sangregorio, C.; Sessoli, R.; Venturi, G.; Vindigni, A.; Rettori, A.; Pini, M. G.; Novak, M. A., *Angew. Chem., Int. Ed.* **2001**, *40* (9), 1760.

8. Cambi, L.; Szegö, L., *Ber. Dtsch. Chem. Ges.* **1931**, *64* (10), 2591.

9. Pichon, C.; Suaud, N.; Duhayon, C.; Guihéry, N.; Sutter, J.-P., *J. Am. Chem. Soc.* **2018**, *140* (24), 7698.

10. DeGayner, J. A.; Wang, K.; Harris, T. D., *J. Am. Chem. Soc.* **2018**, *140* (21), 6550.

11. Jiang, W.; Jiao, C.; Meng, Y.; Zhao, L.; Liu, Q.; Liu, T., *Chem. Sci.* **2018**, *9* (3), 617.

12. Wang, M.; Gou, X.; Shi, W.; Cheng, P., *Chem. Commun.* **2019**, *55* (74), 11000.

13. Zheng, H.; Meng, Y.-S.; Zhou, G.-L.; Duan, C.-Y.; Sato, O.; Hayami, S.; Luo, Y.; Liu, T., *Angew. Chem. Int. Ed.* **2018**, *57* (28), 8468.

14. Wang, J.-L.; Liu, Q.; Meng, Y.-S.; Liu, X.; Zheng, H.; Shi, Q.; Duan, C.-Y.; Liu, T., *Chem. Sci.* **2018**, *9* (11), 2892.

15. Shao, D.; Shi, L.; Yin, L.; Wang, B.-L.; Wang, Z.-X.; Zhang, Y.-Q.; Wang, X.-Y., *Chem. Sci.* **2018**, *9* (41), 7986.

16. Dhers, S.; Mondal, A.; Aguilà, D.; Ramírez, J.; Vela, S.; Dechambenoit, P.; Rouzières, M.; Nitschke, J. R.; Clérac, R.; Lehn, J.-M., *J. Am. Chem. Soc.* **2018**, *140* (26), 8218.

17. (a) Rajca, A.; Shiraishi, K.; Vale, M.; Han, H.; Rajca, S. *J. Am. Chem. Soc.* **2005**, *127* (25), 9014. (b) Gallagher, N.; Zhang, H.; Junghoefer, T.; Giangrisostomi, E.; Ovsyannikov, M.P.; Rajca, S.; Casu, M.B.; Rajca, A. *J. Am. Chem. Soc.* **2019**, 141, 4764.

18. Su, Y.; Wang, X.; Wang, L.; Zhang, Z.; Wang, X.; Song, Y.; Power, P.P., *Chem. Sci*., **2016**, *7*, 6514

CHAPTER 2: INCORPORATION OF PYRAZINE AND BIPYRIDINE LINKERS WITH HIGH-SPIN FE(II) AND CO(II) IN A METAL-ORGANIC FRAMEWORK

2.1 Abstract

A series of isoreticular metal-organic frameworks (MOFs) of the formula M(BDC)(L) (M = Fe(II) or Co(II), BDC = 1,4-benzenedicarboxylate, L = pyrazine (pyz) or 4,4′-bipyridine (bipy)) were synthesized and characterized by N_2 gas uptake measurements, SXRD and XRPD, magnetometry, X-ray absorption spectroscopy, and Mössbauer spectroscopy. These studies indicate the formation of a permanently porous solid with high-spin Fe(II) and Co(II) centers that are weakly coupled, consistent with first principles density functional theory calculations. This family of materials represents unusual examples of paramagnetic metal centers coordinated by linkers capable of mediating magnetic or electronic coupling in a porous framework. While only weak interactions are observed, the rigid 3D framework of the MOF dramatically impacts the properties of these materials when compared with close structural analogues.

2.2 Introduction

This chapter examines many basic concepts necessary for understanding some of the more complex magnetism and electronic structures of the materials in subsequent chapters. These materials feature exclusively high-spin Fe(II) and Co(II) ions in the absence of significant anisotropy and with only minor coupling due to superexchange. Interestingly, the extended 3Dimensional framework appears to have significant impacts on the magnetic behavior of the Fe centers. These materials therefore serve as an appropriate introduction to the fundamental components of the behaviors seen in later chapters—particularly structure-property relationships—while also exhibiting permanent porosity and unique structural features.

Metal-organic frameworks (MOFs) are characterized by high surface area and porosity that make them a natural choice for applications such as gas storage and separation, as well as heterogeneous catalysis.[1-4] In addition to studies utilizing MOFs for these applications, the electronic and magnetic properties of these porous systems have recently attracted increasing interest.[5] Typically, MOFs include diamagnetic metal centers (e.g. Zn(II), Al(III), Zr(IV), etc.) or clusters combined with diamagnetic, insulating linkers which have no charge or spin carriers accessible for magnetic and electronic phenomena. Systems that do feature suitable paramagnetic ions frequently feature linkers that mediate weak electronic and magnetic coupling. Nevertheless, there has been substantial effort in developing porous materials that display antiferromagnetic or ferromagnetic coupling,[6,7] spin canting,[8] or conductivity.[9]

In the context of expanding this class of materials, we have been investigating metal centers with high *S* values, in conjunction with linkers that may support strong electronic or magnetic coupling. One such bidentate linker is pyrazine (pyz) which, along with its expanded analogue 4,4′-bipyridine (bipy), has been shown to engender strong electronic coupling.[10] Despite the ubiquity of these linkers in both discrete complexes and 1D coordination polymers, the properties of 3D materials that incorporate these linkers and paramagnetic metal centers have not been thoroughly investigated.[10,11] This limited depth of study has prompted us to investigate the ability of these linkers to mediate magnetic and electronic coupling between paramagnetic centers in a structurally confined 3D MOF scaffold. The combination of pyz or bipy with Fe(II) and Co(II) salts and 1,4-benzenedicarboxylate (BDC) provides a new family of MOFs that feature high-spin metal centers forming infinite chains with these linkers.

2.3 Results and Discussion

2.3.1. Syntheses and Structures Mixing $Fe(OAc)_2$, H_2BDC and pyz in DMF with a modulating agent results in the formation of brown crystals which can be activated to provide Fe(BDC)(pyz) (**1**) in good yield. SXRD of solvated **1** reveals a structure consisting of Fe(BDC) sheets with 7 Å triangular pores and 17.5 Å hexagonal pores (Figure 2.1A) pillared through each Fe(II) atom by pyz (Figure 2.1B). Within the Fe(BDC) sheet, Fe(II) is coordinated to two O atoms from one chelated BDC and two O atoms from two separate BDC μ-OCO bridges to an adjacent Fe(II). The chelated κ^2 O–Fe–O bond angle is 60.4(1)°, while the μ-κO:κO' bridged O–Fe–O bond angle is 125.3(2)°. The N-Fe-N bond is very nearly linear with a 178.1(2)° angle. The coordination

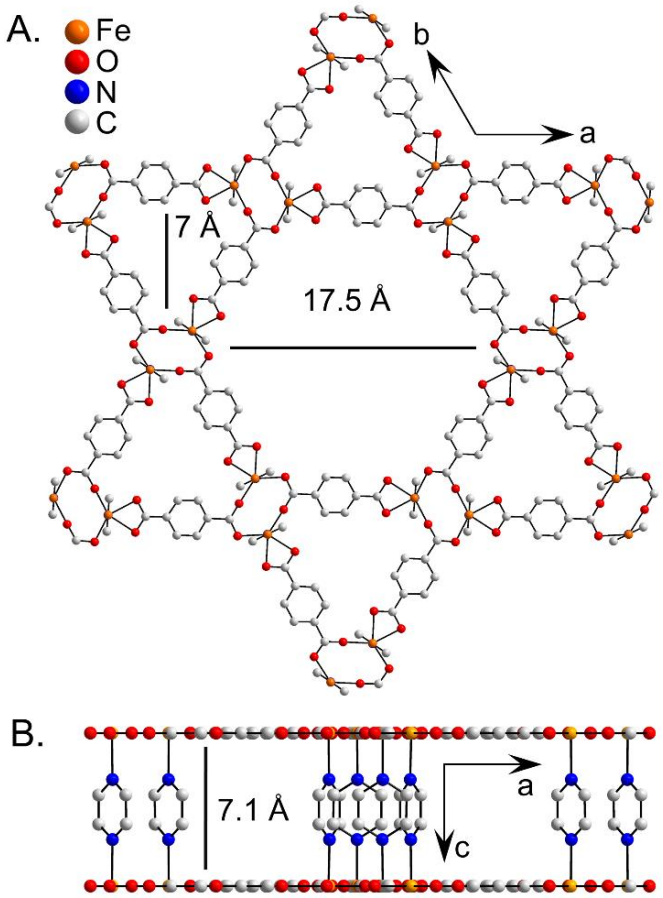

Figure 2.1 SXRD structure of solvated **1** showing (A) the hexagonal and triangular pores and (B) the pyrazine axial ligands. H-atoms and disordered solvent have been omitted for clarity.

environment around Fe(II) is similar to that previously reported for $[Fe_2(\mu\text{-}Bz)_2(\mu\text{-}pyz)_2(Bz)_2]\cdot(HBz)$ (Bz = benzoate) which features benzoate ligands instead of the BDC linkers in **1**, rendering a 1D chain material. The bond length differences between **1** and $[Fe_2(\mu\text{-}Bz)_2(\mu\text{-}pyz)_2(Bz)_2]\cdot(HBz)$ are < 0.1 Å with the most notable difference being the rigorous planarity of the Fe(BDC) sheets in **1** which are orthogonal to the Fe(pyz) chains.[12]

The FeO_4 units in $[Fe_2(\mu\text{-}Bz)_2(\mu\text{-}pyz)_2(Bz)_2]\cdot(HBz)$ are non-planar and are slightly bent at an 86° angle to the axial Fe(pyz) chains. The structure of solvated **1** is representative of the bulk

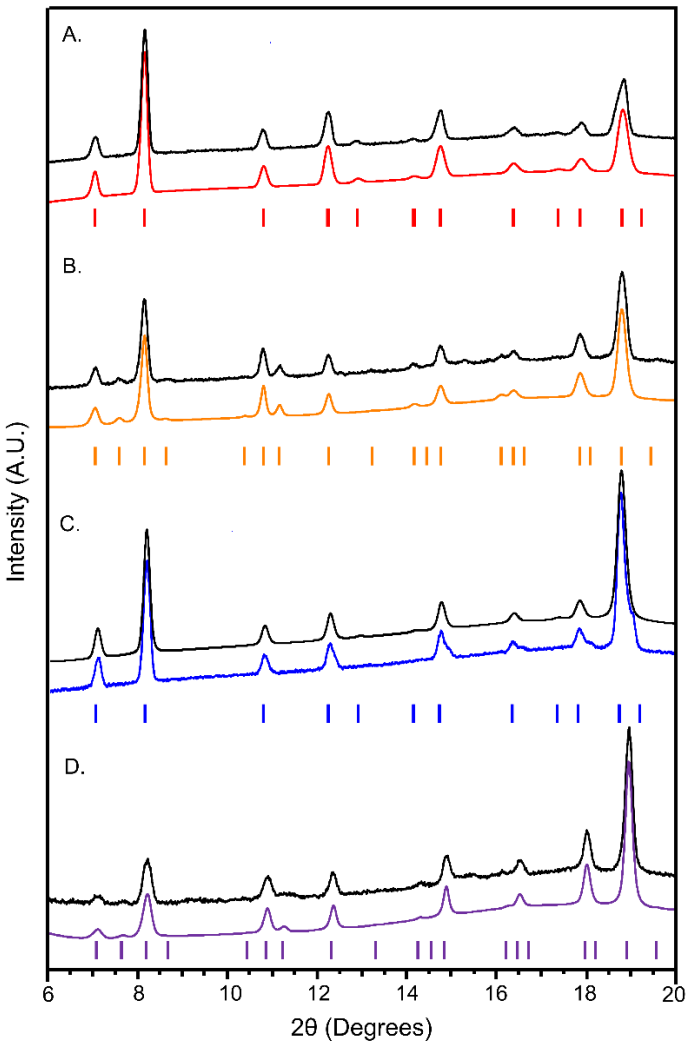

Figure 2.2 Experimental XRPD (black) and the calculated Le Bail fits (color) of (A) **1**, (B) **3**, (C) **2** and (D) **4** in P6/m. The theoretical peak positions are shown at the bottom as lines.

Table 2.1. XRPD fit parameters for **1**, **2**, **3** and **4** from the Le Bail fit to space group P6/m.

	Fe(BDC)(pyz)	Fe(BDC)(bipy)	Co(BDC)(pyz)	Co(BDC)(bipy)
a	25.020(2)	24.957(2)	25.06(1)	24.83(1)
c	7.238(1)	11.598(3)	7.23(1)	11.53(1)
V	3924(1)	6256(2)	3930(5)	6153(5)

material as the XRPD pattern of **1** was fit to the space group (*P*6/*m*) obtained from SXRD (Figure 2.2A, Table 2.1) by University of Chicago staff crystallographer Dr. Alexander S. Filatov. The permanent porosity of this material after activation was verified by nitrogen uptake measurements, which indicated a surface area of 1360 m^2/g using Brunauer-Emmett-Teller (BET) theory (Figure 2.3).[13]

Co(BDC)(pyz) (**2**) was synthesized under analogous conditions to **1** and yielded pink, translucent crystals. The N_2 adsorption isotherm yields a BET surface area of 1,370 m^2/g (Figure 2.3). This value is very similar to that obtained for **1** and suggests that these two species may be

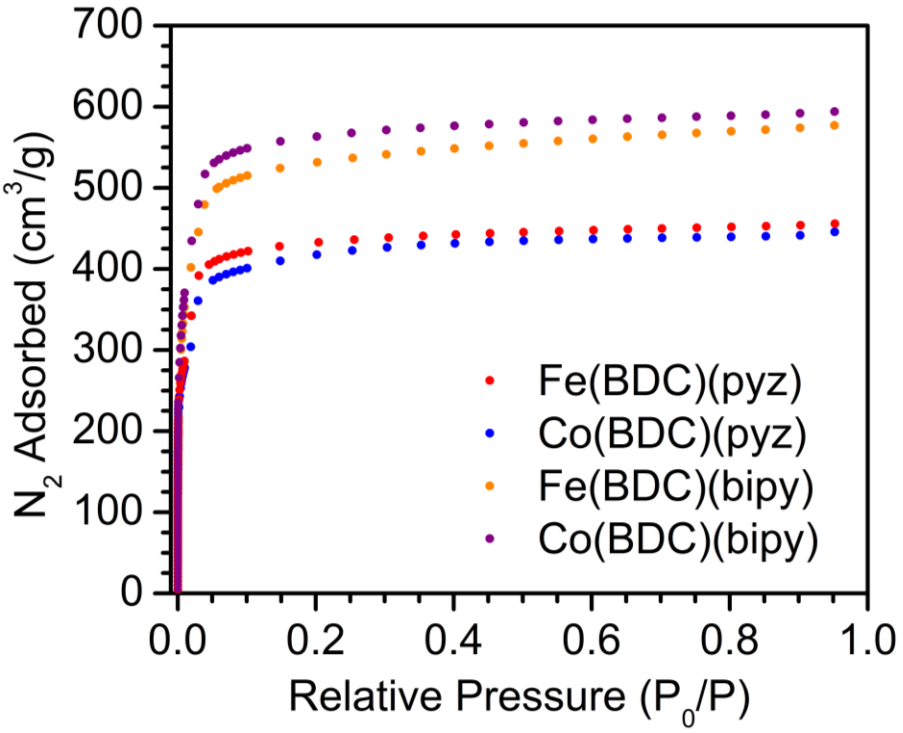

Figure 2.3. Nitrogen uptake isotherms for **1**, **2**, **3**, and **4** at 77 K.

isoreticular. Indeed, fitting of the XRPD pattern of **2** to the SXRD parameters of **1** provides a good fit with a comparable unit cell parameter *c* of 7.23(1) Å and *a/b* parameters of 25.06(1) Å (vs 7.238(1) Å and 25.020(2) Å, for **1** (Figure 2.2C, Table 2.1)). While single crystal data could not be obtained for **2**, extended X-ray absorption fine structure (EXAFS) spectroscopy, analyzed by Dr. Filatov, indicates that the primary coordination sphere in **2** is similar to that determined by SXRD for **1** (Figure 2.4, Table 2.2). The calculated Co-N/O bond lengths are within <0.1 Å of the analogous bonds crystallographically determined for **1**. Given the consistency between the EXAFS and XRPD pattern fits, as well as in the surface areas, we conclude that **1** and **2** are isostructural.

Direct formation of Fe(BDC)(bipy) (**3**) or Co(BDC)(bipy) (**4**) was not successful under analogous synthetic conditions to **1** and **2**. Materials **3** and **4** were formed by post–synthetic modification by exchange of the pyz ligand in **1** and **2** with bipy.[14] Progress of the exchange was monitored over the course of 63 hours by analyzing the ^{1}H NMR spectra of digested aliquots for the relative intensity of the pyz and bipy signals (Figure 2.5). The solid samples which were separated, washed, and digested at the indicated intervals show a decrease and eventual elimination

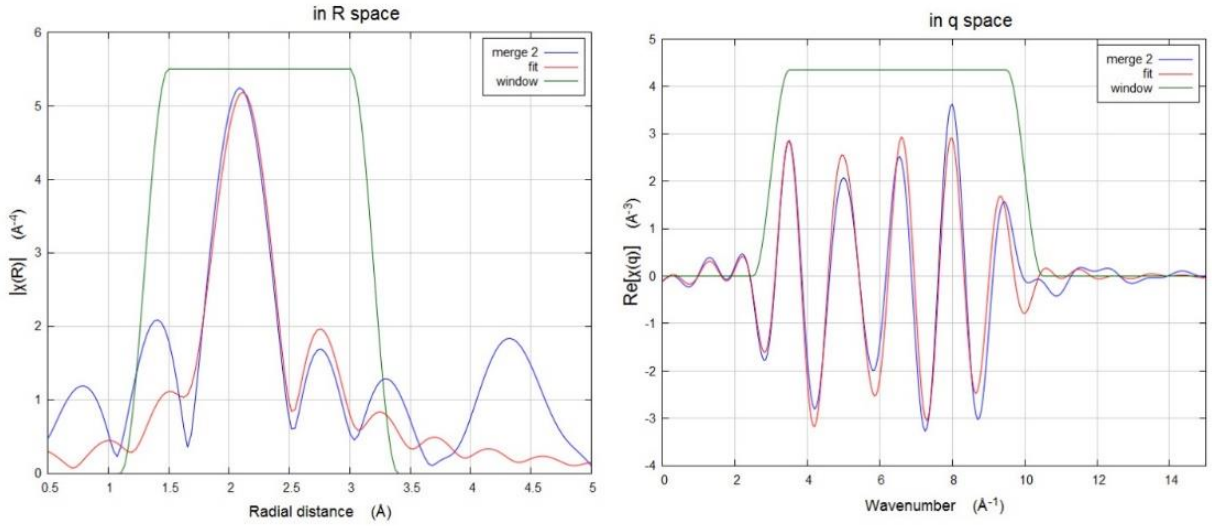

Figure 2.4. Fit results of EXAFS data for **2** at the Co edge.

Table 2.2. EXAFS fit parameters for **2**

Edge	Fitting range	Paths	Bond length R (Å)	Coordination Number (n)	Debye Waller Factor	Energy Shift ΔE (eV)
Co edge S_o^2=1.00	R=1.3-3.2 Å dr=0.4 k= 3.0-10.5 $Å^{-1}$ dk = 1	Co-O	2.02 ± 0.04	1	0.009 ± 0.002	9.4 ± 1.7
		Co-O	2.06 ± 0.04	1	0.009 ± 0.002	
		Co-N	2.16 ± 0.02	2	0.015 ± 0.016	
		Co-O	2.19 ± 0.02	2	0.015 ± 0.016	

of the peak corresponding to pyz and the growth of peaks arising from bipy, clearly indicating linker exchange. The exchange of pyz (2.77 Å) for bipy (7.08 Å) is further corroborated by the increase in BET surface areas of **3** (1,828 m^2/g) and **4** (1,818 m^2/g) over the pyz analogues (Figure 2.3).

Single crystals suitable for SXRD could not be attained, however XRPD patterns of **3** and **4** were fit by the Le Bail method by Dr. Filatov. The pattern fits of **3** and **4** correspond to similar *a/b* unit cell parameters with a large (>4 Å) increase in *c*, as expected for the expansion in the axial (*c*) direction upon exchange of pyz for bipy (Table 2.1). XRPD patterns of the pyz and bipy analogs have high similarity in their strongest reflections, which arise from Miller planes intersecting only the *ab* face, however the increase in *c* can be observed in the development of several weak intensity peaks (Figure 2.2). In sum, we have verified the complete exchange of the pyz ligands for bipy by digesting **3** and **4** and analyzing their linker composition. Similarly, both of these compounds have virtually identical surface areas as determined by gas uptake measurements. Finally, both **3** and **4** have nearly identical XRPD patterns, with the appearance of new peaks corresponding to the expansion of the unit cell in the *c* direction. These combined data strongly suggest that the structures of **3** and **4** are closely related to **1** and **2**, showing the synthesis and isolation of a new

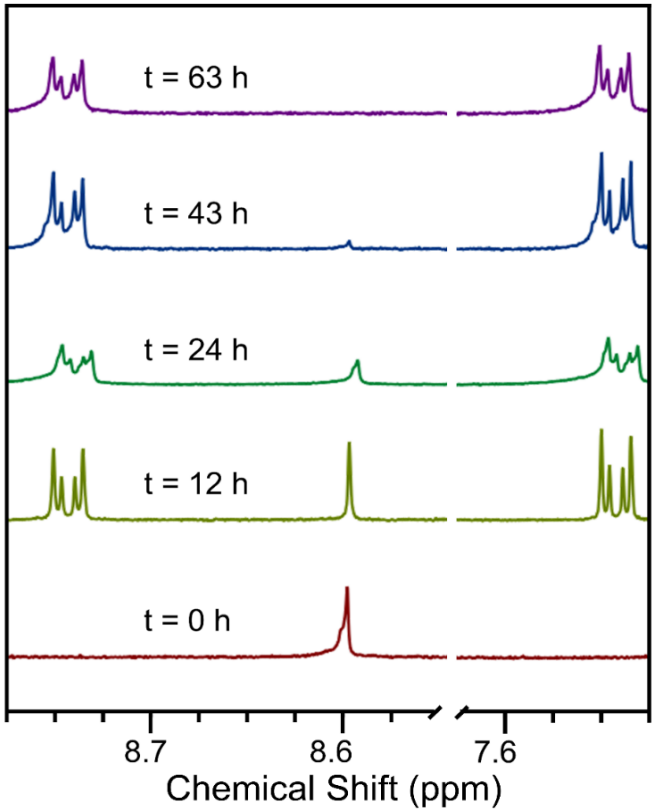

Figure 2.5. ^{1}H NMR spectra of aliquots from the transformation of **1** to **3**. Solid aliquots were washed, digested in nitric acid, neutralized and extracted into $CDCl_3$. The pyz peak is at 8.60 ppm and the bipy peaks are centered at 7.52 and 8.72 ppm. The x-axis has been truncated to remove the peak at 8.02 ppm from DMF.

isoreticular family of MOFs incorporating pyz and bipy linkers.

2.3.2. Conductivity, Magnetism and Mössbauer Measurements Room temperature, isotropic pressed pellet conductivity measurements were carried out on **1**. The conductivity was too low to yield a linear potential vs. current relationship, providing an upper limit of ~10^{-14} S/cm. First principles DFT+U calculations were carried out by our collaborators Arin R. Greenwood and Professor Giulia Galli of the Pritzker School of Molecular Engineering. These calculations confirmed the insulating band structure of **1**, with a filled valence band of primarily Fe *d* and O *p* character and an unpopulated N-based conduction band (Figure 2.6A).

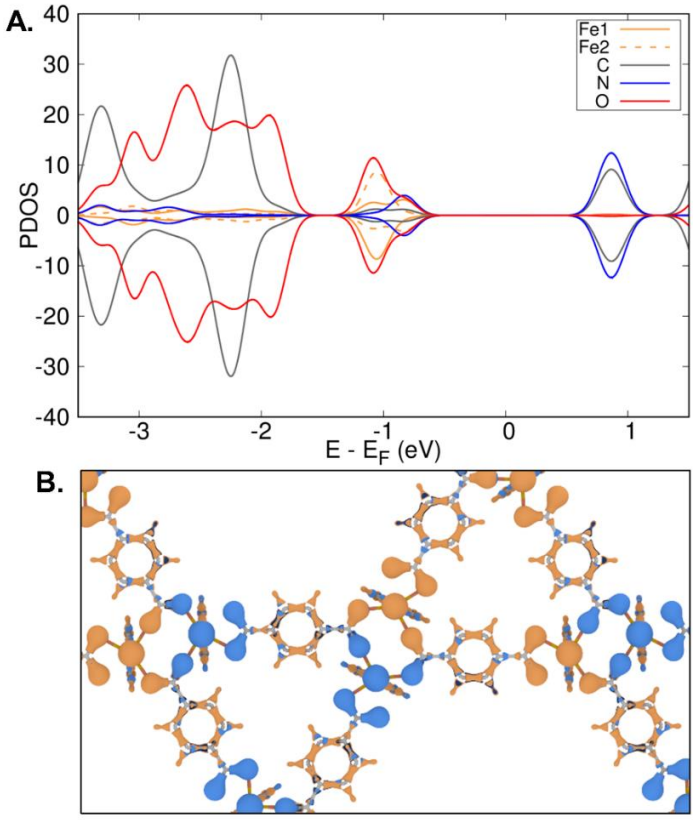

Figure 2.6. (A) Projected electronic density of states for an AFM structure of **1**. States with Fe character are partitioned into primarily spin-up (Fe1) and spin-down (Fe2) which are illustrated in the spin density plot (B) as spin up (orange) and spin down (blue) electron density. Isosurfaces are shown at 9% of maximum value.

The electronic structure and magnetic properties of **1**-**4** were also probed by temperature dependent magnetometry. The χT_{300} of **1** is 2.74 cm^3 K/mol, which is comparable with the spin-only χT of 3 cm^3 K/mol expected for an $S = 2$ center. This corresponds to a g value of 1.93(4), a value which is consistent over several samples. Fe(II) ions with $S = 2$, however, typically exhibit higher g values in the range of 2.00 – 2.29.[15,16]

To exclude the possibility of low-spin impurities, Mössbauer data was acquired for **1**. Fits and data collection were done by our collaborator Dr. Audrey Gallagher at Northwestern University and yielded an δ of 1.171(1) mm/s and ΔE_Q of 3.198(2) mm/s (Figure 2.7), both of which are consistent with high–spin Fe(II).[17] The magnetic and Mössbauer data strongly support

a high-spin Fe(II) center, although the origin of the lower than expected χT values is not entirely clear. As temperature decreases, the χT value of **1** also decreases, suggesting some combination of antiferromagnetic coupling and zero–field splitting effects (Figure 2.8A, Table 2.5).

The DFT+U calculations indicate that antiferromagnetic coupling is energetically favorable over the ferro- and non-magnetic systems by 0.03 eV (Table 2.3). While this value is small, we found that different relaxed geometries for the three spin states suggest unfavorable switching and high energy barriers between states (Table 2.4). To quantify the degree of coupling the χT vs. T data was fit to an isotropic Heisenberg model with the following Hamiltonian:

$$\hat{\mathbf{H}} = g\mu_B \boldsymbol{H}\cdot\boldsymbol{S} - J\,\boldsymbol{S}_i\boldsymbol{S}_j + D_i[\boldsymbol{S}_i^2 - (\boldsymbol{S}_{i+1})/3] + D_j[\boldsymbol{S}_j^2 - \boldsymbol{S}_j(\boldsymbol{S}_{j+1})/3] \qquad \textbf{2.1}$$

An exchange parameter, J, of -4(1) cm^{-1} was found for **1**. One expected magnetic exchange

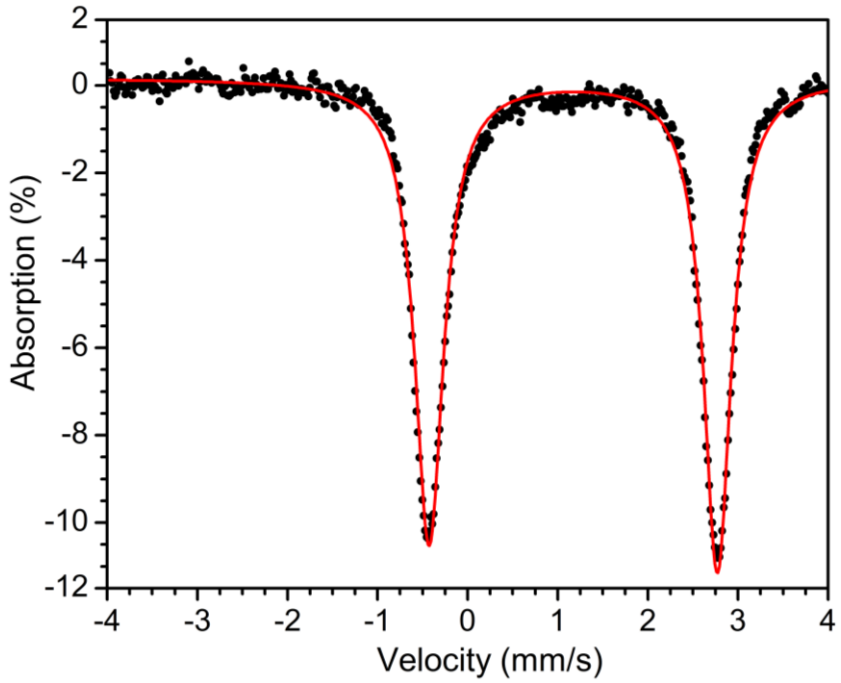

Figure 2.7. Mössbauer spectrum for **1** collected at 80 K exhibits a quadrupole doublet with an isomer shift of δ = 1.171(1) mm/s and a quadrupole splitting of ΔE_Q = 3.198(2) mm/s, indicative of a high-spin Fe(II) center.

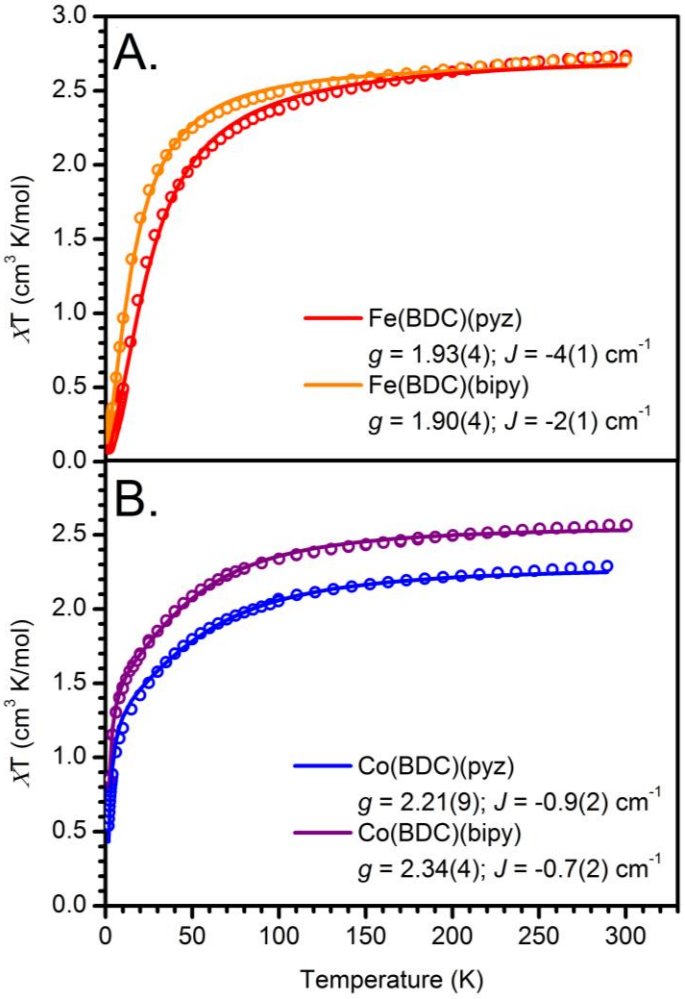

Figure 2.8. Temperature dependent χT data for (A) **1** and **3**, and (B) **2** and **4**. Solid lines are the fit to the isotropic Heisenberg model.

pathway in **1** is superexchange mediated by pyz. Reported values for Fe(II)–pyz–Fe(II) couplings, however, are typically in the range of J = -1.1 – -2.4 cm^{-1}.[15a,b,d] While carboxylate bridges can mediate ferromagnetic coupling, antiferromagnetic exchange is more commonly observed, and likely contributes to the J value of **1**.[17a,18]

The magnetic data for **2** gives a χT_{300} = 2.29 cm^3 K/mol. This is higher than the spin only value (χT = 1.87 cm^3 K/mol) as expected for an S = 3/2 Co(II) center with unquenched orbital angular

Table 2.3. DFT+U calculated energy differences between antiferromagnetically (AFM), ferromagnetically (FM) and non-magnetically (NM, i.e. low-spin) coupled systems of **1**.

	Energy Difference
AFM - FM	-0.0323 eV
AFM - NM	-14.1178 eV
FM - NM	-14.0855 eV

momentum (Figure 2.8B, Table 2.5). The antiferromagnetic coupling in **2** is much weaker than in **1**, with a *J* value of -0.9(2) cm^{-1}. Previous reports of pyz bridged Co(II) units give *J* values of -0.38 and -0.32 cm^{-1}.[19] Additional antiferromagnetic exchange via the bridging carboxylates again likely contributes to the *J* value of **2** as in **1**. The calculations indicate a substantial amount of antiferromagnetically coupled spin density across the Fe_2O_6 unit in **1** (Figure 2.6B), supporting the involvement of this exchange pathway in **1** and, correspondingly, in **3**.

The χT_{300} = 2.71 cm^3 K/mol for **3** is in good agreement with that of **1** (Figure 2.8A, Table 2.5). As in **1**, the observed χT is lower than expected. The strength of the antiferromagnetic coupling in **3** is expected to be weaker than in **1**, due to the larger separation and weakening of the axial ligand superexchange pathway. This is seen in other pyz/bipy analogues previously reported. A *J* value of -2(1) cm^{-1} was acquired from fitting of the magnetic data. In reports of analogous 1D chains of pyz or bipy, a decrease in *J* from -3.85 to -0.72 cm^{-1} has been observed.[15d] The larger than expected antiferromagnetic coupling observed for **3** can again be attributed to an antiferromagnetic exchange contribution from the carboxylate bridges. The magnetic data for **4** is

Table 2.4. Stress on the unit cell for the three spin states at the experimental lattice constant and PBE relaxed geometry, and for the same geometry with the additional U parameter.

	Stress at PBE (kbar)	Stress at PBE + U (kbar)
AFM	3.25	7.41
FM	-0.65	7.57
NM	-13.34	-8.09

Table 2.5. Fitting parameters and error from the magnetic data of **1**, **2**, **3** and **4**

1		
Parameter	**Value**	**Error**
g	1.93	0.04
J (cm^{-1})	-4.2	0.96
D (cm^{-1})	10	20

3		
Parameter	**Value**	**Error**
g	1.9	0.04
J (cm^{-1})	-2.1	1
D (cm^{-1})	20	20

2		
Parameter	**Value**	**Error**
g	2.21	0.09
J (cm^{-1})	-0.9	0.2
D (cm^{-1})	60	40

4		
Parameter	**Value**	**Error**
g	2.34	0.04
J (cm^{-1})	-0.7	0.2
D (cm^{-1})	60	20

similarly related to **2**. The χT at 300 K is 2.56 cm^3 K/mol (Figure 2.8B, Table 2.5) and g = 2.34(4), consistent with **2**. The antiferromagnetic coupling of **4** (J = -0.7(2) cm^{-1}) is similar, within error, to that of **2**. This smaller decrease in J from pyz to bipy bridged Co(II) systems is consistent with previous reports in which only a slightly lower value is observed in the bipy (-0.34 cm^{-1}) vs. pyz (-0.38 cm^{-1}) mediated coupling.[19a]

2.3.3. Discussion of Magnetic Properties Interestingly, the magnetic properties of **1** and **2** are distinct from the structurally similar $[M_2(\mu\text{-}Bz)_2(\mu\text{-}pyz)_2(Bz)_2]\cdot(HBz)$ (M = Co(II) and Fe(II)) systems which are 1D chains with benzoate ligands. These materials exhibit spin canted antiferromagnetism and metamagnetism for the Co(II) material and spin crossover in the Fe(II) material.[12] Because spin crossover is accompanied by a change in bond length, as seen in $[Fe_2(\mu\text{-}Bz)_2(\mu\text{-}pyz)_2(Bz)_2]\cdot(HBz)$, the lack of such behavior in **1** may be attributed to the structural restriction of the lattice.[12,20] Indeed, it has previously been shown that Fe(II) spin crossover in MOFs is dependent on structural flexibility.[21] Our DFT+U calculations of **1** predict that the lattice strain of d^6 Fe in a low-spin state would be energetically unfavorable by more than 5 eV, supporting that the rigid framework prevents spin crossover (Table 2.4). Similarly, the spin canting observed in the Co(II) material should be associated with a lack of collinearity of the magnetic and structural

axes of Co(II).[16,22] This is observed in the coordination polymer, which does not have a rigorously planar equatorial CoO_4 unit, but which shows a bisecting angle of the axial chain and equatorial planes of roughly 86°. As previously discussed, the structure of **2** should be nearly identical to that of **1**, in which the axial chain and equatorial plane bisect at 90°, disallowing non-collinearity of magnetic and crystallographic axes and thus prohibiting spin canting. While it is difficult to compare two different materials, it seems likely that the rigid 3D structure in **1** and **2** modifies their magnetic behavior when compared with the 1D systems.

In the following chapter, a case of spin canting of Co(II) will be discussed in which the structure enforces non-collinearity of magnetic axes, in contrast to the case here. Additionally, in Chapter 6 spin crossover of a Fe(II) complex will be featured. In this case even packing effects of the discrete complex will lead to hindered spin transition.

2.4 Conclusions

In summary, an isoreticular series of metal-organic frameworks was synthesized and characterized. Magnetometry measurements confirmed that the metal centers (Fe and Co) are high-spin and in a 2+ oxidation state, which is supported by Mössbauer spectroscopy and DFT calculations for **1**. The M(BDC)(L) series exhibits antiferromagnetic coupling, likely mediated by a combined effect from both the BDC and L ligands. The effect of structural confinement in these systems appears to quench possible spin canting or spin crossover phenomena and illustrates the effect of the rigid 3D MOF structure. These materials represent rare examples where high-spin metal centers have been combined with pyrazine and bipyridine linkers in a highly porous extended solid.

2.5 Experimental Methods

General Considerations. Unless otherwise noted, all chemicals were purchased from suppliers and used without further purification. All syntheses were carried out under an atmosphere of N_2 in an MBraun UniLab Pro glove box. All solvents were dried and degassed in a Pure Process Technologies solvent system and stored over 4 Å molecular sieves. Solvents were tested for O_2 and H_2O with a standard solution of sodium benzophenone ketyl radical. Details of the characterization methods can be found in the Supporting Information. Elemental C, H, and N analysis was performed on samples of **1**, **2**, **3**, and **4**. The small discrepancies between the theoretical and measured C, H, and N mass percent may be the effect of residual solvent, water, linker or templating agent. In the case of **3** and **4**, the lower activation temperatures necessary to retain crystallinity may be responsible for the larger deviations from the theoretical mass percent likely due to residual solvent.

Fe(BDC)(pyz) (**1**)**.** Iron (II) acetate (0.085 g, 0.5 mmol) was dissolved in DMF (6 mL) at 100 °C. Malonic acid (1.3 g, 12.5 mmol) and pyrazine (0.4 g, 5 mmol) were dissolved in DMF (6 mL). Terephthalic acid (0.081 g, 0.5 mmol) was dissolved in DMF (6 mL) at 100 °C. The malonic acid/pyrazine and terephthalic acid solutions were added sequentially to the iron (II) acetate solution and the resulting mixture was heated at 100 °C for 2 days to yield brown crystals. The polycrystalline material was then washed twice with fresh DMF. Analytically pure material was activated by heating the crystals under vacuum at 50 - 100 °C for 1 week to give a 62% yield (0.094 g, 0.31 mmol). Elemental analysis: expected for $FeC_{12}H_8N_2O_4$: % C, 48.04; H, 2.69; N, 9.34. Found: % C, 47.25; H, 3.08; N, 9.62.

Co(BDC)(pyz) (**2**). Cobalt (II) acetate · $4H_2O$ was dried overnight in a vacuum oven at 80 °C to produce anhydrous cobalt (II) acetate. Cobalt (II) acetate (0.041 g, 0.25 mmol) was dissolved in DMF (6 mL) at 100 °C. Malonic acid (0.39 g, 3.75 mmol) and pyrazine (0.2 g, 2.5 mmol) were dissolved in DMF (6 mL) Terephthalic acid (0.042 g, 0.25 mmol) was dissolved in DMF (6 mL) at 100 °C. The malonic acid/pyrazine and terephthalic acid solutions were added sequentially to the cobalt (II) acetate solution and the resulting mixture was heated at 100 °C for 2.5 days to yield pink crystals. The polycrystalline material was then washed twice with fresh DMF. Analytically pure material was activated by heating the crystals under vacuum at 50 - 100 °C for 1 week to give a 70% yield (0.053 g, 0.17 mmol). Elemental analysis: expected for $CoC_{12}H_8N_2O_4$: % C, 47.55; H, 2.66; N, 9.24. Found: % C, 47.58; H, 3.18; N, 9.77.

Fe(BDC)(4,4'-bipyridine) (**3**). 4,4'-bipyridine (2.3 g, 15 mmol) was dissolved in DMF (10 mL) and pipetted over **1** (0.22 g, 0.75 mmol). After 24 hours at 100 °C, the solution was decanted and a fresh solution of 4,4'-bipyridine (2.3 g, 15 mmol) in DMF (10 mL) was added. The reaction was heated for an additional 24 hours. Activated material was produced by exchanging DMF solvent with THF by decanting and soaking material in fresh THF at 100 °C three times, decanting, then placing under vacuum for 2 days at 0 °C. Ligand exchange was monitored by ^{1}H NMR ($CDCl_3$) shifts of pyrazine δ 8.6 (s, 4H) and 4,4'-bipyridine δ 8.7 (dd, 4H) and 7.5 (dd, 4H). Activated yield: 70% (0.199 g, 0.53 mmol). Elemental analysis: expected for $FeC_{18}H_{12}N_2O_4$: % C, 57.48; H, 3.22; N, 7.45. Found: % C, 55.36; H, 3.53; N, 8.03.

Co(BDC)(4,4'-bipyridine) (**4**). 4,4'-bipyridine (0.78 g, 5 mmol) was dissolved in DMF (5 mL) and pipetted over **2** (0.076 g, 0.25 mmol). After 24 hours at 100 °C, the solution was decanted and a fresh solution of 4,4'-bipyridine (0.78 g, 5.0 mmol) in DMF (5 mL) was added. The reaction was

heated for an additional 24 hours. Activated material was produced by exchanging DMF solvent with THF by decanting and soaking material in fresh THF at 100 °C three times, decanting, then placing under vacuum for 2 days at 0 °C. Ligand exchange was monitored by ^{1}H NMR ($CDCl_3$) shifts of pyrazine δ 8.6 (s, 4H) and 4,4'-bipyridine δ 8.7 (dd, 4H) and 7.5 (dd, 4H). Activated yield: 65% (0.062 g, 0.16 mmol). Elemental analysis: expected for $CoC_{18}H_{12}N_2O_4$: % C, 57.01; H, 3.19; N, 7.39. Found: % C, 55.73; H, 3.10; N, 8.21.

*^{1}H NMR Monitoring of **3** and **4**.* The progress of S.A.L.E. between pyrazine and 4,4'-bipyridine was monitored by ^{1}H NMR. Solid samples were washed with fresh DMF, digested in 1 mL of concentrated nitric acid and neutralized with an aqueous NaOH solution (3 mL, 8 M). The heterogeneous mixture was then extracted with $CDCl_3$. Spectra were acquired on a Bruker DRX 400 at 400 MHz.

Crystal Structure Determination. The diffraction data were measured at 100 K on a Bruker D8 VENTURE with PHOTON 100 CMOS detector system equipped with a Mo-target micro-focus X-ray tube (λ = 0.71073 Å). Data reduction and integration were performed with the Bruker APEX3 software package (Bruker AXS, version 2015.5-2, 2015). Data were scaled and corrected for absorption effects using the multi-scan procedure as implemented in SADABS (Bruker AXS, version 2014/5, 2015, part of Bruker APEX3 software package). The structure was solved by the dual method implemented in SHELXT[28] and refined by a full-matrix least-squares procedure using OLEX2[29] software package (XL refinement program version 2014/7).[30] The porous frameworks are known to contain large accessible solvent voids that can be filled with disordered solvent molecules degrading the overall quality of the single crystal X-ray diffraction experiments. Crystal of **1** contained large pores and the diffuse contribution to scattering from the disordered solvent

molecules located in them was treated by application of the program SQUEZZE[31] as implemented in Platon[32] using the "fab" file construct. This construct allows the solvent density distribution to be added to calculation of structure factors without modifying the observed intensities through the subtraction of a solvent contribution. Overall, the SQUEEZE algorithm located "Solvent Accessible Volume" of 2255 $Å^3$ with an electron count of 507. This can account for approximately 12 molecules of DMF per unit cell or 2 molecules of DMF per 1 Fe atom. Crystallographic data and details of the data collection and structure refinement are listed in Table 6.

Gas Adsorption Measurements. Activation and measurements were performed on a Micromeritics ASAP 2020. Surface area was calculated from the N_2 adsorption isotherm using Brunauer–Emmett–Teller (BET) theory. Samples were loaded into a quartz tube fitted with a TranSeal cap and activated as described in the synthetic protocol. Measurements were performed at 77 K, in a liquid N_2 bath.

Magnetometry. Magnetic measurements were performed on a Quantum Design MPMS 3 equipped with a superconducting quantum interference device (SQUID). Corrections were made for the diamagnetic contributions from the polycarbonate capsules and eicosane used to secure the sample by measuring field vs. moment in triplicate for each to determine a moment per gram correction. The χ values reported are the molar magnetic susceptibilities. χT vs. T data was calculated as a $[M(BDC)L]_2$ dimer and fit to an isotropic Heisenberg model with axial ZFS (Eq. S1) in MagProp[33] where ions *i* and *j* are nearest neighbors and have the same values. The axial ZFS parameter (D) was used to fit the data (see Equation **2.1**), however there was large error in the D value for all data sets making their values unreliable.

Magnetic data (χT vs. T) plots and reported values have been normalized to one formula unit. All reported literature J values of magnetic systems have been normalized to Eq. S1.

XRPD. Powder X-ray diffraction patterns were acquired on a Bruker D8 powder X-ray diffractometer with a General Area Detector Diffraction System (GADDS) using Cu Kα radiation (λ = 0.15418 nm). Samples were measured under heavy mineral oil to reduce air exposure. Powder diffraction data were analyzed by the Le Bail method (A. Le Bail Powder Diffr. 20, 316-326) as implemented in TOPAS.[34]

Mössbauer Measurements. Zero-field iron-57 Mössbauer spectra were obtained at 80 K with a constant acceleration spectrometer and a cobalt-57 rhodium source. Prior to measurements, the spectrometer was calibrated at 295 K with α-iron foil. Samples were prepared in a N_2-filled glovebox where powdered **1** was placed in a polyethylene cup, covered in Paratone-N oil and frozen in liquid nitrogen prior to handling in air. The sample contained approximately 100 mg. All spectra were analyzed using the WMOSS Mössbauer Spectral Analysis Software (www.wmoss.org).

X-ray Absorption Spectroscopy. X-ray near-edge absorption spectra (XANES) and X-ray absorption fine structure (XAFS) spectra were employed to probe the local environment around Co. Data were acquired at the Advanced Photon Source at Argonne National Labs with a bending magnet source with ring energy at 7.00 GeV. Co K-edge data were acquired at the MRCAT 10-BM beam line. EXAFS data were collected in the fluorescence mode using fluorescence ion chamber in Stern-Heald geometry. Absorption was calibrated and concurrently referenced during measurement to a Co foil set to 7709.00 keV. Data collected was processed using Athena software[35] by extracting the EXAFS oscillations χ(k) as a function of photoelectron wavenumber

k.[36] The theoretical paths were generated using FEFF6[37] and the models were done in the conventional way using the fitting program Artemis.[35] The initial model was taken from an X-ray crystal structure of an Fe-containing analogue compound. EXAFS data were modelled in R-space with k-weights of 1, 2 and 3 until a satisfactory fit describing the system was obtained.

Computational Methods. DFT calculations were performed using the Quantum Espresso[23] code under the Generalized Gradient Approximation (GGA) with Perdew-Burke-Ernzerhof (PBE)[24] parametrization and a plane-wave basis. Optimized Norm-Conserving Vanderbilt (ONCV) pseudopotentials[25] were chosen to approximate the potential of the core electrons, using a kinetic energy cutoff of 75 Ry. To account for the electronic interaction between partially filled Fe d states and open up a gap between the valence and conduction bands, the DFT+U method was employed using a correlation energy (U) of 5 eV. The value of U was chosen by scanning over a range of 2-6 eV and choosing the smallest value for which the pseudo-octahedral field Fe *d* electrons and the insulating band structure were accurately represented. This value of U is close to what has been used for DFT+U calculations in literature for other MOF and similar systems.[26,27]

All calculations were performed at the Gamma point and at the experimental lattice constant with a unit cell containing 162 atoms and including 6 Fe centers and two triangular pores (for a total of 636 valence electrons). Both antiferromagnetic (AFM) and ferromagnetic (FM) high-spin Fe systems were considered, as well as a non-magnetic (NM) low-spin Fe case. The geometry for each of these three systems was optimized at the PBE level of theory until forces on all atoms were less than 10^{-5} Ry Bohr $^{-1}$. Relaxed geometries were found to vary for the three spin configurations, with the most notable difference coming from the non-magnetic low-spin system which is the most strained at the fixed lattice constant.

Stable spin states were found by varying the initial local magnetic moments of the Fe, O and N atoms, and enforcing a total magnetization of zero for AFM coupling. The experimentally predicted high-spin occupation was confirmed for both the AFM and FM ordered systems, while the higher-energy non-magnetic system exhibited low-spin occupation of the Fe centers.

2.6 Supplementary Data

Table 2.6. Crystal data and structure refinement for **1**

Identification code	1
Empirical formula	$C_{12}H_8FeN_2O_4$
Formula weight	300.05
Temperature/K	100(2)
Crystal system	hexagonal
Space group	*P*6/*m*
a/Å	24.644(2)
b/Å	24.644(2)
c/Å	7.1068(6)
α/°	90
β/°	90
γ/°	120
Volume/Å^3	3738.0(7)
Z	6
ρ_{calc}g/cm^3	0.800
μ/mm^{-1}	0.610
F(000)	912.0
Crystal size/mm^3	0.32 × 0.11 × 0.09
Radiation	MoKα (λ = 0.71073)
2Θ range for data collection/°	5.05 to 50.074
Index ranges	-27 ≤ h ≤ 29, -28 ≤ k ≤ 29, -8 ≤ l ≤ 7
Reflections collected	23375
Independent reflections	2407 [R_{int} = 0.1013, R_{sigma} = 0.0529]
Data/restraints/parameters	2407/33/106
Goodness-of-fit on F^2	1.098
Final R indexes [I>=2σ (I)]	R_1 = 0.0643, wR_2 = 0.1645
Final R indexes [all data]	R_1 = 0.0786, wR_2 = 0.1699
Largest diff. peak/hole / e Å^{-3}	0.70/-1.71

Table 2.7. Fractional Atomic Coordinates ($\times 10^4$) and Equivalent Isotropic Displacement Parameters ($Å^2 \times 10^3$) for **1**. U_{eq} is defined as 1/3 of of the trace of the orthogonalised U_{IJ} tensor.

Atom	*x*	*y*	*z*	U(eq)
Fe1	4104.4(4)	9375.3(4)	10000	17.9(3)
O1	4904.8(18)	9331.7(17)	10000	22.1(9)
O2	5941.5(18)	9810.1(17)	10000	22.5(9)
O3	4796.3(17)	6444.7(18)	10000	23.1(9)
O4	5828.1(17)	6923.5(17)	10000	20.8(8)
N1	4117.2(15)	9390.6(14)	6960(4)	20.6(7)
C1	5404(3)	9320(3)	10000	18.3(12)
C2	5387(3)	8704(2)	10000	19.9(12)
C3	5931(3)	8682(3)	10000	23.8(13)
C4	5921(3)	8113(3)	10000	24.2(13)
C5	5340(3)	7553(3)	10000	24.9(12)
C6	4805(3)	7591(3)	10000	20.7(12)
C7	4804(3)	8148(3)	10000	27.0(14)
C8	5332(3)	6951(3)	10000	21.2(11)
C9	4345(2)	9088.7(19)	5971(6)	30.7(10)
C10	3890.2(19)	9693(2)	5965(6)	28.5(10)

Table 2.8. Anisotropic Displacement Parameters ($Å^2 \times 10^3$) for **1**. The Anisotropic displacement factor exponent takes the form: $-2\pi^2[h^2a^{*2}U_{11}+2hka^*b^*U_{12}+\ldots]$.

Atom	U_{11}	U_{22}	U_{33}	U_{23}	U_{13}	U_{12}
Fe1	21.8(5)	15.8(4)	13.1(4)	0	0	7.1(4)
O1	26(2)	20(2)	24(2)	0	0	14.9(17)
O2	33(2)	20(2)	13.4(19)	0	0	12.1(19)
O3	24(2)	26(2)	24(2)	0	0	16.1(17)
O4	19.3(19)	23(2)	23(2)	0	0	12.9(16)
N1	25.6(17)	15.2(16)	13.8(15)	-1.4(13)	-2.1(14)	4.8(14)
C1	26(3)	28(3)	9(3)	0	0	20(3)
C2	32(3)	15(3)	8(2)	0	0	9(3)
C3	17(3)	34(3)	17(3)	0	0	11(3)
C4	26(3)	28(3)	28(3)	0	0	20(2)
C5	37(3)	21(3)	21(3)	0	0	18(2)
C6	24(3)	20(3)	16(3)	0	0	9(2)
C7	17(3)	36(4)	29(3)	0	0	14(3)
C8	35(3)	24(3)	7(2)	0	0	16(2)
C9	47(3)	33(2)	20(2)	1.0(18)	-0.6(19)	26(2)
C10	31(2)	40(2)	20(2)	0.1(19)	3.1(18)	22(2)

Table 2.9. Bond Lengths for **1**

Atom	Atom	Length/Å	Atom	Atom	Length/Å
Fe1	O1	2.028(4)	N1	C10	1.335(5)
Fe1	O2[1]	2.066(4)	C1	C2	1.498(8)
Fe1	O3[2]	2.187(4)	C2	C3	1.369(8)
Fe1	O4[2]	2.196(4)	C2	C7	1.405(8)
Fe1	N1[3]	2.161(3)	C3	C4	1.389(8)
Fe1	N1	2.161(3)	C4	C5	1.407(8)
O1	C1	1.246(6)	C5	C6	1.365(8)
O2	C1	1.270(7)	C5	C8	1.476(8)
O3	C8	1.286(7)	C6	C7	1.376(8)
O4	C8	1.256(7)	C9	C9[4]	1.380(8)
N1	C9	1.334(5)	C10	C10[4]	1.372(8)

[1]1-X,2-Y,2-Z; [2]1-Y,1+X-Y,+Z; [3]+X,+Y,2-Z; [4]+X,+Y,1-Z

Table 2.10. Bond Angles for **1**

Atom	Atom	Atom	Angle/˚	Atom	Atom	Atom	Angle/˚
O1	Fe1	O2[1]	125.34(15)	C9	N1	C10	116.2(3)
O1	Fe1	O3[2]	89.78(15)	C10	N1	Fe1	122.2(3)
O1	Fe1	O4[2]	150.16(15)	O1	C1	O2	123.3(5)
O1	Fe1	N1[3]	89.70(9)	O1	C1	C2	119.8(5)
O1	Fe1	N1	89.71(9)	O2	C1	C2	116.9(5)
O2[1]	Fe1	O3[2]	144.88(16)	C3	C2	C1	120.6(5)
O2[1]	Fe1	O4[2]	84.50(15)	C3	C2	C7	120.5(5)
O2[1]	Fe1	N1[3]	89.45(9)	C7	C2	C1	119.0(5)
O2[1]	Fe1	N1	89.45(9)	C2	C3	C4	121.1(5)
O3[2]	Fe1	O4[2]	60.38(13)	C3	C4	C5	119.0(5)
N1	Fe1	O3[2]	90.88(8)	C4	C5	C8	118.7(5)
N1[3]	Fe1	O3[2]	90.88(8)	C6	C5	C4	118.5(5)
N1[3]	Fe1	O4[2]	90.69(9)	C6	C5	C8	122.7(5)
N1	Fe1	O4[2]	90.69(9)	C5	C6	C7	123.5(5)
N1[3]	Fe1	N1	178.14(18)	C6	C7	C2	117.4(5)
C1	O1	Fe1	178.5(4)	O3	C8	C5	117.7(5)
C1	O2	Fe1[1]	112.8(3)	O4	C8	O3	120.2(5)
C8	O3	Fe1[4]	89.5(3)	O4	C8	C5	122.0(5)
C8	O4	Fe1[4]	89.9(3)	N1	C9	C9[5]	121.8(2)
C9	N1	Fe1	121.6(3)	N1	C10	C10[5]	122.0(2)

[1]1-X,2-Y,2-Z; [2]1-Y,1+X-Y,+Z; [3]+X,+Y,2-Z; [4]+Y-X,1-X,+Z; [5]+X,+Y,1-Z

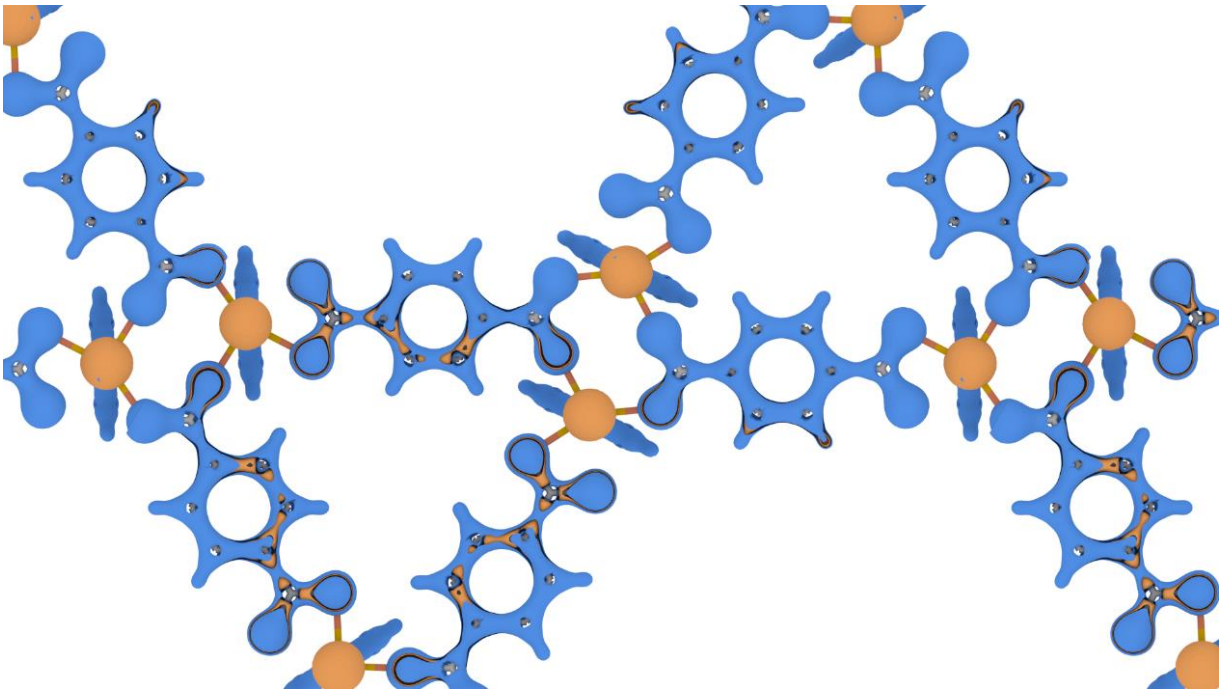

Figure 2.9. Spin up (orange) and spin down (blue) electron density showing FM ordering for **1**. Isosurfaces are shown at 9% of maximum value.

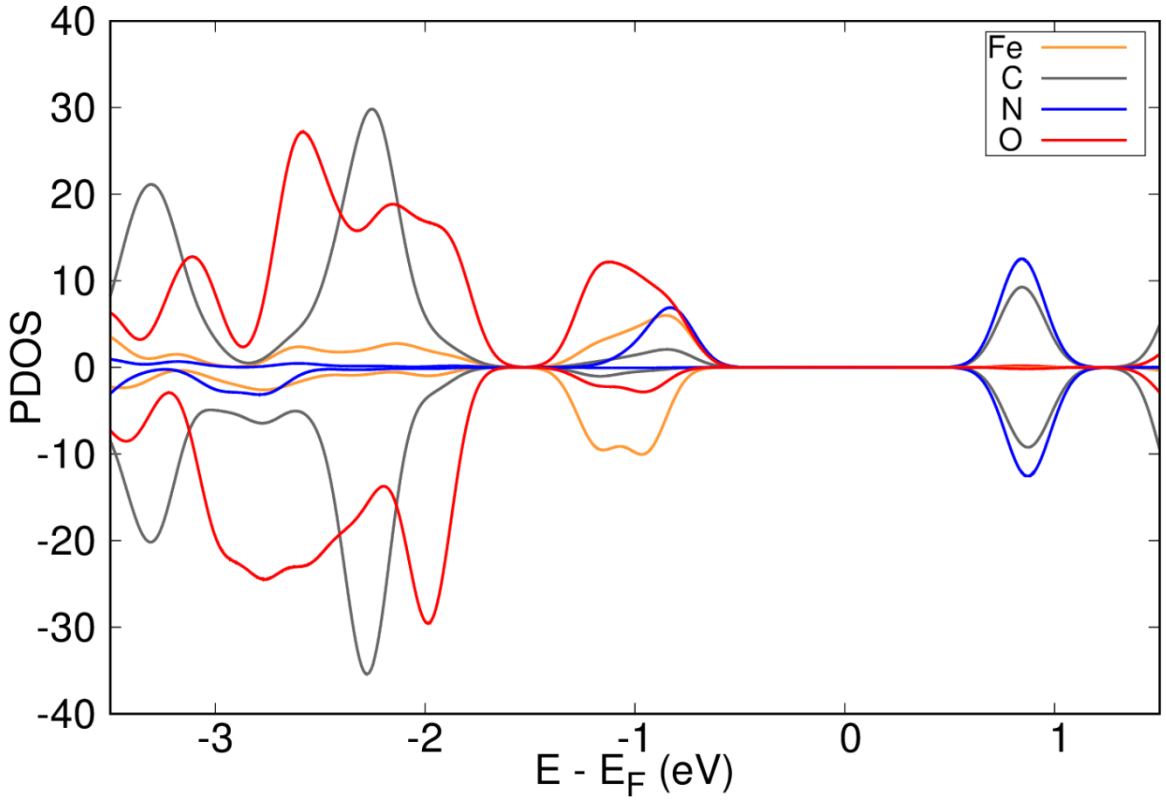

Figure 2.10. Projected electronic density of states showing FM ordering for **1**.

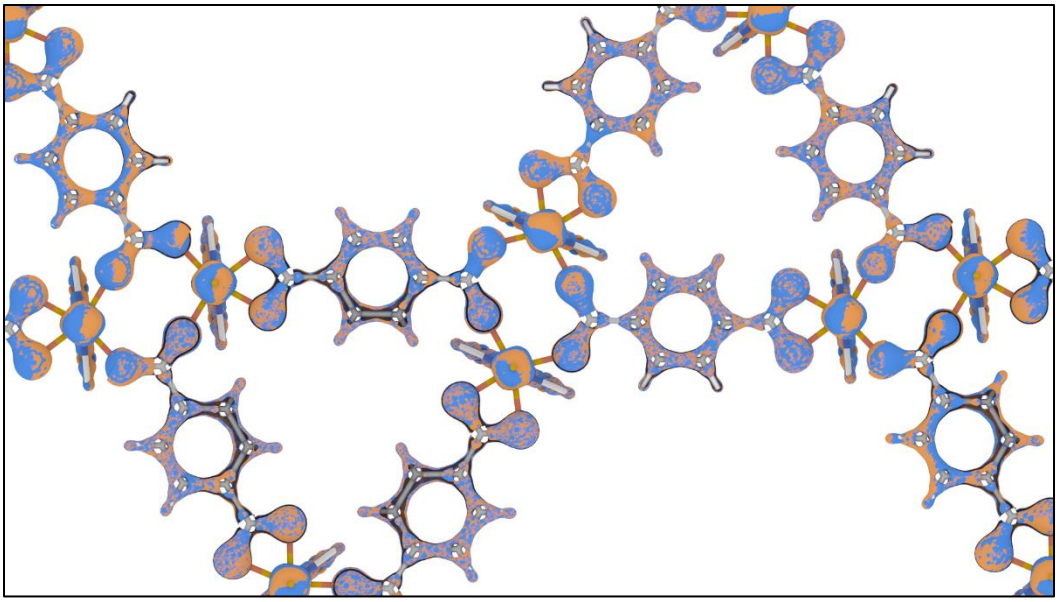

Figure 2.11. Spin up (orange) and spin down (blue) electron density showing NM (low-spin Fe) ordering for **1**. Isosurfaces are shown at 9% of maximum value.

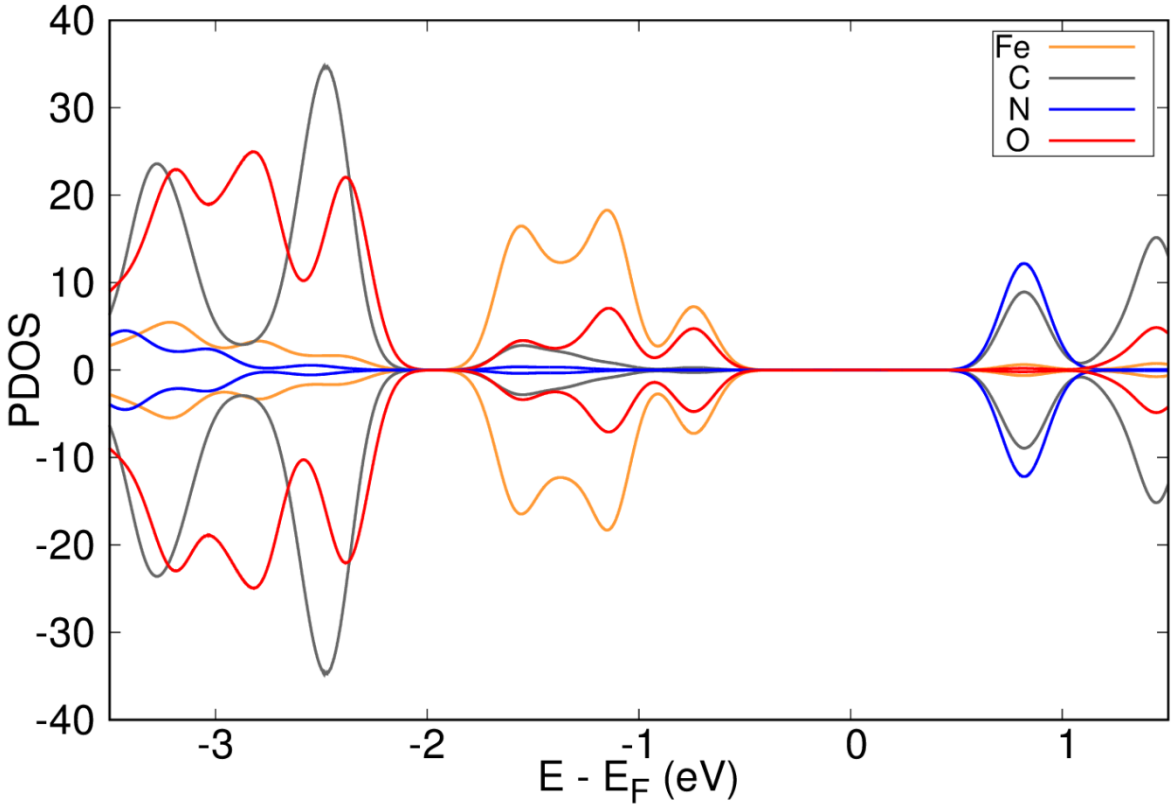

Figure 2.12. Projected electronic density of states showing NM ordering for **1**.

Table 2.11. Comparison of bond angles for the three DFT systems and experimental AFM system

	Exp. (AFM)	AFM Up (avg)	% difference	AFM Down (avg)	% difference	FM (avg)	% difference	NM (avg)	% difference
Chelated O-Fe-O	60.38(13)°	**61.712°**	**2.18%**	61.681°	2.13%	**61.757°**	**2.52%**	65.764°	8.53%
Bridging O-Fe-O	125.34(15)°	**112.057°**	**11.2%**	112.796°	10.5%	**113.522°**	**9.0%**	104.666°	18.0%
N-Fe-N	178.14(18)°	**176.992°**	**0.65%**	177.061°	-0.61%	**177.369°**	**0.44%**	179.592°	0.81%

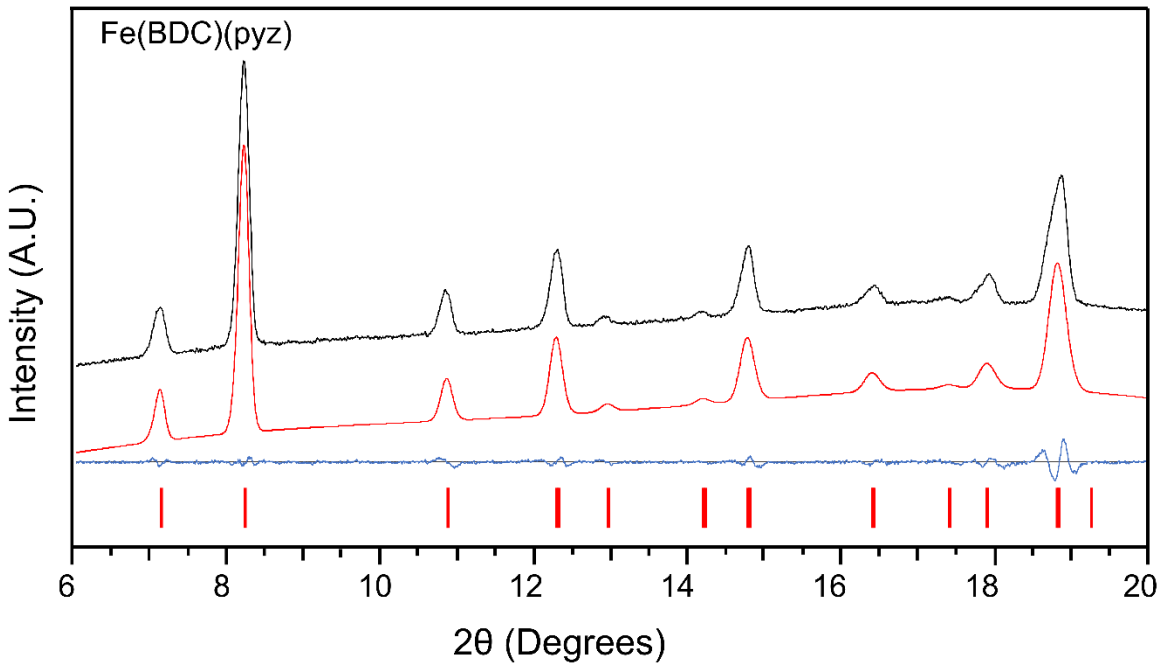

Figure 2.13. Experimental XRPD pattern (black) for **1** with the Le Bail fit (red) with the residual difference (blue). Theoretical peaks are shown as red lines at the bottom.

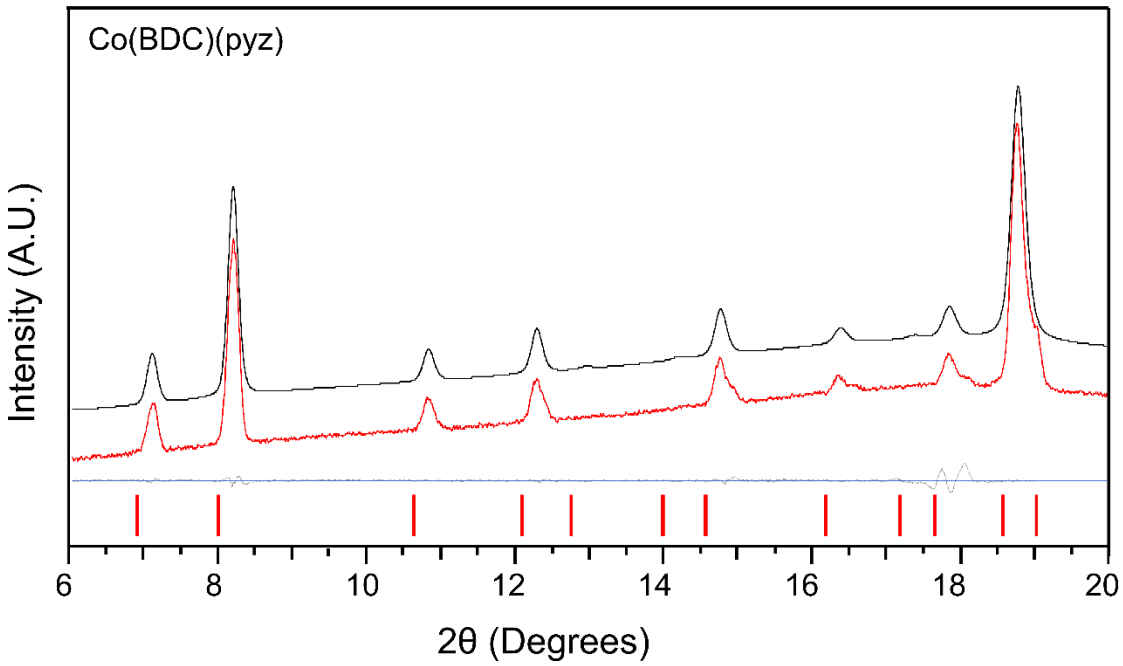

Figure 2.14. Experimental XRPD pattern (black) for **2** with the Le Bail fit (red) with the residual difference (blue). Theoretical peaks are shown as red lines at the bottom.

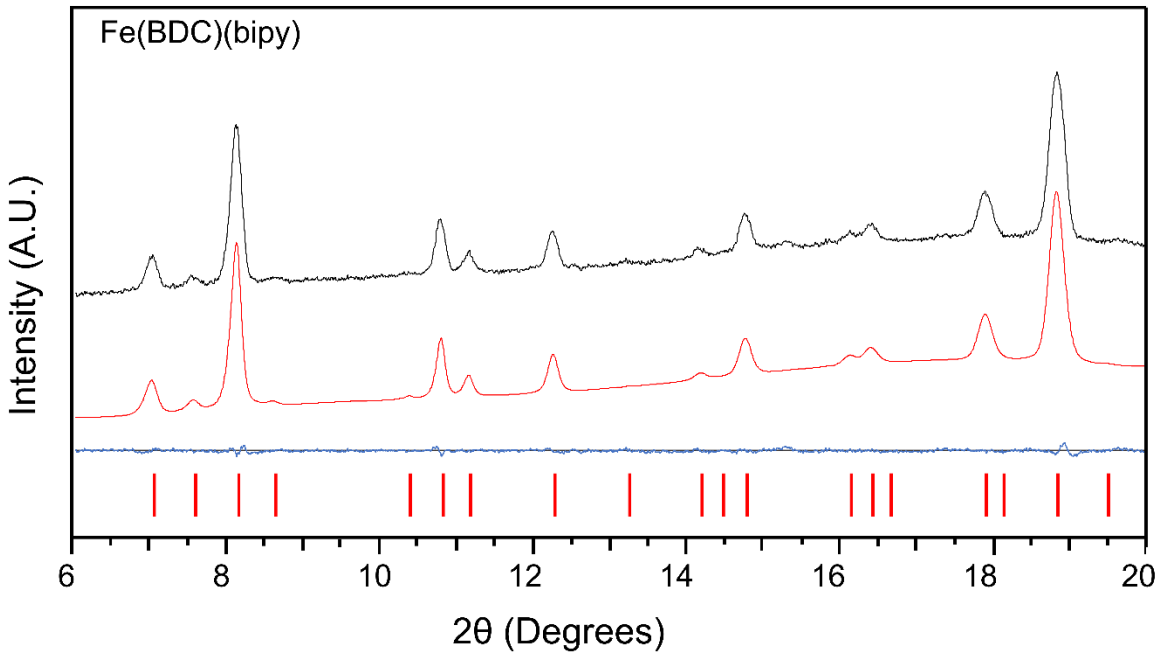

Figure 2.15. Experimental XRPD pattern (black) for **3** with the Le Bail fit (red) with the residual difference (blue). Theoretical peaks are shown as red lines at the bottom.

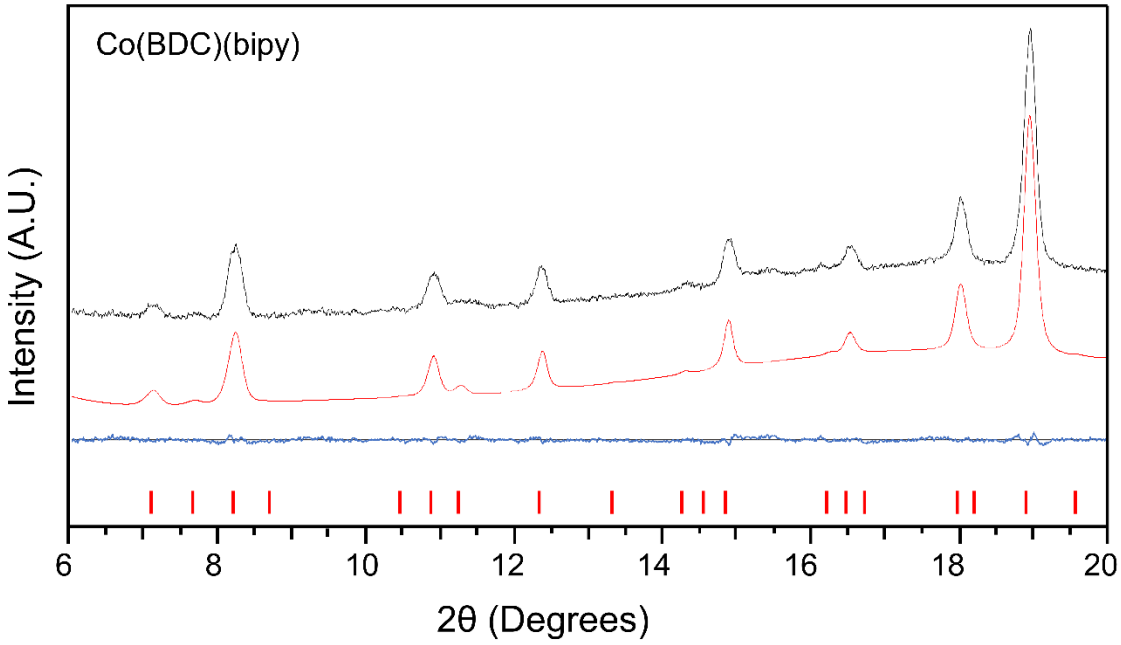

Figure 2.16. Experimental XRPD pattern (black) for **4** with the Le Bail fit (red) with the residual difference (blue). Theoretical peaks are shown as red lines.

2.7 Notes and References

Authorship and prior publication. This majority of this chapter was reproduced from the following publication, with additional edits:: *Inorg. Chem.* **2017**, *56(6)*, 3349-3356. Portions of the work, including all of the computational calculations, were completed by coauthors.

1. (a) Zhou, H.-C.; Long, J. R.; Yaghi, O. M., *Chem. Rev.* **2012,** *112* (2), 673-674. (b) Wang, C.; Liu, D.; Lin, W., *J. Am. Chem. Soc.* **2013,** *135* (36), 13222. (c) Furukawa, H.; Cordova, K. E.; O'Keeffe, M.; Yaghi, O. M., *Science* **2013,** *341* (6149), 974.

2. (a) Farha, O. K.; Oezguer Yazaydin, A.; Eryazici, I.; Malliakas, C. D.; Hauser, B. G.; Kanatzidis, M. G.; Nguyen, S.-B. T.; Snurr, R. Q.; Hupp, J. T. *Nat. Chem.* **2010,** *2* (11), 944. (b) Mason, J. A.; Oktawiec, J.; Taylor, M. K.; Hudson, M. R.; Rodriguez, J.; Bachman, J. E.; Gonzalez, M. I.; Cervellino, A.; Guagliardi, A.; Brown, C. M.; Llewellyn, P. L.; Masciocchi, N.; Long, J. R.,. *Nature* **2015,** *527* (7578), 357. (c) Islamoglu, T.; Chen, Z.; Wasson, M. C.; Buru, C. T.; Kirlikovali, K. O.; Afrin, U.; Mian, M. R.; Farha, O. K., *Chem. Rev.* **2020**.

3. (a) Britt, D.; Furukawa, H.; Wang, B.; Glover, T. G.; Yaghi, O. M. *Proc. Natl. Acad. Sci. U. S. A.* **2009,** *106* (49), 20637. (b) Bloch, W. M.; Babarao, R.; Hill, M. R.; Doonan, C. J.; Sumby, C. J. *J. Am. Chem. Soc.* **2013,** *135* (28), 10441. (c) Zhu, L.; Liu, X.-Q.; Jiang, H.-L.; Sun, L.-B., *Chem. Rev.* **2017,** *117* (12), 8129.

4. (a) Manna, K.; Ji, P.; Lin, Z.; Greene, F. X.; Urban, A.; Thacker, N. C.; Lin, W., *Nat. Commun.* **2016,** *7*, 12610. (b) Yu, X.; Cohen, S. M., *J. Am. Chem. Soc.* **2016,** *138* (38), 12320.

5. (a) Kurmoo, M., *Chem. Soc. Rev.* **2009,** *38* (5), 1353. (b) Dechambenoit, P.; Long, J. R., *Chem. Soc. Rev.* **2011,** *40* (6), 3249. (c) Sun, L.; Campbell, M. G.; Dinca, M. *Angew. Chem., Int. Ed.* **2016,** *55* (11), 3566. (d) Thorarinsdottir, A. E.; Harris, T. D., *Chem. Rev.* **2020**. (e) Xie, L. S.; Skorupskii, G.; Dincă, M., *Chem. Rev.* **2020**.

6. (a) Kong, D.; Li, Y.; Ouyang, X.; Prosvirin, A. V.; Zhao, H.; Ross, J. H., Jr.; Dunbar, K. R.; Clearfield, A., *Chem. Mater.* **2004,** *16* (16), 3020. (b) Nayak, S.; Harms, K.; Dehnen, S., *Inorg. Chem.* **2011,** *50* (7), 2714. (c) Yao, R.-X.; Xu, X.; Zhang, X.-M. *Chem. Mater.* **2012,** *24* (2), 303. (d) Horike, S.; Sugimoto, M.; Kongpatpanich, K.; Hijikata, Y.; Inukai, M.; Umeyama, D.; Kitao, S.; Seto, M.; Kitagawa, S., *J. Mater. Chem. A* **2013,** *1* (11), 3675.

7. (a) Guillou, N.; Livage, C.; Drillon, M.; Ferey, G., *Angew. Chem., Int. Ed.* **2003,** *42* (43), 5314. (b) Wang, Z.; Zhang, B.; Fujiwara, H.; Kobayashi, H.; Kurmoo, M., *Chem. Commun.* **2004,** (4), 416. (c) Hu, B.-W.; Zhao, J.-P.; Sanudo, E. C.; Liu, F.-C.; Zeng, Y.-F.; Bu, X.-H. *Dalton Trans.* **2008,** (41), 5556. (d) Jia, Q.-X.; Wang, Y.-Q.; Yue, Q.; Wang, Q.-L.; Gao, E.-Q., *Chem. Commun.* **2008,** (40), 4894. (e) Datcu, A.; Roques, N.; Jubera, V.; Maspoch, D.; Fontrodona, X.; Wurst, K.; Imaz, I.; Mouchaham, G.; Sutter, J.-P.; Rovira, C.; Veciana, J., *Chem. - Eur. J.* **2012,** *18* (1), 152. (f) Jeon, I.-R.; Negru, B.; Van Duyne, R. P.; Harris, T. D., *J. Am. Chem. Soc.* **2015,** *137* (50), 15699. (g) Darago, L. E.; Aubrey, M. L.; Yu, C. J.; Gonzalez, M. I.; Long, J. R., *J. Am. Chem. Soc.* **2015,** *137* (50), 15703.

8. (a) Marino, N.; Mastropietro, T. F.; Armentano, D.; De Munno, G.; Doyle, R. P.; Lloret, F.; Julve, M., *Dalton Trans.* **2008,** (38), 5152. (b) Han, Z.-B.; Lu, R.-Y.; Liang, Y.-F.; Zhou, Y.-L.; Chen, Q.; Zeng, M.-H., *Inorg. Chem.* **2012,** *51* (1), 674. (c) Liu, B.; Shang, R.; Hu, K.-L.; Wang, Z.-M.; Gao, S., *Inorg. Chem.* **2012,** *51* (24), 13363.

9. (a) Gandara, F.; Uribe-Romo, F. J.; Britt, D. K.; Furukawa, H.; Lei, L.; Cheng, R.; Duan, X.; O'Keeffe, M.; Yaghi, O. M., *Chem. - Eur. J.* **2012,** *18* (34), 10595, S10595/1-S10595/30. (b) Park, S. S.; Hontz, E. R.; Sun, L.; Hendon, C. H.; Walsh, A.; Van Voorhis, T.; Dinca, M., *J. Am. Chem. Soc.* **2015,** *137* (5), 1774. (c) Sun, L.; Hendon, C. H.; Minier, M. A.; Walsh, A.; Dinca, M., *J. Am. Chem. Soc.* **2015,** *137* (19), 6164.

10. (a) Creutz, C.; Taube, H., *J. Am. Chem. Soc.* **1969,** *91* (14), 3988. (b) Tom, G. M.; Creutz, C.; Taube, H., *J. Am. Chem. Soc.* **1974,** *96* (25), 7827. (c) Collman, J. P.; McDevitt, J. T.; Leidner, C. R.; Yee, G. T.; Torrance, J. B.; Little, W. A., *J. Am. Chem. Soc.* **1987,** *109* (15), 4606.

11. Shekhah, O.; Belmabkhout, Y.; Chen, Z.; Guillerm, V.; Cairns, A.; Adil, K.; Eddaoudi, M., *Nat. Commun.* **2014,** *5*, 4228.

12. Amo-Ochoa, P.; Castillo, O.; Zamora, F., *Dalton Trans.* **2013,** *42* (37), 13453.

13. Brunauer, S.; Emmett, P. H.; Teller, E., *J. Am. Chem. Soc.* **1938,** *60*, 309.

14. Karagiaridi, O.; Bury, W.; Mondloch, J. E.; Hupp, J. T.; Farha, O. K., *Angew. Chem., Int. Ed.* **2014,** *53* (18), 4530.

15. (a) Real, J. A.; De Munno, G.; Munoz, M. C.; Julve, M., *Inorg. Chem.* **1991,** *30* (12), 2701. (b) Hao, X.; Wei, Y.; Zhang, S., *Chem. Commun.* **2000,** (22), 2271. (c) Zheng, Y.-Z.; Xue, W.; Tong, M.-L.; Chen, X.-M.; Grandjean, F.; Long, G. J., *Inorg. Chem.* **2008,** *47* (10), 4077. (d) Li, L.; Becker, J. M.; Allan, L. E. N.; Clarkson, G. J.; Turner, S. S.; Scott, P., *Inorg. Chem.* **2011,** *50* (13), 5925.

16. Kahn, O., *Molecular magnetism*. VCH: New York, NY, 1993.

17. (a) Martinez-Lorente, M. A.; Petrouleas, V.; Savariault, J. M.; Poinsot, R.; Drillon, M.; Tuchagues, J. P., *Inorg. Chem.* **1991,** *30* (19), 3587. (b) Solomon, E. I.; Brunold, T. C.; Davis, M. I.; Kemsley, J. N.; Lee, S.-K.; Lehnert, N.; Neese, F.; Skulan, A. J.; Yang, Y.-S.; Zhou, J., *Chem. Rev.* **2000,** *100* (1), 235.

18. (a) Colacio, E.; Dominguez-Vera, J. M.; Kivekaes, R.; Moreno, J. M.; Romerosa, A.; Ruiz, J., *Inorg. Chim. Acta* **1993,** *212* (1-2), 115. (b Colacio, E.; Dominguez-Vera, J. M.; Ghazi, M.; Kivekas, R.; Klinga, M.; Moreno, J. M., *Eur. J. Inorg. Chem.* **1999,** (3), 441. (c) Baldoma, R.; Monfort, M.; Ribas, J.; Solans, X.; Maestro, M. A., *Inorg. Chem.* **2006,** *45* (20), 8144.

19. (a) Ma, B. Q.; Gao, S.; Yi, T.; Xu, G. X., *Polyhedron* **2001,** *20* (11-14), 1255. (b) Zhang, K.-L.; Wang, Z.; Huang, H.; Zhu, Y.; You, X.-Z., *J. Mol. Struct.* **2004,** *693* (1-3), 193.

20. Gutlich, P.; Garcia, Y.; Goodwin, H. A., *Chem. Soc. Rev.* **2000,** *29* (6), 419.

21. (a) Halder, G. J.; Kepert, C. J.; Moubaraki, B.; Murray, K. S.; Cashion, J. D., *Science* **2002,** *298* (5599), 1762. (b) Ohba, M.; Yoneda, K.; Agusti, G.; Munoz, M. C.; Gaspar, A. B.; Real, J. A.; Yamasaki, M.; Ando, H.; Nakao, Y.; Sakaki, S.; Kitagawa, S., *Angew. Chem., Int. Ed.* **2009,** *48* (26), 4767, S4767/1-S4767/16.

22. Boonmak, J.; Nakano, M.; Chaichit, N.; Pakawatchai, C.; Youngme, S., *Inorg. Chem.* **2011,** *50* (15), 7324.

23. Giannozzi, P.; Baroni, S.; Bonini, N.; Calandra, M.; Car, R.; Cavazzoni, C.; Ceresoli, D.; Chiarotti Guido, L.; Cococcioni, M.; Dabo, I.; Dal Corso, A.; de Gironcoli, S.; Fabris, S.; Fratesi, G.; Gebauer, R.; Gerstmann, U.; Gougoussis, C.; Kokalj, A.; Lazzeri, M.; Martin-Samos, L.; Marzari, N.; Mauri, F.; Mazzarello, R.; Paolini, S.; Pasquarello, A.; Paulatto, L.; Sbraccia, C.; Scandolo, S.; Sclauzero, G.; Seitsonen Ari, P.; Smogunov, A.; Umari, P.; Wentzcovitch Renata, M., *J. Phys. Condens. Matter* **2009,** *21* (39), 395502.

24. Hamann, D. R., *Physical Review B* **2013,** *88* (8), 085117.

25. Perdew, J. P.; Burke, K.; Ernzerhof, M., *Phys. Rev. Lett.* **1996,** *77* (18), 3865.

26. Zhang, Q.; Li, B.; Chen, L., *Inorg. Chem.* **2013,** *52* (16), 9356.

27. Zhou, J.; Sun, Q., *J. Am. Chem. Soc.* **2011,** *133* (38), 15113

28. Sheldrick, G. M. *Acta Cryst.* **2015**, *A71*, 3.

29. Dolomanov, O.V.; Bourhis, L.J.; Gildea, R.J.; Howard, J.A.K.; Puschmann, H.; *J. Appl. Cryst.* **2009**, *42*, 339.

30. (a) Sheldrick, G. M. *Acta Cryst.* **2008**, A64, 112. (b) Sheldrick, G. M. Acta Cryst. **2015**, C71, 3.

31. Spek, A.L. *Acta Cryst.* **2015**, C71, 9.

32. Spek, A. L., *Acta Cryst*. **2009**, D65, 148.

33. Azuah, R. T. et al, *J. Res. Natl. Inst. Stand. Technol.* **2009**, *114* (6), 341.

34. (a) Coelho, A. A. *J. Appl. Crystallogr*. **2003**, *36*, 86. (b) TOPAS version 5.0; Bruker AXS, 2015.

35. Ravel, B., Newville, M., *J. Synchr. Radn.*, **2005**, 12, 537.

36. Newville, M. *J. Synchr. Radn*. **2001**, *8*, 322.

37. Rehr, J. J.; Albers, R. C. *Rev. Mod. Phys.* **2000**, *72*, 621.

CHAPTER 3: SLOW MAGNETIC RELAXATION OF CO(II) SINGLE CHAINS EMBEDDED WITHIN METAL–ORGANIC SUPERSTRUCTURES

3.1 Abstract

Two coordination polymers of the type Co(BPDC)(N-ox), with BPDC being 4,4′-biphenyldicarboxylate and N-ox being pyridine N-oxide (PNO) or isoquinoline N-oxide (IQNO), were synthesized and characterized. The compounds feature 2D and 3D metal−organic networks that encapsulate Co(II)-based chains in a rigid superstructure. The dc and ac magnetic properties of these Co(BPDC)(N-ox) materials were investigated alongside those of a related Co(BDC)(PNO) compound (where BDC is 1,4-benzenedicarboxylate), which contains a smaller dicarboxylate linker. These Co(II)-containing coordination polymers exhibit slow magnetic relaxation, as observed by ac susceptibility measurements. The observed magnetic behavior of all compounds is consistent with an antiferromagnetic interaction between canted Co spins along the 1D skeleton, resulting in single-chain magnet behavior. In the case of Co(BPDC)(IQNO), weak interchain magnetic interactions yield 3D antiferromagnetic order while the inherent magnetic behavior stemming from the chain component is maintained. The combination of these effects in this material puts it at the frontier between single-chain magnets and classical bulk antiferromagnets. This work contributes to the limited group of materials featuring the organization of single-chain magnets within a coordination polymer superstructure.

3.2 Introduction

In this chapter, more intriguing properties are observed beyond the magnetism of a simple high-spin magnetic center, as seen in the previous chapter. The inclusion of significant anisotropy on the Co(II) ions, superexchange coupling between Co(II) ions facilitated by short N-oxide bridges, and an extended structure featuring structurally canted Co(II) ions allow for spin canted

antiferromagnetism yielding slow relaxation of single chain magnets. In the subsequent chapter another example of spin canted antiferromagnetism will be discussed relating to a Fe(II) containing chain material.

The magnetic properties of extended molecule-based systems, including coordination polymers and metal−organic frameworks (MOFs), have been an area of increasing interest in recent years.[1] Within the class of 3D structurally ordered materials, magnetic correlation may exist in different dimensions depending on the efficiency of magnetic communication mediated by ligands. The related study of single-molecule magnets (0D magnetism, SMMs) and single chain magnets (1D magnetism, SCMs) are relatively new areas of research with reports of experimentally observed phenomena only appearing within the last few decades.[2] Attention for these fields has grown rapidly since their initial reports.[3,4] In this context, a strategy that has gained increasing interest is the control of magnetic properties by the encapsulation of molecular magnetic units within a rigid coordination polymer superstructure such as in MOFs.[5,6] This strategy may also offer a unique opportunity to explore the frontier between molecular magnets and classical bulk magnets.

To this end, we have investigated a series of structurally related coordination polymers, Co(BDC)(PNO) (**1**) and Co- (BPDC)(N-ox), with B[P]DC being 1,4-benzenedicarboxylate (BDC) or 4,4′-biphenyldicarboxylate (BPDC) and N-ox being pyridine N-oxide (PNO) or isoquinoline N-oxide (IQNO). These materials feature Co-based chains separated by the organic linkers within coordination polymer superstructures. The BDC analogue of this series has been previously reported and is a member of the well-known MIL-53 type frameworks.[7] The incorporation of the extended BPDC linkers yielded new materials with 2D and 3D structures for the IQNO and PNO

ligands, respectively. These three related compounds exhibit slow magnetic relaxation consistent with single-chain magnet dynamics. Based on detailed studies of this magnetic behavior, we posit that the observed slow relaxation of the magnetization arises from spin canting between antiferromagnetically coupled Co spins within the chain skeleton. These interactions likely stem from a combination of the typically large magnetic anisotropy of high-spin Co(II) ions and the structural canting between two different orientations of Co ions along the chain. Interestingly, the 2D structurally ordered Co(BPDC)(IQNO) is the only member of this series which shows 3D magnetic ordering.

3.3 Results and Discussion

3.3.1. Synthesis and Structures Co(BDC)(PNO) was synthesized by methods adapted from reported literature procedures.[7c,d] The Co(BPDC)(N-ox) materials were isolated from related solvothermal syntheses. The structure of **1** has been reported previously.[7c] The structures of the Co(BPDC)(PNO) (**2**) and Co(BPDC)(IQNO) (**3**) have been determined by SXRD (Figure 3.1 and Figure 3.2) with assistance from Dr. Filatov. All of the structures feature Co(II) centers bridged by syn-syn μ_2- carboxylate groups from a B[P]DC ligand and one μ_2-O from the N-oxide group to form infinite 1D chains. These chains are interconnected by the B[P]DC ligand to extend the structure in two or three dimensions. The coordination polymers containing PNO crystallize in the monoclinic C2/c space group. Material **3**, with its 2D layered structure, crystallizes in the space group $P\bar{1}$. While **3** shares the same local structural environment around the Co(II) ions as the rest of the Co(B[P]DC)(N-ox) series, bending of the BPDC units forms infinite 2D sheets as opposed to the 3D diamond topology created by the planar B[P]DC units in the other members of the series. The 2D sheets of **3** are joined together in a 3D arrangement by π–π stacking interactions with the

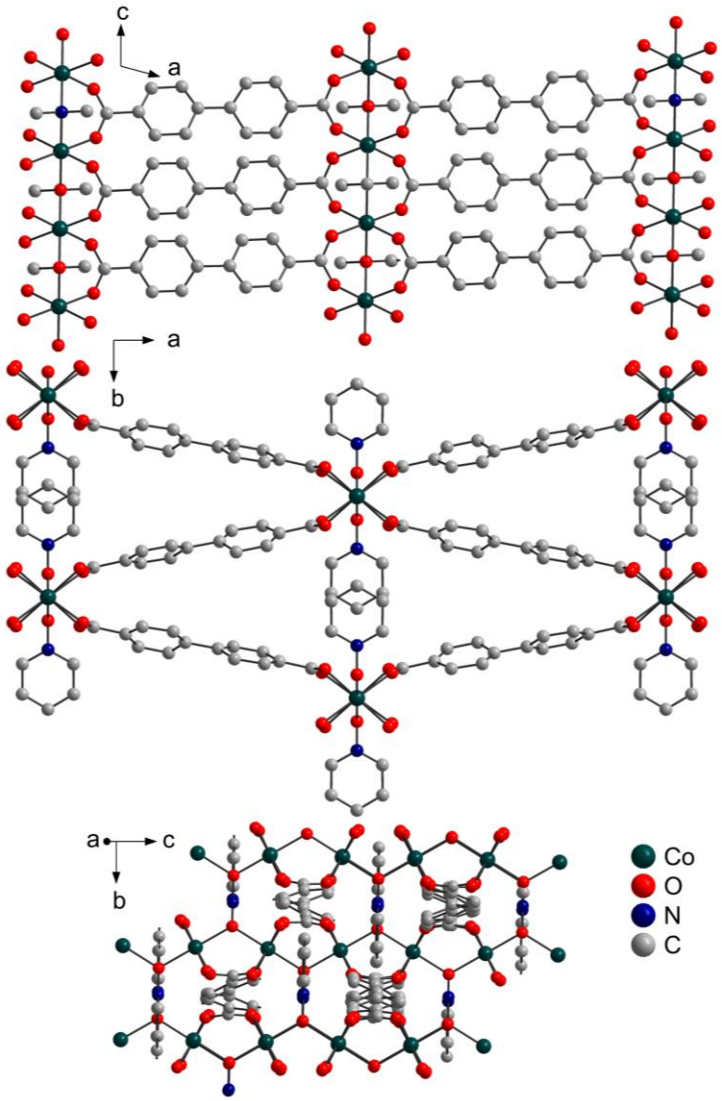

Figure 3.1. Crystal structure solved from single crystal X-ray diffraction data for **2**. H atoms have been omitted for clarity.

shortest centroid−centroid distance of 3.69 Å between the aryl rings of the IQNO ligands. This separation is typical for π−π interactions.[8`]

This observed distance is significantly shorter than those found in **1** and **2**, where the centroid−centroid distances between pyridine rings are 3.96 and 3.95 Å, respectively. The Co−$O_{N\text{-}ox}$−Co bond angles of the Co(B[P]DC)(N-ox) series are slightly wider (Table 3.1) than average for aromatic N-oxide bridged Co ions (112.8°, σ = 8.5°).[9] Similarly, the carboxylate

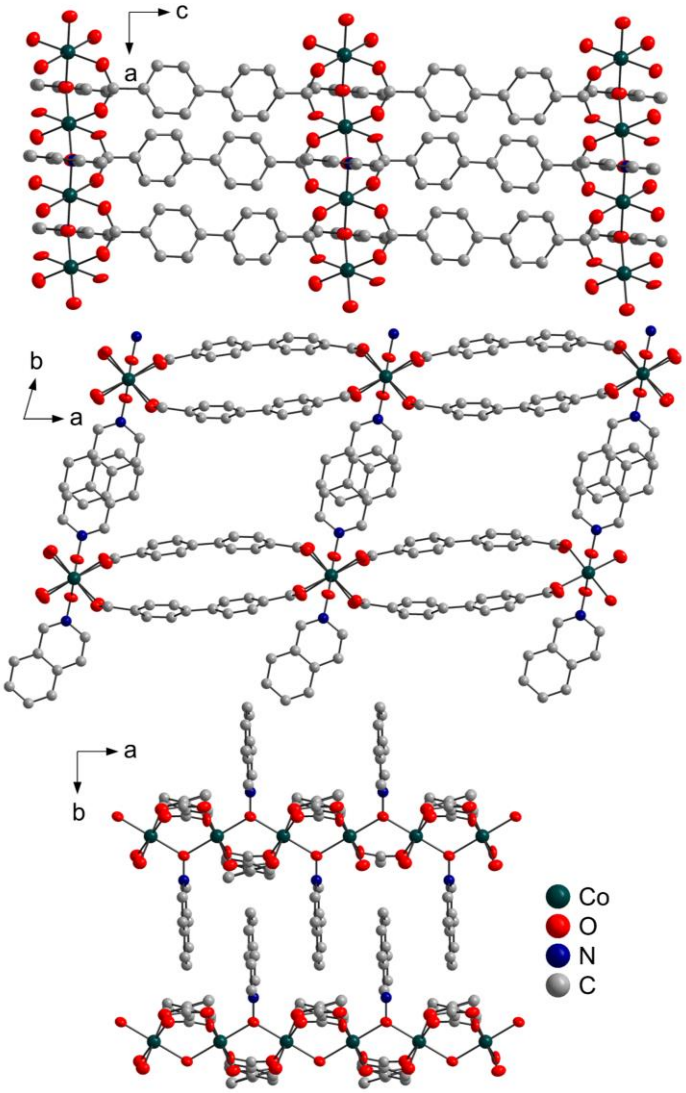

Figure 3.2. Crystal structure solved from single crystal X-ray diffraction data for **3**. H atoms have been omitted for clarity.

bridges are slightly bowed out and are on the larger end of the average range for O−C−O bond angles (125.4°, σ = 1.8) for carboxylate bridges between two Co ions.

In these types of carboxylate materials, the Co−O−C bond angle varies substantially (average 131.3°, σ = 10.4),[9] and the values in the Co(B[P]DC)(N-ox) series are within this range.

The XRPD for the series are shown in Figure 3.3 and match well with the patterns

Table 3.1. Selected geometric and magnetic data from the Co(B[P]DC)(N-ox) series. The interchain distances are with respect to the orientation of the ligands, where N-ox is the distance across the N-oxide ligand. The data from **1** is from CCDC 947944.

	Co···Co (Intra-chain) (Å)	Co···Co (Inter-chain, N-ox) (Å)	Co···Co (Inter-chain, B{P}DC) (Å)	Co–O_{ox} (Å)	Co–$O_{B\{P\}DC}$ (Å)	Co–O_{ox}–Co (°)	Co–$O_{B\{P\}DC}$–C (°)	$O_{B\{P\}DC}$–C–$O_{B\{P\}DC}$ (°)	t_0 (s)	Δ (cm^{-1})
1	3.5671(2)	9.1206(5)	10.6537(6)	2.100(3)	2.075(4), 2.056(4)	116.3(1)	131.9(3), 131.7(3)	127.4(4)	$5x10^{-9}$	17
2	3.5611(3)	9.1697(7)	14.777(1)	2.073(2)	2.066(4), 2.077(5)	118.4(2)	131.3(4), 131.2(4)	126.9(4)	$2x10^{-8}$	19
Co(BDC) (IQNO)	3.5980(2)	11.7957(6)	10.7658(4)	2.087(1)	2.067(2), 2.074(2)	119.08(1)	135.8(1), 134.0(1)	126.5(3)	$9x10^{-8}$	20
3	3.5283(5)	11.358(2)	14.178 (2)	2.056(7)	2.076(6), 2.055(8)	118.2(3)	132.9(7), 125.6(7)	126(1)	$4x10^{-8}$	20

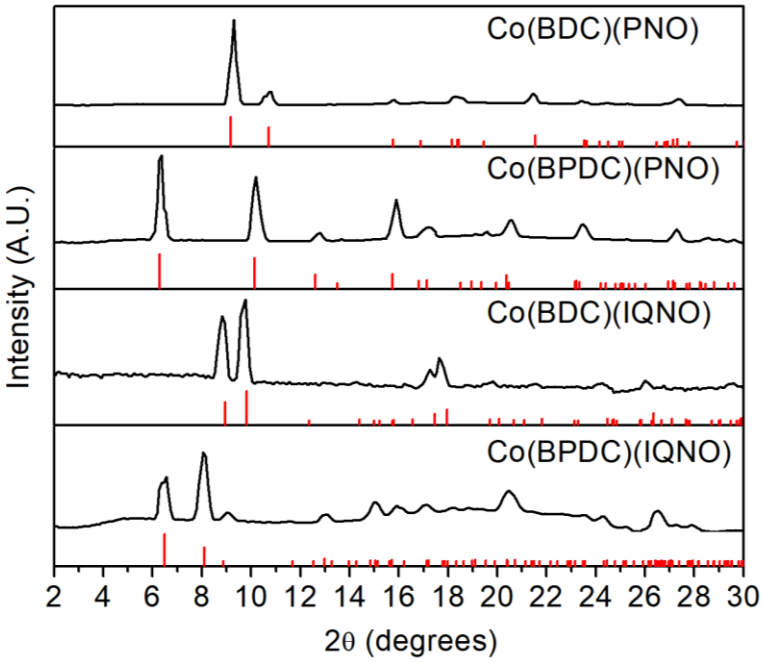

Figure 3.3. XRPD of **1**, **2**, Co(BDC)(IQNO), and **3** (black), and the simulated patterns (red).

simulated from the SXRD determined space groups and unit cell parameters, which indicates a single bulk crystalline phase. Finally, these Co(BPDC)(N-ox) materials are nonporous, as predicted from the structural data and confirmed by N_2 adsorption measurements (Figure 3.11).

3.3.2. Dc Magnetic Properties Material **1** has a χT (where χ is the molar magnetic susceptibility) value of 3.05 cm^3 K/mol at 300 K, which is significantly higher than the spin-only value of 1.875 cm^3 K/mol for an S = 3/2 ion. An elevated χT at high temperature is well documented for octahedral, high-spin Co(II) ions due to unquenched spin−orbit coupling.[10] As the temperature decreases, χT decreases slightly to attain a minimum value of 2.29 cm^3 K/mol at 24 K, consistent with a combined effect from intrachain antiferromagnetic interactions and spin−orbit coupling. Below 10 K, an increase in χT is observed (Figure 3.4A) to a peak of 10.37 cm^3 K/mol at 3.4 K under an applied dc field of 1000 Oe, which we assign to be the result of 1D correlation. This observed 1D correlation can arise from either a ferromagnetic coupling between Co centers or an antiferromagnetic coupling between canted Co spins. Given the moderate increase of χT below ~10 K and slight decrease in χT from 300 to 20 K, it is likely that the intrachain coupling is antiferromagnetic with spin canting. The absolute value of this peak in χT shows field dependence (Figure 3.12A), with suppressed χT_{max} values at higher fields indicating saturation effects. After this peak is reached, χT decreases again with decreasing temperature, likely due to saturation effects, interchain antiferromagnetic coupling, or some combination of these factors. Walton et al. previously reported the variable-field magnetization at 300 and 5 K and the variable-temperature susceptibility of **1**. Their report of the room-temperature magnetic moment of this material is consistent with our measurements, and they also conjectured that the increase in χT at low temperature may be a result of spin canting. The IQNO-containing material **3** has dc magnetic properties qualitatively similar to those of the PNO analogues and has a χT value of 2.73 cm^3 K/mol at 300 K (Figure 3.4C). This material also shows a low-temperature increase in χT to 15.9 cm^3 K/mol, similar to the case for the PNO materials, all of which are field dependent (Figure 3.12C).

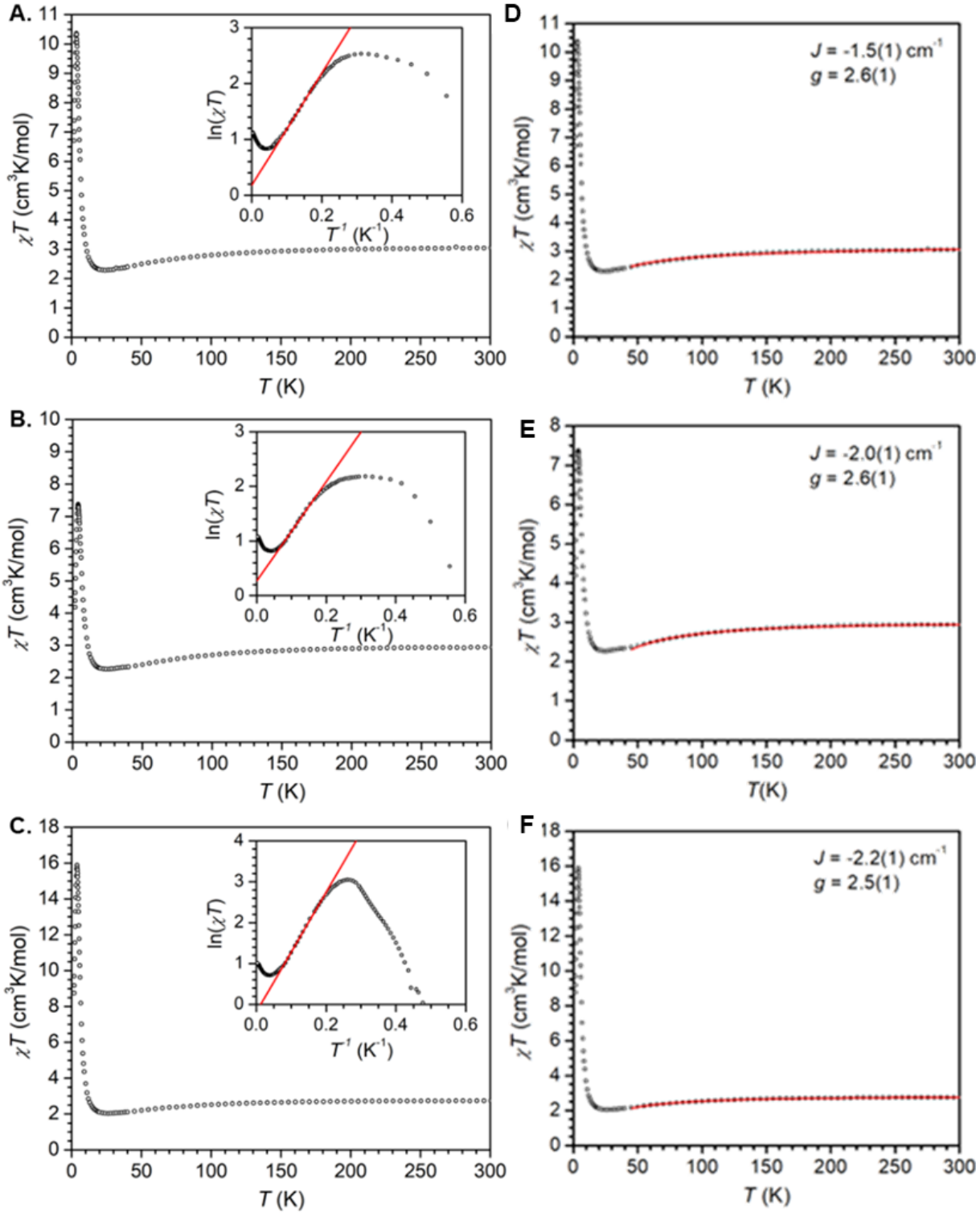

Figure 3.4. Variable temperature χT data for (A) **1**, (B) **2**, (C) **3** with insets of the low temperature (<20 K) region. Fisher model fits above 45 K for (D) **1**, (E) **2**, and (F) **3**.

In the presence of Co(II) orbital contributions and canting, no physically meaningful simulation of the magnetic susceptibility data can be obtained with an exact analytical model, although the Fisher model has been applied to a number of Co(II) chain systems in the literature.[11,12] It should be noted that, in the present case, the magnitude of the magnetic exchange estimated from the Fisher model

$$\chi = \frac{N\beta^2 g^2 S(S+1)}{3kT}\,\frac{u+1}{u-1} \text{ where } u = \coth\left(\frac{JS(S+1)}{kT}\right) - \frac{kT}{JS(S+1)} \qquad \textbf{3.1}$$

(Figure 3.4) is very close to literature values reported for molecular [Co_2(μ-O)(μ-O_2CR)] cores where antiferromagnetic coupling is favored when the Co−$O_{N\text{-}ox}$−Co angle is larger than 110°, as is observed in this series.[13]

To probe the 1D nature of the observed magnetic properties, our collaborator, Professor Ie-Rang Jeon investigated the temperature dependence of the correlation length (ξ) which is proportional to the χT value at zero applied dc field (Figure 3.4, insets). [1c,14] As shown in the plot of ln(χT) vs T^{-1}, the χT value increases exponentially upon cooling from 10 to 5 K, confirming the behavior of Ising-like or anisotropic Heisenberg spin chains.[15] A linear fit to the data gives an estimation of the energy to create a domain wall along the chain: Δ_ξ = 6.8, 6.6, and 10.1 cm^{-1} for **1**, **2**, and **3**, respectively.[15b,16] Below the linear regime, ln(χT) saturates and decreases due to a limited correlation length caused by structural defects and/or possible antiferromagnetic interactions. In particular, the plot of ln(χT) vs T^{-1} for **3** shows a sharp decrease at low temperature, likely implying the presence of an antiferromagnetic phase.

Variable-field magnetization for these materials was measured below 8 K (Figure 3.5). At low field, the magnetization value rapidly increases to a modest value, which is far from the expected value for a Co(II) ion.

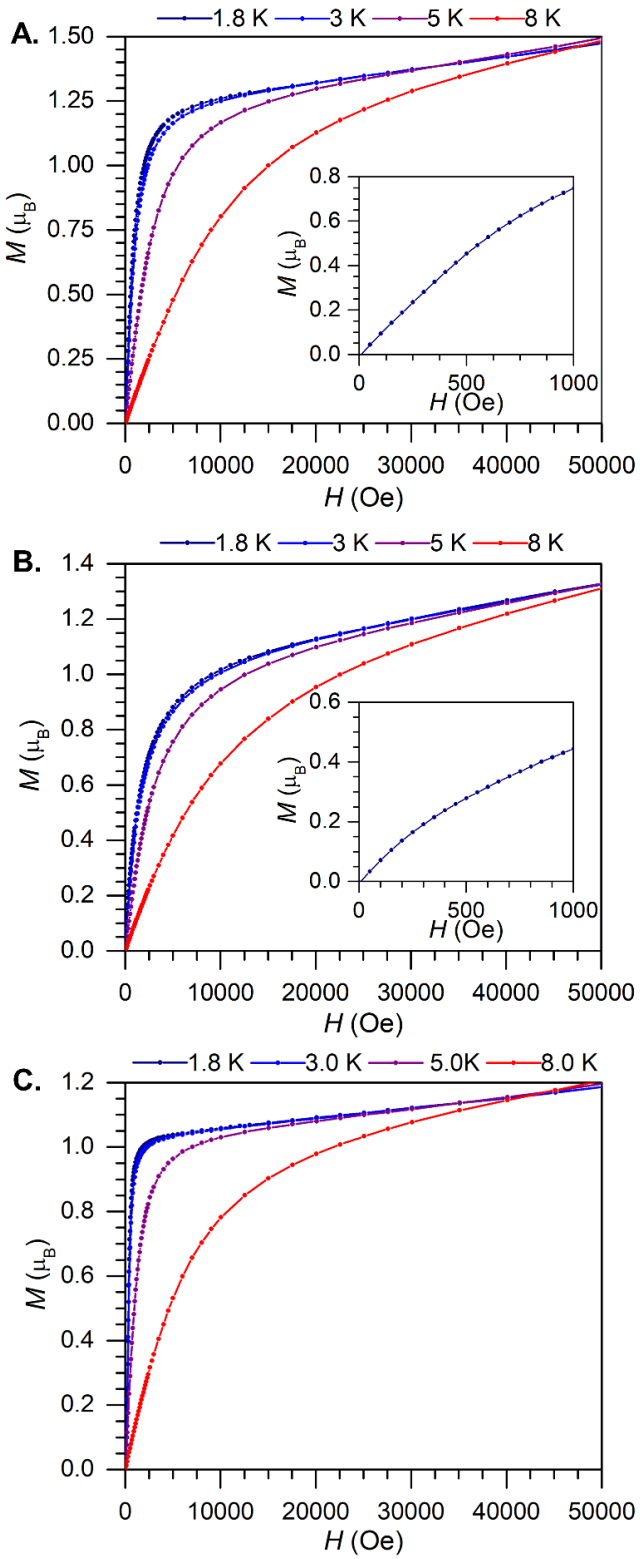

Figure 3.5. Variable-field (H_C) magnetization (M) for (A) **1**, (B) **2**, and (C) **3**. Insets on A,B: Region from 0 – 0.1 T at 1.8 K. Lines are guides to the eye.

This qualitative analysis also precludes, in conjunction with the susceptibility data, the presence of a ferromagnetic interaction and an antiferromagnetic interaction with a perfect spin cancelation and therefore implies the presence of canted spins along the chain in these compounds. The magnetization curves at high field increase linearly without achieving saturation due to the strong magnetic anisotropy of the Co(II) ion. Note that no inflection point is observed in the plot of M vs *H* for the PNO-containing materials, suggesting the absence of notable antiferromagnetic interactions between chains and thus the lack of 3D magnetic order.

In contrast, the data for **3** shows a typical S-shaped curve below 3.5 K (Figure 3.6 and Figure 3.5), highlighting the presence of a field-induced phenomenon overcoming interchain antiferromagnetic interactions (vide infra). This behavior is further confirmed by variable temperature susceptibility data collected under different applied dc fields (Figure 3.6, inset).

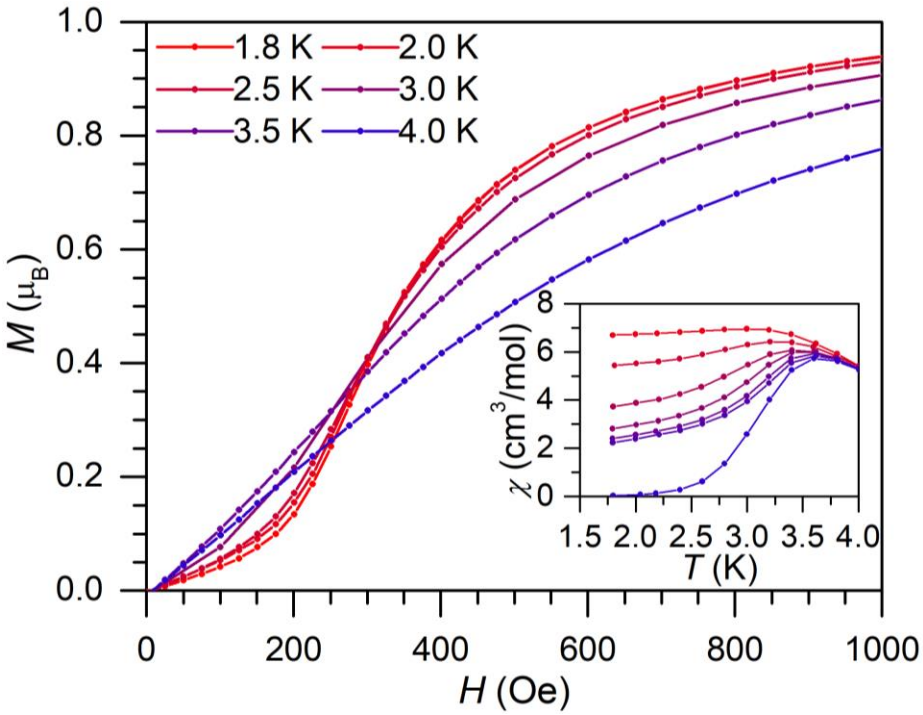

Figure 3.6. Variable-field magnetization (*M*) of **3** at different temperatures as shown in the legend. Inset: χ vs *T* at applied fields of 0 Oe (blue) to 350 Oe (red) at 50 Oe increments. Lines are guides to the eye.

From the dM/dH vs H (Figure 3.13) and χ vs T data, Prof. Jeon built an (H,T) magnetic phase diagram (Figure 3.7). The phase diagram reveals a transition line from an antiferromagnetic phase to a paramagnetic phase with a characteristic field of H_C = 250 Oe and a Neel´ temperature of T_N = 3.65 K, indicating that **3** is a metamagnetic material. The average interchain magnetic exchange (zJ') was estimated at 0.01 cm^{-1} from the relation $g\mu_B H_C S = 2|zJ'|S^2$.[17]

3.3.3. Ac Magnetic Properties Consistent with the proposal by Walton et al.,[7c] we assert that the source of the peak in the χT values of these materials at low temperature is likely due to antiferromagnetic interactions between canted Co spins along the Co−O−Co/Co−O−C−O−Co chain. Variable-frequency ac magnetic data were collected to probe the relaxation dynamics in this series. The in-phase (χ') and out-of-phase (χ'') susceptibilities of the members of this series show strong frequency dependence below 3 K (Figure 3.8). The relaxation time was deduced by fitting

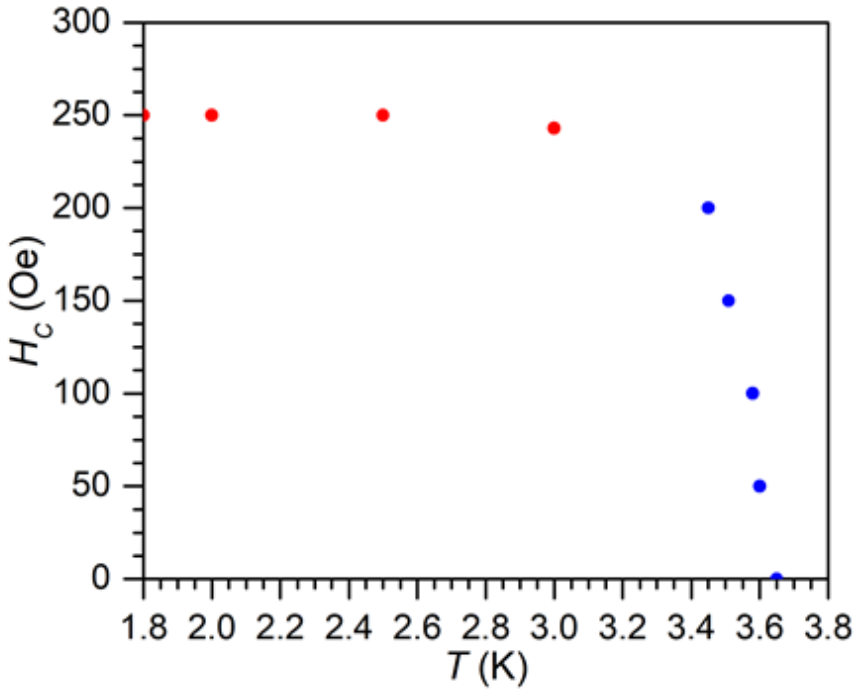

Figure 3.7. The (H,T) magnetic phase diagram for **3**. The points were obtained from *dM/dH* vs. H (red) or χ vs T (blue) data.

the data to the generalized Debye model.[18] The resulting Arrhenius plots for these materials feature a linear region, indicative of thermally activated relaxation of the magnetization (Figure 3.9 and Figure 3.13). The energy barrier of the relaxation was fit as $\Delta\tau$ = 24, 20, and 20 cm^{-1} with $\tau_0 = 2.8 \times 10^{-12}$, 1.0×10^{-9}, and 5.8×10^{-9} s for **1**, **2**, and **3**, respectively.

Given the temperature range in which the relaxation times were obtained, the energy barriers are induced by finite-size chain dynamics.[1c,4a] On the basis of the known theory for single-chain magnets, the anisotropy contribution (Δ_A) to the energy barrier in the finite-size regime is evaluated from the relation $\Delta\tau = \Delta_\xi + \Delta_A$. Using the Δ_ξ values determined from the ln(χT) vs T^{-1} data, values of Δ_A = 17, 14, and 10 cm^{-1} were calculated for **1**, **2**, and **3**, respectively, implying that the anisotropies of the Co(II) ions are relatively similar within this series. We note that these values are in the range of those reported for Co(II) ions in an octahedral coordination environment.[19]

The antiferromagnetic ground state of **3** was further confirmed by variable-temperature ac susceptibility measurements (Figure 3.10). The real component (χ') shows a maximum at 3.65 K that is invariable with frequency, while no peak is observed in the imaginary component (χ'') at this temperature. Below 3.65 K, both χ' and χ'' reveal frequency dependence, indicating the onset of slow magnetic relaxation.

It is interesting to note that the 3D antiferromagnetic order of **3** does not prevent the manifestation of chain dynamics. Such behavior has been only recently investigated in a small number of compounds.[16b,19a,20] To probe the influence of the applied dc magnetic field on the dynamics of the chain component, variable-frequency ac susceptibility measurements were performed at various applied fields below H_{dc} = 500 Oe (Figure S8). As expected, the slowest

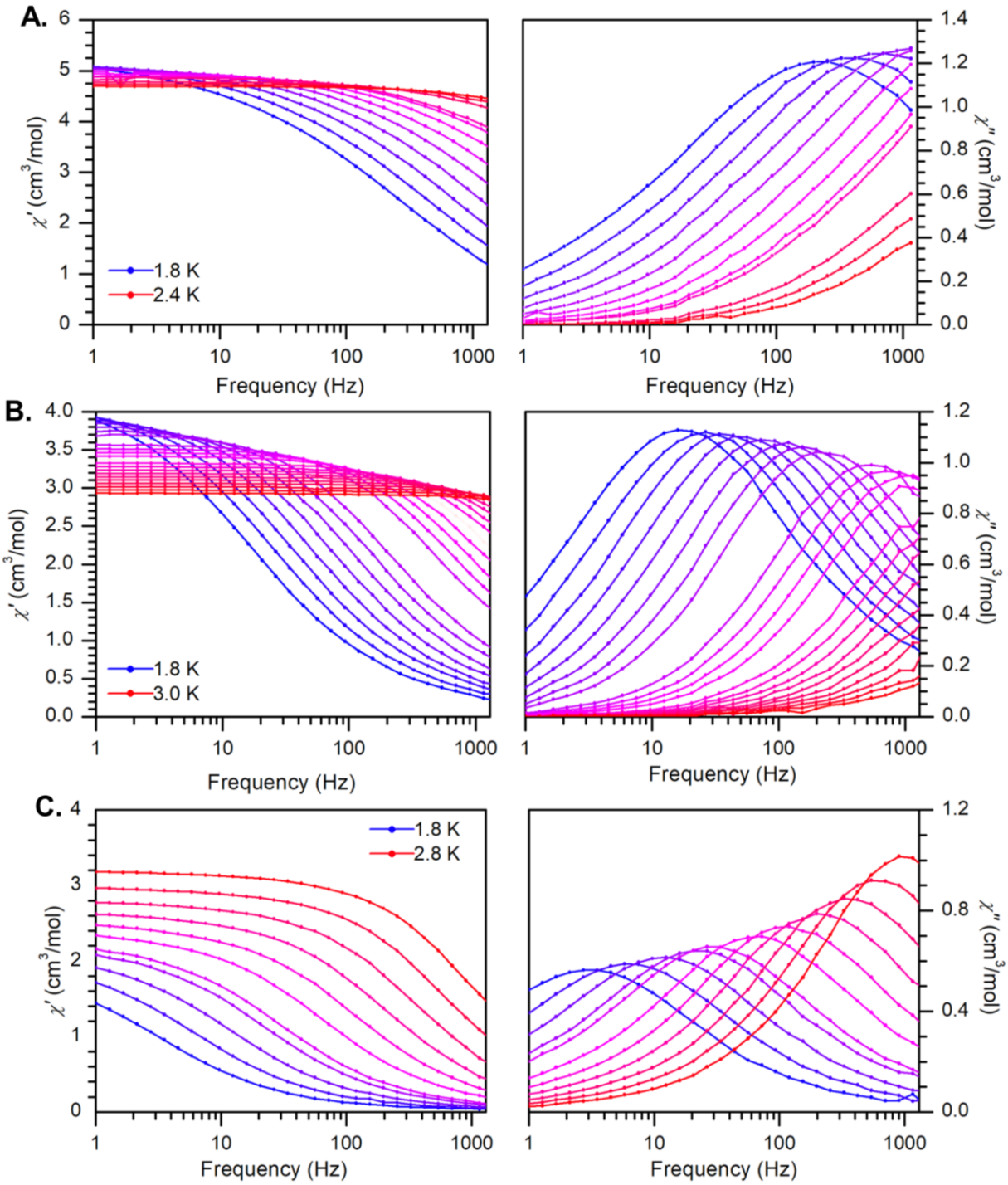

Figure 3.8. Frequency dependences of the in-phase (χ') and out-of-phase (χ'') susceptibility for (A) **1**, (B) **2**, and (C) **3** under zero dc field with a 3 Oe ac field at 0.05 – 0.15 K increments below 3 K. Solid lines are guides to the eye.

dynamics were observed at H_{dc} = 250 Oe, which is near the metamagnetic transition line observed in the magnetic phase diagram (Figure 3.7).[16] Ac susceptibility measurements were consequently

performed under an applied dc field of 250 Oe, and the resulting Arrhenius plot (Figure 3.9) exhibits two thermally activated regimes above and below 2.5 K as opposed to the single regime observed under zero applied dc field. These two regimes, with energy barriers of $\Delta\tau$ = 31 and 20 cm^{-1}, correspond to infinite and finite-size chain dynamics, respectively. The difference between the two energy barriers (11 cm^{-1}) is consistent with the energy required to create a domain wall(Δ_ξ = 10 cm^{-1}) obtained from the plot of ln(χT) vs T^{-1}. This observation also supports the presence of single chain magnet behavior in this material.

In order to exhibit single-chain magnet behavior, a system must possess ions with significant uniaxial magnetic anisotropy, magnetic coupling between these ions, and noncollinearity of these magnetic easy axes in the case of homospin systems with antiferromagnetic exchange. Many high-spin, octahedral Co(II) ions have significant uniaxial anisotropy, which has resulted in their prodigious use in the field of SMMs.[3a]

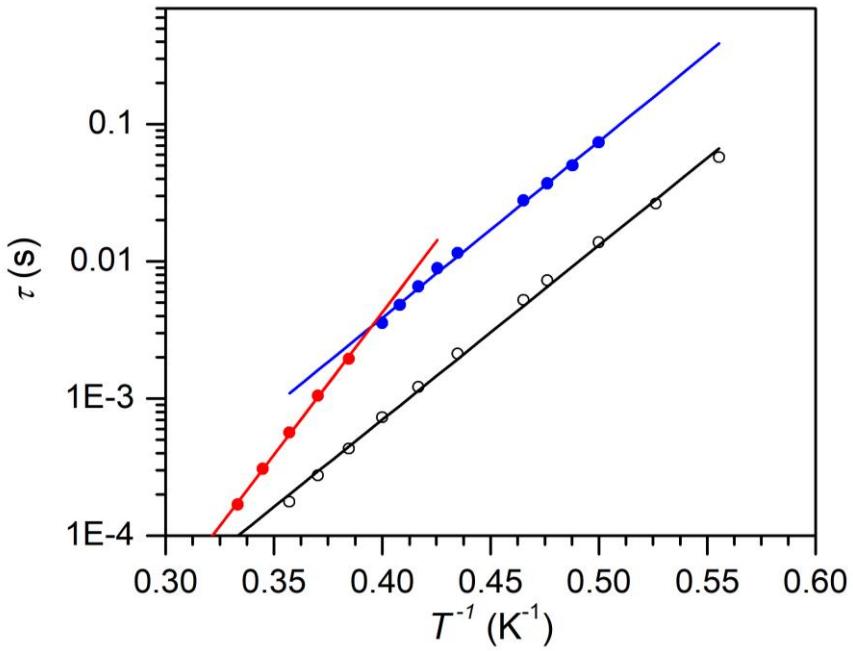

Figure 3.9. Plots of magnetization relaxation time (τ) versus T^{-1} for **3** under zero dc field (empty) and 250 Oe (filled). Solid lines are best fits ($r^2 > 0.997$) of the experimental data to the Arrhenius law.

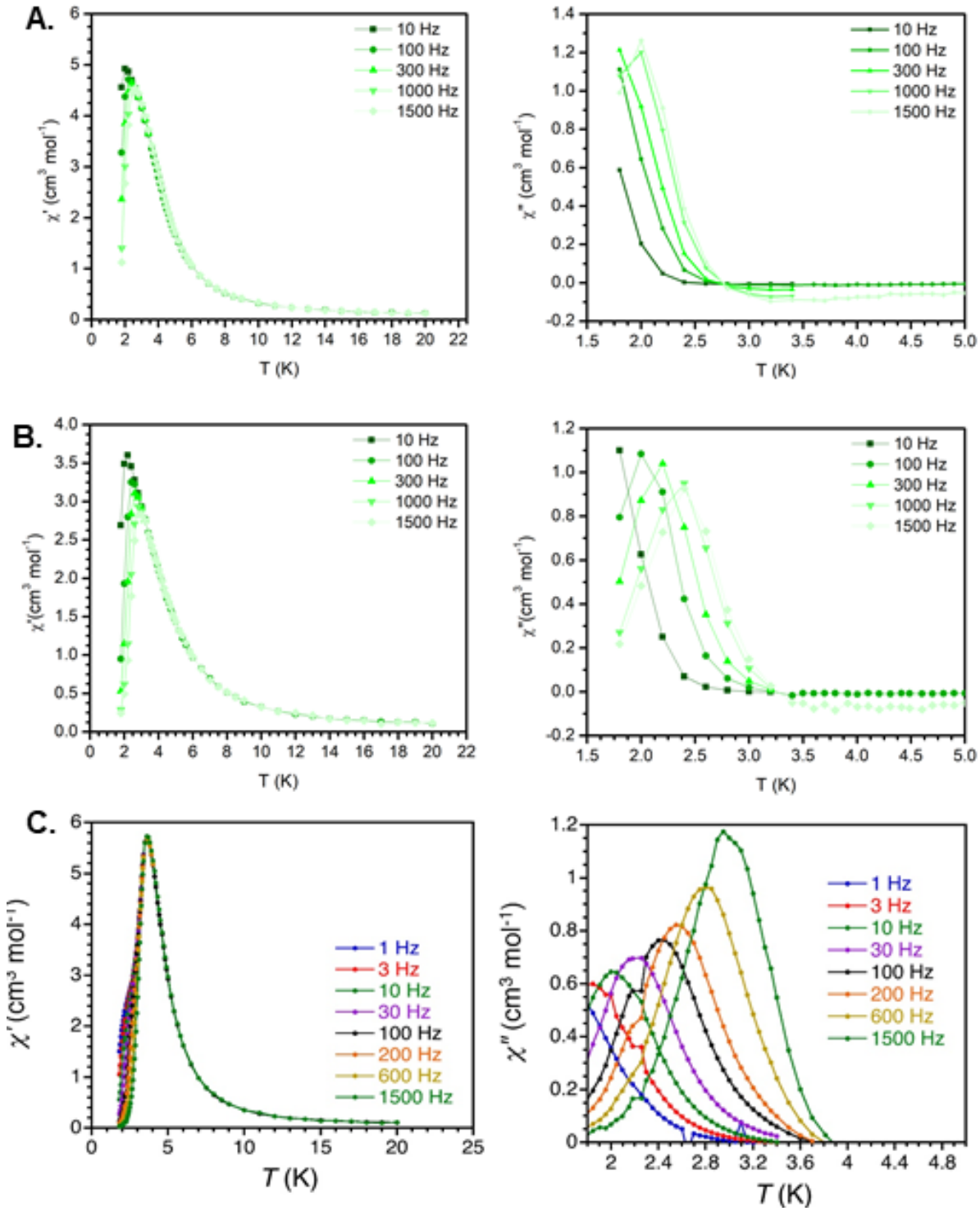

Figure 3.10. Variable-temperature measurement of the real (χ') and imaginary (χ'') components of the ac susceptibility of (A) **1**, (B) **2**, and (C) **3**. Lines are guides to the eye.

In the present systems, there are two different orientations of Co(II) ions, albeit crystallographically equivalent ones. Because Co(II) in an octahedral environment exhibits an uniaxial anisotropy, this structural feature likely avoids a collinear arrangement between Co spins. From the crystallographic data, we observe a small variation in angle between the Co−$O_{N\text{-}ox}$−Co bonds (~116−119°) and in the $O_{B\{P\}DC}$−C−$O_{B\{P\}DC}$ bowing angle of the bridging carboxylates (~126−127.4°). While small changes in either of these parameters may have an effect on the magnetic anisotropy and the canting angle, we observe that only the bowing angle of the carboxylates systematically increases with the anisotropy energy estimated from the chain dynamics. Nevertheless, we have not directly probed the anisotropy of the current systems and therefore cannot conclusively interpret the relationship between the magnetic anisotropy and geometric changes within this series.

The Co−$O_{N\text{-}ox}$−Co angle should also influence the magnetic exchange mediated by the N-oxide O bridge. While both oxygen and carboxylate bridges mediate magnetic coupling via a superexchange pathway and likely have some effect on overall coupling, the coupling through a single-atom bridge will generally be much stronger than that through a three-atom bridge. The superexchange coupling (i.e. the sign and magnitude of the *J* coupling parameter) of these materials should depend on the Co−$O_{N\text{-}ox}$−Co angle, and by extension the relaxation dynamics will be dependent on this angle as well. The magnetic characterization of these materials suggests a weak antiferromagnetic coupling between the Co(II) centers, which is consistent with the coupling reported between similarly bridged materials, but there is no clear trend between the Co−$O_{N\text{-}ox}$−Co angle and the *J* coupling parameter.[12] Taken together, the effects of small structural changes within the series likely have a combination of independent consequences on the magnetic properties of the materials, such as the strength of the magnetic exchange, the magnetic anisotropy, and the

angle between these axes all of which influence chain dynamics. The convolution of these effects makes precise structure−property analysis difficult. Furthermore, caution must always be employed in interpreting the magnetic behavior of low-dimensional magnetic materials, particularly with highly magnetically anisotropic ions such as Co(II). Finally, our inability to grow sufficiently large and high-quality single crystals of these materials for anisotropic, single crystal magnetometry measurements has limited our investigations of magnetic properties. Nonetheless, all of the data which have been presented are consistent with single-chain magnet behavior in this series of materials, and we have assigned the source of this phenomenon as being an antiferromagnetic interaction between canted Co spins along the chains. There are some previous reports which assign related spin-canted behavior in Co(II) chains,[5b,10b,21] but of these only a small number report a frequency-dependent peak in χ''.[5b,10b,11c,21j]

Along the present series, only the 2D material **3** undergoes 3D magnetic ordering, while the two other structurally 3D materials do not show any evidence of long-range magnetic order. Structural analyses indicate that the interchain Co···Co distance across the N-oxide linker in **3** is more than 2 Å longer than those found in the other two compounds (Table 3.1), and the interchain Co···Co distance through the B[P]DC linker, which is decided by the length of each ligand, is also large. Despite these long intermetallic distances, the ring centroid distance of 3.69 Å between the N-oxide linkers in **3** is markedly short in comparison to the related distances of 3.96 and 3.95 Å found in **1** and **2**, respectively. The observed structural features suggest that intermolecular magnetic exchange is efficiently mediated by π–π interactions which overcome the larger separation between the magnetic metal centers. In sum, the addition of an aromatic ring on the auxiliary linking ligand expanded the dimension of efficient magnetic correlations inside the material, providing a system lying at the frontier between single-chain magnets and classical bulk

antiferromagnets.

3.4 Conclusions

A series of related extended molecular solids have been synthesized, characterized, and investigated by ac and dc magnetometry. The materials in this series exhibit slow relaxation of the magnetization with slight variations in their magnetic dynamics. The origin of the slow magnetic relaxation in these materials is likely due to a Co-based 1D substructure featuring antiferromagnetic interactions with spin canting between the metal centers. The 2D material **3** is unique among the series in that it is a metamagnetic material which exhibits 3D antiferromagnetic order at low temperatures while exhibiting molecular magnetic dynamics stemming from the chain component.

3.5 Experimental Methods

General Considerations. All syntheses were carried out under an N2 atmosphere in an MBraun UniLab Pro glovebox. Reagents were used as purchased without further purification. Appropriate solvents were dried and degassed in a Pure Process Technologies solvent system and stored over 4 Å molecular sieves. Solvents were tested for O_2 and H_2O with a standard solution of sodium benzophenone ketyl radical.

Co(BDC)(PNO) (**1**). This compound was synthesized by a method analogous to reported procedures, with modifications. Specifically, MeOH was used in place of water. The analytical and spectroscopic properties were identical with those previously reported.[8c]

Co(BPDC)(PNO) (**2**). This compound was synthesized by mixing $Co(NO_3)_2 \cdot 6H_2O$ (0.082 g, 0.45 mmol), H_2BPDC (0.109 g, 0.450 mmol), and PNO (0.043 g, 0.45 mmol) in 2 mL of MeOH and 10 mL of DMF in a Teflon-capped glass vial. The mixture was then heated at 100 °C overnight to

yield pink crystals (0.124 g, 0.310 mmol, 70%). The crystals were washed with DMF (3 × 5 mL) and then THF before being dried under reduced pressure at room temperature. Anal. Calcd for $CoC_{19}H_{13}O_5N$: C, 57.88; H, 3.32; N, 3.55. Found: C, 57.77; H, 3.42; N, 3.44.

Co(BPDC)(IQNO) (**3**). This compound was synthesized by mixing $Co(NO_3)_2 \cdot 6H_2O$ (0.082 g, 0.45 mmol), H_2BPDC (0.109 g, 0.45 mmol), and IQNO (0.065 g, 0.45 mmol) in 2 mL of MeOH and 10 mL of DMF. The mixture was then heated at 100 °C overnight to yield orange crystals (0.138 g, 0.31 mmol, 69%). The crystals were washed three times with DMF (3 × 5 mL) and then THF (3 × 5 mL) before being dried under reduced pressure at room temperature. Anal. Calcd for $CoC_{23}H_{15}O_5N$: C, 62.18; H, 3.40; N, 3.15. Found: C, 62.11; H, 3.88; N, 3.21.

Magnetometry. Magnetic measurements were carried out with a MPMS-XL Quantum Design SQUID operating at temperatures between 1.8 and 400 K and dc magnetic fields ranging from −5 to 5 T. Measurements were performed on polycrystalline samples of **1** (22.14 mg), **2** (12.04 mg), and **3** (21.10 mg), previously introduced in a sealed polypropylene bag (17.07, 14.31, and 12.45 mg for **1**, **2**, and **3**, respectively).

Ac susceptibility measurements were collected with an oscillating field of 3 Oe with a frequency range from 1 to 1500 Hz. Prior to measurements, the field-dependent magnetization was measured at 100 K in order to confirm the absence of any bulk ferromagnetic impurity (Figure S9). Dc susceptibility data were corrected for the intrinsic diamagnetic contributions of each sample and those from the sample holder.

X-ray Powder Diffraction (XRPD). The XRPD patterns were collected on a SAXSLAB Ganesha instrument in wide-angle X-ray scattering (WAXS) transmission mode. The samples were contained in either a clear, adhesive tape packet or a borosilicate capillary tube. In the case of the

capillary tube, a correction was made to subtract the broad peak from the capillary around 16−25° (2θ) from the baseline.

Single-Crystal X-ray Diffraction (SXRD). The diffraction data for **3** were measured at 100 K on a Bruker D8 fixed-chi with PILATUS1M (CdTe) pixel array detector (synchrotron radiation, λ = 0.41328 Å (30 keV)) at the Chem-MatCARS 15-ID-B beamline at the Advanced Photon Source (Argonne National Laboratory). The diffraction data for **2** were measured at 100 K on a Bruker D8 VENTURE diffractometer equipped with a microfocus Mo-target X-ray tube (λ = 0.71073 Å) and PHOTON 100 CMOS detector. The diffraction data for **2** were measured at room temperature on a Bruker D8 VENTURE with PHOTON 100 CMOS detector system equipped with a Mo-target microfocus X-ray tube (λ = 0.71073 Å). Data reduction and integration for all structures were performed with the Bruker APEX3 software package (Bruker AXS, version 2015.5-2, 2015). Data were scaled and corrected for absorption effects using the multiscan procedure as implemented in SADABS (Bruker AXS, version 2014/522). The structures were solved by SHELXT (version 2014/523) and refined by a full-matrix least-squares procedure using OLEX224 (XL refinement program version 2018/125). Note that for the structure of **3** there is one level B alert which corresponds to a limited data collection due to the geometry of the detector and source at the beamline.

Gas Adsorption. Activation and measurements were performed on a Micromeritics ASAP 2020 instrument. The surface area was calculated from the N_2 adsorption isotherm using Brunauer−Emmett−Teller (BET) theory. Samples were loaded into a quartz tube fitted with a TranSeal cap and activated at 100 °C until the outgas rate was <1 μm Hg/min. Measurements were performed at 77 K, in a liquid N_2 bath.

3.6 Supplementary Data

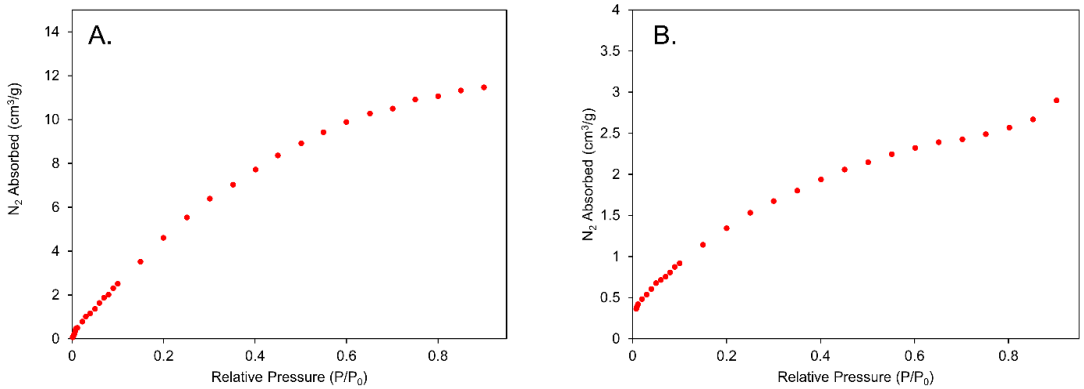

Figure 3.11. N_2 gas uptake measurements for (A) **2**, and (B) **3**

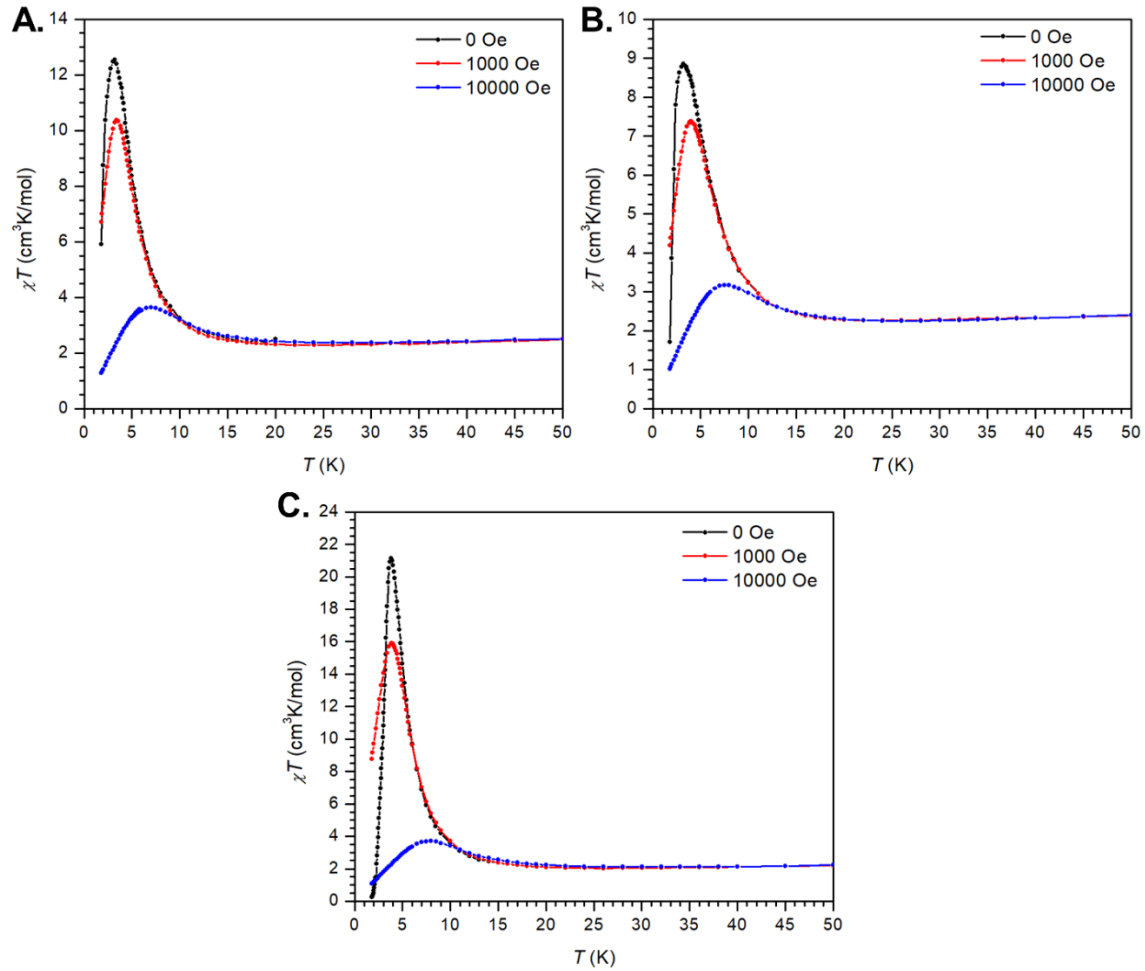

Figure 3.12. Field dependent inflection in χT for (A) **1**, (B) **2**, and (C) **3**. Lines are guides to the eye. The χ values under an applied field of 1000 and 10000 Oe were calculated as M/H under a dc field. The zero-field data were estimated to be M'/H_{ac} with an ac field (H_{ac}) of 3 Oe, under the assumption that χ is linear at low fields.

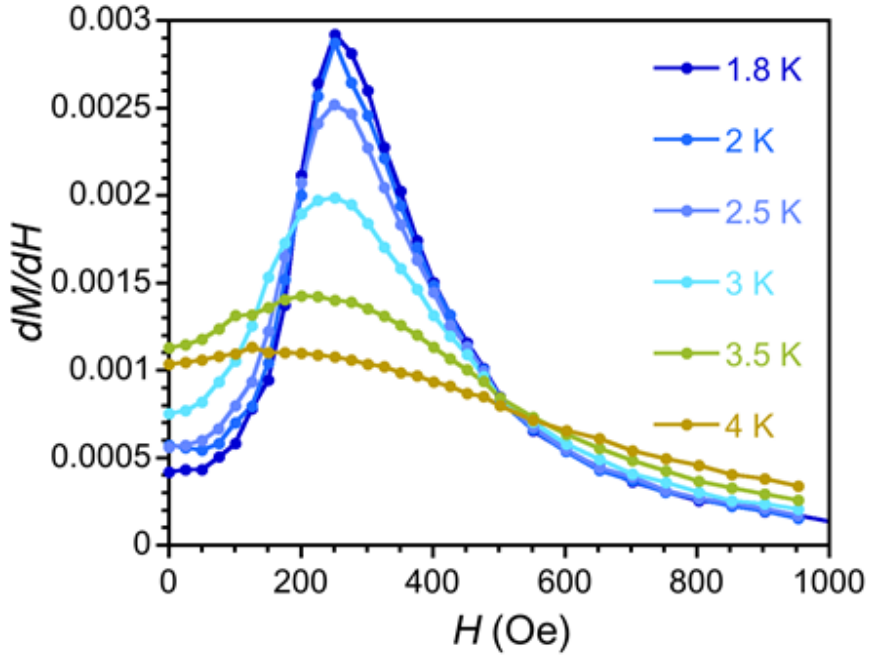

Figure 3.13. *dM*/*dH* vs *H* plot from the variable-field magnetization data collected under various temperatures for **3**. Lines are guides to the eye.

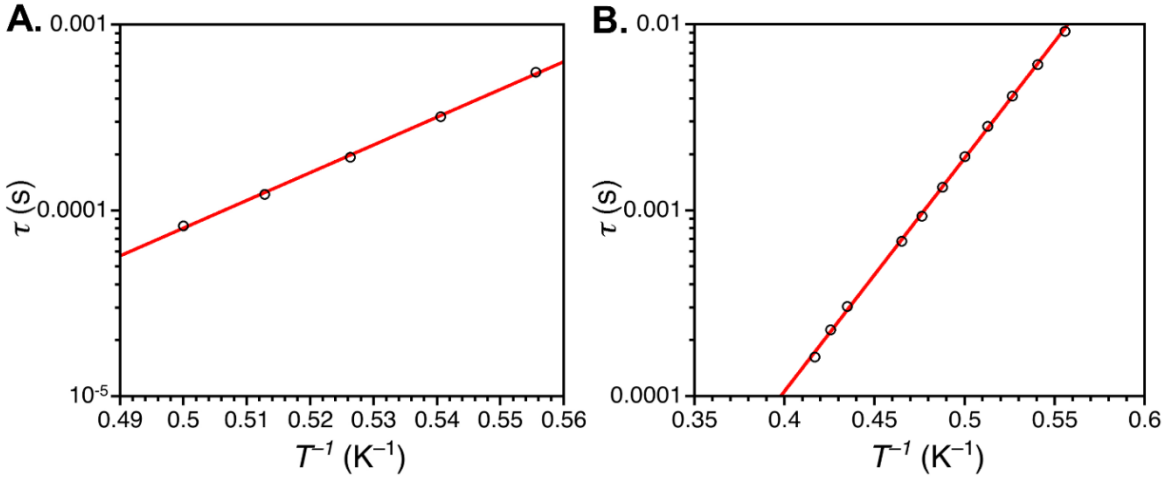

Figure 3.14. Arrhenius plots from the ac magnetic susceptibility data for (A) **1** and (B) **2**. Lines are fits are outlined in the text.

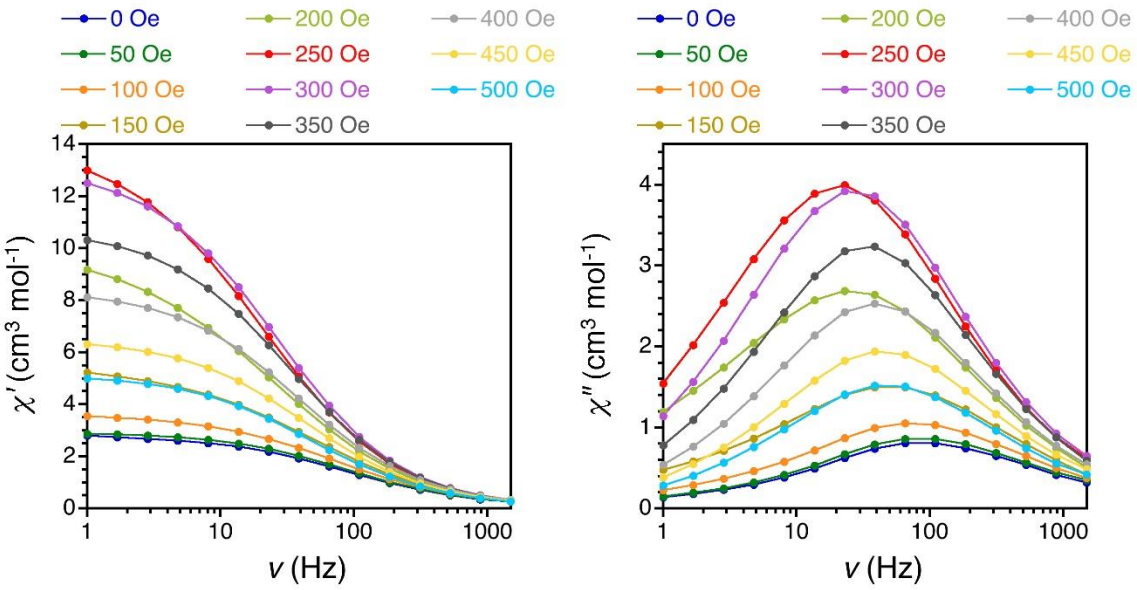

Figure 3.15. Variable-frequency ac susceptibility measurements at various applied fields for **3**. Lines are guides to the eye.

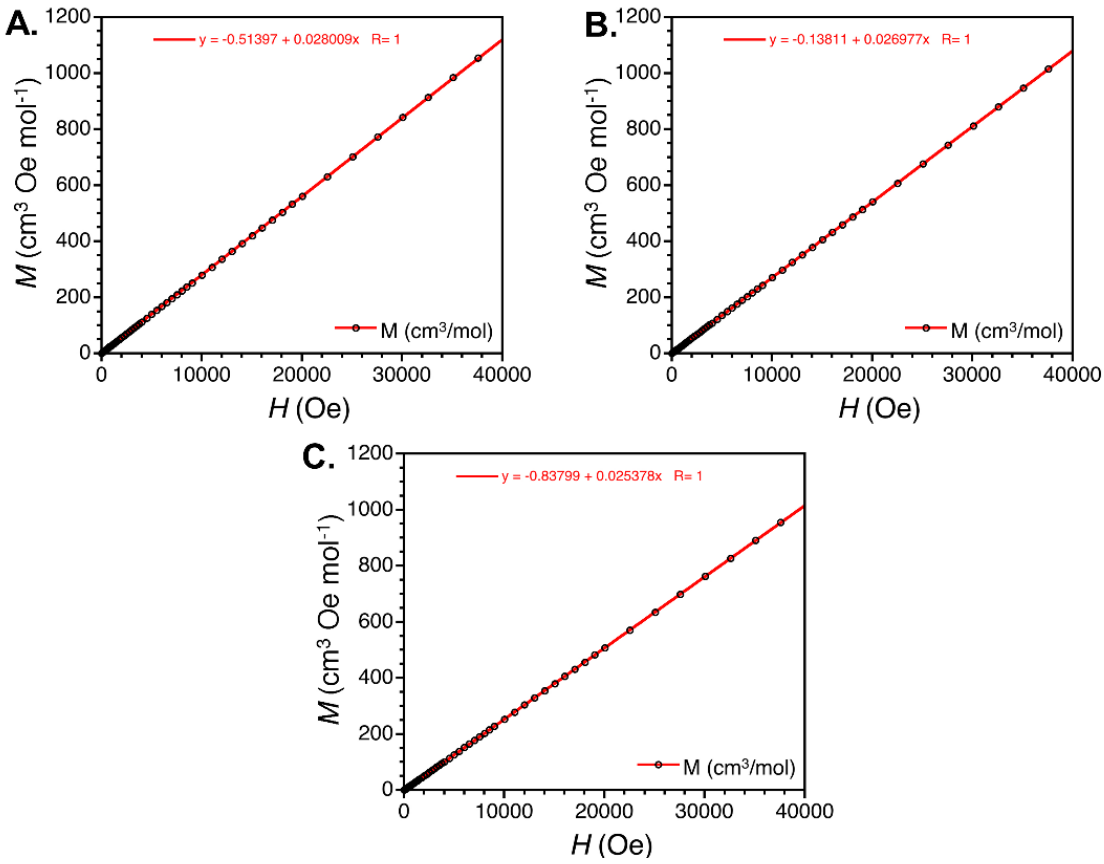

Figure 3.16. Field-dependent magnetization measured at 100 K to confirm the absence of any bulk ferromagnetic impurity for (A) **1**, (B) **2**, and (C) **3**.

Table 3.2. Crystal data and structure refinement for **2**

Identification code	tw4c2c
Empirical formula	$C_{19}H_{13}CoNO_5$
Formula weight	394.23
Temperature/K	296(2)
Crystal system	monoclinic
Space group	*C*2/*c*
a/Å	28.751(2)
b/Å	9.1697(7)
c/Å	7.1222(5)
α/°	90
β/°	102.407(4)
γ/°	90
Volume/Å^3	1833.8(2)
Z	4
ρ_{calc}g/cm^3	1.428
μ/mm^{-1}	0.964
F(000)	804.0
Crystal size/mm^3	0.219 × 0.096 × 0.079
Radiation	MoKα (λ = 0.71073)
2Θ range for data collection/°	4.674 to 50.214
Index ranges	-34 ≤ h ≤ 33, 0 ≤ k ≤ 10, 0 ≤ l ≤ 8
Reflections collected	1664
Independent reflections	1664 [R_{int} = 0.0773, R_{sigma} = 0.0568]
Data/restraints/parameters	1664/222/168
Goodness-of-fit on F^2	1.091
Final R indexes [I>=2σ (I)]	R_1 = 0.0500, wR_2 = 0.1023
Final R indexes [all data]	R_1 = 0.0816, wR_2 = 0.1168
Largest diff. peak/hole / e Å^{-3}	0.76/-0.39

Table 3.3. Fractional Atomic Coordinates ($\times 10^4$) and Equivalent Isotropic Displacement Parameters ($Å^2 \times 10^3$) for 2. U_{eq} is defined as 1/3 of of the trace of the orthogonalised U_{IJ} tensor.

Atom	*x*	*y*	*z*	U(eq)
Co1	5000	0	5000	17.5(2)
O1	5000	1158(4)	7500	26.1(9)
O2	5517.9(17)	1424(6)	4460(6)	28.9(13)
O3	5565.9(16)	1266(5)	1374(6)	29.6(12)
N1	5000	2601(6)	7500	31.1(12)
C1	5412.3(18)	3309(6)	7951(13)	43.1(12)
C2	5416(2)	4806(6)	7952(15)	54.2(15)
C3	5000	5558(8)	7500	51(2)
C4	5736.2(14)	1473(5)	3103(12)	24.0(9)
C5	6257.6(15)	1824(5)	3684(11)	32.6(11)
C8	7220(20)	2240(80)	4810(100)	49(7)
C6	6527(8)	1460(40)	2440(30)	44(5)
C7	7028(8)	1700(40)	2990(40)	55(6)
C9	6955(10)	2760(40)	5950(40)	57(6)
C10	6459(10)	2450(40)	5390(40)	50(6)
C6A	6518(6)	2280(30)	2350(20)	54(5)
C7A	7000(7)	2550(30)	2870(30)	58(5)
C9A	6984(7)	1940(30)	6050(30)	56(5)
C10A	6498(7)	1700(30)	5580(30)	46(5)
C8A	7248(17)	2450(60)	4660(80)	48(5)

Table 3.4. Anisotropic Displacement Parameters ($Å^2 \times 10^3$) for **2**. The Anisotropic displacement factor exponent takes the form: $-2\pi^2[h^2a^{*2}U_{11}+2hka^*b^*U_{12}+\ldots]$.

Atom	U_{11}	U_{22}	U_{33}	U_{23}	U_{13}	U_{12}
Co1	13.3(3)	22.7(4)	16.0(4)	-0.7(5)	2.1(5)	-0.1(9)
O1	38(2)	19.6(19)	20(2)	0	6(4)	0
O2	19(2)	36(3)	31(3)	-1(2)	4(2)	-11(2)
O3	23(2)	41(3)	24(2)	-1(3)	1(2)	-10(2)
N1	42(3)	27(3)	25(3)	0	10(5)	0
C1	47(3)	40(3)	41(3)	1(6)	8(5)	-3(2)
C2	61(3)	38(3)	62(4)	2(6)	9(5)	-16(3)
C3	68(5)	29(3)	56(6)	0	12(8)	0
C4	20(2)	23(2)	31(3)	6(4)	10(4)	-5.1(16)
C5	21(2)	46(3)	30(3)	3(4)	4(3)	-7(2)
C8	14(8)	93(19)	37(11)	-5(13)	-2(7)	-16(11)
C6	21(6)	70(14)	38(8)	-22(9)	0(5)	-22(8)
C7	17(6)	103(16)	47(9)	-18(11)	8(6)	-20(10)
C9	31(7)	98(16)	40(9)	-15(11)	6(6)	-21(10)
C10	26(7)	84(16)	39(8)	-11(10)	7(6)	-18(10)
C6A	32(6)	95(14)	31(6)	8(9)	1(4)	-31(9)
C7A	30(6)	104(14)	39(6)	20(9)	6(5)	-34(9)
C9A	34(6)	103(13)	29(6)	2(9)	4(5)	-28(9)
C10A	32(6)	80(13)	28(5)	5(8)	9(4)	-21(9)
C8A	21(7)	86(13)	35(7)	2(8)	4(5)	-26(7)

Table 3.5. Bond Lengths for **2**

Atom	Atom	Length/Å	Atom	Atom	Length/Å
Co1	O1[1]	2.0729(19)	C5	C6	1.34(2)
Co1	O1	2.0729(19)	C5	C10	1.36(3)
Co1	O2	2.077(5)	C5	C6A	1.393(18)
Co1	O2[1]	2.077(5)	C5	C10A	1.381(19)
Co1	O3[2]	2.066(4)	C8	C8[5]	1.62(12)
Co1	O3[3]	2.066(4)	C8	C7	1.39(7)
O1	N1	1.324(7)	C8	C9	1.32(7)
O2	C4	1.261(8)	C6	C7	1.43(3)
O3	C4	1.238(8)	C9	C10	1.42(3)
N1	C1	1.329(6)	C6A	C7A	1.38(2)
N1	C1[4]	1.329(6)	C7A	C8A	1.32(5)
C1	C2	1.373(7)	C9A	C10A	1.38(2)
C2	C3	1.358(7)	C9A	C8A	1.45(5)
C4	C5	1.502(5)	C8A	C8A[5]	1.43(10)

[1]1-X,-Y,1-Z; [2]1-X,+Y,1/2-Z; [3]+X,-Y,1/2+Z; [4]1-X,+Y,3/2-Z; [5]3/2-X,1/2-Y,1-Z

Table 3. 6. Bond Angles for **2**

Atom	Atom	Atom	Angle/˚	Atom	Atom	Atom	Angle/˚
O1	Co1	O1[1]	180.0	C2	C3	C2[4]	119.0(7)
O1[1]	Co1	O2	91.74(14)	O2	C4	C5	115.4(7)
O1[1]	Co1	O2[1]	88.26(15)	O3	C4	O2	126.9(4)
O1	Co1	O2	88.26(14)	O3	C4	C5	117.7(7)
O1	Co1	O2[1]	91.74(14)	C6	C5	C4	116.6(11)
O2[1]	Co1	O2	180.00(18)	C6	C5	C10	120.3(16)
O3[2]	Co1	O1[1]	91.49(14)	C10	C5	C4	123.1(13)
O3[3]	Co1	O1	91.49(14)	C6A	C5	C4	121.8(10)
O3[3]	Co1	O1[1]	88.51(14)	C10A	C5	C4	120.7(10)
O3[2]	Co1	O1	88.51(14)	C10A	C5	C6A	117.5(13)
O3[3]	Co1	O2[1]	94.71(15)	C7	C8	C8[5]	117(6)
O3[3]	Co1	O2	85.29(15)	C9	C8	C8[5]	118(8)
O3[2]	Co1	O2[1]	85.29(15)	C9	C8	C7	122(5)
O3[2]	Co1	O2	94.71(15)	C5	C6	C7	117.9(18)
O3[3]	Co1	O3[2]	180.00(18)	C8	C7	C6	120(3)
Co1	O1	Co1[4]	118.40(18)	C8	C9	C10	116(4)
N1	O1	Co1[4]	120.80(9)	C5	C10	C9	123(2)
N1	O1	Co1	120.80(9)	C7A	C6A	C5	121.7(14)
C4	O2	Co1	131.2(4)	C8A	C7A	C6A	124(2)
C4	O3	Co1[2]	131.3(4)	C10A	C9A	C8A	123(3)
O1	N1	C1[4]	119.2(3)	C5	C10A	C9A	119.3(16)
O1	N1	C1	119.2(3)	C7A	C8A	C9A	115(3)
C1[4]	N1	C1	121.6(6)	C7A	C8A	C8A[5]	129(5)
N1	C1	C2	119.7(5)	C8A[5]	C8A	C9A	116(6)
C3	C2	C1	120.1(5)				

[1]1-X,-Y,1-Z; [2]1-X,+Y,1/2-Z; [3]+X,-Y,1/2+Z; [4]1-X,+Y,3/2-Z; [5]3/2-X,1/2-Y,1-Z

Table 3.7. Atomic Occupancy for **2**

Atom	*Occupancy*	Atom	*Occupancy*	Atom	*Occupancy*
C8	0.43(3)	C6	0.43(3)	H6	0.43(3)
C7	0.43(3)	H7	0.43(3)	C9	0.43(3)
H9	0.43(3)	C10	0.43(3)	H10	0.43(3)
C6A	0.57(3)	H6A	0.57(3)	C7A	0.57(3)
H7A	0.57(3)	C9A	0.57(3)	H9A	0.57(3)
C10A	0.57(3)	H10A	0.57(3)	C8A	0.57(3)

Table 3.8. Crystal data and structure refinement for **3**

Identification code	Co
Empirical formula	$C_{23}H_{15}CoNO_5$
Formula weight	444.29
Temperature/K	100(2)
Crystal system	triclinic
Space group	*P*-1
a/Å	7.0517(12)
b/Å	11.353(2)
c/Å	14.175(3)
α/°	73.988(3)
β/°	88.252(4)
γ/°	88.698(4)
Volume/Å^3	1090.2(3)
Z	2
ρ_{calc}g/cm^3	1.353
μ/mm^{-1}	0.196
F(000)	454.0
Crystal size/mm^3	0.3 × 0.2 × 0.2
Radiation	synchrotron (λ = 0.41328)
2Θ range for data collection/°	2.378 to 28.864
Index ranges	-8 ≤ h ≤ 8, -13 ≤ k ≤ 13, -17 ≤ l ≤ 17
Reflections collected	24362
Independent reflections	3774 [R_{int} = 0.0836, R_{sigma} = 0.0485]
Data/restraints/parameters	3774/0/274
Goodness-of-fit on F^2	1.052
Final R indexes [I>=2σ (I)]	R_1 = 0.0657, wR_2 = 0.1701
Final R indexes [all data]	R_1 = 0.0840, wR_2 = 0.1833
Largest diff. peak/hole / e Å^{-3}	1.69/-1.01

n: number of independent reflections; p: number of refined parameters

Table 3.9. Fractional Atomic Coordinates ($\times 10^4$) and Equivalent Isotropic Displacement Parameters ($Å^2 \times 10^3$) for **3**. U_{eq} is defined as 1/3 of of the trace of the orthogonalised U_{IJ} tensor.

Atom	*x*	*y*	*z*	U(eq)
Co1	0	5000	10000	19.2(3)
Co2	5000	5000	10000	19.3(3)
O1	2470(5)	5946(3)	9920(2)	20.8(7)
O2	1069(5)	4036(3)	9026(2)	24.7(7)
O3	4234(5)	4201(3)	8929(2)	23.9(7)
O4	4038(5)	3574(3)	1175(2)	23.5(7)
O5	861(5)	3702(3)	1252(2)	24.7(7)
N1	2452(6)	7143(3)	9851(3)	20.6(8)
C1	2584(7)	7498(4)	10656(3)	22.9(10)
C2	2584(7)	8764(4)	10603(4)	23(1)
C3	2731(7)	9157(4)	11454(4)	27.9(11)
C4	2720(8)	10400(4)	11378(4)	30.7(12)
C5	2563(8)	11273(4)	10446(4)	29.0(11)
C6	2421(8)	10890(4)	9613(4)	29.7(12)
C7	2440(7)	9624(4)	9671(3)	23.1(10)
C8	2299(8)	9181(4)	8836(4)	25.4(10)
C9	2311(7)	7959(4)	8935(4)	23.9(10)
C10	2645(7)	4008(4)	8617(3)	20.1(9)
C11	2694(7)	3734(4)	7629(3)	23.3(10)
C12	1084(8)	3325(5)	7292(4)	32.6(12)
C13	1069(8)	3137(5)	6368(4)	35.0(12)
C14	2673(8)	3380(4)	5744(3)	26.7(11)
C15	4317(8)	3743(5)	6101(4)	28.7(11)
C16	4327(8)	3916(5)	7038(4)	28.2(11)
C17	2600(8)	3294(4)	4711(3)	26.5(11)
C18	965(8)	3603(5)	4196(4)	33.2(12)
C19	906(8)	3623(5)	3226(4)	31.1(11)
C20	2509(7)	3346(4)	2732(3)	23.5(10)
C21	4154(8)	3025(5)	3240(4)	29.9(11)
C22	4212(8)	2984(5)	4219(4)	34.4(12)
C23	2472(7)	3548(4)	1628(3)	21.2(10)

Table 3.10. Anisotropic Displacement Parameters ($Å^2 \times 10^3$) for **3**. The Anisotropic displacement factor exponent takes the form: $-2\pi^2[h^2a^{*2}U_{11}+2hka^*b^*U_{12}+\ldots]$.

Atom	U_{11}	U_{22}	U_{33}	U_{23}	U_{13}	U_{12}
Co1	22.8(6)	16.6(4)	21.5(5)	-10.5(3)	-3.7(3)	0.2(3)
Co2	21.6(6)	17.5(4)	21.8(5)	-10.6(3)	-3.9(3)	1.1(3)
O1	18.5(19)	14.2(15)	32.6(18)	-11.3(12)	-3.5(13)	2.1(12)
O2	24(2)	25.7(17)	27.3(17)	-12.4(13)	-1.6(14)	-1.6(13)
O3	17(2)	30.6(18)	28.0(17)	-15.3(14)	-4.1(13)	5.6(13)
O4	25(2)	18.3(15)	29.1(18)	-10.3(13)	-5.0(14)	1.0(13)
O5	26(2)	26.8(17)	23.6(17)	-9.9(13)	-3.5(14)	-1.0(13)
N1	20(2)	16.3(18)	26(2)	-7.2(15)	-4.0(15)	1.7(14)
C1	21(3)	20(2)	30(3)	-9.2(18)	-4.4(19)	1.2(18)
C2	21(3)	20(2)	32(3)	-13.0(19)	-4.7(19)	0.2(17)
C3	28(3)	25(2)	33(3)	-13(2)	-1(2)	-3(2)
C4	36(3)	22(2)	39(3)	-17(2)	-1(2)	-1(2)
C5	28(3)	22(2)	41(3)	-15(2)	-3(2)	1.6(19)
C6	35(3)	18(2)	38(3)	-10(2)	-5(2)	1.3(19)
C7	23(3)	19(2)	29(2)	-10.6(19)	-2.1(19)	0.5(17)
C8	31(3)	20(2)	25(2)	-5.3(18)	-4(2)	-2.3(19)
C9	18(3)	25(2)	31(3)	-12(2)	-2.4(19)	3.2(18)
C10	17(3)	14(2)	30(2)	-5.9(17)	-4.3(19)	0.2(16)
C11	30(3)	16(2)	25(2)	-8.1(17)	-2.9(19)	1.1(18)
C12	31(3)	41(3)	31(3)	-19(2)	2(2)	-5(2)
C13	34(3)	45(3)	33(3)	-22(2)	-3(2)	-6(2)
C14	35(3)	25(2)	23(2)	-10.9(19)	-1(2)	1(2)
C15	28(3)	34(3)	28(3)	-14(2)	-3(2)	1(2)
C16	24(3)	35(3)	30(3)	-15(2)	-7(2)	1(2)
C17	33(3)	24(2)	25(2)	-10.8(19)	-2(2)	0.3(19)
C18	24(3)	45(3)	36(3)	-20(2)	0(2)	4(2)
C19	24(3)	42(3)	30(3)	-15(2)	-4(2)	6(2)
C20	26(3)	18(2)	28(3)	-9.0(18)	-1.1(19)	-1.8(18)
C21	23(3)	39(3)	32(3)	-16(2)	0(2)	3(2)
C22	29(3)	41(3)	36(3)	-17(2)	-6(2)	7(2)
C23	18(3)	18(2)	31(3)	-12.8(18)	-5.7(19)	2.5(17)

Table 3.11. Bond Lengths for **3**

Atom	Atom	Length/Å	Atom	Atom	Length/Å
Co1	O1[1]	2.051(3)	C3	C4	1.385(7)
Co1	O1	2.051(3)	C4	C5	1.422(7)
Co1	O2[1]	2.099(3)	C5	C6	1.374(7)
Co1	O2	2.099(3)	C6	C7	1.416(6)
Co1	O5[2]	2.067(3)	C7	C8	1.414(6)
Co1	O5[3]	2.067(3)	C8	C9	1.355(6)
Co2	O1[4]	2.051(3)	C10	C11	1.516(6)
Co2	O1	2.051(3)	C11	C12	1.383(7)
Co2	O3[4]	2.062(3)	C11	C16	1.388(7)
Co2	O3	2.062(3)	C12	C13	1.384(7)
Co2	O4[5]	2.086(3)	C13	C14	1.399(8)
Co2	O4[3]	2.086(3)	C14	C15	1.394(7)
O1	N1	1.335(5)	C14	C17	1.496(6)
O2	C10	1.241(6)	C15	C16	1.395(7)
O3	C10	1.262(6)	C17	C18	1.369(8)
O4	C23	1.257(6)	C17	C22	1.404(8)
O5	C23	1.258(6)	C18	C19	1.371(7)
N1	C1	1.317(6)	C19	C20	1.388(7)
N1	C9	1.376(6)	C20	C21	1.372(7)
C1	C2	1.418(6)	C20	C23	1.519(6)
C2	C3	1.404(7)	C21	C22	1.378(7)
C2	C7	1.415(7)			

[1]-X,1-Y,2-Z; [2]-X,1-Y,1-Z; [3]+X,+Y,1+Z; [4]1-X,1-Y,2-Z; [5]1-X,1-Y,1-Z

Table 3.12. Bond Angles for **3**

Atom	Atom	Atom	Angle/˚	Atom	Atom	Atom	Angle/˚
O1[1]	Co1	O1	180.0	N1	C1	C2	120.2(4)
O1[1]	Co1	O2[1]	92.41(13)	C3	C2	C1	121.0(4)
O1	Co1	O2[1]	87.59(13)	C3	C2	C7	120.6(4)
O1	Co1	O2	92.41(13)	C7	C2	C1	118.4(4)
O1[1]	Co1	O2	87.59(13)	C4	C3	C2	119.5(5)
O1[1]	Co1	O5[2]	91.43(13)	C3	C4	C5	120.4(5)
O1	Co1	O5[2]	88.57(13)	C6	C5	C4	120.2(4)
O1[1]	Co1	O5[3]	88.57(13)	C5	C6	C7	120.5(5)
O1	Co1	O5[3]	91.43(13)	C2	C7	C6	118.8(4)
O2	Co1	O2[1]	180.0	C8	C7	C2	118.5(4)
O5[2]	Co1	O2	84.98(13)	C8	C7	C6	122.8(4)
O5[3]	Co1	O2	95.02(13)	C9	C8	C7	120.3(4)
O5[2]	Co1	O2[1]	95.01(13)	C8	C9	N1	120.0(4)
O5[3]	Co1	O2[1]	84.99(13)	O2	C10	O3	127.1(4)
O5[2]	Co1	O5[3]	180.0	O2	C10	C11	117.4(4)
O1[4]	Co2	O1	180.0	O3	C10	C11	115.6(4)
O1[4]	Co2	O3	87.94(12)	C12	C11	C10	120.1(4)
O1	Co2	O3[4]	87.94(12)	C12	C11	C16	118.9(4)
O1	Co2	O3	92.06(12)	C16	C11	C10	121.0(4)
O1[4]	Co2	O3[4]	92.06(12)	C11	C12	C13	120.9(5)
O1	Co2	O4[3]	92.84(13)	C12	C13	C14	120.8(5)
O1[4]	Co2	O4[3]	87.16(13)	C13	C14	C17	120.8(5)
O1	Co2	O4[5]	87.16(13)	C15	C14	C13	118.0(5)
O1[4]	Co2	O4[5]	92.84(13)	C15	C14	C17	121.1(5)
O3[4]	Co2	O3	180.0	C14	C15	C16	120.7(5)
O3[4]	Co2	O4[3]	84.73(13)	C11	C16	C15	120.4(5)
O3	Co2	O4[3]	95.27(13)	C18	C17	C14	120.0(5)
O3[4]	Co2	O4[5]	95.27(13)	C18	C17	C22	118.1(5)
O3	Co2	O4[5]	84.73(13)	C22	C17	C14	121.7(5)
O4[5]	Co2	O4[3]	180.0	C17	C18	C19	121.1(5)
Co1	O1	Co2	118.53(14)	C18	C19	C20	120.9(5)
N1	O1	Co1	121.4(3)	C19	C20	C23	119.5(4)
N1	O1	Co2	120.1(3)	C21	C20	C19	118.6(5)
C10	O2	Co1	132.8(3)	C21	C20	C23	121.4(4)
C10	O3	Co2	132.6(3)	C20	C21	C22	120.7(5)
C23	O4	Co2[6]	125.9(3)	C21	C22	C17	120.6(5)
C23	O5	Co1[6]	128.6(3)	O4	C23	O5	126.2(4)
O1	N1	C9	118.4(4)	O4	C23	C20	117.6(4)
C1	N1	O1	119.0(4)	O5	C23	C20	116.2(4)
C1	N1	C9	122.6(4)				

[1]-X,1-Y,2-Z; [2]-X,1-Y,1-Z; [3]+X,+Y,1+Z; [4]1-X,1-Y,2-Z; [5]1-X,1-Y,1-Z; [6]+X,+Y,-1+Z

3.7 Notes and References

Authorship and prior publication. This majority of this chapter was reproduced from the following publication, with additional edits: *Inorg. Chem.* **2019**, *58(6)*, 3764-3773. Portions of the work were completed by coauthors.

1. (a) Kurmoo, M. *Chem. Soc. Rev.* **2009**, *38* (5), 1353. (b) Dechambenoit, P.; Long, J. R. *Chem. Soc. Rev.* **2011**, *40* (6), 3249. (c) Coulon, C.; Miyasaka, H.; Clérac, R. *Structure and Bonding*; Springer, Berlin, Heidelberg; 163. (d) Espallargas, G. M.; Coronado, E. *Chem. Soc. Rev.* **2018**, *47*, 533. (e) J. S. Miller, *Mater. Today* **2014**, *17*, 224. (f) Verdaguer, M.; Girolami, G. In *Magnetism – Molecules to Materials*, Miller, J. S., Drillon, M., Eds.; Wiley-VCH, Weinheim; 2004; 5, 283. (g) Clement-León, M.; Coronado, E.; Martí-Gastaldo, C.; Romero, F. M. *Chem. Soc. Rev.* **2011**, *40*, 473. (h) Ferrando-Soria, J.; Vallejo, J.; Castellano, M.; Martínez-Lillo, J.; Pardo, E.; Cano, J.; Castro, I.; Lloret, F.; Ruiz-García, R.; Julve, M. *Coord. Chem. Rev.* **2017**, *339*, 17. (i) Ohkoshi, S.-I.; Tokoro, H. *Acc. Chem. Res.* **2012**, *45*, 1749-1758. (j) Miyasaka, H. *Acc. Chem. Res.* **2013**, *2*, 248. (k) Coronado, E.; Espallargas, G. M. *Chem.Soc.Rev.* **2013**, *42*, 1525.

2. (a) Caneschi, A.; Gatteschi, D.; Sessoli, R.; Barra, A. L.; Brunel, L. C.; Guillot, M. *J. Am. Chem. Soc.* **1991**, *113* (15), 5873. (b) Sessoli, R.; Gatteschi, D.; Caneschi, A.; Novak, M. A. *Nature* **1993**, *365* (6442), 141. (c) Sessoli, R.; Tsai, H. L.; Schake, A. R.; Wang, S.; Vincent, J. B.; Folting, K.; Gatteschi, D.; Christou, G.; Hendrickson, D. N. *J. Am. Chem. Soc.* **1993**, *115* (5), 1804. (d) Caneschi, A.; Gatteschi, D.; Lalioti, N.; Sangregorio, C.; Sessoli, R.; Venturi, G.; Vindigni, A.; Rettori, A.; Pini, M. G.; Novak, M. A. *Angew. Chem. Int. Ed.* **2001**, *40* (9), 1760. (e) Clérac, R.; Miyasaka, H.; Yamashita, M.; Coulon, C. *J. Am. Chem. Soc.* **2002**, 124, 12837.

3. Reviews and references therein: (a) Murrie, M. *Chem. Soc. Rev.* **2010**, *39*, 1986-1995. (b) Woodruff, D. N.; Winpenny, R. E. P. *Chem. Rev.* **2013**, *113*, 5110. (c) Milios, C. J.; Winpenny, R. E. P. *Struct. Bonding (Berlin)* **2014**, *164*, 1-110. (d) Jiang, S. D.; Wang, B. W.; Gao, S. *Struct. Bonding (Berlin)* **2014**, *164*, 111. (e) Pedersen, K. S.; Bendix, J.; Clérac, R. *Chem. Commun.* **2014**, *50*, 4396. (f) Feltham, H. L. C.; Brooker, S. *Coord. Chem. Rev.* **2014**, *276*, 1-33. (g) Liu, K.; Shi, W.; Cheng, P. *Coord. Chem. Rev.* **2015**, *74*, 289. (h) Demir, S.; Jeon, I.-R.; Long, J. R.; Harris, T. D. *Coord. Chem. Rev.* **2015**, *289-290*, 149. (i) Atanasov, M.; Aravena, D.; Suturina, E.; Bill, E.; Maganas, D.; Neese, F. *Coord. Chem. Rev.* **2015**, *289-290*, 177. (j) Chilton, N. F. *Inorg. Chem.* **2015**, *54*, 2097-2099. (k) Craig, G. A.; Murrie, M. *Chem. Soc. Rev.* **2015**, *44*, 2135. (l) Harriman, K. L. M.; Murugesu, M. *Acc. Chem. Res.* **2016**, *49*, 1158. (m) Frost, J. M.; Harriman, K. L. M.; Murugesu, M. *Chem. Sci.* **2016**, *7*, 2470. (n) Pointillart, F.; Cador, O.; Le Guennic, B.; Ouahab, L. *Coord. Chem. Rev.* **2017**, *346*, 150. (o) Yamashita, M.; Katoh, K. *Single Molecule Magnets.* In *Molecular Magnetic Materials: Concepts and Applications*; Sieklucka, B., Pinkowicz, D., Eds.; Wiley-VCH: Weinheim, Germany, 2017; 1, 131. (p) Liu, J.-L.; Chen, Y.-C.; Tong, M.-L *Chem. Soc. Rev.* **2018**, *47*, 2431.

4. Reviews and references therein: (a) Sun, H. L.; Wang, Z.-M.; Gao, S. *Coord. Chem. Rev.* **2010**, *254*, 1081. (b) Zhang, W.-X.; Ishikawa, R.; Breedlove, B.; Yamashita, M. *RSC Adv.* **2013**, *3*, 3772. (c) Coulon, C.; Pianet, V.; Urdampilleta, M.; Clérac, R. *Struct. Bonding (Berlin)* **2014**,

164, 143. (d) Dhers, S.; Feltham, H. L. C.; Brooker, S. *Coord. Chem. Rev.* **2015**, *296*, 24. (e) Pedersen, K. S.; Vindigni, A.; Sessoli, R.; Coulon, C.; Clérac, R. *Single-Chain Magnets.* In *Molecular Magnetic Materials: Concepts and Applications*; Sieklucka, B., Pinkowicz, D., Eds.; Wiley-VCH: Weinheim, Germany, 2017; 1, 131.

5. (a) Zheng, Y.-Z.; Tong, M.-L.; Zhang, W.-X.; Chen, X.-M. *Angew. Chem. Int. Ed.* **2006**, *45*, 6310. (b) Zhang, X.-M.; Hao, Z.-M.; Zhang, W.-X.; Chen, X.-M. *Angew. Chem. Int. Ed.* **2007**, *46*, 3456. (c) Zheng, Y.-Z.; Xue, W.; Tong, M.-L.; Chen, X.-M.; Grandjean, F.; Long, G. J. *Inorg. Chem.* **2008**, *47*, 4077. (d) Ouellette, W.; Prosvirin, A. V. ; Whitenack, K. ; Dunbar, K. R.; Zubieta, J. *Angew. Chem. Int. Ed.* **2009**, *48*, 2140. (e) Zhao, J.-P.; Yang, Q.; Liu, Z.-Y.; Zhao, R.; Hu, B.-W.; Du, M.; Chang, Z.; Bu, X.-B. *Chem. Commun.* **2012**, *48*, 6568. (f) Wang, Y.-Q.; Yue, Q.; Qi, Y.; Wang, K.; Sun, Q.; Gao, E.-Q. *Inorg. Chem.* **2013**, *52*, 4259. (g) Zeng, M.-H.; Yin, Z.; Tan, Y.-X.; Zhang, W.-X.; He, Y.-P. Kurmoo, M. *J. Am. Chem. Soc.* **2014**, *136*, 4680. (h) Zhang, J.-Y.; Wang, K.; Li, X.-B.; Gao, E.-Q. *Inorg. Chem.* **2014**, *53*, 9306. (i) Aono, Y.; Yoshida, H.; Katoh, K.; Breedlove, B. K.; Kagesawa, K.; Yamashita, M. *Inorg. Chem.* **2015**, *54*, 7096. (j) Su, L.; Song, W.-C.; Zhao, J.-P.; Liu, F. C. *Chem. Commun.* **2016**, *52*, 8722. (k) Wu, Y.-L.; Guo, F.-S.; Yang, G.-P.; Wang, L.; Jin, J.-C.; Zhou, X.; Zhang, W.-Y.; Wang, Y.-Y. *Inorg. Chem.* **2016**, *55*, 6592. (l) Li, R.; Xiao, Y.; Wang, S.-H.; Jiang, X.-M.; Tang, Y.-Y.; Xu, J.-G.; Yan, Y.; Zheng, F.-K.; Guo, G.-C. *J. Mater. Chem. C* **2017**, *5*, 513.

6. (a) Jeon, I.-R.; Clérac, R. *Dalton Trans.* **2012**, *41*, 9569 and references therein. (b) Chen, M.; Sañudo, E. C.; Jiménez, E.; Fang, S.-M.; Liu, C.-S.; Du, M *Inorg. Chem.* **2014**, *53*, 6708. (c) Zhang, X.; Vieru, V.; Feng, X.; Liu, J.-L.; Zhang, Z. ; Na, B. ; Shi, W. ; Wang, B.-W.; Powell, A. K.; Chibotaru, L. F.; Gao, S.; Cheng, P.; Long, J. R *Angew. Chem. Int. Ed.* **2015**, *54*, 9861. (d) Yi, X.; Calvez, G.; Daiguebonne, C.; Guillou, O. Bernot, K. *Inorg. Chem.* **2015**, *54*, 5213. (e) Liu, C.-M.; Zhang, D.-Q.; Zhu, D.-B. *Chem.Commun.* **2016**, 52, 4804. (f) Vallejo, J.; Fortea-Perez, F. R.; Pardo, E.; Benmansour, S.; Castro, I.; Krzystek, J.; Armentano, D.; Cano, J. *Chem. Sci.* **2016**, *7*, 2286. (g) Liu, C.-M.; Zhang, D.; Hao, X.; Zhu, D. B. *ACS Omega* **2016**, *1*, 286-292. (h) Jiang, X.; Liu, C.-M.; Kou, H.-Z. *Inorg. Chem.* **2016**, *55*, 5880. (i) Zhang, S.; Li, H.; Duan, E.; Han, Z.; Li, L.; Tang, J.; Shi, W.; Cheng, P. *Inorg. Chem.* **2016**, *55*, 1202. (j) Huang, G.; Fernandez-Garcia, G.; Badiane, I.; Camarra, M.; Freslon, S. ; Guillou, O. ; Daiguebonne, C. ; Totti, F. ; Cador, O. ; Guizouarn, T. ; Le Guennic, B. ; Bernot, K. *Chem. Eur. J.* **2018**, *24*, 6983. (k) Wang, M.; Meng, X.; Song, F.; He, Y.; Shi, W.; Gao, H.; Tang, J.; Peng, C. *Chem. Commun.* **2018**, *54*, 10183.

7. (a) Serre, C.; Millange, F.; Thouvenot, C.; Noguès, M.; Marsolier, G.; Louër, D.; Férey, G. *J. Am. Chem. Soc.* **2002**, *124* (45), 13519. (b) Millange, F.; Guillou, N.; Walton, R. I.; Grenèche, J.-M.; Margiolaki, I.; Férey, G. *Chem. Comm.* **2008**, *0* (39), 4732. (c) Munn, A. S.; Clarkson, G. J.; Millange, F.; Dumont, Y.; Walton, R. I. *CrystEngComm* **2013**, *15* (45), 9679. (d) Munn, A. S.; Clarkson, G. J.; Walton, R. I. *Acta Crystallogr. B*, **2014**, *70* (1), 11.

8. Hunter, C. A.; Sanders, J. K. M. *J. Am. Chem. Soc.* **1990**, *112* (14), 5525.

9. Allen, F. According to a Search of the Cambridge Structural Database. *Acta Crystallogr. B* **2002**, version 5.35.0 (58), 380.

10. (a) Lloret, F.; Julve, M.; Cano, J.; Ruiz-García, R.; Pardo, E. *Inorganica Chim. Acta* **2008**, *361* (12), 3432-3445. (b) Palii, A. V.; Reu, O. S.; Ostrovsky, S. M.; Klokishner, S. I.; Tsukerblat,

B. S.; Sun, Z.-M.; Mao, J.-G.; Prosvirin, A. V.; Zhao, H.-H.; Dunbar, K. R. *J. Am. Chem. Soc.* **2008**, *130* (44), 14729.

11. (a) Fisher, M. E. *Am. J. Phys.* **1964**, 32, 343. (b) Panja, A.; Shaikh, N.; Vojtíšek, P.; Gao, S.; Banerjee, P., *New J. Chem.* **2002**, 26 (8), 1025. (c) Naiya, S.; Biswas, S.; Drew, M. G. B.; Gómez-García, C. J.; Ghosh, A. *Inorg. Chem.* **2012,** *51* (9), 5332.

12. (a) Liu, T.-F.; Fu, D.; Gao, S.; Zhang, Y.-Z.; Sun, H.-L.; Su, G.; Liu, Y.-J.; *J. Am. Chem. Soc* **2003**, 125 (46), 13976. (b) Rodríguez-Diéguez A.; Seco José Manuel; Colacio E. *Eur. J. Inorg. Chem.* **2011**, **2012** (2), 203. (c) Cai, Z.-S.; Ren, M.; Bao, S.-S.; Hoshino, N.; Akutagawa, T.; Zheng, L.-M. *Inorg. Chem.* **2014**, *53*, 12546.

13. (a) Boeer, A. B.; Barra, A.-L.; Chibotaru, L. F.; Collison, D.; McInnes, E. J. L.; Mole, R. A.; Simeoni, G. G.; Timco, G. A.; Ungur, L.; Unruh, T.; Winpenny, R. E. P. *Angew. Chem. Int. Ed.* **2011**, *50*, 4007. (b) Z. Tomkowicz, S. Ostrovsky, S. Foro, V. Calvo-Perez, W. Haase, *Inorg. Chem.* **2012**, *51*, 6046.

14. Thompson, C. J. *Phase transitions and critical phenomena*; Domb, C., Green, M. S., Eds.; Academic Press: London, NY, 1972; 1, 177.

15. (a) Loveluck, J. M.; Lovesey, S. W.; Aubry, S. *J. Phys. C: Solid State Phys.* **1975**, *8*, 3841. (b) Nakamura, K.; Sasada, T. *J. Phys. C: Solid State Phys.* **1978**, *11*, 331.

16. (a) Nakamura, K.; Sasada, T. *Solid State Commun.* **1977**, *21*, 891. (b) Coulon, C.; Clérac, R.; Wernsdorfer, W.; Colin, T.; Miyasaka, H. *Phys. Rev. Lett.* **2009**, *102*, 167204.

17. (a) Jongh, L.J.; Miedena, A.R. *Adv In Physics* **1974**, *23*, 1. (b) Chikazumi, S. *Physics of Ferromagnetism.* Oxford: Clarendon Press, 1997, 521.

18. (a) Cole, K. S.; Cole, R. H. *J. Chem. Phys.* **1941**, *9*, 341-351. (b) Boettcher, C. J. F. *Theory of electric polarisation*; Elsevier: Amsterdam, 1952. (c) Aubin, S. M.; Sun, Z.; Pardi, L.; Krzysteck, J.; Folting, K.; Brunel, L.-J.; Rheingold, A. L.; Christou, G.; Hendrickson, D. N. *Inorg. Chem.* **1999**, *38*, 5329.

19. (a) Zhao, X.-H.; Deng, L.-D.; Zhou, Y.; Shao, D.; Wu, D.-Q.; Wei, X.-Q.; Wang, X.-Y. *Inorg. Chem.* **2017**, *56*, 8058. (b) Zhang, X.-M.; Wang, Y.-Q.; Wang, K.; Gao, E.-Q.; Liu, C.-M. *Chem. Commun.* **2011**, *47*, 1815. (c) Wöhlert, S.; Fic, T.; Tomkowicz, Z.; Ebbinghaus, S. G.; Rams, M.; Haase, W.; Näther, C. *Inorg. Chem.* **2013**, *52*, 12947. (d) Yang, F.; Li, B.; Xu, W.; Li, G.; Zhou, Q.; Hua, J.; Shi, Z. ; Feng, S. *Inorg. Chem.* **2012**, *51*, 6813.

20. (a) Miyasaka, H.; Takayama, K.; Saitoh, A.; Furukawa, S.; Yamashita, M.; Clérac, R. *Chem. Eur. J.* **2010**, *16*, 3656. (b) Yang, C.-I.; Tsai, Y.-J.; Hung, S.-P.; Tsai, H.-L.; Nakano, M. *Chem. Commun*. **2010**, *46*, 5716. (c) Zhang, S.-Y.; Shi, W.; Lan, Y.; Xu, N.; Zhao, X.-Q.; Powell, A. K.; Zhao, B.; Cheng, P.; Liao, D.-Z; Yan, S.-P. *Chem. Commun.* **2011**, *47*, 2859. (d) Shao, D.; Zhang, S.-L.; Zhao, X.-H.; Wang, X.-Y. *Chem. Commun.* **2015**, *51*, 4360. (e) Kagesawa, K.; Nishimura, Y.; Yoshida, H.; Breedlove, B. K.; Yamashita, M.; Miyasaka, H. *Dalton Trans*. **2017**, *46*, 3170. (f) Aguilà, D.; Jeannin, O.; Fourmigué, M.; Jeon, I.-R. *Inorg. Chem.* **2018**, 57, 7892.

21. (a) Sun, Z.-M.; Prosvirin, A. V.; Zhao, H.-H.; Mao, J.-G.; Dunbar, K. R. *J. Appl. Phys.* **2005**, *97* (10), 10B305. (b) Huang, Y.-G.; Yuan, D.-Q.; Pan, L.; Jiang, F.-L.; Wu, M.-Y.; Zhang,

X.-D.; Wei; Gao, Q.; Lee, J. Y.; Li, J.; et al. *Inorg. Chem.* **2007**, *46* (23), 9609. (c) Boonmak, J.; Nakano, M.; Chaichit, N.; Pakawatchai, C.; Youngme, S. *Inorg. Chem.* **2011**, *50* (15), 7324. (e) Li Zuo-Xi; Jie Wanqi; Zha Gangqiang; Wang Tao; Xu Yadong. *Eur. J. Inorg. Chem.* **2012**, **2012** (22), 3537. (f) Mautner, F. A.; Sudy, B.; Berger, C.; Fischer, R. C.; Vicente, R. *Polyhedron* **2012**, *42* (1), 95. (g) Huang, F.-P.; Yao, P.-F.; Yu, Q.; Yao, D.; Bian, H.-D.; Li, H.-Y.; Tian, J.-L.; Yan, S.-P. *Inorg. Chem. Commun.* **2013**, *31*, 18. (h) Yao, R.-X.; Qin, Y.-L.; Ji, F.; Zhao, Y.-F.; Zhang, X.-M. *Dalton Trans*. **2013**, *42* (18), 6611. (i) Zou, J.-Y.; Shi, W.; Gao, H.-L.; Cui, J.-Z.; Cheng, P. *Inorg. Chem. Front.* **2014**, *1* (3), 242. (k) Li, B.; Li, Z.; Wei, R.; Yu, F.; Chen, X.; Xie, Y.; Zhang, T.; Tao, J. *Inorg. Chem.* **2015**, *54* (7), 3331. (l) Li, Z.-Y.; Cao, Y.-Q.; Zhang, X.-M.; Xu, Y.-L.; Cao, G.-X.; Zhang, F.-L.; Li, S.-Z.; Zhang, F.-Q.; Zhai, B. *New J. Chem.* **2017**, *41* (2), 457.

22. Krause, L.; Herbst-Irmer, R.; Sheldrick, G. M.; Stalke, D. *J. Appl. Crystallogr.* **2015**, *48* (1), 3.

23. Sheldrick, G. M. *Acta Crystallogr., Sect. A: Found. Adv.* **2015**, 71, 3-8.

24. Dolomanov, O. V.; Bourhis, L. J.; Gildea, R. J.; Howard, J. A. K.; Puschmann, H. *J. Appl. Crystallogr.* **2009**, 42, 339.

25. Sheldrick, G. M. *Acta Crystallogr., Sect. C: Struct. Chem.* **2015**, 71, 3.

CHAPTER 4: MAGNETICALLY COUPLED AZIDE CHAINS

4.1 Abstract

Three well-defined iron(II) compounds $Cz^{tBu}(Pyr^{iPr})_2FeCl$ (**1**), $Cz^{tBu}(Pyr^{iPr})_2FeCl(THF)$ (**2**), and $Cz^{tBu}(Pyr^{iPr})_2FeN_3$ (**3**), supported by the NNN pincer ligand $Cz^{tBu}(Pyr^{iPr})_2^-$ were synthesized and characterized. Compound **3** features a one-dimensional chain structure built by $Cz^{tBu}(Pyr^{iPr})_2Fe$ units and bridged by end-to-end azido ligands. This chain material exhibits magnetic hysteresis at low temperatures and non-superimposable zero field cooled and field cooled magnetization. These properties are consistent with single-chain magnet behavior, likely arising from superexchange coupling of Fe(II) centers via the azide bridges.

4.2 Introduction

In this chapter, as in the previous chapter, the key magnetic phenomenon observed is slow magnetic relaxation, likely arising from spin canted antiferromagnetism. In this case, the primary feature of slow relaxation—a peak in out-of-phase susceptibility—is less pronounced, likely due to less anisotropy, a smaller canting angle, or both, given that the magnetic coupling (*J*) in this case is actually estimated to be larger than in the Co(II) systems of the previous chapter.

Molecule-based nanomagnets which exhibit magnetic bistable states and slow magnetic relaxation are promising for potential applications in molecular switching, quantum computing, high-density magnetic information storage, *etc*.[1-2] Molecular single-chain magnets (SCMs) are a class of molecular magnets which have been rapidly developed since their first report nearly two decades ago.[3-5] The characteristic behavior of SCMs depends on magnetically coupled uniaxially anisotropic units. Much of the focus on designing these low dimensional magnetic materials has centered on utilizing heavy lanthanide ions due to their intrinsically large spin-orbit coupling which is necessary for single ion magnetic anisotropy.[6,7] Lanthanide based materials, however,

suffer from weak coupling due to the poor radial extension of f-orbitals. SCMs based on 3d transition metal units are an evolving area in the field of coordination chemistry due to the superior coupling properties of these ions as compared to the lanthanides, as well as featuring other desirable attributes such as low cost and high abundance.[8-13]

First-row transition metal ions benefit from much stronger coupling interactions than observed with f-block elements, but also generally suffer from lower spin-orbit coupling. The tunability of the electronic structure of 3d metals via alterations in the ligand field, however, makes exploration of different SCMs featuring these ions an attractive area of study in order to optimize strong coupling with significant magnetic anisotropy.

Azide (N_3^-) ions have played an important role as linkers in the development of SCM research and can mediate either ferromagnetic (FM) or antiferromagnetic (AF) coupling, depending on binding mode and other factors.[14-19] High-spin (HS) Fe(II) centers have the possibility of large magnetic anistotropy, but there are only a few examples of their combination with bridging azides as potential SCMs that have been reported.[20-22]

Herein we report the combination of Fe(II) centers with bridging azide ligands in an infinite 1D array supported by the tridentate ligand $Cz^{tBu}(Pyr^{iPr})_2^-$. We have synthesized and characterized the complexes $Cz^{tBu}(Pyr^{iPr})_2FeCl$ (**1**) and $Cz^{tBu}(Pyr^{iPr})_2FeCl(THF)$ (**2**). These synthons have enabled the synthesis of the novel chain compound $Cz^{tBu}(Pyr^{iPr})_2FeN_3$ (**3**), bridged by single end-to-end (EE or $\mu_{1,3}$) azido ligands. Compounds **1**–**3** have been thoroughly characterized by SQUID magnetometry and other spectroscopic techniques. This chain is a rare example of a homospin Fe(II) material[23-29] and displays features consistent with SCMs, including hysteresis at low temperatures, bifurcation of zero-field cooled (ZFC) and field cooled (FC) magnetization, and a peak in the out-of- phase susceptibility (χ'').

4.3 Results and Discussion

4.3.1. Synthesis and Characterization of 1 The synthesis, SXRD, and NMR characterization in this chapter were carried out by our collaborators, Professor Wei-Tsung Lee and Adrianna Lugosan. A general synthetic route for the Fe(II) compounds is shown in Figure 4.1. Green complex **1** was prepared in high yield by the addition of $FeCl_2 \cdot THF_{1.5}$ to *in situ* prepared $Cz^{tBu}(Pyr^{iPr})_2Li$, and was thoroughly characterized by NMR spectroscopy, elemental analysis, SXRD, and SQUID magnetometry. In a C_6D_6 solution of complex **1** one set of paramagnetic shifts was observed in the ^1H NMR spectrum (Figure 4.12), indicating C_s symmetry with the mirror plane passing through the carbazole nitrogen, the Fe center, and the Cl atom. Upon dissolving **1** in THF, a color change was observed, suggesting the coordination of solvent at the Fe center. The significantly different paramagnetic shifts observed in THF-d_8 imply that the formation of higher coordinate Fe(II) complexes is possible (Figure 4.13). However, octahedral Fe(II) seems unlikely, due to the steric bulk of the two *i*Pr groups in the position *trans* to the carbazole nitrogen. The reversibility of solvation is evidenced from the observation that the green four-coordinate complex turns yellow in THF and again becomes green on removal of THF *in vacuo*. Crystals of **1** were

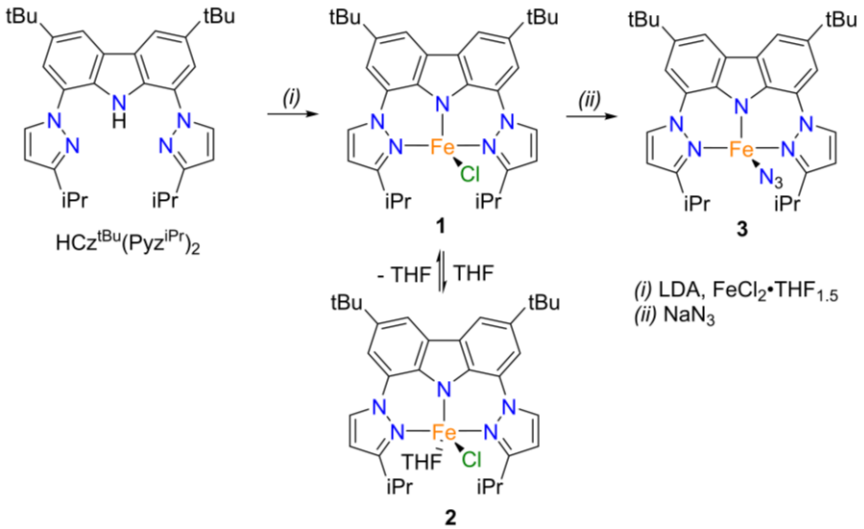

Figure 4.1. Synthesis of complexes **1**–**3**.

obtained by the slow evaporation of a toluene solution. In the structure of **1** (Figure 4.14), the Fe(II) atom is coordinated by one carbazolide-nitrogen (N_{cz}), two pyrazole-nitrogen atoms (N_{pyr}) from $Cz^{tBu}(Pyr^{iPr})_2^-$ in a meridional arrangement, and one Cl atom. This distorted tetrahedral environment is best described as a seesaw geometry (τ_4 = 0.53).[30-31] The average Fe–N bond lengths of 2.080 Å indicate that the Fe(II) ion is in a typical H.S. state.

Evans method solution magnetic data for **1** is consistent with a H.S. Fe(II) system (μ_{eff} = 5.2(2) μ_B). In the solid state, the compound was also confirmed to be S = 2, as evidenced by the room temperature χT (where χ is the molar magnetic susceptibility and T is the temperature) of 3.5 cm^3K/mol (Figure 4.2). This value is consistent with a H.S. Fe(II) center in a seesaw geometry which has some contribution from spin-orbit coupling.[31] The χT of **1** decreases moderately over the temperature range from 300–50 K, likely due to a combination of ZFS effects and weak through-space AF coupling facilitated by the relatively close intermolecular Fe···Fe contacts (≥6.103(1) Å) in the solid state.

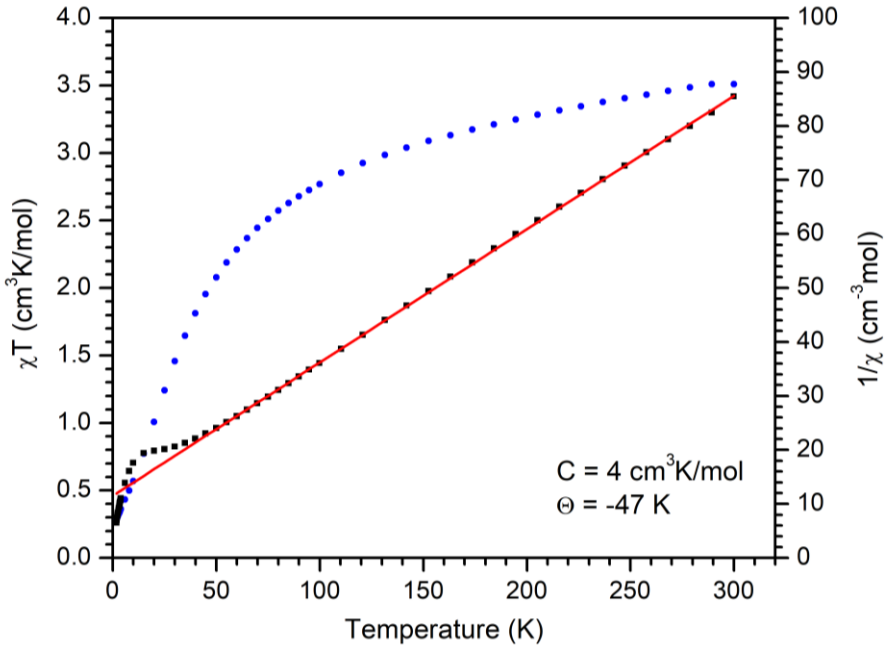

Figure 4.2. Fit (red) of the DC magnetic data (black) for **1** to the Curie-Weiss law above 50 K. Fit parameters are given. The 1/χ data is shown in blue.

4.3.2. Characterization of 2 Crystals of **2** were grown in concentrated THF solutions. The molecular structure of **2** is shown in Figure 4.15. Each Fe(II) center is coordinated by three nitrogens, one chloride, and one oxygen atom in a distorted trigonal bipyramidal (TBP) fashion (τ_5 = 0.67). The additional ligation results in several features that are different from **1**. The average Fe–N bond lengths of the THF-bonded complex are longer (*ca.* 0.18 Å), and the N3–Fe1–Cl1 angles decrease by ca. 12°. These results could be attributed to the diminished out-of-plane[32] movement (0.56 and 0.12 Å) of the Fe(II) ion in five-coordinate complexes, which in turn increases the steric hindrance around the Fe center.[33] In the solid state, **2** has a room temperature χT of 3.2 cm^3K/mol (Figure 4.3). A smaller contribution from spin-orbit coupling is expected for Fe(II) complexes in TBP geometry, as compared to that from the seesaw geometry in **1**.[34] Complex **2** shows an even more subtle decrease in χT upon cooling, as compared to **1**, perhaps due to the much larger Fe···Fe separations (≥12.3414(9) Å) resulting in extremely weak through-space coupling or more moderate ZFS.

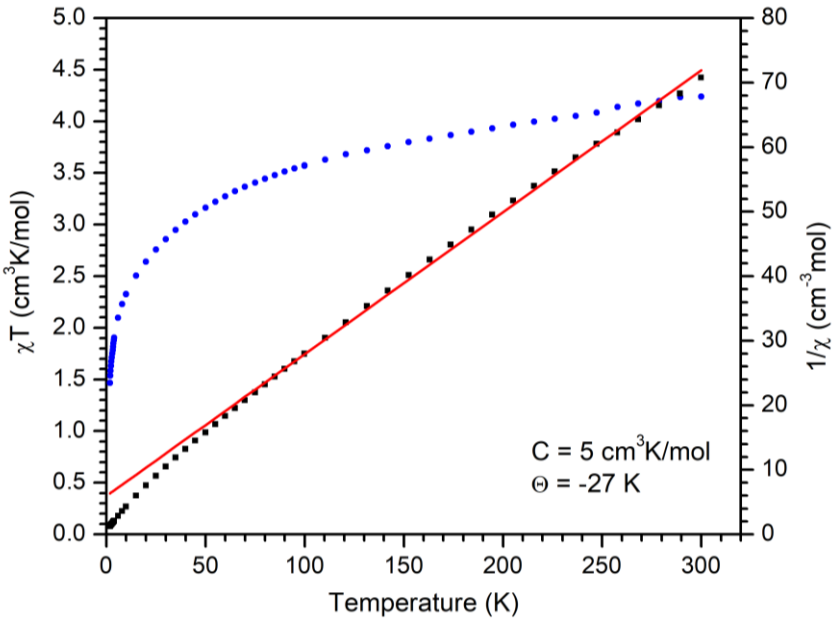

Figure 4.3. Fit (red) of the DC magnetic data (black) for **2** to the Curie-Weiss law above 50 K. Fit parameters are given. The $1/\chi$ data is shown in blue.

4.3.3. Synthesis and Characterization of 3 Material **3** was prepared by treating either **1** or **2** with excess NaN_3. Compound **3** crystallizes in the orthorhombic space group $P2_12_12_1$, and the solid state structure of **3** reveals infinite 1D Fe(II) chains bridged by single EE azido ligands with solvent molecules co-crystallized in voids between the chains (Figure 4.5A, ORTEP is shown in Figure 4.4). Each Fe(II) ion adopts TBP geometry (τ_5 = 0.90), and is coordinated by five nitrogen atoms, three of which are from the NNN pincer, $Cz^{tBu}(Pyr^{iPr})_2^-$ and the rest from bridging azides.

The average Fe–N bond length in the basal plane (2.027 Å) is shorter than that of Fe–N_{pyr} (2.181 Å). The Fe(II) ions are spaced by bridging N_3^- along the crystallographic *a* direction in the 1D chain with an Fe···Fe distance of 6.124 Å. The average Fe−N_{azide} = 2.074(4) Å bond is shorter than usual iron–EE azide bonds (2.136 to 2.169 Å),[19,21] and the azido ligand is quasi-linear with a N−N−N angle of 178.2(3)°. The Fe1–N6–N7 and Fe1#1–N8–N7 angles and the dihedral Fe1–NNN–Fe1#1 torsion angle are 141.2(2)°, 154.5(2)°, and 139.4(2)°, respectively. The orthogonal

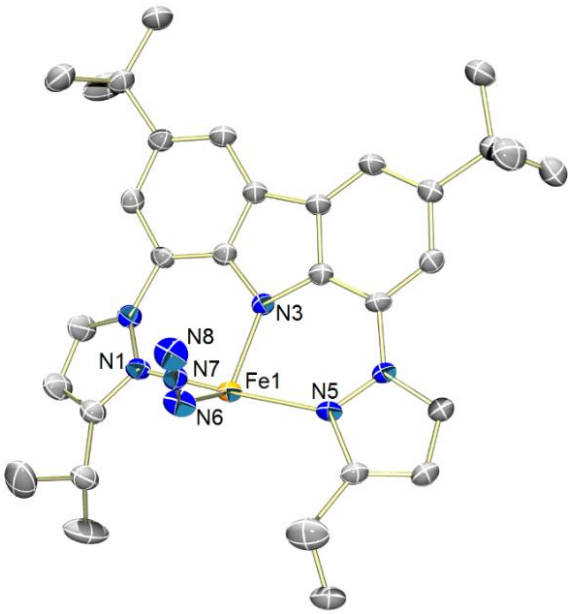

Figure 4.4. ORTEP diagram of **3** (one unit is shown) with thermal ellipsoids at the 50% probability level. Solvent molecules and hydrogen atoms are omitted for clarity. Color key: orange = Fe, blue = N, gray = C.

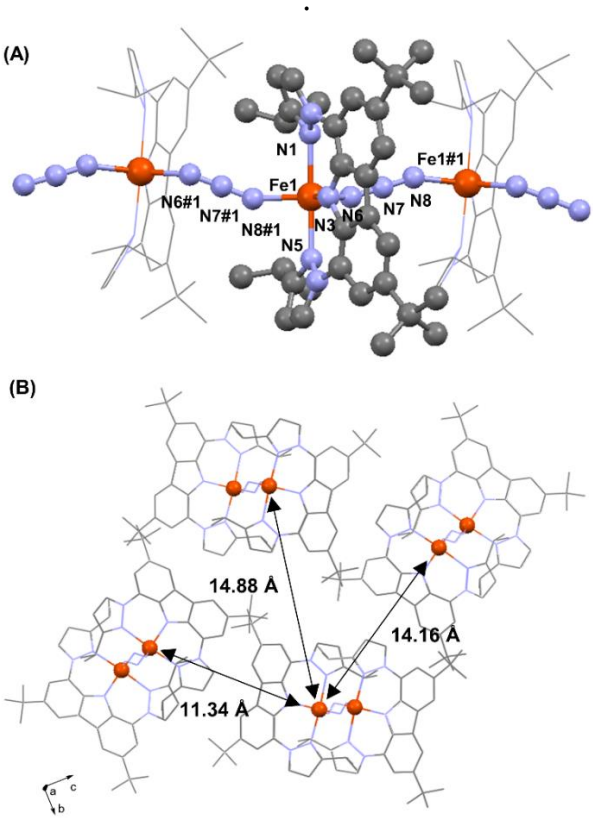

Figure 4.5. (A) The 1D view of **3** along the a axis. (B) Crystal packing of **3** in the bc plane. The three shortest interchain Fe···Fe distances are labeled. Hydrogen atoms and THF molecules are omitted for clarity. Color key: orange = Fe, blue = N, gray = C.

axes, which are defined as N1–Fe1–N5, are slightly tilted antiparallel which may enable spin-canted antiferromagnetic behavior as described below.[35] Finally, it is noteworthy that SCM behavior usually requires negligible interchain interactions.[5] It is clear that the peripheral bulky *i*Pr and *t*Bu groups keep these chains apart from each other with the nearest interchain Fe···Fe distances being 11.34 Å (Figure 4.5B). Even at these long distances, however, it is difficult to rigorously exclude any weak interchain interactions. In the solid state, the XRPD of **3** (Figure 4.18) is generally consistent overall with the predicted pattern calculated from the SXRD data, however there is some peak shifting observed, likely due to the temperature difference in the measurements (i.e. 100 K for SXRD and room temperature for XRPD) and desolvation of THF, as confirmed by

elemental analysis. The room temperature χT of **3** in the solid state is 3.20(5) cm^3K/mol (Figure 4.6), which is consistent with the spin-only value for an S = 2 Fe(II) center. Typically, H.S. Fe(II) ions have a room temperature χT that is higher than the spin-only value (χT = 3 for S = 2) due to contributions from spin-orbit coupling, as is observed here. As temperature is decreased a significant drop in the χT of **3** is observed. This decrease is consistent with AF interactions, some contribution from single ion effects, or a combination of both phenomena. Most previously reported materials with metal centers bridged by EE azides exhibit AF coupling, however a few exceptions exist.[36-39] In the temperature region above 50 K, the inverse susceptibility ($1/\chi$) was fit to the Curie-Weiss law, $\chi = C/(T-\theta)$, to obtain a Curie constant of C = 5.13(3) cm^3 K/mol and a Weiss constant of θ = -169.0(2.0) K. This Weiss constant is markedly larger in magnitude than those for **1** and **2** (θ = -46.5(5) and -27.0(2.0), respectively).

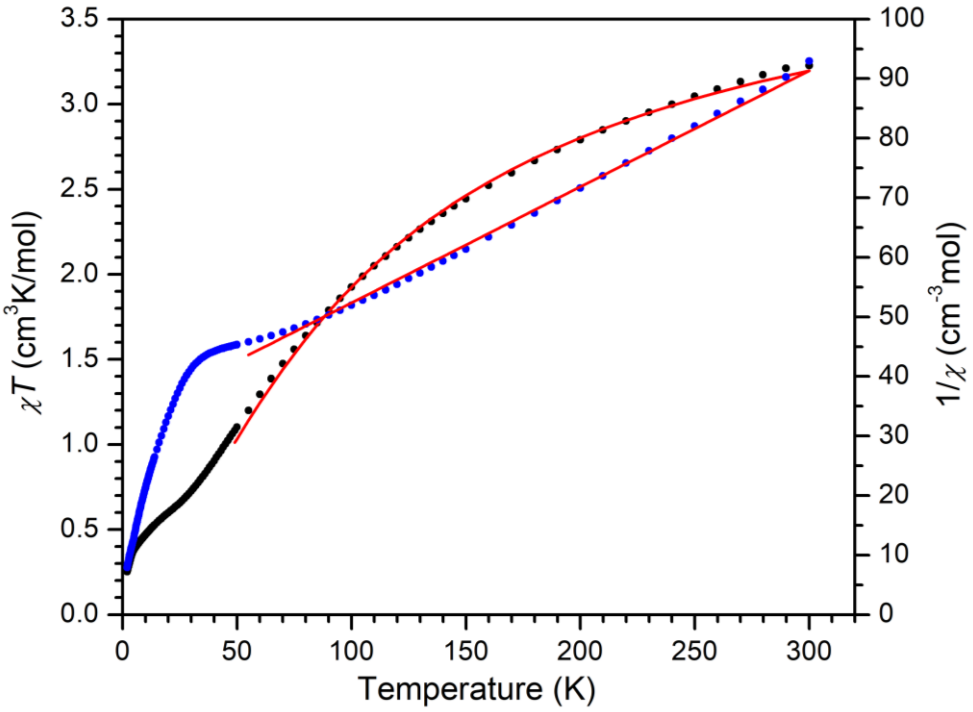

Figure 4.6. DC magnetic data for **3** taken with an applied field of 0.1 T (black: χT vs. T, blue: $1/\chi$). The red lines are the fits to the above 50 K, as described in the text.

Below 50 K, a small, field-dependent inflection in χT was observed for **3**, suggesting the possibility of some more complicated phenomena at these temperatures (Figure 4.7). Further analysis via variable temperature magnetization vs. field measurements show clear hysteresis for**3** up to 5 K (Figure 4.8) with a small remnant magnetization (<20 cm^3 Oe/mol), a coercivity of ~240 G, and no saturation in the magnetization up to an applied field of 7 T at 1.8 K. Furthermore, the FC and ZFC magnetization were non-superimposable below ~12.5 K (Figure 4.9). The inflection in χT below 50 K, the hysteresis, and the bifurcation of the FC and ZFC data all indicate some magnetic phenomenon, as has been observed in blocking in SCM materials, spin glassing, or SMM behavior.[40-43] Complexes **1** and **2**, by comparison, did not show any of these behaviors (Figure 4.2,

$$\chi = \frac{\mathrm{N}\,\beta^2 g^2 S(S+1)}{3\mathrm{kT}} \frac{u+1}{u-1} \qquad \textbf{4.1}$$

$$\text{where } u = \coth\left(\frac{JS(S+1)}{\mathrm{kT}}\right) - \frac{\mathrm{kT}}{JS(S+1)}$$

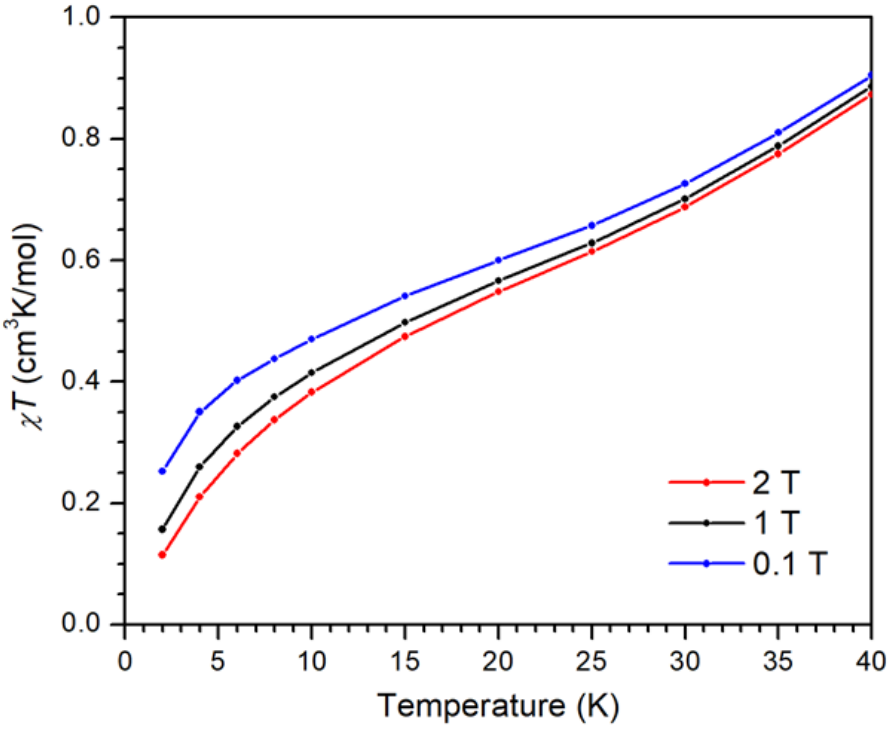

Figure 4.7. Field dependence of the increase in χT below 40 K for **3**. Lines are guides to the eye.

The model had a good fit when $R(\Sigma(\chi_{fit}-\chi_{obs})^2/\Sigma(\chi_{obs}))$ was minimized, giving J = -14.0(1.0) cm^{-1}, and g = 2.36(1) (Figure 4.6). AC magnetic data was collected (Figure 4.10) to further investigate the low temperature magnetic phenomenon, however the low magnitude of the moment in these measurements introduced significant noise into the data, making precise interpretation difficult. AC data for **1** and **2** was also obtained for comparison and it is clear that compound **3** displays a temperature dependent feature in χ'' which is absent from either of the discrete molecular complexes (Figure 4.21, Figure 4.22).

A possible explanation of the magnetic behavior can be found in the single crystal data, which show a small noncollinearity (~6°) in the N1–Fe1–N5 axes of neighboring Fe(II) ions. If some uniaxial anisotropy (i.e. an appreciable and negative D value) exists in these Fe(II) ions, when coupled with the aforementioned AF coupling mediated by $\mu_{1,3}$-azide bridges, overall spin-canted antiferromagnetism could arise. Indeed, spin-canted antiferromagnetism has been

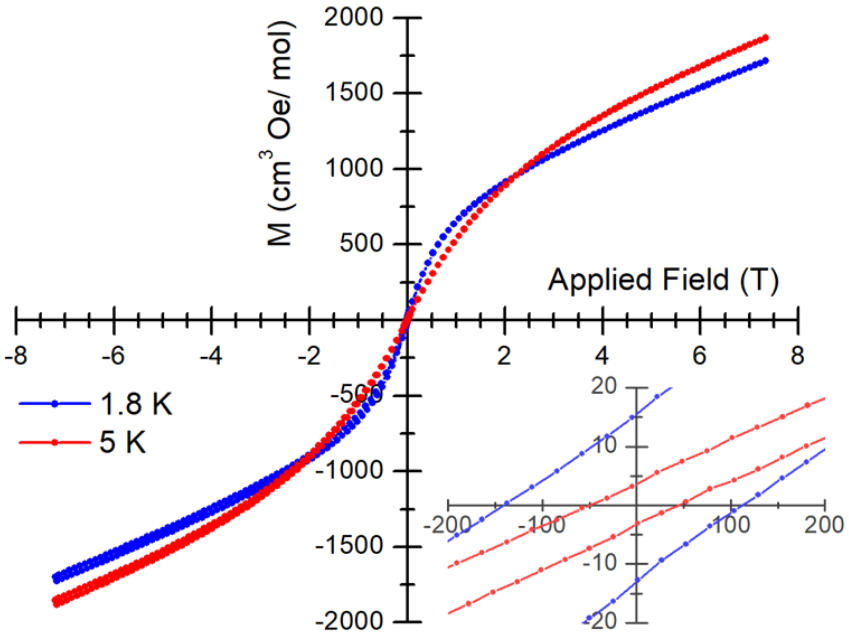

Figure 4.8. Hysteresis of **3** at 1.8 and 5 K. Inset is the region from -200–200 Oe (-0.02–0.02 T), where hysteresis is observed.

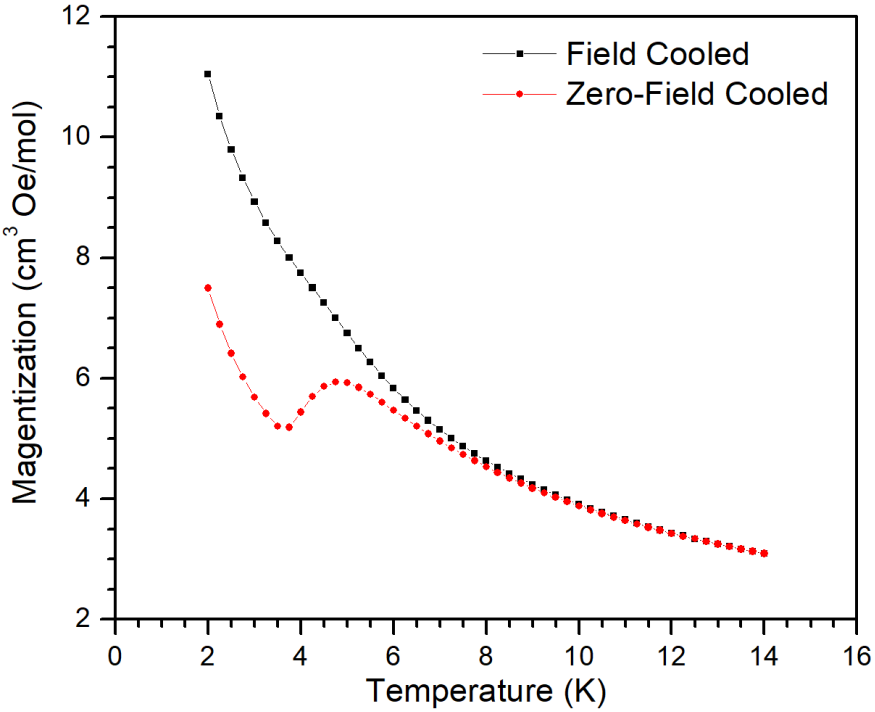

Figure 4.9. The field cooled (FC) and zero field cooled (ZFC) magnetization of **3**. The applied field was 100 Oe.

observed in several M–$\mu_{1,3}$-azide–M (M = transition metal) chain materials.[46-48] We have been unable to accurately determine a *D* value for **3** from the data we have collected, and thus are not able to comment on the effect of anisotropy of the Fe(II) centers on the observed magnetic phenomena. In lieu of these measurements, we have attempted to estimate the anisotropy of the Fe(II) ions in this system via measurements on the mononuclear complexes.

The discrete 5-coordinate synthon **2** was measured by variable-field, variable-temperature (VFVT) magnetization measurements, and the data was fit to the standard spin Hamiltonian (see Experimental Methods)[49] to estimate a value of *D* (Figure 4.11). The small, negative *D* value (weak uniaxial anisotropy) from the VFVT data of **2** implies that a similarly small, negative value of *D* may be expected for the Fe(II) in **3** which is in a similar coordination environment. Further, while

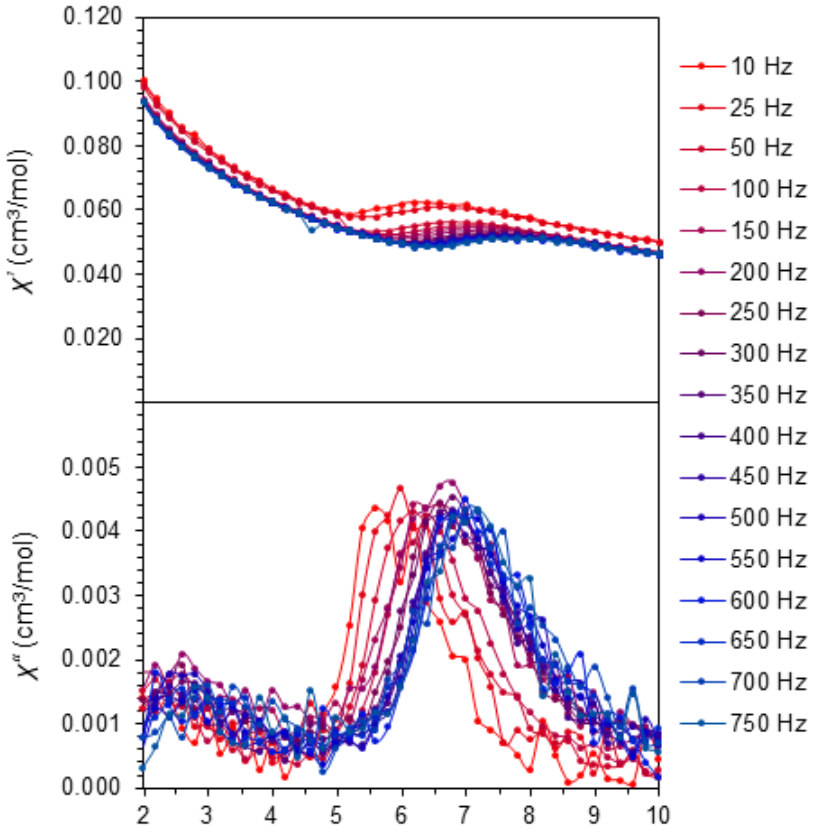

Figure 4.10. The in-phase (χ') and out-of-phase (χ'') susceptibilities for **3** from 2 to 10 K. Lines are guides to the eye.

a negative *D* value is observed for **2**, there is no peak in the χ'' data. This fact suggests that these5-coordinate Fe(II)–$Cz^{tBu}(Pyr^{iPr})_2$ materials do not operate as SMMs, arising from single-ion anisotropy alone, but rather exhibit SCM behavior facilitated by superexchange interactions across the azide bridges.

For **3**, we expect that superexchange via the EE azide bridge is the major magnetic coupling pathway. The large interchain and intrachain Fe···Fe separations of 11.3360(6) Å and 6.1235(5) Å, respectively, likely indicate that only a small degree of through-space interaction occurs, however there are some reports of interactions over such distances producing measurable bulk magnetic phenomena.[50] Regardless, complexes **1** and **2** have comparable nearest Fe···Fe

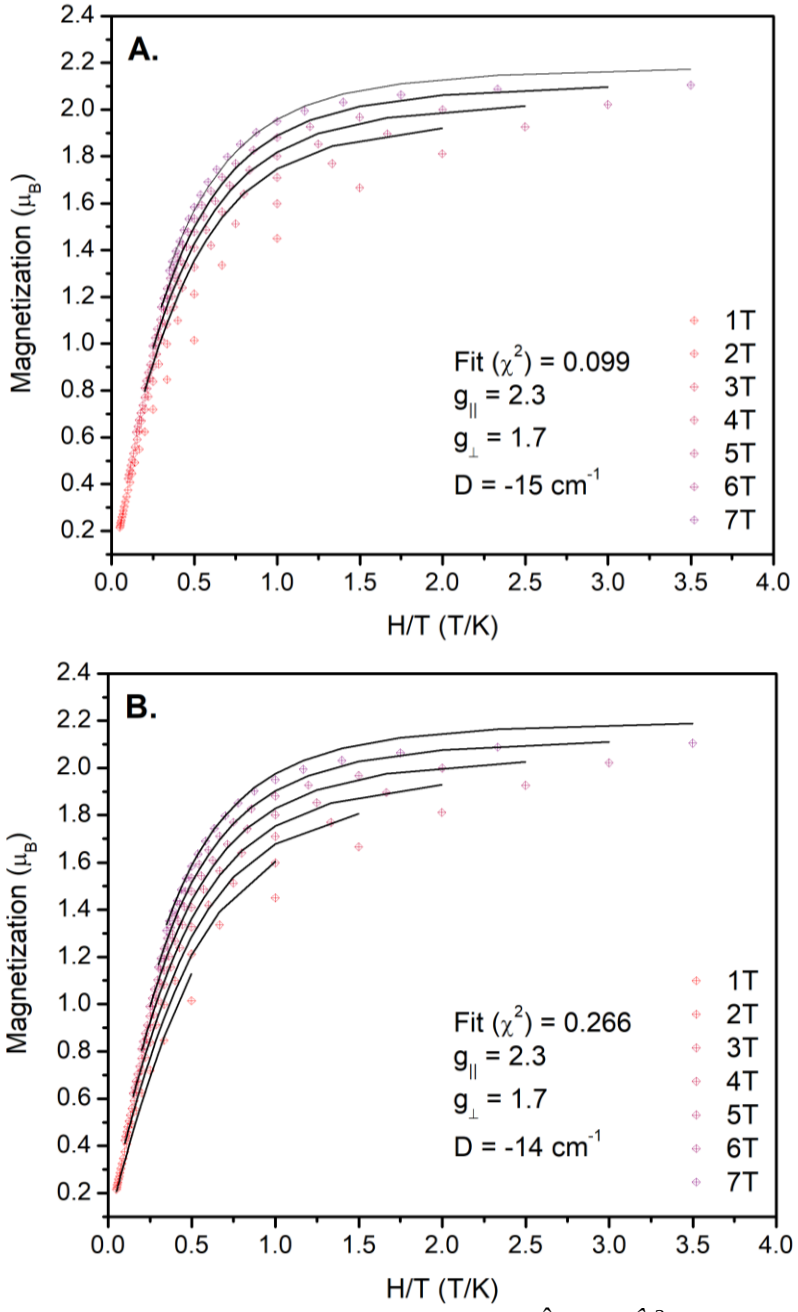

Figure 4.11. Black lines are fits to the spin Hamiltonian $\hat{H} = D[\hat{S}_z^2 - \frac{1}{3} S(S+1)] + (g_{\perp} + g_{||})\mu_B SH$. Modeling to the data in the range of 4T – 7T (A) gave better fits than modeling the full (1 T –7 T) field range (B), however both produced similar fit parameters.

separations of 6.103(1) Å and 7.9211(7) Å, respectively, while showing no signs of bulk magnetic effects or slow relaxation which argues against the likelihood of through-space interactions leading to observed magnetic behaviors of **3**.

4.4 Conclusions

We have designed and synthesized several mononuclear Fe(II) compounds supported by a pincer ligand, $Cz^{tBu}(Pyr^{iPr})_2$. Compound **3** exhibits a 1D chain motif in its solid-state structure. This compound exhibits interesting magnetic phenomena, such as slow magnetic relaxation, hysteresis, and bifurcation of zero-field cooled and field cooled magnetization. These phenomena may arise from several possible sources including single ion anisotropy, weak bulk ferromagnetic ordering, or SCM behavior. A suite of detailed studies on this chain material and closely related mononuclear complexes, however, suggest that the most likely scenario is spin-canted antiferromagnetism yielding a single chain magnet. The extended 1D material joins a limited number of previously reported Fe(II) azide chain materials that exhibit single chain magnetic behavior.

4.5 Experimental Methods

Material and Methods. All manipulations were performed under a nitrogen atmosphere by standard Schlenk techniques or in an M. Braun UNIlab glovebox. Glassware was dried at 150 °C overnight. Diethyl ether, *n*-pentane, tetrahydrofuran, and toluene were purified by the Pure Process Technology solvent purification system. Deuterated solvents were tested with a drop of sodium benzophenone ketyl in THF solution. All reagents were purchased from commercial vendors and used as received. 1,8-Dibromo-3,6-di-*tert*-butyl-9*H*-carbazole ($HCz^{tBu}Br_2$) and 3-*iso*-propylpyrazole were prepared according to literature procedures.[51-52] ^{1}H NMR data were recorded on Varian Inova 300 or 500 MHz spectrometer at 22 °C. Resonances in the ^{1}H NMR spectra are referenced either to residual $CHCl_3$ at 7.26 ppm, C_6D_5H at 7.16 ppm, or C_4D_7HO at 3.58 ppm. Solution magnetic susceptibilities were determined by the Evans method.[53] Fourier transform-infrared (FTIR) spectroscopy was performed using a Shimadzu IRAffinity-1S FTIR spectrometer. Elemental analysis was conducted by Midwest Microlab, LLC (Indianapolis, IN).

HCz^{tBu}(Pyr^{iPr})$_2$. The synthetic method was adapted from literature procedures with slight modification.[54] 1.28 g (2.93 mmol) of 1,8-dibromo-3,6-di-*tert*-butyl-9*H*-carbazole, 3.19 g (29.2 mmol) of 3-*iso*-propylpyrazole, 1.80 mL (1.40 g, 12.0 mmol) of N,N,N',N'-tetramethylethylenediamine, 3.30 g (29.4 mmol) of potassium *tert*-butoxide and 15 mL of DMF were combined in a round bottomed flask. The resulting slurry was degassed by three freeze-pump-thaw cycles. 2.08 g (14.5 mmol) of copper(I) oxide was added, and the reaction mixture was heated to 150 °C for 4.5 days under N_2. After cooling, 50 mL of diethyl ether was added, and the diluted solution was washed with 4 × 50 mL of 1 M hydrochloric acid, followed by 3 × 50 mL of 1 M ammonium hydroxide, 6 × 50 mL of 3 M ammonium chloride. The organic layer was dried over anhydrous $MgSO_4$, filtered, and evaporated under reduced pressure to give an off-white solid, which was recrystallized from a concentrated *n*-hexane solution (1.5 g, 92%). ^{1}H NMR (500 MHz, $CDCl_3$, δ): 10.3 (br, 1H, N*H*), 8.03 (d, 2H, *J* = 3.0, Ar*H*), 7.99 (d, 2H, *J* = 4.0, Ar*H*), 7.57 (d, 2H, *J* = 2.5, Ar*H*), 6.40 (d, 2H, *J* = 4.0, Ar*H*), 1.50 (s, 9H, C(C*H*$_3$)$_3$), 1.42 (s, 9H, C(C*H*$_3$)$_3$). Anal. Calcd for $C_{34}H_{45}N_5$: C 77.97, H 8.66, N 13.37. Found: C 78.04, H 8.59, N 13.39.

*Cz^{tBu}(Pyr^{iPr})$_2$FeCl (**1**)*. To 1,069 mg (0.2156 mmol) of HCz^{tBu}Pz^{iPr} dissolved in tetrahydrofuran at room temperature under inert N_2 atmosphere was added 24.3 mg (0.2268 mmol) of lithium diisopropylamine. The resulting fluorescent yellow mixture was stirred for 1 hour. The fluorescent mixture was then added to 58.0 mg (0.2485 mmol) of $FeCl_2 \cdot THF_{1.5}$ dissolved in THF and stirred overnight at ambient temperature. Volatiles were removed by vacuum to produce the desired green product (77.1 mg, 61%). Crystals suitable for X-ray diffraction were grown from a concentrated toluene solution at room temperature. ^{1}H NMR (500 MHz, C_6D_6, δ): 55.6, 13.9, 13.6, 4.11, 2.94. μ_{eff} (C_6D_6) = 5.2(2) μ_B. Anal. Calcd for molecular formula $C_{32}H_{40}ClFeN_5$: C 65.59, H 6.88, N 11.95. Found: C 65.38, H 6.80, N 11.61.

*$Cz^{tBu}(Pyr^{iPr})_2FeCl(THF)$ (**2**).* Dissolving $Cz^{tBu}(Pyr^{iPr})_2FeCl$ in THF yields the yellow THF coordinated complex. Crystals suitable for X-ray diffraction were grown from a concentrated THF solution at room temperature. ^{1}H NMR (500 MHz, C_6D_6, δ): 43.9, 25.6, 18.3, 2.30, -10.2. μ_{eff} (THF-d_8) = 5.4(3) μ_B. Anal. Calcd for molecular formula $C_{36}H_{48}ClFeN_5O$: C 65.70, H 7.35, N 10.64. Found: C 65.91, H 6.86, N 10.71.

*$Cz^{tBu}(Pyr^{iPr})_2FeN_3$ (**3**).* To 58.5 mg (0.0888 mmol) of $Cz^{tBu}(Pz^{iPr})FeCl(THF)$ suspended in THF at ambient temperature under N_2 atmosphere was added 8.7 mg (0.1339 mmol) of NaN_3. The resulting yellow solution was stirred overnight at ambient temperature. Volatiles were removed under reduced pressure. The solid was washed with toluene to leave behind a bright yellow solid (38.6 mg, 82%). Rod-like crystals suitable for X-ray diffraction were grown from a concentrated THF solution at room temperature. ^{1}H NMR (500 MHz, THF-d_8, δ): 40.3, 35.5, 26.1, 12.9, 1.96. Anal. Calcd for molecular formula $C_{32}H_{40}FeN_8\cdot$THF: C 65.05, H 7.28, N 16.86. Found: C 64.78, H 6.86, N 16.74. IR: (THF) ν_{N3} = 2075 cm^{-1}.

Crystallography. Data were collected using either a Bruker Quest CMOS diffractometer (**1**) or Bruker Kappa APEXII diffractometer (**2**–**3**) with Mo-K_α radiation (λ = 0.71073 Å). The Quest CMOS instrument features a fixed chi angle, a sealed tube fine focus X-ray tube, single crystal curved graphite incident beam monochromator, a Photon100 CMOS area detector and an Oxford Cryosystems low temperature device. Single crystals were mounted on Mitegen loop or micromesh mounts using a trace of mineral oil and cooled *in situ* to 150 K for **1** and 120 K for **2**–**3**. Frames were collected, reflections were indexed and processed, and the files scaled and corrected for absorption using APEX3.[55] The space groups were assigned and the structures solved by direct methods using XPREP within the SHELXTL suite of programs[56] and either ShelXS[57] or ShelXT,[58]

and refined by full matrix least squares against F^2 with all reflections using Shelxl2016 or 2018[59] using the graphical interface Shelxle[60, 61] or OLEX2.[62] H atoms attached to carbon atoms were positioned geometrically and constrained to ride on their parent atoms, with carbon−hydrogen bond distances of 0.95 Å for aromatic C–H, 1.00, 0.99, and 0.98 Å for aliphatic C– H, CH_2, and CH_3 moieties, respectively. Methyl and H atoms were allowed to rotate, but not to tip to best fit the experimental electron density. U_{iso}(H) values were set to a multiple of U_{eq}(C) with 1.5 for CH_3 and 1.2 for C–H units.

The Fe-Cl unit in the structure of **1** is disordered with a minor moiety flipped to the opposite side of the ligand than its major counterpart. The disorder extends to directly adjacent segments of the ligand, especially the isopropyl groups. The major and minor moieties were restrained to have similar geometries, and U^{ij} components of ADPs were restrained to be similar for atoms closer to each other than 2.0 Å. Subject to these conditions the occupancy ratio refined to 0.9319(13) to 0.681(13). A pentane molecule is disordered around an inversion center. U^{ij} components of ADPs were restrained to be similar for atoms closer to each other than 2.0 Å.

For the structure **2**, two chemically equivalent but crystallographically independent Fe-Cl units were found in the asymmetric unit. On each, the coordinated THF solvent and one of the two t-butyl groups were found to be disordered over two positions. The relative occupancies of each disordered moiety was freely refined, converging at 52/48 for the major and minor components of the C21-C24 t-butyl, 60/40 for the C46-49 t-butyl, 62/38 for the C33-C36 THF and 58/42 for the C69-C72 THF. Restraints and/or constraints were used on the geometries and U^{ij} components of ADPs of the disordered fragments as needed. Two molecules of toluene were also found in the asymmetric unit, one of which was disordered. The relative occupancies of the major and minor

components of the disordered toluene was freely refined to a 72/28 ratio, and constraints were used on the U^{ij} components of ADPs of each pair of disordered atoms. Finally, additional disordered solvent was accounted for using SQUEEZE,[63] which found solvent voids of 1342 $Å^3$ containing 316 e^-. This corresponds to roughly one more toluene solvent molecule per asymmetric unit.

For the structure **3**, one solvent position was modeled as a combination of THF and toluene. No restraints or constraints were needed on the positions or displacement parameters. The occupancies refined to 57.4(8)% toluene and 42.6(8)% THF.

Complete crystallographic data, in CIF format, have been deposited with the Cambridge Crystallographic Data Centre. CCDC 1818956-1818958 contains the supplementary crystallographic data for this chapter. These data can be obtained free of charge from The Cambridge Crystallographic Data Centre via www.ccdc.cam.ac.uk/data_request/cif.

Magnetic Measurements. AC and DC magnetometry measurements of polycrystalline samples of **1–3** were carried out on a Quantum Design MPMS 3 equipped with a superconducting quantum interference device (SQUID) detector. Corrections were made for the diamagnetic contributions from the polycarbonate capsules and eicosane wax used to secure the sample by measuring field vs. moment or temperature vs. moment, as appropriate, in triplicate for each component to determine a moment per gram correction. Pascal's constants were used to make the diamagnetic corrections for the ligands. Corrections were applied to account for the effects of trapped flux in the magnet by measuring a Pd standard in the same applied field ranges to determine the true field values. These corrections were applied to the hysteresis measurements to insure that observed hysteresis was not an instrument artefact. Reported χ values are molar susceptibilities per unit formula with one THF solvent molecule of crystallization ($Cz^{tBu}(Pyr^{iPr})_2FeN_3 \cdot THF$), as consistent

with the elemental analysis. The data points collected for the hysteresis measurements were acquired at stable fields (i.e. not measured at a continuous sweep rate). χ' and χ'' are derived from the total susceptibility: $\chi' = \chi \cos\Phi$ and $\chi'' = \chi \sin\Phi$, where Φ is the phase. The variable-field, variable temperature data were fit to the spin Hamiltonian $\hat{H} = D[\hat{S}_z^2 - \frac{1}{3} S(S+1)] + (g_\perp + g_{||})\mu_B SH$, where $g_\perp$ and $g_{||}$ are the perpendicular and parallel components of g, respectively. The data was fit using MagProp analysis in the DAVE 2.0 program.[64]

4.6 Supplementary Data

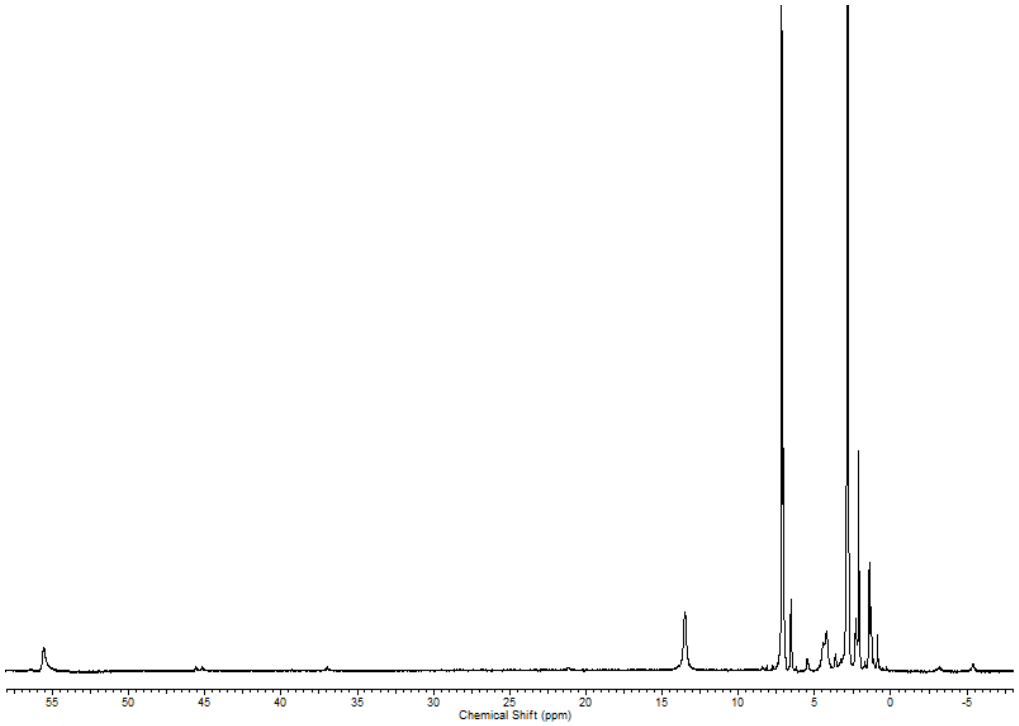

Figure 4.12. ^{1}H NMR spectrum of **1** in C_6D_6. * Solvent residues.

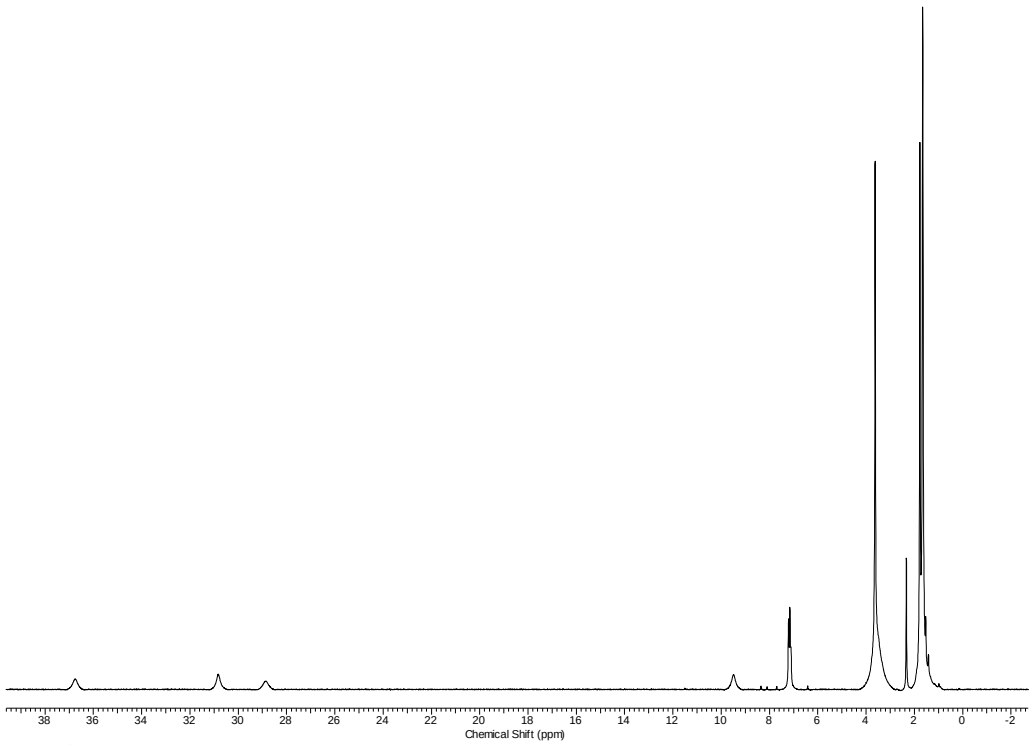

Figure 4.13. ^{1}H NMR spectrum of **1** in THF-d_8. * Solvent residues.

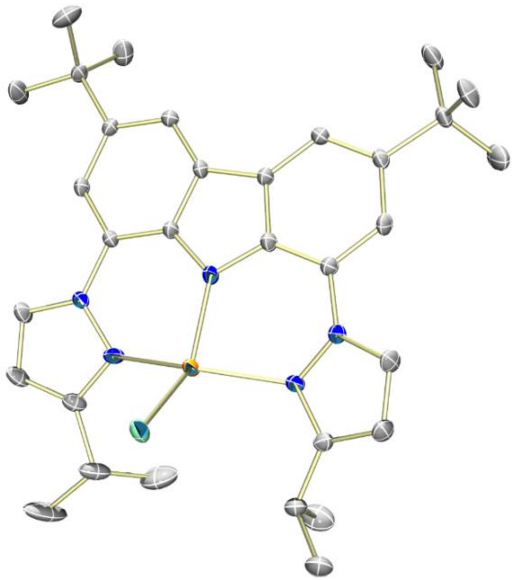

Figure 4.14. Molecular structure of **1** with thermal ellipsoids at the 50% probability level. Solvent molecules and hydrogen atoms are omitted for clarity. Color key: orange = Fe, blue = N, gray = C.

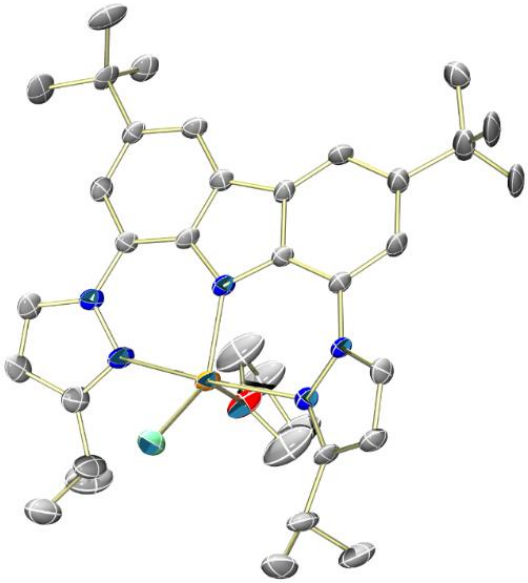

Figure 4.15. Molecular structure of **2** with thermal ellipsoids at the 50% probability level. One of two crystallographically independent molecules is shown. Non-coordinated solvent molecules and hydrogen atoms are omitted for clarity. Color key: orange = Fe, blue = N, gray = C, red = O.

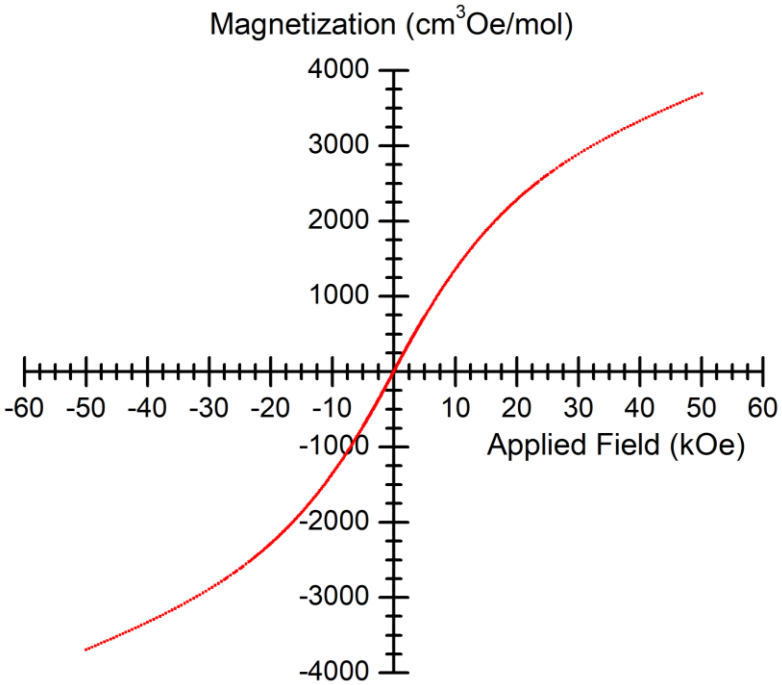

Figure 4.16. Magnetization of **1** at 1.8 K. No hysteresis was observed.

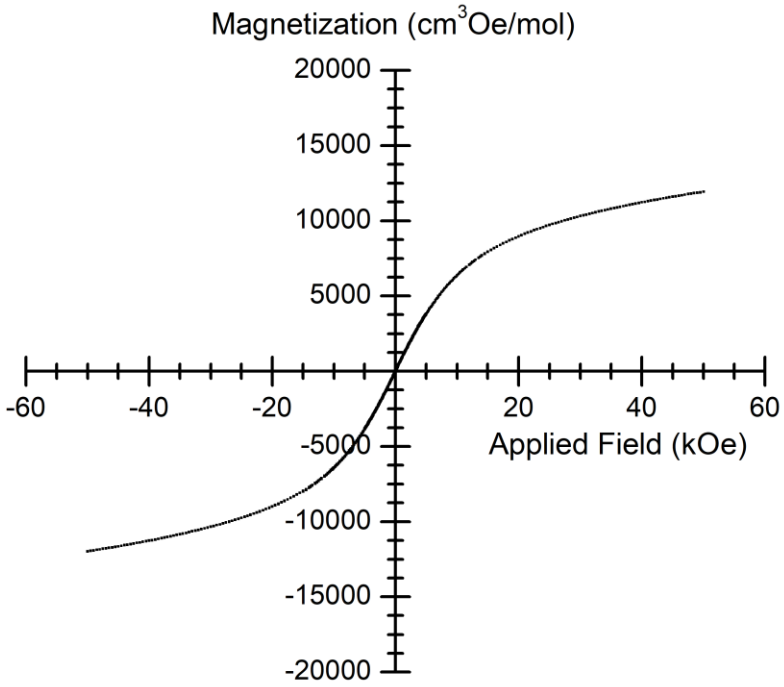

Figure 4.17. Magnetization of **2** at 1.8 K. No hysteresis was observed.

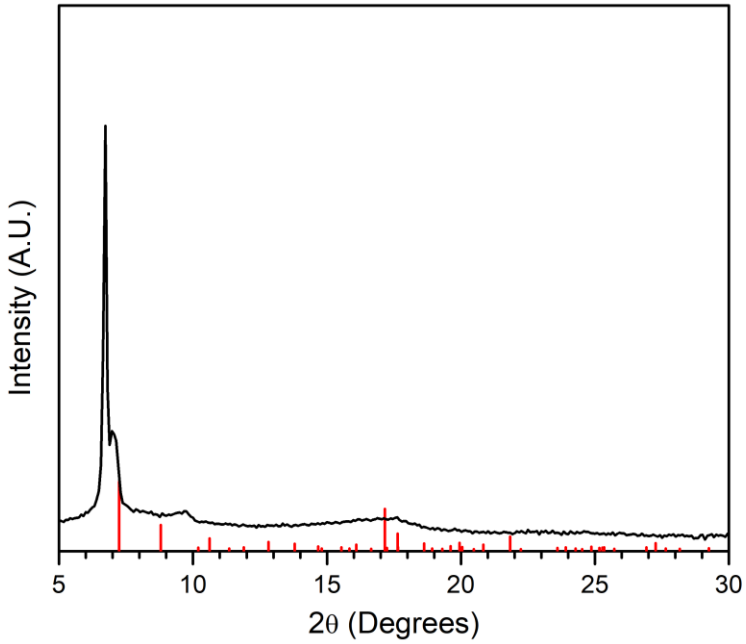

Figure 4.18. XRPD of **3** collected at room temperature. Red lines are peak positions calculated from the SXRD structure of **3** collected at 100 K.

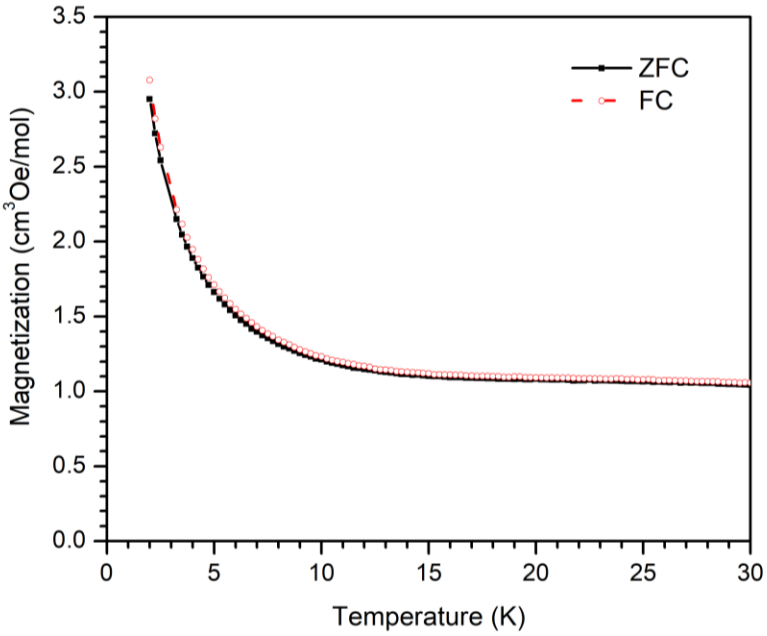

Figure 4.19. The field cooled (FC) and zero field cooled (ZFC) magnetization of **1**. The applied field was 20 Oe.

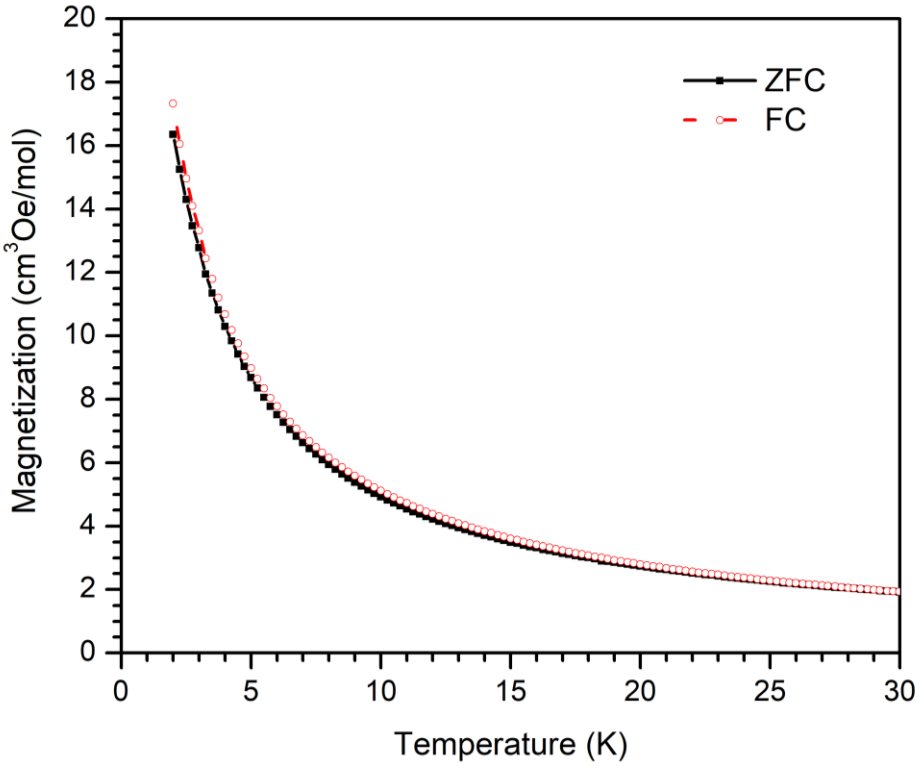

Figure 4.20. The field cooled (FC) and zero field cooled (ZFC) magnetization of **2**. The applied field was 20 Oe.

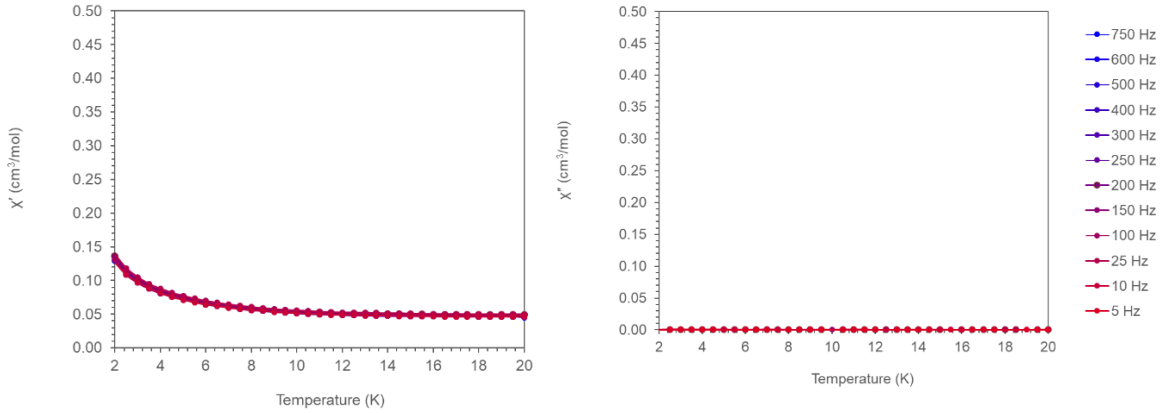

Figure 4.21. χ' (left) and χ'' (right) for **1** from 2 to 20 K. Lines are guides to the eye.

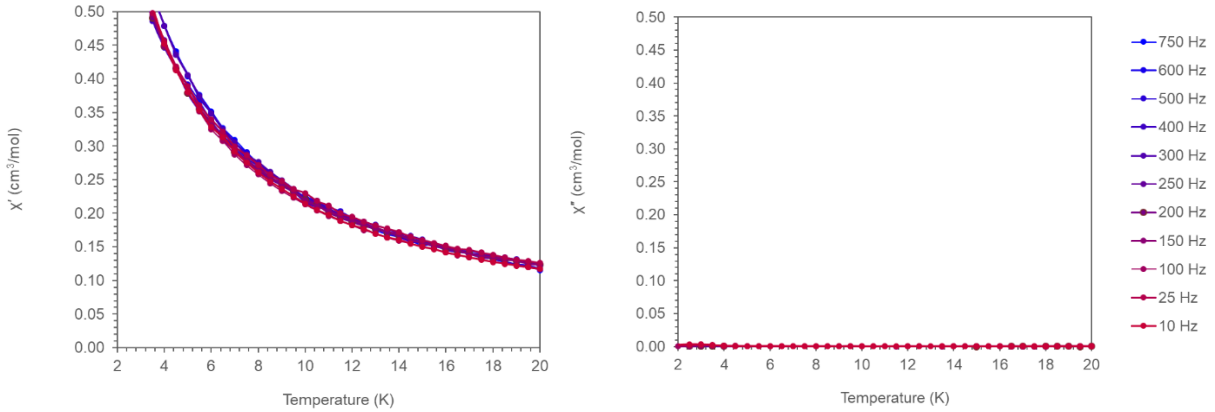

Figure 4.22. χ' (left) and χ'' (right) for **2** from 2 to 20 K. Lines are guides to the eye.

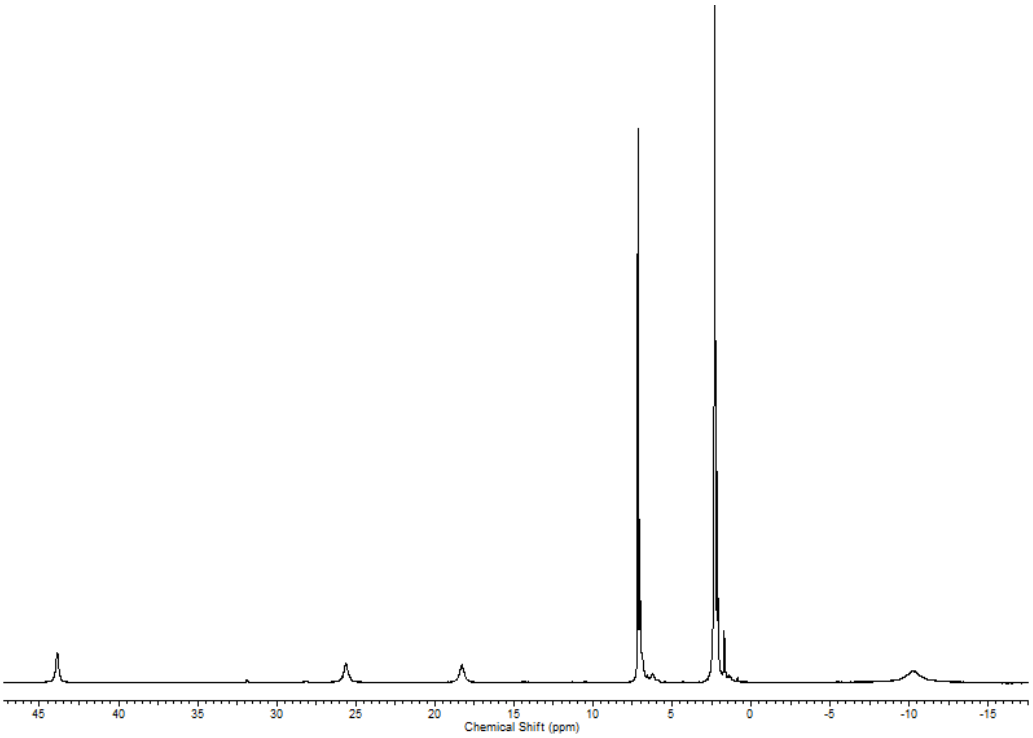

Figure 4.23. ^{1}H NMR spectrum of **2**. * Solvent residues

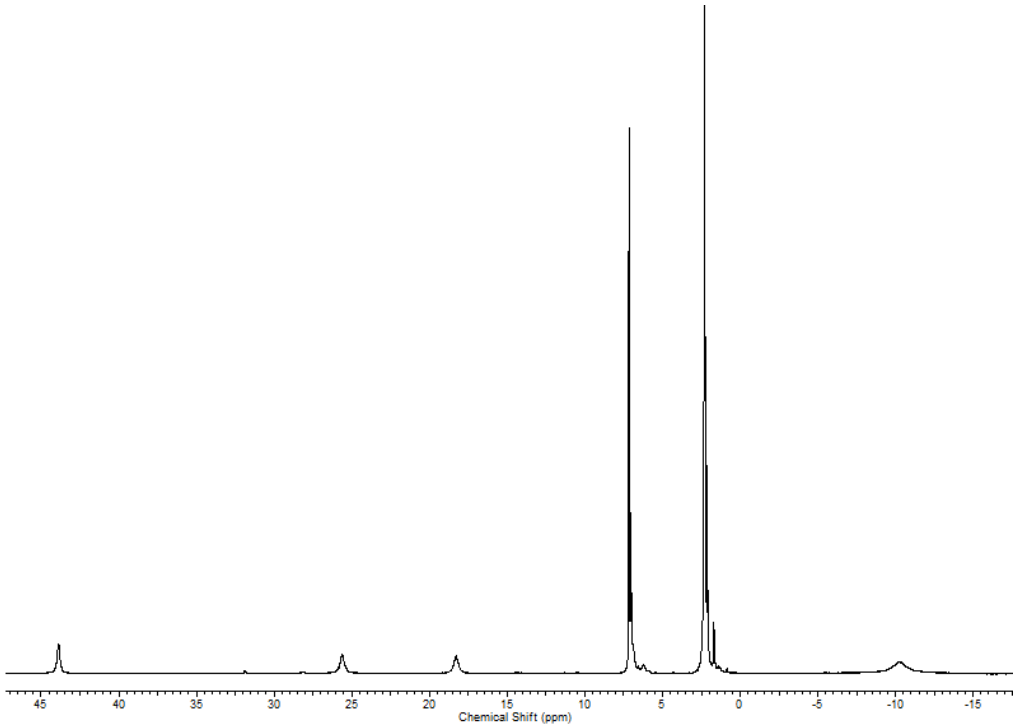

Figure 4.24. ^{1}H NMR spectrum of **3**. * Solvent residues.

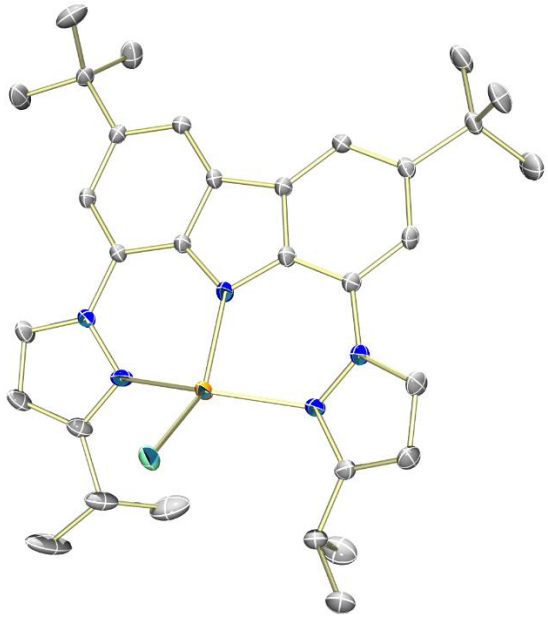

Figure 4.25. Molecular structure of **1** with thermal ellipsoids at the 50% probability level. Solvent molecules and hydrogen atoms are omitted for clarity. Color key: orange = Fe, blue = N, gray = C.

Table 4.1. Selected Bond Distances (Å) and Angles (°) for **1–3**[a]

1		**2**		**3**[b]	
Fe1–N1	2.154(2)	Fe1–N1	2.193(3)	Fe1–N1	2.197(2)
Fe1–N3	1.952(2)	Fe1–N3	2.000(3)	Fe1–N3	1.989(2)
Fe1–N5	2.135(2)	Fe1–N5	2.226(3)	Fe1–N5	2.165(2)
Fe1–Cl1	2.2595(7)	Fe1–Cl1	2.2895(12)	Fe1–N6	2.046(2)
		Fe1–O1	2.132(3)	Fe1–N8#1	2.047(3)
N1–Fe1–N3	88.14(9)	N1–Fe1–N3	87.58(11)	N1–Fe1–N3	88.30(9)
N3–Fe1–N5	87.38(9)	N3–Fe1–N5	88.88(11)	N3–Fe1–N5	88.50(9)
N1–Fe1–N5	149.4(1)	N1–Fe1–N5	172.73(13)	N1–Fe1–N5	176.37(8)
N3–Fe1–Cl1	135.93(6)	N3–Fe1–Cl1	123.83(11)	N3–Fe1–N6	120.45(10)
		N3–Fe1–O1	103.52(13)	N3–Fe1–N8#1	116.92(10)
		O1–Fe1–Cl1	132.52(9)	N6–Fe1–N8#1	122.58(10)
				Fe···Fe	6.124
t_4	0.53	t_5	0.67	t_5	0.90

[a] Numbers in parentheses are standard uncertainties in the last significant figures. Atoms are labeled as indicated in Figure 1, S4, and S5. [b] Symmetry operations: #1 = -1/2 + x, 3/2-y, 1-z

Table 4.2. Crystal data and structure refinement details for **1–3**

	1	**2**	**3**
Empirical formula	$C_{32}H_{40}ClFeN_5$	$C_{86}H_{112}Cl_2Fe_2N_{10}O_2$	$C_{37.72}H_{48}FeN_8O_{0.43}$
Formula weight	622.07	1500.45	676.16
Space group	$P2_1/c$	$P2_1/c$	$P2_12_12_1$
a/Å	11.6810(6)	16.2239(5)	11.3958(3)
b/Å	25.2821(14)	25.4708(10)	14.8759(3)
c/Å	11.2777(6)	22.2526(7)	21.3345(5)
a/°	90	90	90
b/°	102.8005(18)	100.880(2)	90
g/°	90	90	90
V/Å^3	3247.8(3)	9030.3(5)	3616.68(15)
Z	2	4	4
D_{calcd}, g cm^{-3}	1.272	1.104	1.242
F(000)	1324.0	1500.45	1439.0
Temp, K	150	120	120
R(F), %	4.95	6.73	4.46
R_w(F), %	10.83	17.77	8.37

4.7 Notes and References

Authorship and prior publication. This majority of this content in this chapter is under revision for publication at the time of submission of this thesis. Portions of the work were completed by coauthors.

1. Gatteschi, D.; Sessoli, R.; Villain, J., *Molecular Nanomagnets*. Oxford Scholarship Online: Oxford, **2006**.

2. Mannini, M.; Pineider, F.; Sainctavit, P.; Danieli, C.; Otero, E.; Sciancalepore, C.; Talarico, A. M.; Arrio, M.-A.; Cornia, A.; Gatteschi, D.; Sessoli, R. *Nat. Mater.* **2009,** *8*, 194.

3. Caneschi, A.; Gatteschi, D.; Lalioti, N.; Sessoli, R.; Sorace, L.; Tangoulis, V.; Vindigni, A. *Chem. Eur. J.*, **2002**, 8 (1), 286.

4. Caneschi A.;, Gatteschi, D.; Lalioti, N.; Sangregorio, C.; Sessoli, R.; Venturi, G.; Vindigni, A.; Rettori, A.; Pini, M.G.; Novak, M.A.; *Angew. Chem. Int. Ed.* **2001**, *40*, 1760.

5. Sun, H.-L.; Wang, Z.-M.; Gao, S., *Coord. Chem. Rev.* **2010,** *254* (9), 1081.

6. Sorace, L.; Benelli, C.; Gatteschi, D. *Chem. Soc. Rev.*, **2011**,*40*, 3092.

7. Woodruff, D.N.; Winpenny, R.E.P.; Layfield, R.A. *Chem. Rev.*, **2013**, *113* (7), 5110.

8. Miyasaka, H.; Julve, M.; Yamashita, M.; Clérac, R. *Inorg. Chem.* **2009,** *48* (8), 3420.

9. Bao, S.-S.; Zheng, L.-M., *Coord. Chem. Rev.* **2016,** *319* (Supplement C), 63.

10. Harris, T. D.; Bennett, M. V.; Clérac, R.; Long, J. R., *J. Am. Chem. Soc.* **2010,** *132* (11), 3980.

11. Liu, C.-M.; Zhang, D.-Q.; Zhu, D.-B., *Inorg. Chem.* **2009,** *48* (11), 4980.

12. DeGayner, J. A.; Wang, K; Harris, T.D.; *J. Am. Chem. Soc.,* **2018,** *140 (21)*, 6550.

13. Jeon, I.-R.; Clerac, R., *Dalton Trans.* **2012,** *41* (32), 9569.

14. Liu, T.-F.; Fu, D.; Gao, S.; Zhang, Y.-Z.; Sun, H.-L.; Su, G.; Liu, Y.-J., *J. Am. Chem. Soc.* **2003,** *125* (46), 13976.

15. Liu, J.; Qu, M.; Rouzières, M.; Zhang, X.-M.; Clérac, R. *Inorg. Chem.* **2014,** *53* (15), 7870.

16. Zeng, Y.-F.; Hu, X.; Liu, F.-C.; Bu, X.-H., *Chem. Soc. Rev.* **2009,** *38* (2), 469.

17. Xu, H.-B.; Wang, B.-W.; Pan, F.; Wang, Z.-M.; Gao, S., *Angew. Chem. Int. Ed.* **2007,** *46* (39), 7388.

18. Gao, E.-Q.; Yue, Y.-F.; Bai, S.-Q.; Zheng, H.; Yan C.-H. *J. Am. Chem. Soc.*, **2004**, *126* (5), 1419.

19. Fu, A.; Huang, X.; Li, J.; Yuen, T.; Lin, C. L., *Chem. Eur. J.* **2002,** *8* (10), 2239.

20. Deng, Y.-F.; Han, T.; Xue, W.; Hayashi, N.; Kageyama, H.; Zheng, Y.-Z. *Dalton Trans.*, **2017**,*46*, 1449.

21. Wang, Y.-Q.; Yue, Q.; Qi, Y.; Wang, K; Sun, Q.; Gao, E.-Q. *Inorg. Chem.*, **2013**, *52* (8), 4259.

22. Abu-Youssef, M. A. M.; Langer, V.; Luneau, D.; Shams, E.; Goher, M. A. S.; Öhrström, L., *Eur. J. Inorg. Chem.* **2008,** *2008* (1), 112.

23. Shao, D.; Zhao, X.-H.; Zhang, S.-L.; Wu, D.-Q.; Wei, X.-Q.; Wang, X.-Y., *Inorg. Chem. Front.* **2015,** *2* (9), 846.

24. Shao, D.; Zhang, S.-L.; Zhao, X.-H.; Wang, X.-Y., *Chem. Commun.* **2015,** *51* (21), 4360.

25. Zheng, Y.-Z.; Xue, W.; Tong, M.-L.; Chen, X.-M.; Grandjean,F.; Long, G.J. *Inorg. Chem.*, **2008**, *47*, 4077.

26. Keene, T. D.; Zimmermann, I.; Neels, A.; Sereda, O.; Hauser, J.; Bonin, M.; Hursthouse, M.B.; Price, D.J.; Decurtins, S. *Dalton Trans.*, **2010**, *39*, 4937.

27. Boeckmann, J.; Wriedt, M.; Näther, C., *Chem. Eur. J.* **2012,** *18* (17), 5284.

28. Przybylak, S. W.; Tuna, F.; Teat, S. J.; Winpenny, R. E. P., *Chem. Commun.* **2008,** (17), 1983.

29. Qin, L.; Zhang, Z.; Zheng, Z.; Speldrich, M.; Kogerler, P.; Xue, W.; Wang, B.-Y.; Chen, X.-M.; Zheng, Y.-Z., *Dalton Trans.* **2015,** *44* (3), 1456.

30. Yang, L.; Powell, D. R.; Houser, R. P., *Dalton Trans.* **2007,** (9), 955.

31. Pascualini, M.E.; Di Russo, N.V.; Thujis, A.E.; Ozarowski, A.; Stoian, S.A.; Abboud, K.A.; Christou, G.; Veige, A.S. *Chem. Sci*., **2015**, *6*, 608.

32. The plane is defined by the three coordinated nitrogen atoms N1N3N5.

33. Basal plane is defined by the three coordinated nitrogen atoms N1N3N5.

34. Ray, M.; Golombek, A. P.; Hendrich, M. P.; Yap, G. P. A.; Liable-Sands, L. M.; Rheingold, A. L.; Borovik, A. S., *Inorg. Chem.* **1999,** *38* (13), 3110.

35. Carlin, R. L.; Duyneveldt, A. J. v., *Magnetic Properties of Transition Metal Compounds*. Springer: New York, 1977.

36. De la Pint, N.; Fidalgo, M.L; Lezama, L.; Madariaga, G.; Callejo, L.; Cortes, R. *Cryst. Growth Des.*, **2011**, *11* (4), 1310.

37. Bai, S.-Q.; Fang, C.-J.; He, Z.; Gao, E.-Q.; Yan, C.-H.; Hor, T. S. A., *Dalton Trans.* **2012,** *41* (43), 13379.

38. Hong, C.S.; Koo, J.-e.; Son, S.-K.; Lee, Y.S.; Kim, Y.-S.; Do, Y.D. *Chem. Eur. J.* **2001**, *7*, 4243.

39. P. S. Mukherjee, S. Dalai, E. Zangrando, F. Lloret and N. R. Chaudhuri, *Chem. Commun*., **2001**, 1444.

40. Coulon, C.; Miyasaka, H.; Clérac, R., In *Single-Molecule Magnets and Related Phenomena*, Springer: Berlin, Heidelberg, 2006; 163.

42. Li, J.; Li, B.; Huang, P.; Shi, H.-Y.; Huang, R.-B.; Zheng, L.-S.; Tao, J., *Inorg. Chem.* **2013,** *52* (19), 11573.

43. Meng, Y.-S.; Jiang, S.-D.; Wang, B.-W.; Gao, S., *Acc. Chem. Res.* **2016,** *49* (11), 2381.

44. Panja, A.; Shaikh, N.; Vojtíšek, P.; Gao, S.; Banerjee, P., *New J. Chem.* **2002**, 26 (8), 1025.

45. Fisher, M. E. *Am. J. Phys.* **1964**, 32, 343.

46. Song, J. H.; Lim, K. S.; Ryu, D. W.; Yoon, S. W.; Suh, B. J.; Hong, C. S., *Inorg. Chem.* **2014,** *53* (15), 7936.

47. Naiya, S.; Biswas, S.; Drew, M. G. B.; Gómez-García, C. J.; Ghosh, A., *Inorg. Chem.* **2012,** *51* (9), 5332.

48. Palii, A. V.; Reu, O. S.; Ostrovsky, S. M.; Klokishner, S. I.; Tsukerblat, B. S.; Sun, Z.-M.; Mao, J.-G.; Prosvirin, A. V.; Zhao, H.-H.; Dunbar, K. R., *J. Am. Chem. Soc.* **2008,** *130* (44), 1472.

49. Coste, S. C.; Vlaisavljevich, B.; Freedman, D. E., *Inorg. Chem.* **2017**, *56*, 8195.

50. Gao, E.-Q.; Liu, P.-P.; Wang, Y.-Q.; Wang, Q.-L. *Chem. Eur. J.*, **2009**, *15* (5), 1217.

51. Trofimenko, S.; Calabrese, J. C.; Thompson, J. S. *Inorg. Chem.* **1987**, *26*, 1507.

52. Gibson, V. C.; Spitzmesser, S. K.; White, A. J. P.; Williams, D. J. *Dalton Trans.* **2003**, 2718.

53. Schubert, E. M. *J. Chem. Edu.* **1992**, *69*(1), 62.

54. Johnson, K. R. D.; Kamenz, B. L.; Hayes, P. G., *Organometallics* **2014**, *33*, 3005.

55. Apex2 v2013.4-1, v2014.11, v2014.1-1, SAINT V8.34A, SAINT V8.30C. Bruker AXS Inc.: Madison(WI), USA, 2013/2014.

56. SHELXTL (Version 6.14) Bruker Advanced X-ray Solutions, Bruker AXS Inc., Madison, Wisconsin: USA, 2000-2003.

57. Sheldrick, G. M. *Acta Cryst.*, **2008**, *A64*, 112.

58. Sheldrick, G. M. *Acta Cryst*., **2015**, *A71*, 3.

59. Sheldrick G. M. *Acta Cryst.* **2015**, *C71*, 3.

60. Sheldrick, G. M. University of Göttingen, Germany, 2016 and 2018.

61. Hübschle, C. B.; Sheldrick, G. M.; Dittrich, B. *J. Appl. Crystallogr.*, **2011**, *44*, 1281.

62. Dolomanov, O. V.; Bourhis, L. J.; Gildea, R. J.; Howard, J. A. K.; Puschmann, H. *J. Appl. Cryst.*, **2009**, *42*, 339.

63. Spek, A. L. *Acta Crystallogr. Sect C: Struct. Chem*. **2015**, *C71*, 9.

64. Azuah, R.T.; Kneller, L.R.; Qiu, Y.; Tregenna-Piggott, P.L.W.; Brown, C.M.; Copley, J.R.D.; Dimeo, R.M. *J. Res. Natl. Inst. Stan. Technol*., **2009**, *114*, 341.

CHAPTER 5: SULFONATE-LIGATED COORDINATION POLYMERS INCORPORATING PARAMAGNETIC TRANSITION METALS

5.1 Abstract

The functionalized linker SNDC (4,8-disulfonyl-2,6-naphthalenedicarboxylate) has been incorporated into 2D extended structures featuring Fe(II) or Co(II). These materials are isostructural and exhibit coordination via both the carboxylate and sulfonate groups of the SNDC linker. The variable temperature magnetic behavior of the Fe(II) and Co(II) materials has also been measured. A simplified model of these systems implies weak ($|J| < 5$ cm^{-1}) antiferromagnetic coupling, as is expected for a superexchange mechanism operating through the carboxylate paddlewheels. The combination of functionalized linkers, such as SNDC, with paramagnetic metal centers is a promising pathway towards functionalized materials, and the coordination polymers reported join a small class of known materials featuring SNDC.

5.2 Introduction

Starting with this chapter, the work in this thesis transitions to a focus on the utilization of sulfur-based ligands. This new focus was prompted by the hypothesis that sulfur-based ligands would be superior to oxygen or nitrogen-based ligands for our purposes, due to superior energy matching of sulfur with first-row transition metals yielding improved electron delocalization and magnetic coupling. In this chapter, the functionalized ligand SNDC is investigated. While the additional coordination via the sulfonate substituent affords an interesting extended structure, the magnetic behavior is more akin to that of the M(BDC)(pyz) materials in Chapter 2—that is, primarily weak superexchange of high-spin Fe(II) and Co(II) centers.

The foundational work in the field of extended metal-organic materials focused primarily on the utilization of commercially available and largely chemically stable linkers such as aryl polycarboxylates, pyrazines, and pyridines, which produced many highly stable and porous materials appropriate for applications such as gas separation and sorption.[1] There has recently been a drive to incorporate additional properties into extended solids such as catalytic activity, exotic magnetic and optical behavior, electrical and ionic conductivity, medicinal functionality and more.[2] However, realization of these properties typically necessitates the inclusion of other linkers or substituents. Classic ligands such as carboxylates are favorable components to incorporate into extended solids as they engender strong metal binding to create stable crystalline materials and have the appropriate size and rigidity to instill porosity. Unfortunately, these same linkers are also typically insulating and diamagnetic, limiting interesting magnetic or electronic properties. Conversely, many ligands with desirable secondary functionalities lack the strong metal binding necessary for stable and crystalline materials. The incorporation of new binding motifs into coordination polymers is therefore both challenging and relatively underexplored. One strategy to expand this area is the further functionalization of classic linkers. In this way, the desirable properties of the classic linkers can be combined with attractive substituent properties such as modulation of electronic properties through the additional coordinating functionalities.

Sulfonate, as a strongly electron withdrawing group, should modulate the redox potentials of a conjugated aryl group and potentially allow redox activity or the installation of radical character. Some stable organic radicals bearing sulfonate or sulfuranyl groups have been reported, but frequently show a poor ability to coordinate to metal sites.[3] Coordination polymers incorporating sulfonate functionalized ligands are fairly rare, and the bulk of reported structures are Ag containing materials.[4,5] There are currently less than a dozen reports of sulfonate

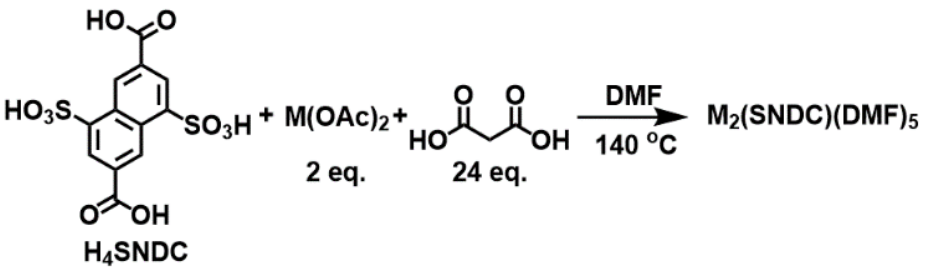

Figure 5.1. Conditions for the solvothermal syntheses of the $M_2(SNDC)(DMF)_5$ materials.

functionalized ligands in coordination polymers containing transition metals,[6] and among these most contain diamagnetic metal sites. Typically, extended networks of metals and sulfonate-functionalized ligands have been layered materials and the primary proposed applications of these compounds have arisen from structural features – for example, gas or dye absorption between layers or in pores.

Of this larger group of potential linkers, the functionalized dicarboxylate ligand SNDC (4,8-disulfonyl-2,6-naphthalenedicarboxylate, Figure 5.1 left) has been utilized in a small number of metalated complexes and extended materials, with preferential binding via sulfonate or carboxylate groups in addition to the multiple binding modes of both groups resulting in a large variety of structural motifs. These reported materials have targeted many of the aforementioned application areas, including proton conductivity, catalysis, magnetism, and luminescence.[6h-k,7] Wanting to further investigate coordination polymers incorporating this linker, we have synthesized two 2D extended materials, $M_2(SNDC)(DMF)_5$ with M = Fe(II), Co(II). These are the first reported examples of extended solids containing SNDC and paramagnetic transition metals and join the single previous example of mixed valent Fe(II)/Fe(III) molecular triangles reported by Trikalitis et al,[7a] as the only reported cases of any paramagnetic transition metal bound to the SNDC ligand.

5.3 Results and Discussion

5.3.1. Synthesis and Stability The H_4SNDC proligand was prepared according to published procedures by sulfonation of 2,6-naphthalenedicarboxylic acid with fuming sulfuric acid.[7,8] The M_2(SNDC)$(DMF)_5$ (M = Fe(II) or Co(II)) materials were prepared by solvothermal synthesis using malonic acid as a templating agent to improve crystallinity (Figure 5.1). The Fe(II) (**1**) and Co(II) (**2**) materials are obtained as orange and purple microcrystalline solids in yields of 71% and 74%, respectively. These materials are stable for over three months under N_2 atmosphere and are stable in dry air, as evidenced by negligible change to overall crystallinity observed by X-ray powder diffraction (XRPD). Under atmospheric air, however, degradation occurs over the course of hours likely due to atmospheric water, as these materials dissolve in water (Figure 5.2 and Figure 5.3).

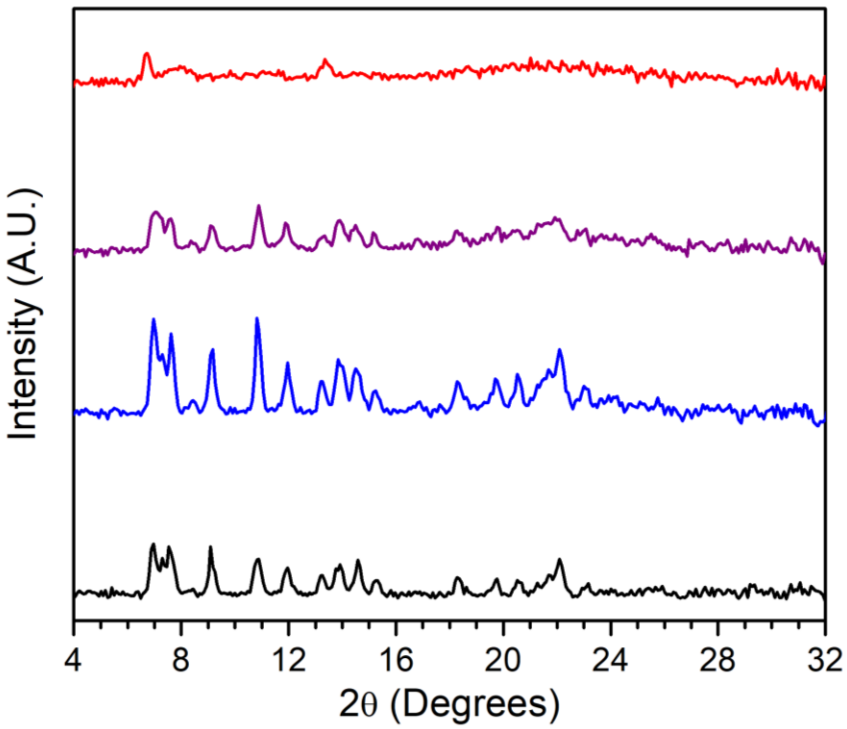

Figure 5.2. XPRD plot of **1** as synthesized (black), after >3 months under N_2 (blue), after 5 hours under a flow of dry air (purple), and after overnight exposure to atmospheric air (red).

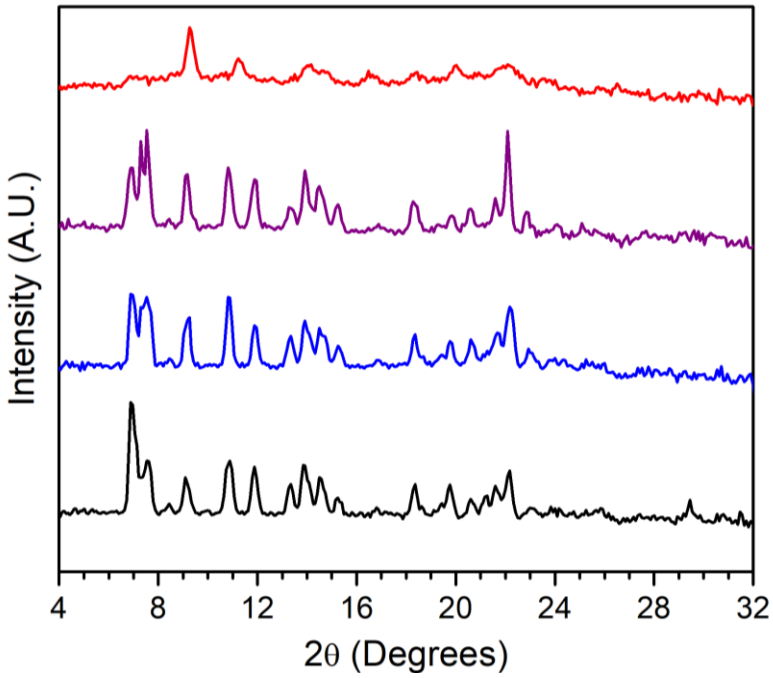

Figure 5.3. XPRD plot of **2** as synthesized (black), after >3 months under N_2 (blue), after 5 hours under a flow of dry air (purple), and after overnight exposure to atmospheric air (red).

Differential scanning calorimetry (DSC) analysis indicates that these materials are thermally stable up to approximately 250 °C under flow of N_2 and do not exhibit any significant endothermic transitions below these temperatures (Figure 5.8 and Figure 5.9).

5.3.2. Structure SXRD data acquired on **1** reveals a triclinic $P\bar{1}$ space group featuring Fe(II) centers bound both through the sulfonate and carboxylate groups of SNDC. The carboxylate bound Fe(II) atoms form a paddlewheel motif which forms an extended 2D plane. The axial site of the paddlewheel is capped by DMF, preventing an extended 3D network from forming via pillaring of the planes. The Fe···Fe separation in these paddlewheels is 2.869(1) Å which is typical for Fe(II)/Fe(II) paddlewheel units.[9] The Fe–O–C–O–Fe planes are almost perfectly orthogonal to one another at 88.8(2)°. The average Fe–O bond length between the carboxylate O atoms and paddlewheel Fe sites is 2.056 Å, σ = 0.008, and the Fe–O bond length corresponding to the bound

DMF is 2.039(5) Å. At the other Fe(II) site, the binding via sulfonates yields zig-zag chains of Fe and SNDC embedded within the 2D plane. The sulfonate O atoms bound to Fe(II) are cis- to one another, and O atoms from DMF occupy the remaining four coordination sites. The geometry of these Fe(II) sites is close to perfectly octahedral with a standard deviation from 90° of $\sigma = 3.2°$. The average Fe–O bond lengths of these Fe sites are markedly longer (2.13 Å, $\sigma = 0.03$ Å) than

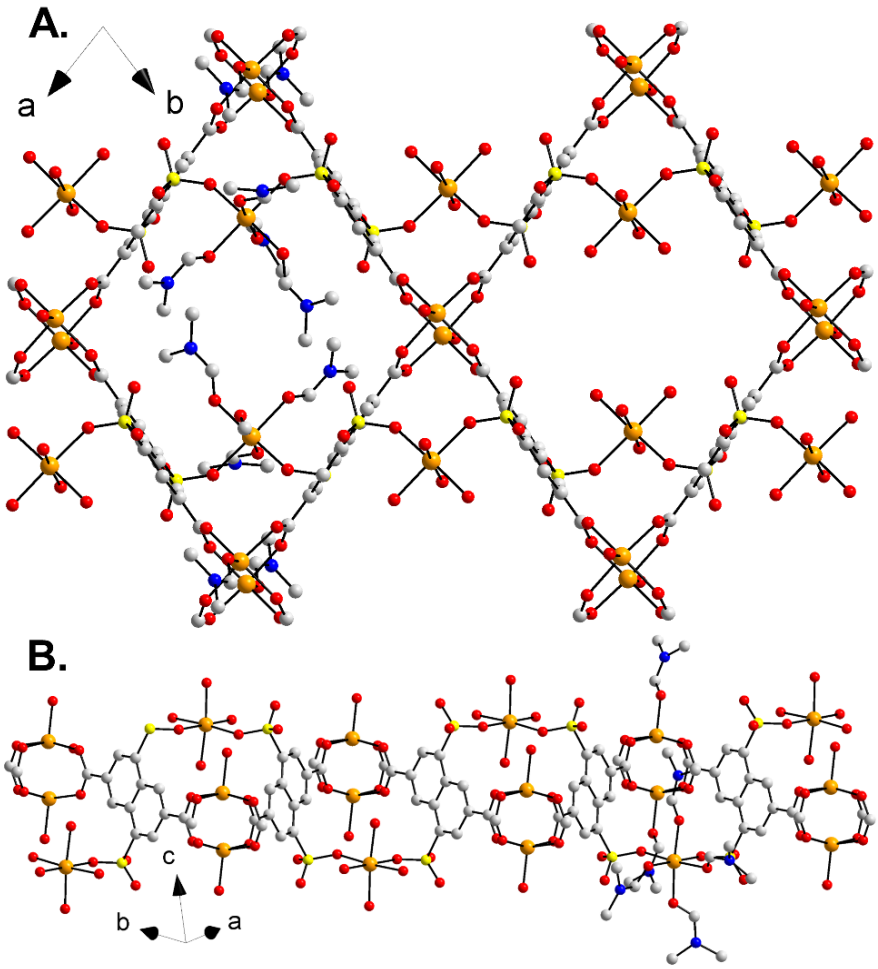

Figure 5.4. The molecular structure of **1** (A) perpendicular to and (B) parallel to the extended 2D plane. The N and C atoms of bound DMF molecules have been omitted for clarity on the right side of figure A, and in all but the right unit of figure B. H atoms have been omitted for clarity. Fe is orange, S is yellow, O is red, N is blue, and C is grey. All atoms are shown in a ball and stick model.

those of the paddlewheel Fe sites. The average lengths of the Fe–O bonds corresponding to the bound SNDC and DMF at this site are fairly similar at 2.14 Å and 2.12 Å, respectively. The nearest Fe···Fe separation outside of the paddlewheel unit is 7.287(2) Å and corresponds to the distance between a carboxylate-bound Fe and a sulfonate-bound Fe, whereas the Fe···Fe separations between the paddlewheel units or between sulfonate bound Fe sites are >10 Å. PLATON analysis indicates that there is minimal solvent accessible void space (4.5%) in the structure. From the structure, it can be observed that the Fe-SNDC framework (Figure 5.4) creates diamond-shaped pores within the layers. However, the Fe-bound DMF molecules occupy these spaces leading to negligible overall void space. The predicted lack of porosity is supported by N_2 gas uptake measurements which imply a low amount of gas adsorption (Figure 5.10). Although a single crystal structure of **2** could not be obtained, XRPD data offer insight on the structure of this

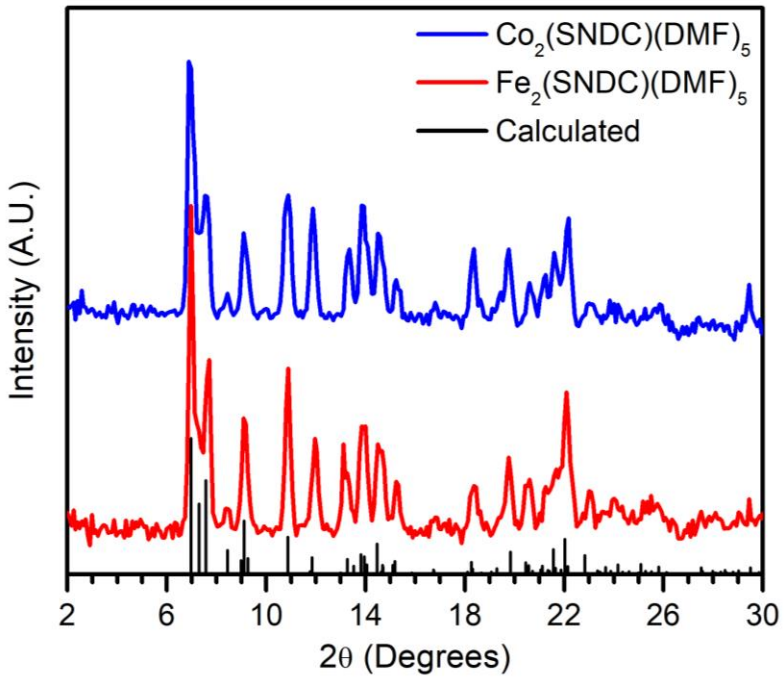

Figure 5.5. The XRPD of $M_2(SNDC)(DMF)_5$, M = Fe(II), Co(II) collected at room temperature and the theoretical diffraction pattern calculated from the SXRD for $Fe_2(SNDC)(DMF)$, collected at 100 K.

material. Both of the $M_2(SNDC)(DMF)_5$ materials exhibit XRPD patterns consistent with the pattern calculated from the space group and unit cell parameters determined from the SXRD data of **1** (Figure 5.5), indicating that these materials are isostructural and consist of a single crystalline phase.

5.3.3. Magnetic Properties In the analysis and discussion of the magnetic behaviors of these materials, we have considered two formula units to capture the coupling pathways which likely have the most significant contribution to the overall magnetic properties (see below). Variable temperature dc molar magnetic susceptibility (χ) was collected for both of the $M_2(SNDC)(DMF)_5$ variants with M = Fe(II) and Co(II). The Fe(II) material has a room temperature χT of 14.0 cm^3K/mol for two formula units (Figure 5.6). The spin-only χT value of four non-interacting S =

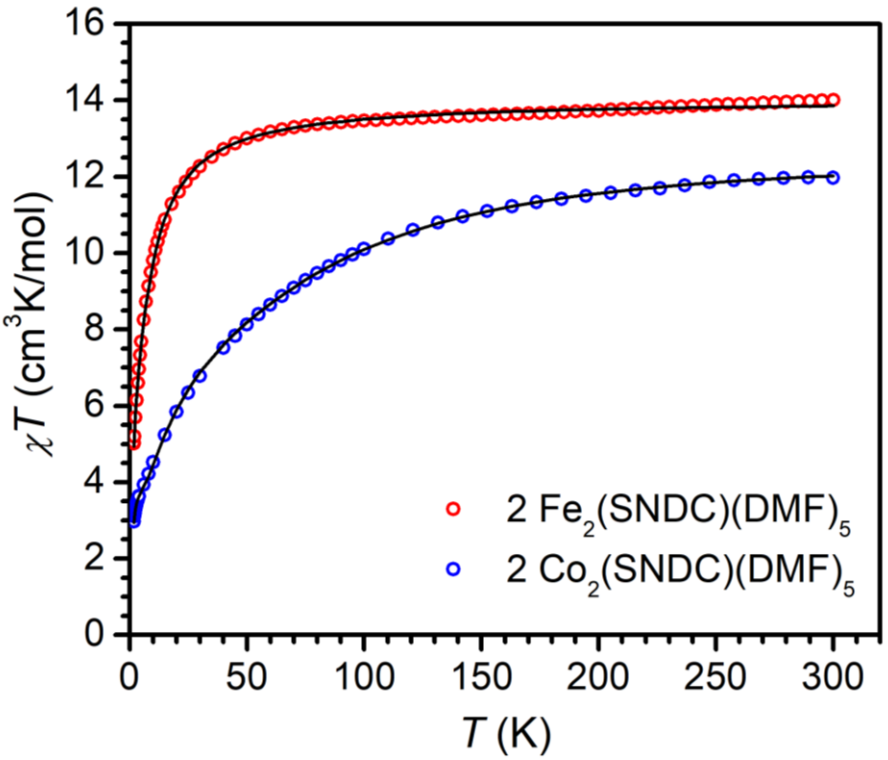

Figure 5.6. Temperature-dependent magnetic susceptibility (χ) data for $M_2(SNDC)(DMF)_5$ with M = Fe(II), Co(II). Black lines are fits to the data as outlined in the text. The data is normalized to two formula units in order to model the relevant magnetic pathways.

2 ions in two formula units is 12.0 cm^3K/mol, which is in good agreement with the experimental values when accounting for spin-orbit effects in 6-coordinate high-spin Fe(II) ions.[10] The χT of **1**is fairly constant above 50 K, indicative of an uncoupled system or very weak coupling. Lippard and coworkers found that one Fe(II)/Fe(II) carboxylate paddlewheel complex exhibited a small increase in magnetic moment at low temperatures, presumably due to ferromagnetic exchange between the Fe(II) centers.[9a] The lack of significant coupling in the present case may be due to the 0.1 Å larger Fe···Fe separation in our system. This hypothesis is consistent with the observation that other related Fe(II)/Fe(II) paddlewheel carboxylate complexes with similarly larger Fe···Fe separations do not exhibit low temperature increases in their χT values.[9a]

The Co(II) material has a room temperature χT of 12.0 cm^3K/mol for two formula units. Although the spin-only χT value of four non-interacting $S = 3/2$ ions in two formula units is 7.50 cm^3K/mol, a significantly elevated χT observed for Co(II) ions is a well-documented phenomenon arising from unquenched spin-orbit coupling.[11] Upon cooling below 300 K, χT decreases continuously. Concretely assigning the origin of this decrease is difficult due to convolutions between antiferromagnetic interactions and spin- orbit coupling effects.

Superexchange coupling can be strong over small one- to three-atom bridges, but is typically weak over longer paths.[12] This trend suggests that the exchange from the shortest M–O–C–O–M pathway is likely dominant over pathways across the aryl portion of SNDC which span 7+ atoms. The net coupling between the two paddlewheel Fe sites with spins S_1 and S_2 (see Figure 5.7) is designated as J_{12} and corresponds to the cumulative exchange mediated by all four carboxylate bridge pathways between these spin centers. The next nearest Fe/Fe interaction (see above) is between a paddlewheel Fe site (S_1 or S_2) and its nearest sulfonate-bound Fe neighbor

(spin center S_3 or S_4, respectively), and a secondary coupling here ($J_{13} = J_{24}$) would be expected to be much smaller than between paddlewheel sites. We can estimate the effects of these couplings using the following Hamiltonian:

$$\hat{H} = g_1\mu_B \boldsymbol{H}\cdot\boldsymbol{S}_1 + g_2\mu_B \boldsymbol{H}\cdot\boldsymbol{S}_2 + g_3\mu_B \boldsymbol{H}\cdot\boldsymbol{S}_3 + g_4\mu_B \boldsymbol{H}\cdot\boldsymbol{S}_4 - J_{12}\boldsymbol{S}_1\boldsymbol{S}_2 - J_{13}\boldsymbol{S}_1\boldsymbol{S}_3 - J_{24}\boldsymbol{S}_2\boldsymbol{S}_4 \quad \textbf{5.1}$$

where we make the assumption that any other J values or orbital contributions should be negligible. Here, g is the g-factor, μ is magnetic moment, β is the Bohr magneton, H is the applied field, and S is the spin. It should also be noted that the paddlewheel Fe sites are crystallographically equivalent, and we therefore set the S and g values of these sites to be equal (e.g. $g_1 = g_2$). The same constraint was placed between the two crystallographically equivalent sulfonate bound Fe sites, and correspondingly between the J_{13} and J_{24} values.

The Fe(II) material is well fit to the above Hamiltonian and estimated to have a J_{12} value on the order of -1.7(2) cm^{-1}, and a J_{13}/J_{24} value of -0.436(8) cm^{-1} with corresponding g values of 2.20(3)

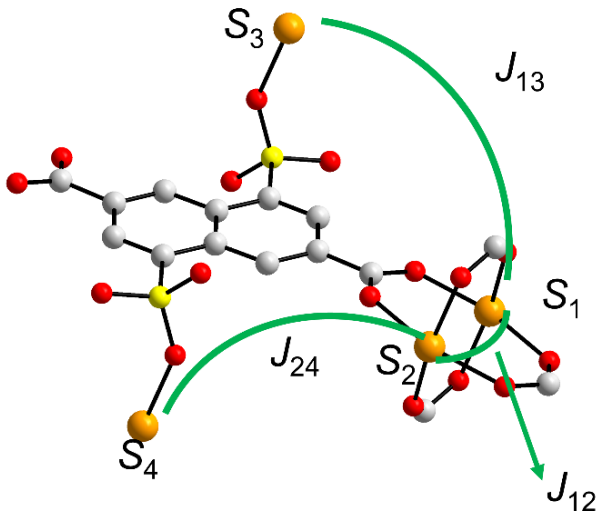

Figure 5.7. Designation of spin centers and the magnetic exchange interactions that are most likely to contribute to the bulk magnetic properties of the $M_2(SNDC)(DMF)_5$ materials. From the molecular structure of **1**: Fe is orange, S is yellow, O is red, and C is grey. Note that sites designated as S_1 and S_2 are crystallographically equivalent, as are sites S_3 and S_4.

and 2.122(2) for sites 1/2 and 3/4, respectively (Figure 5.7). The magnetic data for the Co(II) material can also be fit, however the analysis is less reliable due to significant spin-orbit coupling leading to a large axial component of the ZFS parameter, *D*.[13] The obtained fitting parameters must be interpreted cautiously without an experimentally determined ZFS value to verify how physically reasonable the fit is. Nevertheless, we have fit this data with the following Hamiltonian:

$$\mathrm{H} = g_1\mu_B \boldsymbol{H}\cdot\boldsymbol{S}_1 + g_2\mu_B \boldsymbol{H}\cdot\boldsymbol{S}_2 + g_3\mu_B \boldsymbol{H}\cdot\boldsymbol{S}_3 + g_4\mu_B \boldsymbol{H}\cdot\boldsymbol{S}_4 - J_{12}\boldsymbol{S}_1\boldsymbol{S}_2 - J_{13}\boldsymbol{S}_1\boldsymbol{S}_3 - J_{24}\boldsymbol{S}_2\boldsymbol{S}_4 + D_1[\boldsymbol{S}_1{}^2 - \boldsymbol{S}_1(\boldsymbol{S}_1+1)]/3 + D_2[\boldsymbol{S}_2{}^2 - \boldsymbol{S}_2(\boldsymbol{S}_2+1)]/3 + D_3[\boldsymbol{S}_3{}^2 - \boldsymbol{S}_3(\boldsymbol{S}_3+1)]/3 + D_4[\boldsymbol{S}_4{}^2 - \boldsymbol{S}_4(\boldsymbol{S}_4+1)]/3 \qquad \textbf{5.2}$$

where the additional axial ZFS terms in the Hamiltonian are of the form $D_i[\boldsymbol{S}_i{}^2 - \boldsymbol{S}_i(\boldsymbol{S}_i+1)]/3$. The best fit using this model gives J_{12} and J_{13}/J_{24} values of -4(2) cm^{-1} and -0.3(2) cm^{-1}, respectively (Figure 5.6). This fitting also includes $g_{1/2}$ = 2.6(3) and $g_{3/4}$ = 2.6(2). We reiterate that the fit may have significant error due to uncertainty in the true value of *D*. In the case of both the Fe(II) and Co(II) systems the J_{12} values are in good agreement with previous reports of magnetic exchange via carboxylates in a syn-syn binding mode and suggest weak antiferromagnetic exchange in these materials.[14]

5.4 Conclusions

Coordination polymers of the type $M_2(SNDC)(DMF)_5$ with M = Fe(II), Co(II) were synthesized and magnetically and structurally characterized. These materials feature two distinct metal binding sites – via the sulfonates and carboxylates of the SNDC linker – to form 2D infinite layers. Both materials exhibit weak antiferromagnetic coupling, as evidenced by their temperature-dependent magnetic susceptibilities. These compounds are the first reported to incorporate the SNDC ligand and paramagnetic transition metal centers in an extended solid.

5.5 Experimental Methods

General Considerations. Syntheses of $M_2(SNDC)(DMF)_5$ (SNDC = 4,8-disulfonyl-2,6-naphthalenedicarboxylate; M = Co(II), Fe(II)) materials were carried out in a nitrogen-filled MBraun glovebox. H_4SNDC was prepared according to literature procedures,[1] and the formation and purity of this product was confirmed by ^1H NMR in $CDCl_3$ acquired on a Bruker DRX 400 at 400 MHz. IR samples were prepared as KBr pellets, and spectra were acquired on a Bruker Tensor II and analysed with Bruker's OPUS software. Appropriate solvents were dried and degassed in a Pure Process Technologies solvent system and stored over 4 Å molecular sieves. Solvents were tested for O_2 and H_2O with a standard solution of sodium benzophenone ketyl radical. All other reagents were used as purchased without further purification.

$Fe_2(SNDC)(DMF)_5$ (**1**) Iron (II) acetate (0.50 mmol, 0.086 g) is dissolved in 6 mL of DMF with gentle heating. H_4SNDC (0.25 mmol, 0.097 g) and malonic acid (6.0 mmol, 0.62 g) are dissolved separately in DMF (6 mL each). The malonic acid solution is added to the iron (II) acetate solution, then the H_4SNDC solution is added. The solution is heated overnight at 100 °C to yield a dark orange microcrystalline solid (0.15 g, 71%). Elemental analysis: expected for $C_{27}H_{39}Fe_2N_5O_{15}S_2$: % C, 38.2; H, 4.63; N, 8.24. Found: % C, 37.3; H, 4.76; N, 7.99.

$Co_2(SNDC)(DMF)_5$ (**2**) Cobalt (II) acetate (0.50 mmol, 0.089 g) is dissolved in 6 mL of DMF with gentle heating. H_4SNDC (0.25 mmol, 0.097 g) and malonic acid (6.0 mmol, 0.62 g) are dissolved separately in DMF (6 mL each). The malonic acid solution is added to the iron (II) acetate solution, then the H_4SNDC solution is added. The solution is heated overnight at 100 °C to yield a purple microcrystalline solid (0.16 g, 74%). $C_{27}H_{39}Co_2N_5O_{15}S_2$: % C, 38.2; H, 4.63; N, 8.24. Found: % C, 38.1; H, 4.53; N, 8.08.

X-Ray Powder Diffraction (XRPD). Diffraction patterns were collected on a SAXSLAB Ganesha diffractometer with a Cu K-α source (λ = 1.54 Å) in wide angle X-ray scattering (WAXS) transmission mode. The samples were contained in a ~1 mm diameter borosilicate capillary tube. A correction was made to subtract the broad peak from the capillary around 16–25° (2θ) from the baseline.

*Magnetometry***.** Bulk magnetometry measurements were carried out on a Quantum Design MPMS 3 equipped with a superconducting quantum interference device (SQUID) detector. Corrections were made for the diamagnetic contributions from the polycarbonate capsules and eicosane wax used to secure the sample by measuring temperature vs. moment in triplicate for each to determine a moment per gram correction. Reported χ values are molar susceptibilities per two formula units.

Fitting of the **2** χT vs. T data to the Hamiltonian was carried out using MagProp analysis software within the DAVE suite.[2] All g values were constrained to be isotropic ($g_x = g_y = g_z$). The magnetic data was defined as pertaining to two formula units, such that there were four spin centers ($Co_{PW,A} = Co_{PW,B}$, $Co_{Sulf,A} = Co_{Sulf,B}$) such that a Co_{PW}/Co_{PW} interaction could be modeled, however parameters (g, D) for each site type were constrained to be equal. That is, $g_1 = g_{PW,A} = g_{PW,B}$, etc.

Fitting of the **1** χT vs. T data to the Hamiltonian was carried out using PHI analysis software.[3] The spin centers were fit as $S = 2$ centers with no orbital angular momentum. All g values were constrained to be isotropic ($g_x = g_y = g_z$). The magnetic data was defined as pertaining to two formula units, such that there were four spin centers ($Fe_{PW,A} = Fe_{PW,B}$, $Fe_{Sulf,A} = Fe_{Sulf,B}$) such that a Fe_{PW}/Fe_{PW} interaction could be modeled, however g values for each site type were constrained to be equal. That is, $g_1 = g_{PW,A} = g_{PW,B}$. PHI software defines the exchange Hamiltonian term as $\hat{H} = -2 J_{ij}\boldsymbol{S}_i\boldsymbol{S}_j$, however this has been adjusted to be consistent with the convention of $\hat{H} = -J_{ij}\boldsymbol{S}_i\boldsymbol{S}_j$.

Single Crystal X-Ray Diffraction (SXRD). The diffraction data were measured at 100 K on a Bruker D8 VENTURE diffractometer equipped with a microfocus Mo-target X-ray tube (λ = 0.71073 Å) and PHOTON 100 CMOS detector). Data reduction and integration were performed with the Bruker APEX3 software package (Bruker AXS, version 2015.5-2, 2015). Data were scaled and corrected for absorption effects using the multi-scan procedure as implemented in SADABS (Bruker AXS, version 2014/5[4]). The structures were solved by SHELXT (Version 2014/5[5]) and refined by a full-matrix least-squares procedure using OLEX2[6] (XL refinement program version 2018/1[7]).

Gas Adsorption. Activation and measurements were performed on a Micromeritics ASAP 2020 Plus. Surface area was calculated from the N_2 adsorption isotherm using Brunauer–Emmett–Teller (BET) theory. Samples were loaded into a quartz tube fitted with a TranSeal cap and activated at 100 °C until the outgas rate was <1 μm Hg per minute. Measurements were performed at 77 K, in a liquid N_2 bath.

Differential Scanning Calorimetry. DSC was performed on 4 mg samples of **1** and **2** in aluminum pans with lids, handled under N_2. Measurements were acquired on a TA Instruments DSC 2920 from 25 °C to 350 °C at a ramp rate of 10 °C/minute in under flow of N_2.

5.6 Supplementary Data

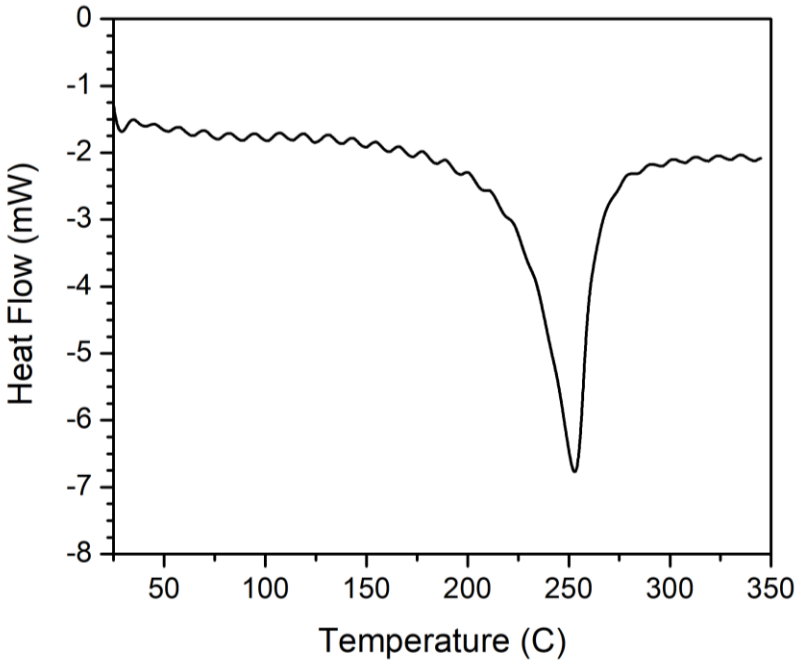

Figure 5.8. DSC plot of **1** acquired under N_2

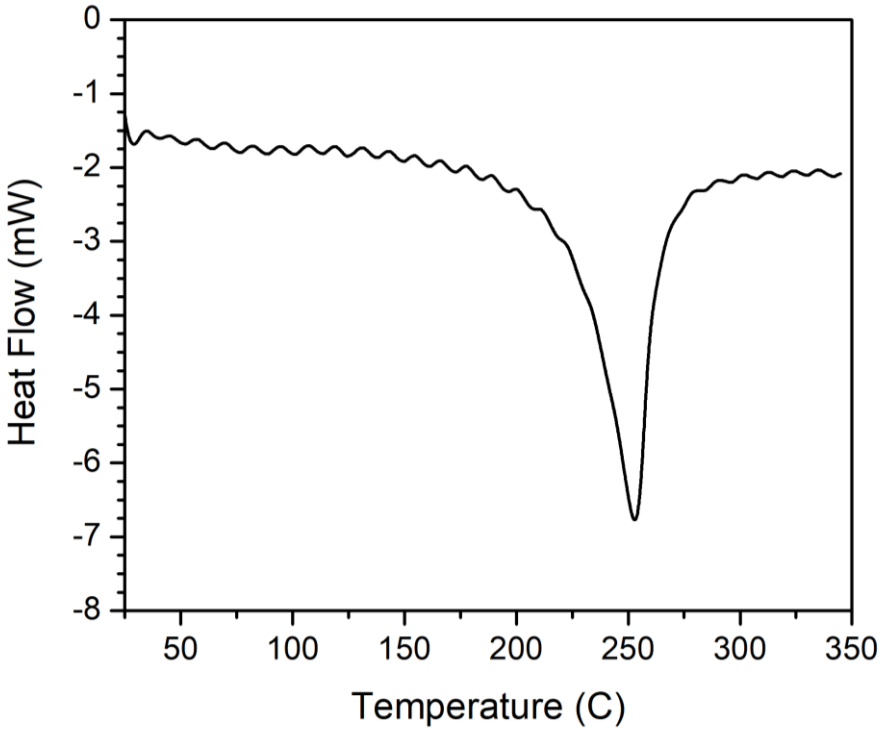

Figure 5.9. DSC plot of **2** acquired under N_2

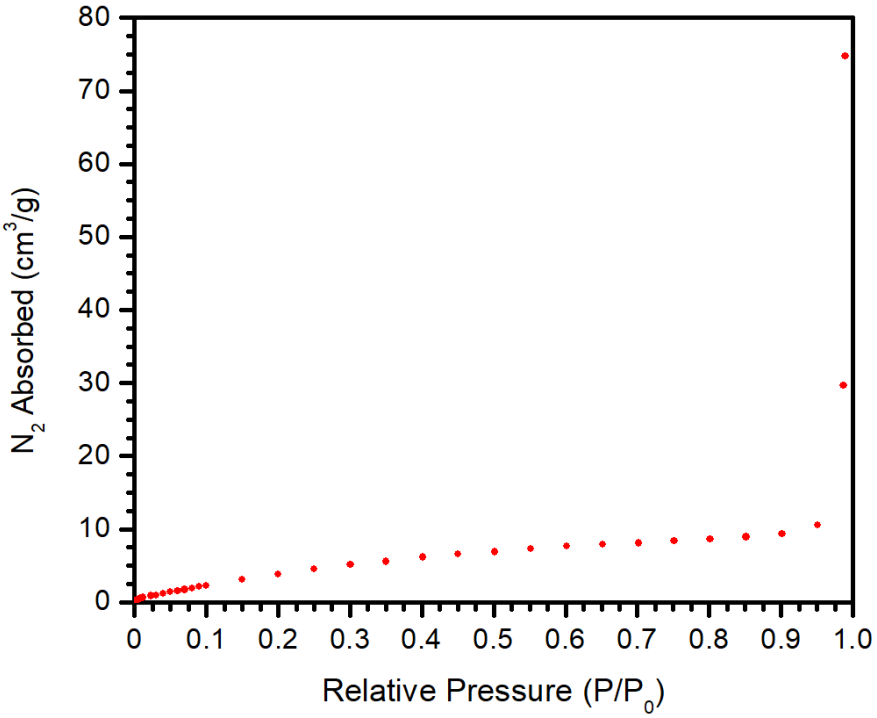

Figure 5.10. Nitrogen gas uptake measurements for **1** which corresponds to a calculated B.E.T. surface area of 22 m^2/g.

Table 5.1 and **Table 5.2.** Magnetic fit data for $M_2(SNDC)(DMF)_5$ (M = Fe, Co).

$Fe_2(SNDC)(DMF)_5$		
Parameter	Value	Error
$g_1 = g_2$	2.20	0.03
$g_3 = g_4$	2.122	0.002
J_{12} (cm^{-1})	-1.7	0.2
$J_{13} = J_{24}$ (cm^{-1})	-0.436	0.008

$Co_2(SNDC)(DMF)_5$		
Parameter	Value	Error
$g_1 = g_2$	2.6	0.3
$g_3 = g_4$	2.6	0.2
J_{12} (cm^{-1})	-4	2
$J_{13} = J_{24}$ (cm^{-1})	-0.3	0.2
$D_1 = D_2$ (cm^{-1})	-97	660
$D_3 = D_4$ (cm^{-1})	-100	830

Table 5.3. Crystal data and structure refinement for **1**

Empirical formula	$C_{27}H_{39}Fe_2N_5O_{15}S_2$
Formula weight	849.45
Temperature/K	100(2)
Crystal system	triclinic
Space group	P-1
a/Å	12.955(3)
b/Å	13.064(2)
c/Å	13.918(3)
α/°	67.410(5)
β/°	74.740(5)
γ/°	71.074(4)
Volume/Å^3	2031.3(7)
Z	2
ρ_{calc}g/cm^3	1.389
μ/mm^{-1}	0.883
F(000)	880.0
Crystal size/mm^3	0.34 × 0.22 × 0.18
Radiation	MoKα (λ = 0.71073)
2Θ range for data collection/°	4.268 to 41.802
Index ranges	-12 ≤ h ≤ 12, -13 ≤ k ≤ 13, -13 ≤ l ≤ 13
Reflections collected	23744
Independent reflections	4259 [R_{int} = 0.1440, R_{sigma} = 0.1033]
Data/restraints/parameters	4259/0/470
Goodness-of-fit on F^2	1.018
Final R indexes [I>=2σ (I)]	R_1 = 0.0528, wR_2 = 0.0914
Final R indexes [all data]	R_1 = 0.1086, wR_2 = 0.1073
Largest diff. peak/hole / e Å^{-3}	0.27/-0.25

Table 5.4. Fractional Atomic Coordinates (×10^4) and Equivalent Isotropic Displacement Parameters (Å^2×10^3) for **1**. U_{eq} is defined as 1/3 of of the trace of the orthogonalised U_{IJ} tensor.

Atom	***x***	***y***	***z***	**U(eq)**
Fe1	9860.1(7)	9684.6(9)	6125.1(6)	45.6(3)
Fe2	7094.9(8)	7362.1(9)	2542.5(7)	55.3(4)
S1	5959.8(15)	10102.3(17)	2412.1(12)	43.4(5)
S2	9909.2(17)	6292.7(17)	2337.2(13)	54.3(6)
O1	8202(4)	9938(4)	6180(4)	69.5(16)
O2	8476(4)	10425(5)	4435(4)	73.0(17)
O3	10071(4)	8086(4)	6061(3)	57.3(14)
O4	10347(4)	8577(4)	4317(4)	62.4(15)
O5	10120(4)	9307(5)	7620(3)	78.6(17)
O6	7254(4)	7877(4)	895(3)	72.6(16)
O7	5365(4)	7518(4)	2688(4)	67.5(15)
O8	7341(5)	5649(5)	2558(5)	78.6(18)
O9	6965(4)	6633(4)	4186(4)	72.9(17)

Table 5.4. (Continued) Fractional Atomic Coordinates (×104) and Equivalent Isotropic Displacement Parameters (Å2×103) for 1. Ueq is defined as 1/3 of of the trace of the orthogonalised UIJ tensor.

Atom	x	y	z	U(eq)
O10	6415(4)	11070(4)	2157(3)	66.1(15)
O11	5314(3)	10199(4)	1664(3)	55.7(13)
O12	6816(3)	9015(4)	2649(3)	51.4(13)
O13	8842(3)	7148(4)	2413(3)	59.8(14)
O14	9989(4)	5714(4)	1608(3)	66.3(15)
O15	10832(4)	6766(4)	2158(3)	63.1(14)
N1	10875(5)	9400(7)	8835(5)	73(2)
N2	8040(5)	7487(6)	-615(5)	84(2)
N3	3785(7)	8089(6)	2033(6)	89(2)
N4	7103(5)	6463(6)	5822(5)	59.3(17)
N5	6907(8)	3932(8)	3269(7)	106(3)
C1	7889(6)	10182(6)	5315(6)	52(2)
C2	6743(5)	10145(5)	5363(5)	33.9(16)
C3	6439(5)	10142(5)	4500(5)	35.7(17)
C4	5386(5)	10038(5)	4523(4)	26.1(15)
C5	5039(5)	10018(5)	3637(4)	26.8(15)
C6	4024(5)	9931(5)	3694(4)	33.1(16)
C7	10210(5)	7864(7)	5225(6)	49(2)
C8	10163(5)	6717(7)	5308(5)	44.8(19)
C9	10076(5)	6506(6)	4447(5)	46.4(19)
C10	9995(5)	5437(6)	4502(4)	40.2(18)
C11	9912(5)	5212(7)	3606(4)	43.6(19)
C12	9814(5)	4170(7)	3712(5)	46(2)
C13	10509(6)	9869(8)	7953(6)	76(3)
C14	11337(6)	10046(8)	9221(5)	99(3)
C15	10991(8)	8221(9)	9448(7)	133(4)
C16	7968(6)	7308(6)	381(6)	65(2)
C17	7257(9)	8380(9)	-1226(7)	182(6)
C18	8926(7)	6789(8)	-1164(6)	116(4)
C19	4825(8)	8013(7)	1966(7)	69(2)
C20	3163(8)	7619(8)	3022(8)	129(4)
C21	3217(9)	8686(10)	1097(9)	176(5)
C22	7112(6)	7025(6)	4798(6)	60(2)
C23	6987(7)	5304(7)	6256(6)	88(3)
C24	7210(6)	6982(6)	6534(5)	84(3)
C25	6819(8)	4982(10)	3210(7)	87(3)
C26	7710(8)	3445(8)	2532(8)	136(4)
C27	6192(11)	3222(10)	4048(10)	188(6)

Table 5.5. Anisotropic Displacement Parameters ($Å^2 \times 10^3$) for **1**. The Anisotropic displacement factor exponent takes the form: $-2\pi^2[h^2a^{*2}U_{11}+2hka^*b^*U_{12}+\ldots]$.

Atom	U_{11}	U_{22}	U_{33}	U_{23}	U_{13}	U_{12}
Fe1	30.9(6)	90.8(9)	28.3(6)	-25.2(6)	0.7(4)	-29.8(6)
Fe2	52.8(8)	69.2(8)	42.9(6)	-31.2(6)	-14.4(5)	7.1(6)
S1	40.5(13)	54.5(14)	31.5(11)	-17.2(10)	3.3(9)	-10.5(11)
S2	47.7(14)	73.0(15)	32.4(11)	-22.7(11)	-14.3(9)	10.4(12)
O1	36(3)	123(5)	71(4)	-46(3)	-16(3)	-25(3)
O2	36(3)	141(5)	71(4)	-56(4)	13(3)	-52(3)
O3	61(4)	79(4)	50(3)	-35(3)	-2(3)	-29(3)
O4	67(4)	86(4)	46(3)	-22(3)	1(3)	-42(3)
O5	89(4)	133(5)	35(3)	-38(3)	-9(3)	-43(4)
O6	67(4)	94(4)	53(3)	-48(3)	-20(3)	24(3)
O7	62(4)	67(4)	81(4)	-36(3)	-30(3)	3(3)
O8	86(5)	76(5)	75(4)	-40(4)	-20(3)	4(4)
O9	91(4)	85(4)	48(3)	-35(3)	-21(3)	-4(3)
O10	76(4)	72(4)	52(3)	-18(3)	18(3)	-45(3)
O11	59(3)	80(4)	31(3)	-24(2)	-16(2)	-7(3)
O12	36(3)	67(3)	55(3)	-41(3)	-4(2)	6(3)
O13	43(3)	76(3)	49(3)	-30(3)	-20(2)	22(3)
O14	77(4)	79(4)	34(3)	-30(3)	-19(2)	14(3)
O15	48(3)	95(4)	41(3)	-18(3)	-6(2)	-16(3)
N1	56(4)	137(7)	30(4)	-34(5)	-2(3)	-26(4)
N2	93(6)	107(6)	42(4)	-46(4)	-24(4)	24(4)
N3	62(6)	97(6)	123(7)	-41(5)	-34(5)	-18(5)
N4	75(5)	61(5)	43(4)	-23(4)	-14(3)	-7(4)
N5	121(8)	62(6)	150(9)	-49(6)	-73(7)	15(6)
C1	34(6)	71(6)	66(6)	-37(5)	-2(5)	-19(4)
C2	16(4)	47(5)	48(5)	-25(4)	2(4)	-15(3)
C3	29(5)	46(5)	36(4)	-15(3)	2(3)	-17(4)
C4	19(4)	28(4)	34(4)	-12(3)	-3(3)	-8(3)
C5	25(4)	21(4)	31(4)	-9(3)	1(3)	-5(3)
C6	29(5)	40(4)	36(4)	-17(3)	-9(4)	-7(4)
C7	32(5)	82(7)	43(5)	-29(5)	-1(4)	-19(4)
C8	32(4)	65(6)	37(5)	-19(5)	-11(3)	-3(4)
C9	30(4)	70(6)	28(4)	-15(4)	-9(3)	4(4)
C10	34(4)	50(6)	32(4)	-20(4)	0(3)	-2(4)
C11	32(4)	64(6)	27(4)	-22(4)	-5(3)	7(4)
C12	35(5)	68(6)	41(5)	-32(5)	-12(3)	2(4)
C13	69(6)	142(9)	23(5)	-31(5)	5(4)	-40(6)
C14	49(6)	217(11)	67(6)	-78(7)	13(4)	-56(6)
C15	175(12)	139(10)	57(7)	-20(7)	-39(7)	-3(8)
C16	57(6)	87(6)	47(5)	-31(5)	-32(4)	16(5)
C17	187(12)	212(12)	73(7)	-51(8)	-88(8)	104(10)
C18	131(9)	146(9)	64(6)	-71(6)	-1(6)	8(7)
C19	56(7)	74(7)	85(7)	-36(5)	-15(5)	-11(5)
C20	101(9)	130(9)	176(11)	-60(8)	9(8)	-67(8)
C21	137(11)	222(13)	204(13)	-59(10)	-115(10)	-31(9)

Table 5.5. (Continued) Anisotropic Displacement Parameters ($Å^2 \times 10^3$) for **1**. The Anisotropic displacement factor exponent takes the form: $-2\pi^2[h^2a^{*2}U_{11}+2hka^*b^*U_{12}+\ldots]$.

Atom	U_{11}	U_{22}	U_{33}	U_{23}	U_{13}	U_{12}
C22	64(6)	51(6)	46(6)	-15(5)	-5(4)	4(4)
C23	112(8)	74(7)	77(6)	-27(5)	-18(5)	-19(6)
C24	110(8)	88(7)	64(5)	-37(5)	-26(5)	-11(5)
C25	101(9)	79(9)	63(7)	-22(6)	-32(6)	14(7)
C26	118(9)	130(10)	197(11)	-120(9)	-75(8)	40(7)
C27	219(16)	111(11)	212(14)	-13(10)	-35(12)	-61(11)

Table 5.6. Bond Lengths for **1**.

Atom	Atom	Length/Å	Atom	Atom	Length/Å
Fe1	Fe1[1]	2.8693(17)	N1	C13	1.283(8)
Fe1	O1	2.050(4)	N1	C14	1.485(9)
Fe1	O2[1]	2.068(4)	N1	C15	1.425(9)
Fe1	O3	2.050(5)	N2	C16	1.297(7)
Fe1	O4[1]	2.055(5)	N2	C17	1.428(9)
Fe1	O5	2.039(5)	N2	C18	1.458(8)
Fe2	O6	2.101(4)	N3	C19	1.300(9)
Fe2	O7	2.145(5)	N3	C20	1.417(10)
Fe2	O8	2.148(6)	N3	C21	1.482(10)
Fe2	O9	2.096(5)	N4	C22	1.328(8)
Fe2	O12	2.128(4)	N4	C23	1.441(8)
Fe2	O13	2.156(4)	N4	C24	1.453(8)
S1	O10	1.449(4)	N5	C25	1.310(10)
S1	O11	1.445(4)	N5	C26	1.432(10)
S1	O12	1.472(4)	N5	C27	1.467(12)
S1	C5	1.792(5)	C1	C2	1.485(8)
S2	O13	1.477(4)	C2	C3	1.360(7)
S2	O14	1.448(4)	C2	C6[2]	1.413(7)
S2	O15	1.442(5)	C3	C4	1.406(7)
S2	C11	1.788(6)	C4	C4[2]	1.427(10)
O1	C1	1.262(7)	C4	C5	1.431(7)
O2	C1	1.244(7)	C5	C6	1.336(7)
O3	C7	1.259(7)	C7	C8	1.478(9)
O4	C7	1.258(7)	C8	C9	1.368(8)
O5	C13	1.278(8)	C8	C12[3]	1.411(8)
O6	C16	1.238(7)	C9	C10	1.406(8)
O7	C19	1.223(8)	C10	C10[3]	1.417(11)
O8	C25	1.221(10)	C10	C11	1.423(8)
O9	C22	1.228(8)	C11	C12	1.356(8)

[1]2-X,2-Y,1-Z; [2]1-X,2-Y,1-Z; [3]2-X,1-Y,1-Z

Table 5.7. Bond Angles for **1**

Atom	Atom	Atom	Angle/˚	Atom	Atom	Atom	Angle/˚
O1	Fe1	Fe1[1]	88.79(14)	S1	O12	Fe2	136.5(3)
O1	Fe1	O2[1]	161.77(18)	S2	O13	Fe2	141.0(3)
O1	Fe1	O4[1]	89.98(19)	C13	N1	C14	120.6(8)
O2[1]	Fe1	Fe1[1]	72.98(14)	C13	N1	C15	124.0(8)
O3	Fe1	Fe1[1]	82.83(13)	C15	N1	C14	115.0(7)
O3	Fe1	O1	87.52(19)	C16	N2	C17	121.5(7)
O3	Fe1	O2[1]	89.88(19)	C16	N2	C18	121.6(6)
O3	Fe1	O4[1]	161.63(17)	C17	N2	C18	116.9(6)
O4[1]	Fe1	Fe1[1]	78.93(13)	C19	N3	C20	119.9(8)
O4[1]	Fe1	O2[1]	86.8(2)	C19	N3	C21	121.5(9)
O5	Fe1	Fe1[1]	163.01(16)	C20	N3	C21	118.7(8)
O5	Fe1	O1	107.7(2)	C22	N4	C23	120.1(6)
O5	Fe1	O2[1]	90.54(19)	C22	N4	C24	121.8(7)
O5	Fe1	O3	101.7(2)	C23	N4	C24	118.1(6)
O5	Fe1	O4[1]	96.4(2)	C25	N5	C26	119.9(10)
O6	Fe2	O7	90.36(19)	C25	N5	C27	123.0(11)
O6	Fe2	O8	87.2(2)	C26	N5	C27	117.2(9)
O6	Fe2	O12	96.86(18)	O1	C1	C2	117.1(6)
O6	Fe2	O13	90.13(17)	O2	C1	O1	124.9(7)
O7	Fe2	O8	86.1(2)	O2	C1	C2	118.0(7)
O7	Fe2	O13	178.22(18)	C3	C2	C1	119.6(6)
O8	Fe2	O13	92.2(2)	C3	C2	C6[2]	119.6(5)
O9	Fe2	O6	172.5(2)	C6[2]	C2	C1	120.8(6)
O9	Fe2	O7	89.1(2)	C2	C3	C4	121.9(5)
O9	Fe2	O8	85.3(2)	C3	C4	C4[2]	118.3(7)
O9	Fe2	O12	90.59(17)	C3	C4	C5	123.6(5)
O9	Fe2	O13	90.25(18)	C4[2]	C4	C5	118.1(6)
O12	Fe2	O7	93.00(17)	C4	C5	S1	120.9(4)
O12	Fe2	O8	175.81(19)	C6	C5	S1	117.8(5)
O12	Fe2	O13	88.64(17)	C6	C5	C4	121.3(5)
O10	S1	O12	111.3(3)	C5	C6	C2[2]	120.8(5)
O10	S1	C5	106.6(3)	O3	C7	C8	118.5(7)
O11	S1	O10	115.1(3)	O4	C7	O3	123.8(8)
O11	S1	O12	112.4(3)	O4	C7	C8	117.6(6)
O11	S1	C5	106.4(3)	C9	C8	C7	120.8(7)
O12	S1	C5	104.2(3)	C9	C8	C12[3]	119.1(7)
O13	S2	C11	105.4(3)	C12[3]	C8	C7	120.1(7)
O14	S2	O13	112.4(3)	C8	C9	C10	122.5(7)
O14	S2	C11	105.4(3)	C9	C10	C10[3]	117.4(8)
O15	S2	O13	111.8(3)	C9	C10	C11	122.6(6)
O15	S2	O14	114.3(3)	C10[3]	C10	C11	120.0(8)
O15	S2	C11	106.8(3)	C10	C11	S2	121.1(6)
C1	O1	Fe1	116.3(4)	C12	C11	S2	119.0(5)
C1	O2	Fe1[1]	136.2(5)	C12	C11	C10	119.9(6)
C7	O3	Fe1	124.6(5)	C11	C12	C8[3]	121.1(6)
C7	O4	Fe1[1]	129.2(5)	O5	C13	N1	120.4(8)

Table 5.7. Bond Angles for **1**

Atom	Atom	Atom	Angle/˚	Atom	Atom	Atom	Angle/˚
C13	O5	Fe1	127.6(5)	O6	C16	N2	125.3(6)
C16	O6	Fe2	121.4(4)	O7	C19	N3	126.0(8)
C19	O7	Fe2	125.1(6)	O9	C22	N4	123.4(7)
C25	O8	Fe2	123.3(7)	O8	C25	N5	127.2(11)
C22	O9	Fe2	127.2(5)				

[1]2-X,2-Y,1-Z; [2]1-X,2-Y,1-Z; [3]2-X,1-Y,1-Z

Table 5.8. Solvent masks information for **1**.

Number	X	Y	Z	Volume	Electron count	Content
1	0.500	0.500	0.000	270.6	67.4	1.5 DMF

5.7 Notes and References

Authorship and prior publication. This majority of the content in this chapter was reproduced from the following publication, with additional edits: *Eur. J. Inorg. Chem.* **2019**, *21*, 2613-2617. Portions of the work were completed by coauthors.

1. (a) Rowsell, J.L.C.; Yaghi, O.M., *Micropor. Mesopor. Mat.*, **2004**, 73, 3.; (b) Li, J.-R.; Kuppler, R.J.; Zhou, H.-C. *Chem. Soc. Rev.*, **2009**, 38, 1477. (c) Yuan, S.; Feng, L.; Wang, K.; Pang, J.; Bosch, M.; Lollar, C.; Sun, Y.; Qin, J.; Yang, X.; Zhang, P.; Wang, Q.; Zou, L.; Zhang, Y.; Zhang, L.; Fang, Y.; Li, J.; Zhou, H.-C. *Adv. Mater.*, **2018**, 30, 1704303. (d) Gonzalez, M.I.; Kapelewski, M.T.; Bloch, E.D; Milner, P.J.; Reed, D.A.; Hudson, M.R.; Mason, J.A.;Barin, G.; Brown, C.M.; Long, J.R. *J. Am. Chem. Soc.*, **2018**, 140, 3412. (e) Rojas, S.; Colinet, I.; Cunha, D.; Hidalgo, T.; Salles, F.; Serre, C.; Guillou, N.; Horcajada, P., *ACS Omega*, **2018**, 3, 2994.

2. (a) Gütlich, P.; Garcia, Y.; Woike, T. *Coord. Chem. Rev.*, **2001**, 219-221, 839. (b) Miyasaka, H. *Acc. Chem. Res.* **2013**, *2*, 248. (c) He, C.; Liu, D.; Lin, W. *Chem. Rev.*, **2015**, 115, 11079. (d) An, W.; Aulakh, D.; Zhang, X.; Verdegaal, W.; Dunbar, K.R.; Wriedt, M. *Chem. Mater.*, **2016**, 28, 7825. (e) Cadiau, A.; Adil, K.; Bhatt, P.M.; Belmabkhout, Y.; Eddaoudi, M. *Science*, **2016**, 353, 137. (f) Cui, Y.; Li, B.; He, H.; Zhou, W.; Chen, B.; Qian, G. *Acc. Chem. Res.*, **2016**, 49, 483. (g) Salunkhe, R.R.; Kaneti, Y.V.; Kim, J., Kim J.H.; Yamauchi, Y. *Acc. Chem. Res.*, **2016**, 49, 2796. (h) Sun, L.; Campbell, M.G.; Dinca, M. *Angew. Chem., Int. Ed.*, **2016**, 55, 3566. (i) Smith, J.A.; Singh-Wilmot, M.A.; Carter, K.P.; Cahill, C.L.; Lough A.J.; Knee, C.S. *New J. Chem.*, **2016**, 40, 7338. (j) DeGayner, J.A.; Wang, K.; Harris, T.D. *J. Am. Chem. Soc.*, **2018**, 140, 6550. (k) Johnson, B.A.; Bhunia, A.; Fei, H.; Cohen, S.M.; Ott, S. *J. Am. Chem. Soc.*, **2018**, 140, 2985. (l) Lapidus, S.H.; Graham, A.G.; Kareis, C.M.; Hawkins, C.G.; Stephens, P.W.; Miller, J.S. *J. Am. Chem. Soc.*, **2019**, 141, 911. (m) Jafri, S.F.; Koumousi, E.S.; Arrio, M.-A.; Juhin, A.; Mitcov, D.; Rouzières, M.; Dechambenoit, P.; Li, D.; Otero, E.; Wilhelm, F.; Rogalev, A.; Joly,

L.; Kappler, J.-P.; Cartier dit Moulin, C.; Mathonière, C.; Clérac, R.; Sainctavit, P. *J. Am. Chem. Soc.*, **2019**, 141, 3470.

3. (a) Perkins, C.W.; Clarkson R.B.; Martin, J.C. *J. Am. Chem. Soc.*, **1986**, 108, 3206. (b) Ribas, X.; Maspoch, D.; Wurst, K.; Veciana, J.; Rovira, C. *Inorg. Chem.*, **2006**, 45, 5383.

4. Shimizu, G.K.H.; Vaidhyanathan, R.; Taylor, J.M. *Chem. Soc. Rev.*, **2009**, 38, 1430.

5. (a) Li, F.-F.; Ma, J.-F.; Song, S.-Y.; Yang, J.; Jia, H.-Q.; Hu, N.-H. *Cryst. Growth Des.*, **2006**, 6, 209. (b) Liu, H.-Y.; Wu, H.; Ma, J.-F.; Song, S.-Y.; Yang, J.; Liu, Y.-Y.; Su, Z.-M *Inorg. Chem.*, **2007**, 46, 7299.

6. (a) Chen, C.-H.; Cai, J.; Liao, C.-Z.; Feng, X.-L.; Chen, X.-M.; Ng, S.W. *Inorg. Chem.*, **2002,** 41,4967. (b) Du, Z.-Y.; Xu, H.-B.; Mao, J.-G. *Inorg. Chem.*, **2006,** 45, 6424. (c) Fernando, I. R.; Jianrattanasawat, S.; Daskalakis, N.; Demadis, K.D.; Mezei, G. *CrystEngComm*, **2012,** 14, 908. (e) Cao, H.-Y.; Liu, Q.-Y.; Li, L.-Q .; Wang, Y.-L.; Chen, L.-L.; Yao, Y. *Z. Anorg. Allg. Chem*, **2014,** 640, 1420. (f) Ramaswamy, P.; Matsuda, R.; Kosaka, W.; Akiyama, G.; Jeon H.J.; Kitagawa, S. *Chem. Commun.*, **2014,** 50, 1144. (g) Shen, S.-S.; Bai, C.; Hu, H.-M.; Yuan, F.; Wang, X.; Xue, G. *Z. Anorg. Allg. Chem.*, **2015,** 641, 1772. (h) Zhao, S.-N.; Song, X.- Z.; Zhu, M.; Meng, X.; Wu, L.-L.; Song, S.-Y.; Wang, C.; Zhang, H.-J *Dalton Trans.*, **2015,** 44, 948. (i) Sheng, S.-N.; Han, Y.; Wang, B.; Zhao, C.; Yang, F.; Zhao, M.-J.; Xie, Y.-B.; Li, J.-R. *J. Solid State Chem.*, **2016,** 233, 143. (j) Wang, G.-B.; Leus, K.; Hendrickx, K.; Wieme, J.; Depauw, H.; Liu, Y.-Y.; Van Speybroeck, V.; Van Der Voort, P. *Dalton Trans.*, **2017,** 46, 14356. (k) Nguyen, M.V.; Lo, T.H.N.; Luu, L.C.; Nguyen, H.T.T.; Tu, T.N. *J. Mater. Chem. A*, **2018**, 6, 1816.

7. (a) Papadaki, I.; Malliakas, C.D.; Bakas, T.; Trikalitis, P.N. *Inorg. Chem.*, **2009**, 48,9968. (b) Liu, Q.-Y.; Wang, W.-F.; Wang, Y.-L.; Shan, Z.-M.; Wang, M.-S.; Tang, J. *Inorg. Chem.*, **2012,** 51, 2381.

8. Kang, S.; Zhang, C.; Xiao, G.; Yan, D.; Sun, G. *J. Membrane Sci.*, **2009**, 334,91.

9. (a) Yoon, S.; Lippard, S.J. *Inorg. Chem.*, **2003**, 42, 8606. (b) Friedle, S.; Kodanko, J.J.; Fornace K.L.; Lippard, S.J. *J. Mol. Struct.*, **2008**, 890, 317. (c) Kongpatpanich, K.; Horike, S.; Sugimoto, M.; Kitao, S,; Seto, M.; Kitagawa, S. *ChemComm*, **2014**, 50, 2292. (d) Fateeva, A.; Clarisse, J.; Pilet, G.; Grenèche, J.-M.; Nouar, F.; Abeykoon, B.K.; Guegan, F.; Goutaudier, C.; Luneau, D.; Warren, J.E.; Rosseinsky, M.J.; Devic, T. *Cryst. Growth Des.*, **2015**, 15, 1819.

10. (a) Wang, H.-Y.; Ge, J.-Y.; Hua, C.; Jiao, C.-Q.; Wu, Y.; Leong, C.F.; D'Alessandro, D.M.; Liu, T.; Zuo, J.-L. *Angew. Chem. Int. Ed.*, **2017**, 56, 5465. (b) Phan, H.; Benjamin, S.M.; Steven, E.; Brooks, J.S.; Shatruk, M. *Angew. Chem. Int. Ed.*, 2017, **2015**, 127, 837. (c) Fei, B.; Chen, X.Q.; Cai, Y.D.; Fang, J.-K.; Tong, M.L.; Tucek, J.; Bao, X. *Inorg. Chem. Front.*, **2018**, 5,1671. (d) Delle Chiaie, K.R.; Biernesser, A.B.; Ortuño, M.A.; Dereli, B.; Iovan, D.A.; Wilding, M.J.T.; Li, B.; Cramer, C.J.; Byers, J.A. *Dalton Trans.*, **2017**, 46,12971.

11. (a) Zhang, X.-M.; Li, P.; Gao, W.; Liu, J.-P.; Gao, E.-Q. *Dalton Trans.*, **2015**, 44, 13581. (b) Wang, Y.-Q.; Tan, Q.-H.; Guo, X.-Y.; Liu, H.-T.; Liu, Z.-L.; Gao, E.-Q. *RSC Adv.*, **2016**, 6, 72326. (c) Kawamura, A.; Greenwood, A.R.; Filatov, A.S.; Gallagher, A.T.; Galli, G.; Anderson, J.S. *Inorg. Chem.*, **2017**, 56, 3349. (d) Kawamura, A.; Filatov, A.S.; Jeon, I.-R.; Anderson, J.S. *Inorg. Chem.*, **2019**, 58, 3764.

12. Roques, N.; Mugnaini, V.; Veciana, J. in Magentic and Porous Molecule-Based Materials in Functional Metal-Organic Frameworks: Gas Storage, Separation and Catalysis (Ed.: M Schroder), Springer, **2010**, 222.

13. (a) Gómez-Coca, S.; Aravena, D.; Morales, R.; Ruiz, E. *Coord. Chem. Rev.*, **2015**, 289-290, 379. (b) Bar, A.K.; Pichon, C.; Sutter, J.-P. *Coord. Chem. Rev.*, **2016**, 308, 346.

14. (a) Mao, B. Zhang, F. Yu, X. Chen, G.-l. Zhuang, Z. Wang, Z. Ouyang, T. Zhang and B. Li, *Dalton Trans.*, **2017**, 46, 4786. (b) Ruiz, J.; Mota, A.J.; Rodríguez-Diéguez, A.; Oyarzabal, I.; Seco, J.M.; Colacio, E. *Dalton Trans.*, **2012**, 41, 14265.

CHAPTER 6: MOLECULAR INORGANIC TO ORGANIC SPIN TRANSFER IN A TETRATHIAFULVALENE-2,3,6,7-TETRATHIOLATE BRIDGED DIIRON COMPLEX

6.1 Abstract

The spatial and temporal control of unpaired spin underlies cutting edge technologies such as quantum information processing and spintronics. In coordination chemistry, complexes that undergo spin transitions, frequently referred to as spin-crossovers, are well known, particularly for ions such as Fe(II). Examples of modulation of diradical character on organic molecules are also known but are comparatively rare. There is a particular lack of examples of transitions with cooperativity between inorganic and organic unpaired spin. Here we demonstrate that a diiron complex bridged by the highly conjugated linker TTFtt (tetrathiafulvalene-2,3,6,7-tetrathiolate) undergoes a temperature dependent conversion of two $S = 2$ Fe centers to $S = 0$ ground states coupled to a significant decrease in the singlet-triplet gap on the TTFtt core. This unusual phenomenon demonstrates that inorganic spin transitions can modulate organic diradical character.

6.2 Introduction

In the final chapter, a rare example of a magnetic complex with spin transitions centered on both a metal and an organic bridging ligand is discussed. In this scope, many of the concepts and experimental techniques from the subsequent chapters are utilized, however the unique properties and experimental techniques established for organic diradicals will also be highlighted.

Spin-transitions (i.e. from high-spin to low-spin, ST) in paramagnetic metal centers may find practical use in high-density memory storage, molecular electronics, or sensing.[1] Similarly, fully organic open-shell di- or polyradicals are touted for potential applications in cutting-edge fields like spintronics and spin filters, as well as memory and sensing devices.[2] Unfortunately,

organic diradicals are typically highly reactive and compounds stable enough to be isolable or practically functional are exceedingly rare.[3] More generally, complexes which have multiple, externally controllable, orthogonal functionalities have evident practical utility in devices. Each of these individual fields are areas of robust continuing interest in the research community, yet the combination or intersection of these properties is an underexplored and poorly understood space.

In the previous chapter and in preceding work by coworkers Dr. Noah Horwitz and Jiaze Xie, sulfur-based ligands in conjunction with first-row transition metals were utilized to investigate and control interesting electronic and structural properties.[4] We have particularly been interested in tetrathiafulvalene-2,3,6,7-tetrathiolate (TTFtt), as there is well established precedent for mildly accessible redox couples in both the core TTF and dithiolene components.[5] Despite this, the synthetic challenges associated with sulfur ligation to metals has led to only a single report of any TTF based ligand coordinated to Fe via the dithiolene sulfurs.[6] Examples of other metallated TTF-type ligands or fully organic TTF-type molecules, however, show distinct promise for a variety of applications.[7]

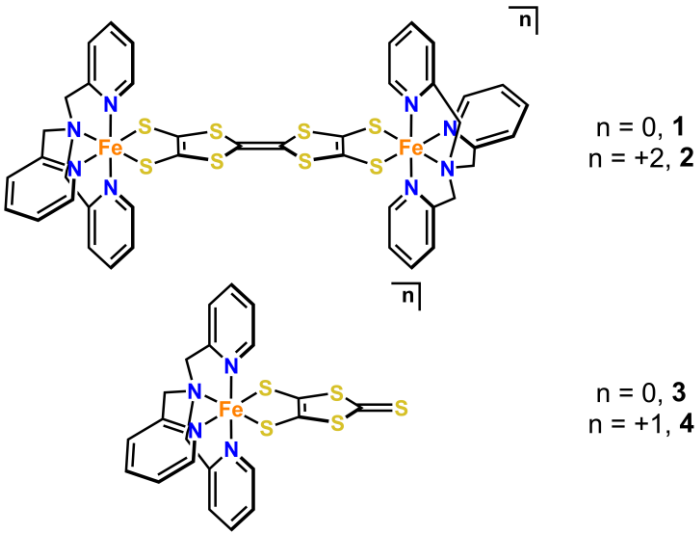

Figure 6.1. Bimetallic complexes of TTFtt as well as monometallic dmit complexes that serve as half-unit models have been synthesized.

Herein, we report the novel complexes $(FeTPA)_2TTFtt$ (**1**) (TPA = tris(2- pyridylmethyl) amine) and $[(FeTPA)_2TTFtt][BAr^F{}_4]_2$ (**2**) ($BAr^F{}_4$ = tetrakis[3,5-bis(trifluoromethyl) phenyl] borate) as well as their monomeric analogues Fe(TPA)(dmit) (**3**) and $[Fe(TPA)(dmit)][BAr^F{}_4]$ (**4**) (where dmit = 1,3Dithiole-2-thione-4,5-dithiolate, Figure 6.1). Complex **2** is the first structurally characterized example of the TTFtt ligand coordinated to an Fe ion. Furthermore, **2** exhibits spin-transition induced modulation of organic (i.e. TTFtt-based) diradical character and is an unusual example showing coupling of these two phenomena.

6.3 Results and Discussion

6.3.1. Synthesis, Structures and Packing The proligand was synthesized by Jiaze Xie. Complex **1** was synthesized in good yield via deprotection of the proligand. Complex **1** is insoluble in all solvents investigated which precluded detailed characterization. Regardless, **1** is analytically pure for the formula $(FeTPA)_2TTFtt$ and behaves as a suitable synthon for subsequent chemistry.

Complex **1** can be doubly oxidized with ferrocenium (Fc^+, as $[Fc][BAr^F{}_4]$) to form **2** which is more soluble, enabling common solution characterization including ^1H NMR and cyclic voltammetry (Figure 6.21 and Figure 6.22). Given the mild oxidation potential of both the $TTFtt^{4-}$ ligand and Fe(II) centers, the oxidation from **1** to **2** could be ligand-centered ($TTFtt^{4-} \rightarrow TTFtt^{2-}$), metal-centered (2 Fe(II)→2 Fe(III)), or some intermediate case. As described below, however, the spectroscopic data on **2** supports a $TTFtt^{2-}$ structure arising from ligand-centered oxidation.

The solubility of **2** also enabled us to obtain its molecular structure with SXRD. Complex **2** grew in two different polymorphs which were analyzed at room temperature (**2-RT**; Figure 6.2)

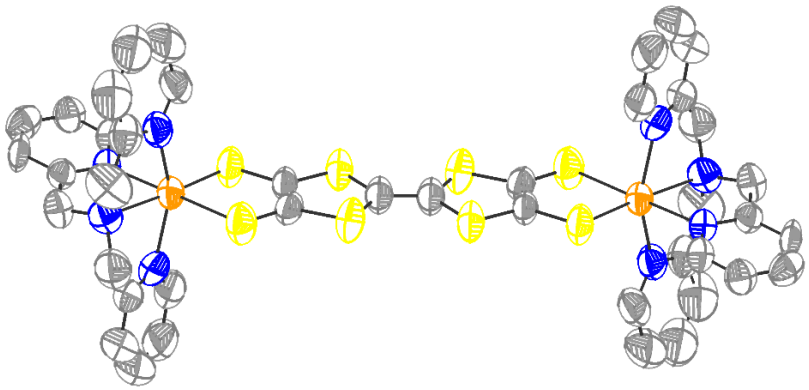

Figure 6.2. Molecular structure of 2 at room temperature. Atom colors: grey – carbon, yellow – sulfur, blue – nitrogen, orange – iron. H-atoms and BAr^{F}_{4} counter anion omitted for clarity. Ellipsoids are shown at 50% probability.

and at 100 K (**2-LT**; Figure 6.3). In both structures, TTFtt is bridged between two Fe centers, each capped with TPA and with two outer-sphere BAr^{F}_{4} counter anions. The most striking structural feature between these two datasets is that **2-RT** has markedly longer Fe bond lengths than **2-LT**. The Fe–N_{pyr} and Fe–N_{amine} bond lengths in **2-LT** are in the range of 1.973(6)–1.979(7) and 2.016(7) Å, respectively. These values are consistent with previously reported Fe–N bonds in low-spin (LS) complexes with a Fe-TPA moiety.[8] In **2-RT**, these bonds are 0.18–0.19 and 0.25(1) Å longer than their counterparts at 100 K, respectively, and are consistent with Fe–N bonds in high-spin (HS) Fe-TPA complexes. The significantly shorter Fe bonds at lower temperature are a strong

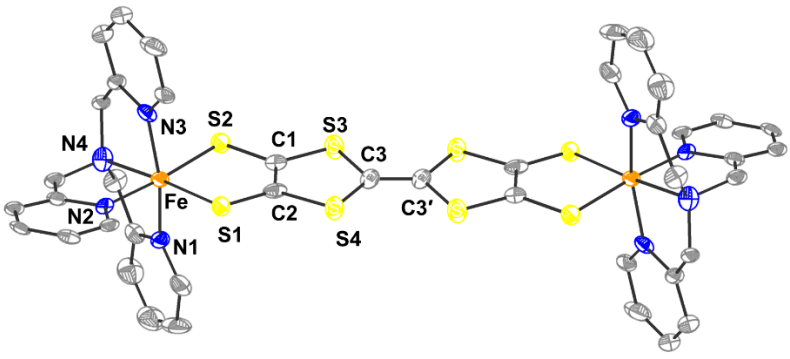

Å	**2** at RT	**2** at 100 K	Δ (from RT)
Fe–S1	2.368(3)	2.238(3)	-0.129(4)
Fe–S2	2.478(3)	2.286(3)	-0.192(4)
Fe–N1	2.16(1)	1.973(6)	-0.19(1)
Fe–N2	2.168(8)	1.979(7)	-0.19(1)
Fe–N3	2.138(8)	1.957(6)	-0.181(9)
Fe–N4	2.260(8)	2.016(7)	-0.25(1)
C3–C3′	1.41(1)	1.37(1)	-0.04(1)
C3–S3	1.70(1)	1.758(9)	+0.06(1)
C3–S4	1.69(1)	1.72(1)	+0.03(1)

Figure 6.3. Molecular structure for **2** collected at 100 K by SXRD. H atoms, counterions, and solvent molecules are omitted for clarity and ellipsoids are shown at 50%. Selected bond length parameters for **2** at room temperature (RT) and 100 K.

indicator that the Fe centers in **2** exhibit a temperature dependent ST between HS and LS, a phenomenon that has been observed in many similar compounds.[8a,9] In addition to the marked geometric changes at Fe, the central C3–C4 bond in the TTF core of **2** shows a small—but significant—difference between temperatures suggesting some electronic structure change on this organic fragment as well. This bond is known to be diagnostic for the oxidation state of the TTF unit, where a 0.03–0.09 Å increase in bond length is correlated to the change from a singly (1.35–1.40 Å) to doubly (1.41–1.44 Å) oxidized TTF unit due to the depopulation of the central C–C π bonding orbital.[4a,10] Theory and experiment, however, suggest that this shortening arises from increased diradical character in the TTF core upon cooling from **2-RT** to **2-LT** (vida infra). There is also a marked lengthening of the central C–S bonds (C3–S3 and C–S4) which computations suggest arises from the simultaneous depopulation/population of bonding/antibonding C–S orbitals, respectively.

The complicated temperature dependent electronic structure of **2** prompted us to synthesize mononuclear analogues as comparative controls. Complexes **3** and **4** were synthesized as half-unit analogs to **1** and **2**, respectively, using the related dmit ligand in place of TTFtt. The neutral compound **3** was synthesized using a similar procedure as has been reported and the oxidized

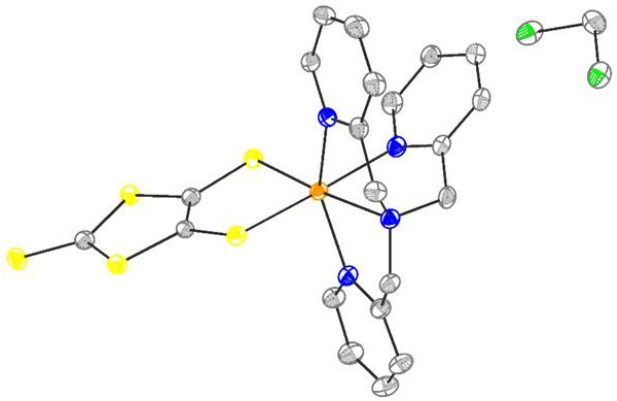

Figure 6.4. Molecular structure of **3** at 100 K. Atom colors: grey – carbon, yellow – sulfur, blue – nitrogen, orange – iron. H-atoms omitted for clarity. Ellipsoids are shown at 50% probability.

congener **4** was generated with [Fc][BAr^F_4].[11] In the structure of **3** (Figure 6.4)—solved by Andrew McNeece—the Fe center has Fe–N bonds in the range commonly observed for HS Fe(II). While of poor quality, the SXRD data for **4** (Figure 6.23) confirms its assignment and short Fe bond lengths imply a LS Fe center.

6.3.2. Variable Temperature UV-Vis-NIR The UV-Vis-NIR spectrum of **2** in 2-chlorobutane was collected between 20 and −100 °C (Figure 6.5a). As expected for a species with a diamagnetic $TTFtt^{2-}$ core, **2** shows an intense and comparatively sharp feature at 1074 nm in the NIR region.

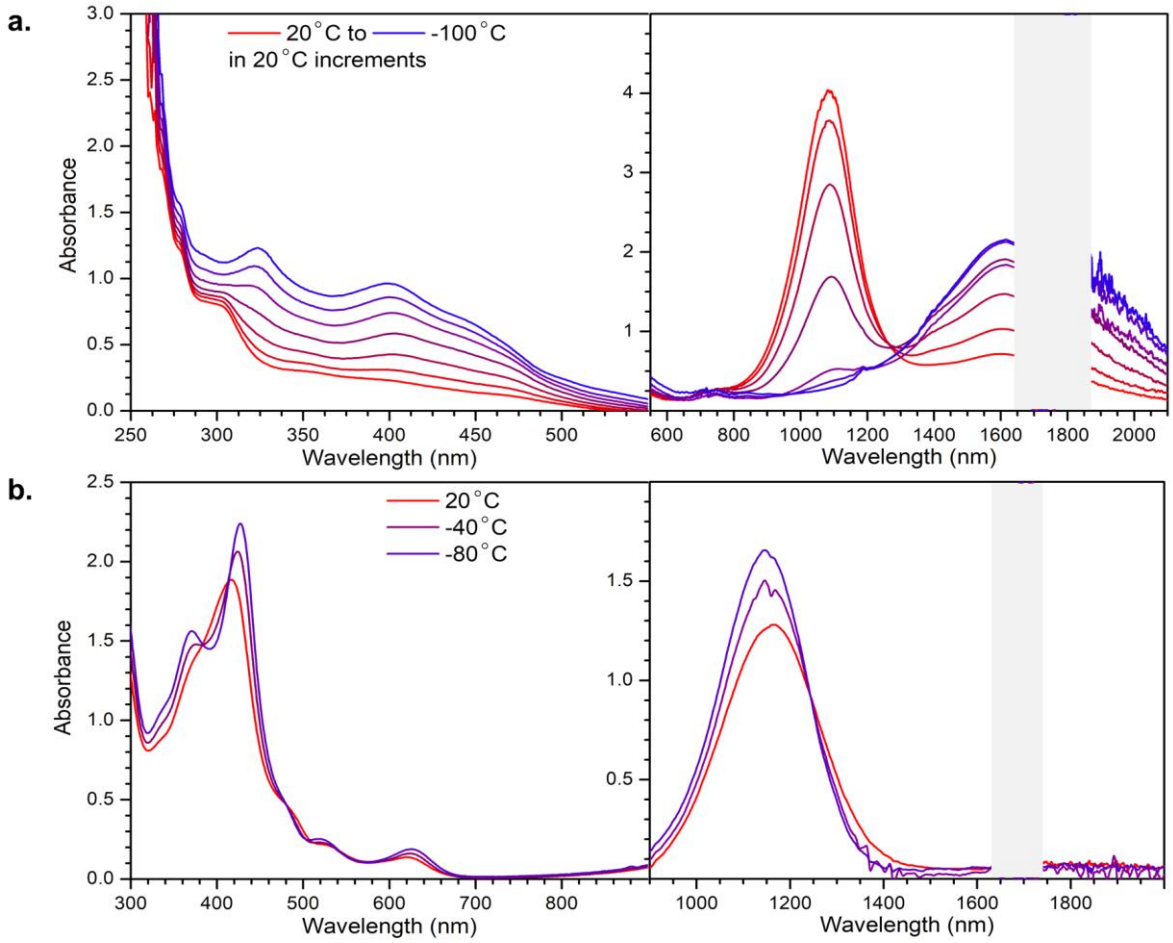

Figure 6.5. (a) Variable temperature electronic spectra of **2** in the UV-Vis (left) and Vis-NIR (right) regions collected in 2-chlorobutane at 50 μM. (b) Variable temperature electronic spectra of **4** in DCM in the UV-Vis (left, 100 μM) and NIR (right, 200 μM). The opaque boxes (right) cover the strong NIR absorbances due to solvent.

Upon cooling, the 1074 nm peak decreases dramatically in intensity, while a broad feature at 1615 nm and sharp features at 325 and 396 nm increase in intensity substantially. Notably, the VT spectroscopic behavior is fully reversible upon warming.

For species with reported singly and doubly oxidized TTFtt units, the radical $TTFtt^{\cdot 3-}$ core tends to have a lower energy NIR feature than the diamagnetic $TTFtt^{2-}$ core.[4a,12] Additionally, the new high energy features (i.e. 325 and 396 nm) of **2** at low temperature are similar to those reported for singly oxidized TTFtt complexes attributed to $\pi \rightarrow \pi^*$ transitions, and their appearance implies a change in the electronic structure of the TTFtt core upon cooling. Overall, the SXRD and UV-vis-NIR data on **2** indicate a significant change in the electronic structure of the TTFtt unit, potentially consistent with either a reduction of the TTFtt core or a change in the spin-state of this unit.

Kate Jesse performed time-dependent density functional theory (TD-DFT) computations, to further investigate the possibility of a spin-state change on TTFtt causing the observed changes in the electronic spectra. A diradical ($S_{total} = 1$, with spin density localized on TTFtt; Figure 6.6)

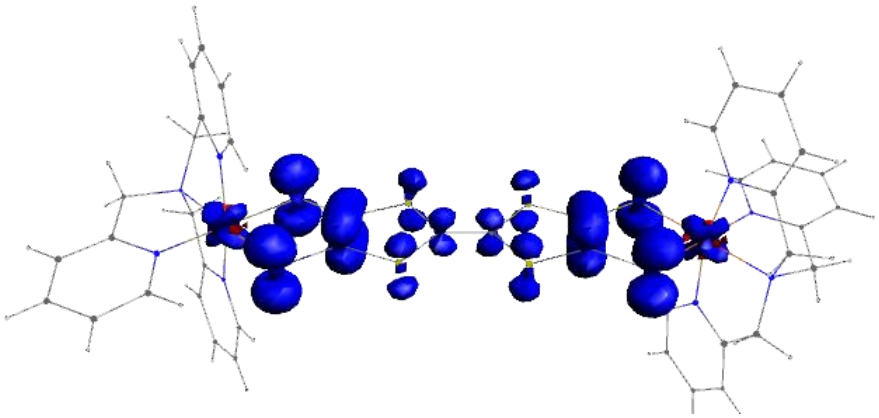

Figure 6.6. Spin density of **2** in open shell configuration. Calculated by TD-DFT for $S = 1$ from the molecular structure of **2** acquired by SXRD.

and closed shell (S = 0) forms of **2** were calculated using the LT structure acquired from SXRD. The NIR transitions were well predicted from TD-DFT as primarily intramolecular TTFtt based π transitions (Figure 6.7). Importantly, the differences in the diradical and closed-shell calculated spectra mirror the VT changes observed in **2** implying that the observed spectroscopic changes could arise from a spin-state change based on TTFtt (Figure 6.8).

The electronic spectrum of **3** in DCM was collected at room temperature and features two absorbances at 310 and 498 nm (Figure 6.24), assignable to dmit transitions.[13] In the visible region, **4** has a strong peak at 417 nm with a shoulder near 370 nm (Figure 6.5b). As this absorbance is between the typical range of a Fe(II)→TPA metal-to-ligand charge transfer[14] and the previously reported π→π* transition of the $dmit^{2-}$ ligand, it is not straightforward to assign on the room temperature spectrum alone (Figure 6.25). A broad band centered near 1050 nm is present in **4**,

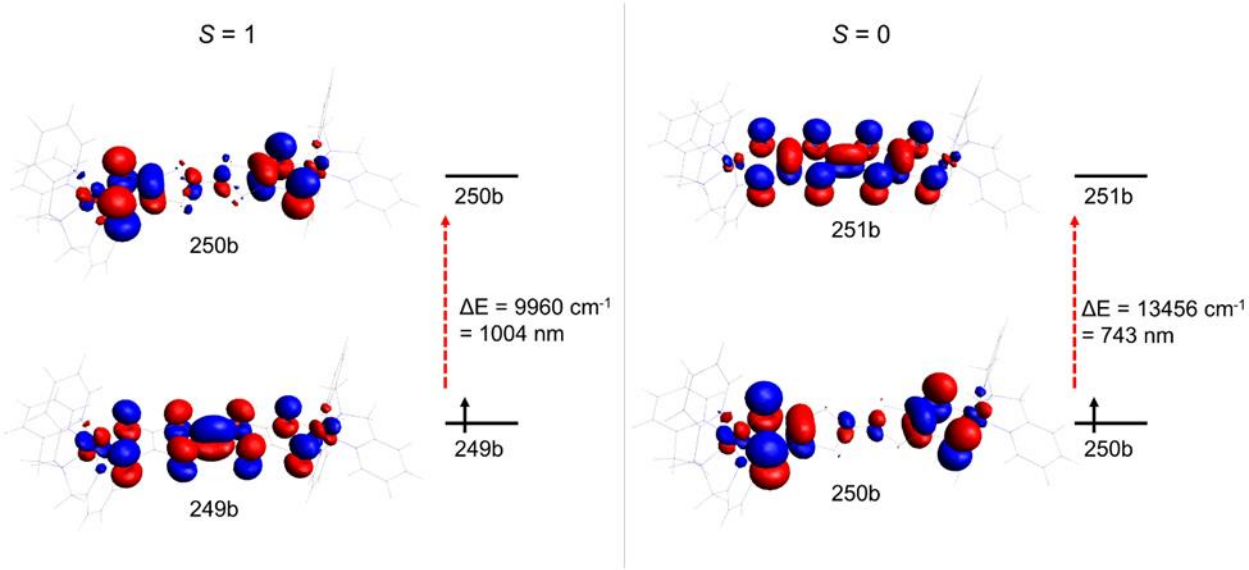

Figure 6.7. Primary molecular orbitals associated with the NIR transition of **2** calculated by TD-DFT. The transitions shown account for >80% of the feature intensity at the associated energy. The listed energies of the transitions are pre-calibration using the Ni standard complex. The calculations of the open shell (left) and closed shell (right) are shown.

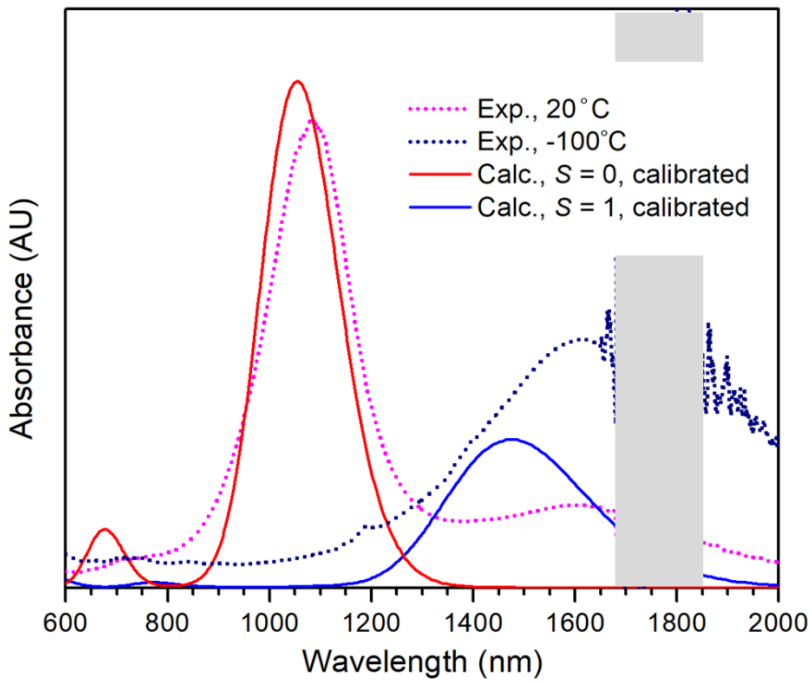

Figure 6.8. Predicted spectra of **2** by TD-DFT versus experimental data. Experimental electronic spectra of **2** collected in 2-chlorobutane at 50 μM at indicated temperatures, grey box at left covers the strong NIR absorptions from solvent. Calculated spectra have been calibrated as noted in the methods section.

and notably absent in **3.** A broad absorbance in this range has been observed to appear when oxidizing a $dmit^{2-}$ containing complex to the radical $dmit^{\cdot-}$ species.[15] Upon cooling to -80 °C, the high energy visible features increase in intensity, although to a lesser degree than was observed in **2**.

6.3.3. Mössbauer Spectroscopy The electronic spectra of **2** suggested either a thermally induced electron transfer or a change in the spin state of the TTF core. As such, ^{57}Fe Mössbauer spectroscopy was collected in order to determine whether Fe redox events occurred upon cooling. Collaborators Juan Valdez-Moreira and Kelsey Collins collected the data. At 250 K the spectrum of **2** shows a species comprising 46(5)% of the sample with an isomer shift (δ) of 0.880(9) mm/s and quadrupole splitting (ΔE_Q) of 3.22(2) mm/s consistent with HS Fe(II) (Figure 6.9).[8a,16] There is also a broad, poorly resolved signal—potentially composed of multiple sites— with an δ of

0.23(2) mm/s and ΔE_Q of 0.81(2) mm/s which we tentatively assign as LS Fe(II) sites. These parameters are outside of the typical ranges for both LS Fe(II) (e.g. δ: 0.36–0.52 mm/s; ΔE_q: 0.23–0.52 mm/s) and LS Fe(III) (δ: 0.20-0.28 mm/s; ΔE_q: 1.5–1.7 mm/s) reported for TPA ligated 6-coordinate complexes, but are similar to other reported LS Fe(II) complexes.[17]

Upon cooling, the proportion of LS Fe(II) in **2** increases while the signal for HS Fe(II) decreases as expected for the proposed ST. At 80 K (Figure 6.10), the LS species (blue) has an δ of 0.314(1) mm/s and ΔE_Q of 0.490(3) mm/s, and constitutes 74(1)% of the sample, while the HS species (green; δ: 0.9(1) mm/s, ΔE_Q: 2.87(2) mm/s) comprises 19(1)%. A small amount (<10%) of an unidentified Fe species is still present (purple; δ: 0.39(2) mm/s, ΔE_Q: 1.26(4) mm/s). This site may either correspond to some HS Fe(III) impurity or another LS Fe(II) species, potentially a

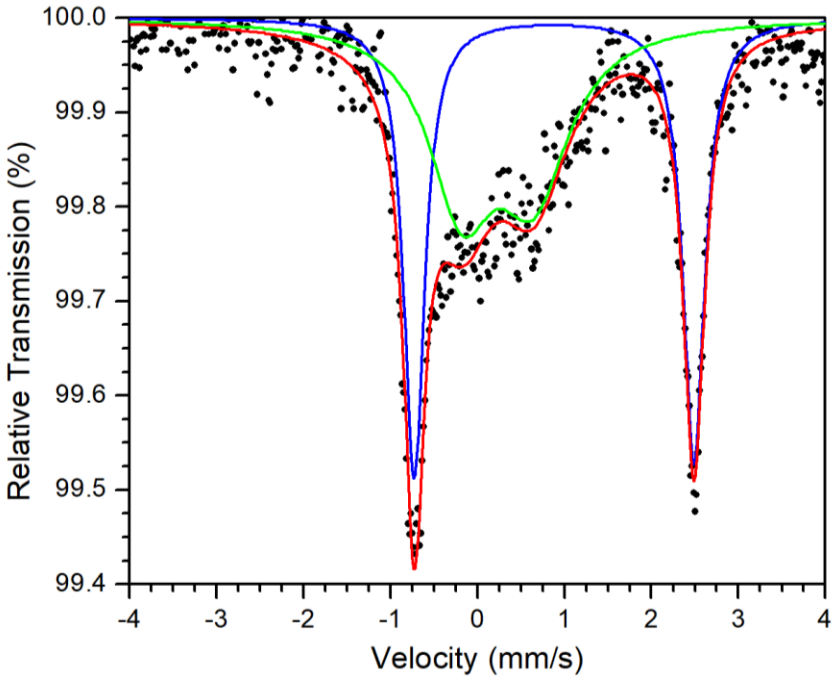

Figure 6.9. Mössbauer spectrum of **2** at 250 K. Site A (green): δ = 0.23(2) mm/s; ΔE_Q = 0.8(1) mm/s; 50(20)%. Site B (blue): δ = 0.880(9) mm/s; ΔE_Q – 3.22(2) mm/s; 46(5)%. Overall Fit (red): Rχ^2 – 0.556

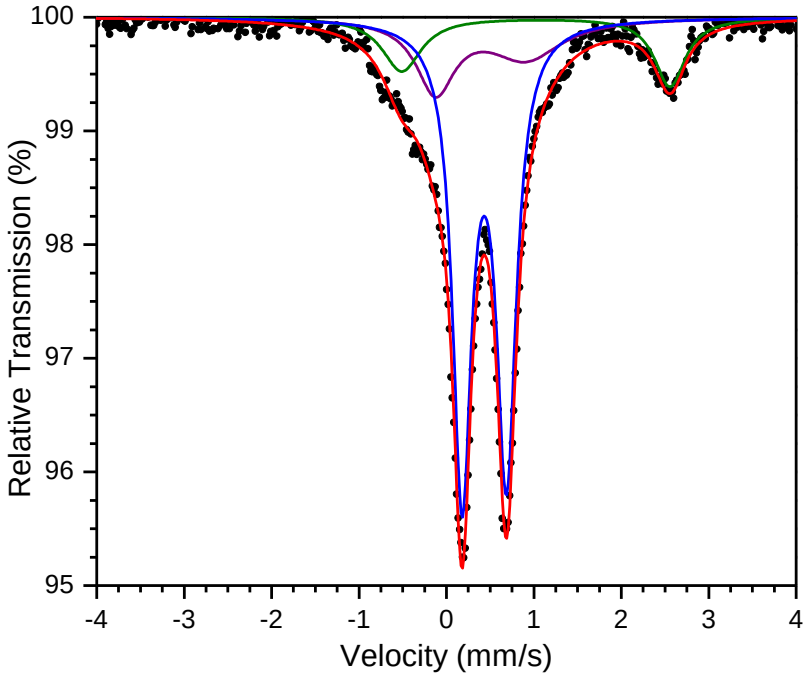

Figure 6.10. ^{57}Fe Mössbauer data for **2** collected at 80 K. The data is in black, the red line is the overall fit and the blue, green, and purple lines show the fits to the three Fe sites, as outlined in the text.

different polymorph of **2**. EPR features indicative of HS Fe(III) are absent in **2** (vide infra) leading us to hypothesize that this small signal does arise from another polymorph of **2**. Spectra of frozen solutions of **2** in PEG-2000 were also collected and are better fit to two sites (Figure 6.26 and Figure 6.27).

We will also note that the solid-state ^{57}Fe Mössbauer spectra of **2** are batch dependent, likely due to different polymorphs and packing (Figure 6.28). If VT spectroscopic changes in **2** represented a reduction of TTFtt (i.e. from $TTFtt^{2-}$ to $TTFtt^{\cdot 3-}$) a concomitant oxidation should be occurring—presumably Fe based. In this case one would either expect: (i) two fully localized, unequal Fe centers (i.e. Fe^{II} and Fe^{III}) or (ii) two mixed-valent $Fe^{II/III}$ centers. The low-temperature (LT) Mössbauer data only has a single new Fe feature eliminating possibility (i). The absence of any additional IVTC band in the LT spectra of **2**, alternatively eliminates possibility (ii). This

suggests that the process observed in the VT electronic spectra of **2** is not an electron transfer from Fe(II) to $TTFtt^{2-}$.

Complex **3** has a straightforward Mössbauer spectrum at both 250 K and 80 K, which features a single signal characteristic of a HS Fe(II) (Figure 6.29 and Figure 6.30). Complex 4 has a single signal with a δ of 0.282 to 0.338 mm/s and ΔE_q of 1.32 to 1.40 mm/s between 250 K and 80 K, respectively (Figure 6.11 and Figure 6.12). These data indicate that **4** is best thought of as a LS Fe(II) center bound to a $dmit^{\cdot-}$ radical, and corroborate similar LS Fe(II) features in **2**.

The neutral compound **1** exhibits two Fe signals over the temperature range from 250 K to 80 K (Figure 6.31–Figure 6.34). Both signals are characteristic of TPA ligated 6-coordinate HS Fe(II) with δ = 0.968(2) mm/s and 1.084(2) mm/s and Δ_{Eq} = 3.588(5) mm/s and 2.773(1) mm/s at

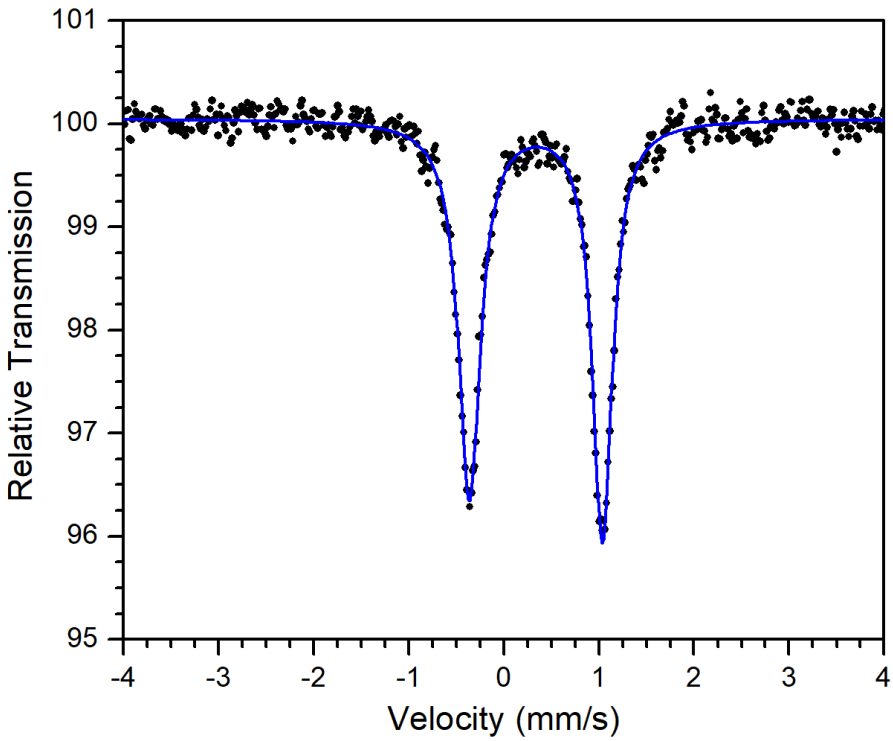

Figure 6.11. Mössbauer spectrum of **4** at 80 K. Parameters: δ = 0.338(5) mm/s; ΔE_Q = 1.398(5) mm/s. Fit (blue): $R\chi^2$ = 0.508.

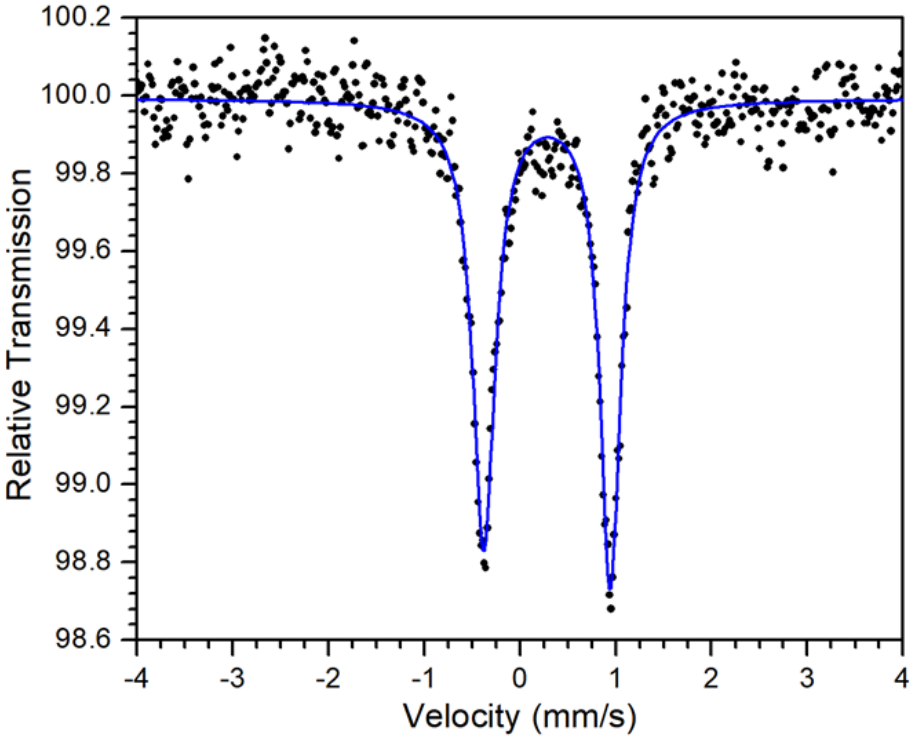

Figure 6.12. Mössbauer spectrum of **4** at 250 K Parameters: δ = 0.282(5) mm/s; ΔE_Q = 1.32(1) mm/s. Fit (blue): Rχ2 = 0.619.

80 K. The percent composition of these two signals varies batch-to-batch, and therefore likely represents different packing morphologies of **1** leading to subtle differences at the Fe sites.

6.3.4. Magnetic Data Variable temperature magnetic susceptibility measurements were undertaken on **1**–**4**. The magnetic properties of **1** exhibit typical behavior for two largely magnetically isolated HS Fe(II) (S = 2) centers (Figure 6.13). Upon oxidation to dicationic **2**, the magnetic properties differ drastically (Figure 6.14). The room temperature susceptibility (χT_{RT}) is near the spin-only value of χT_{SO} = 6 cm^{3}K/mol, implying minimal interaction between two HS Fe(II) centers. Upon cooling, however, χT decreases quickly before resuming a much more subtle decline below 150 K. This behavior is completely reversible upon warming (Figure 6.35). These data indicate two primary regions: a high-temperature (HT) region with high χT and a LT region

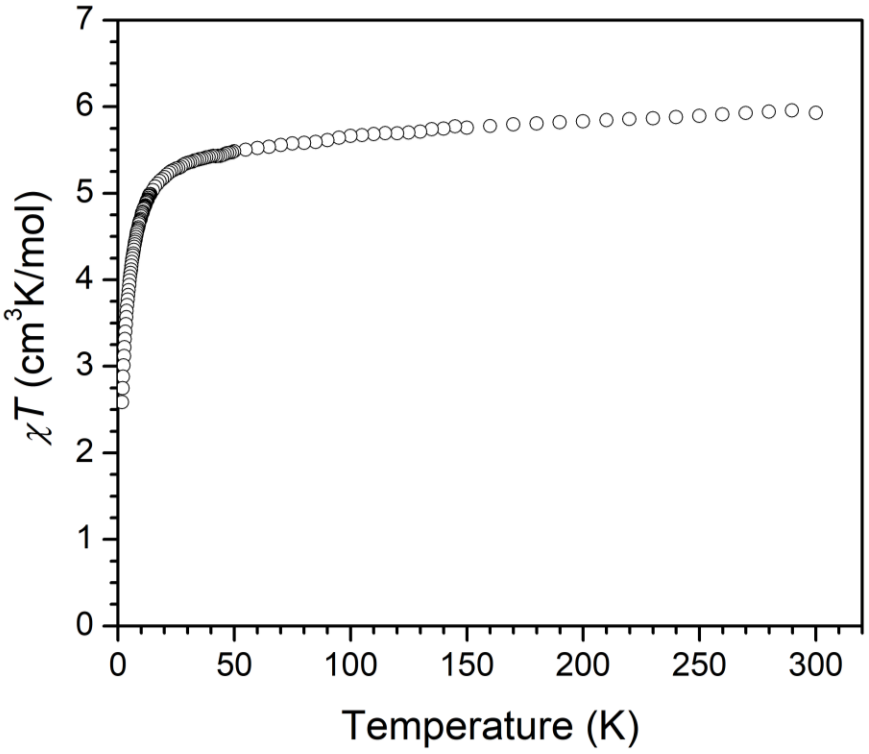

Figure 6.13. Temperature dependent χT of **1**. Collected under an applied field of 0.1 T.

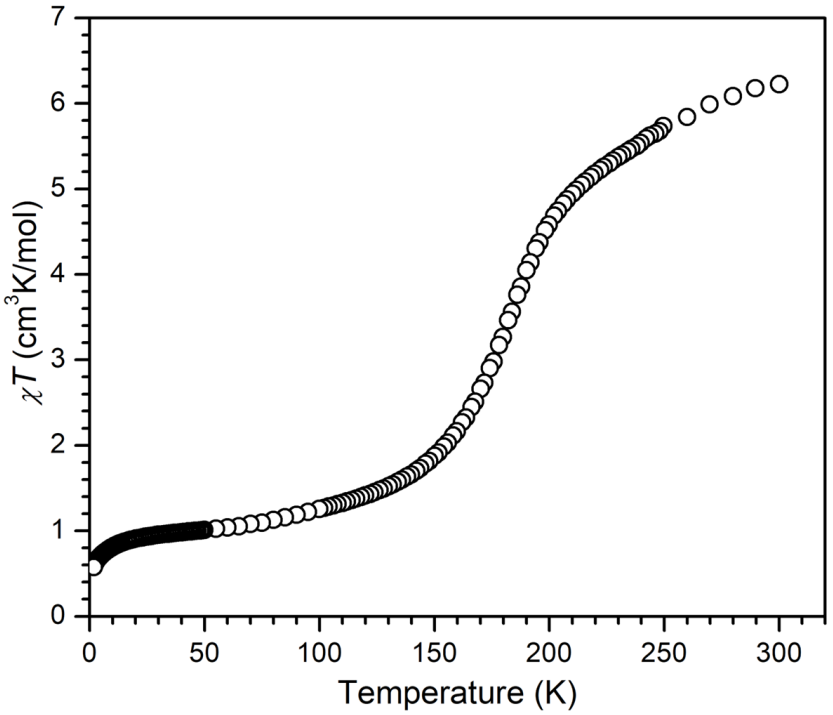

Figure 6.14. Temperature dependent magnetic susceptibility measurements for **2** collected under an applied field of 0.1 T.

with low χT, separated by a ST. From the molecular structures collected well into the HT and LT regions, the Fe centers show clear indications of undergoing ST from HS to LS. This is consistent with the observed low χT in the LT region. However, if the only ST occurring was a change from HS Fe(II) to LS Fe(II), then a low-temperature $\chi T = 0$ would be expected.

One possible explanation is that **2** undergoes incomplete spin crossover as has been observed previously in related systems.[9b,18] Indeed, the magnetic behavior of **2** shows high sensitivity to batch effects, which is a very commonly observed phenomenon in ST materials.[19] The degree of crystallinity, in particular, effects the abruptness of the transition in the χT and overall completeness of the ST between samples of **2** which are pure and solvent-free by elemental analysis and ^{1}H NMR and of the same bulk morphology as seen by X-ray powder diffraction (Figure 6.36 and Figure 6.37). The correlation between high crystallinity and more abrupt

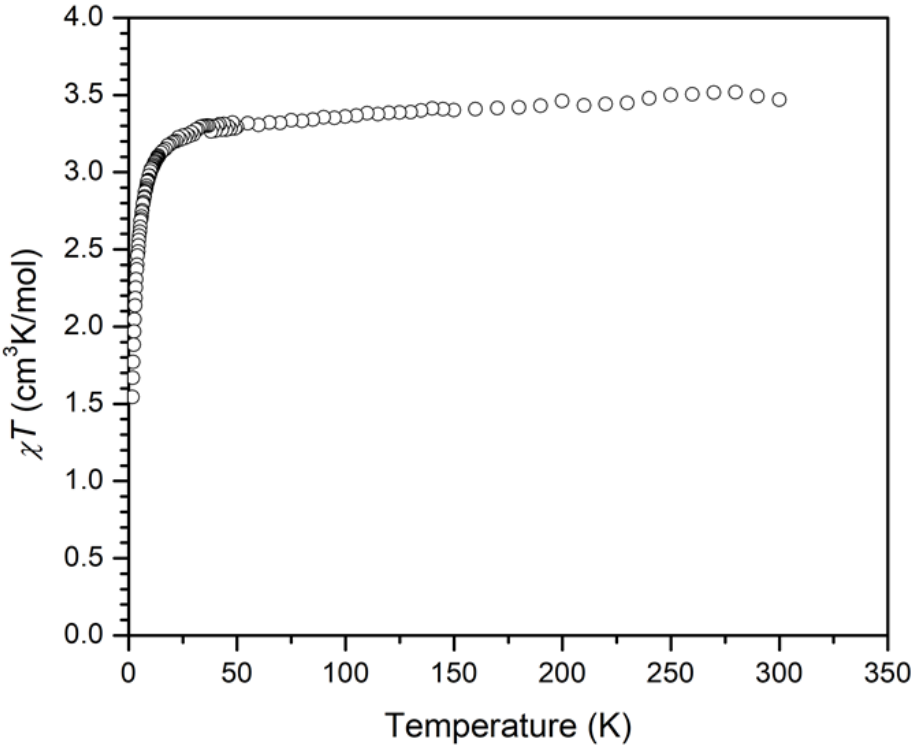

Figure 6.15. Temperature dependent χT of **3**. Collected under an applied field of 0.1 T.

transitions is reasonable given that more crystalline samples should reasonably have higher cooperativity due to packing. Regardless, samples collected in a frozen solution of PEG-2000 show consistent batch-to-batch behavior (Figure 6.38), indicating that the behavior of **2** in the absence of packing effects is consistent across batches. Additionally, the portion of high-spin Fe(II) determined from Mössbauer data of **2** in a frozen solution of PEG-2000 at 80 K is too small to account for the observed χT, implying that the low temperature magnetic behavior of **2** is not arising solely from incomplete spin-crossover.

The magnetic moment of **2** measured by Evan's method at room temperature in DCM is 6.38(7) μ_B (i.e. 5.1(1) cm^3K/mol), which is consistent with the frozen solution measurements in PEG-2000 at this temperature. The lower moment in solution at room temperature is consistent with the general behavior of ST materials wherein solution state transitions are more gradual than

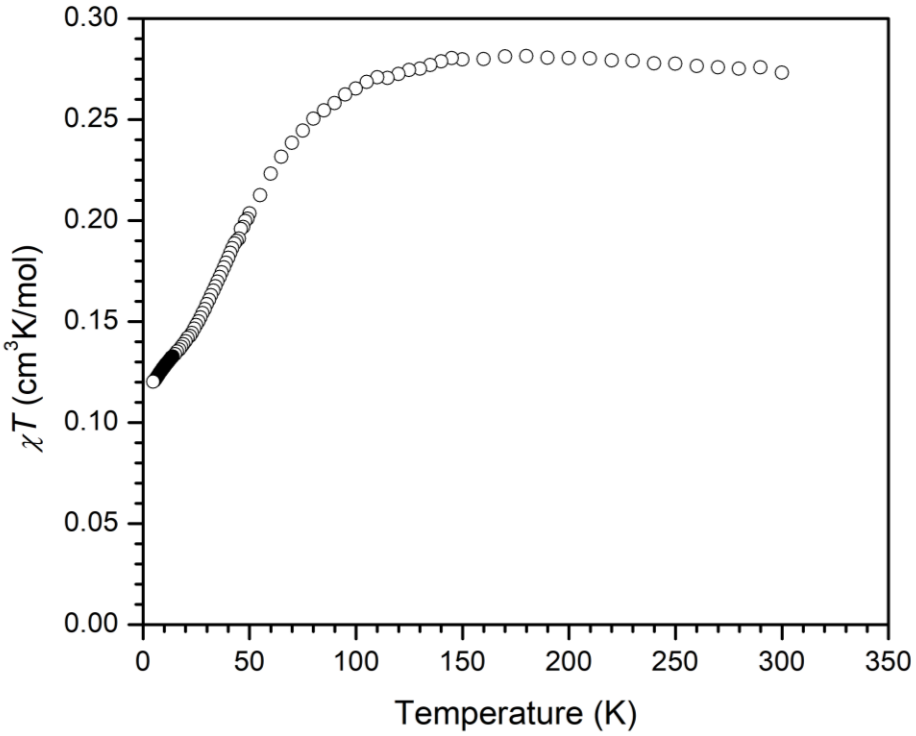

Figure 6.16. Temperature dependent χT of **4**. Collected under an applied field of 0.1 T

in the solid state, due to cooperativity. That is, the ST is likely incomplete at room temperature in solution.

The neutral compound **3** exhibits magnetic behavior as expected for a HS Fe(II) (S = 2) center (Figure 6.15) and cooling to 1.8 K does not yield any notable features which would contradict a simple assignment of a HS Fe(II) and a diamagnetic $dmit^{2-}$ ligand. Monocationic **4** has a χT near the expected value for a S = ½ species (χT_{SO} = 0.375 cm^3K/mol; Figure 6.16). The RT moment in solution was also measured by Evan's method as 2.1(1) μ_B (~ 0.5 cm^3K/mol) and supports the assignment of the species as S = ½ overall.

6.3.5. EPR Spectroscopy The EPR spectrum of **2** was collected at 15 K in DCM by Dr. Ethan Hill (Figure 6.17). The main feature is an intense, largely isotropic signal centered near g = 2,

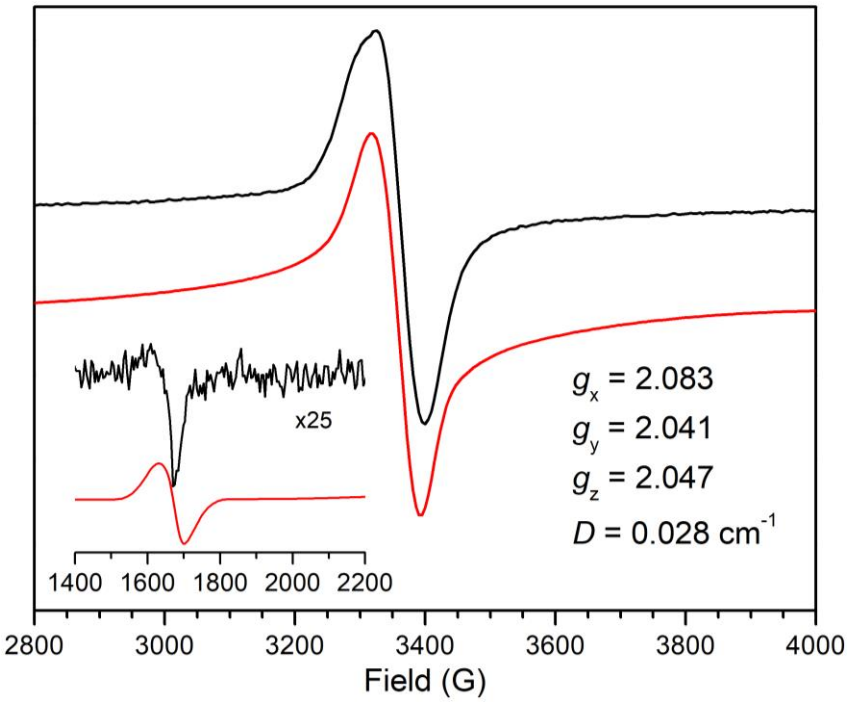

Figure 6.17. X-band EPR spectrum of **2** at 15 K in DCM at 5 mM with a power of 1.99 mW and frequency of 9.633 GHz. The inset shows the half-field signal centered around 1680 G increased in intensity by a factor of 25. Red lines indicate simulations with the parameters shown. Experimental data is shown in black.

consistent with an $|\Delta m_s| = 1$ transition of an organic $S = ½$ or $S = 1$ species. Importantly, a much lower intensity feature around $g = 4$ is characteristic of the $|\Delta m_s| = 2$ feature found at half-field diagnostic of organic diradical species.[2b,3] Using the relative intensity of the $|\Delta m_s| = 2$ and 1 signals, the distance between the organic radicals can be estimated.[3a] In **2** this value is around 3.3–4.6 Å which is similar to the centroid-to-centroid distance between the two 5-membered rings in the TTF core (~4.1 Å). The observed signals for **2** are distinct from possible impurities,[19a] are reproducible over several samples (Figure 6.39 and Figure 6.40), and were reasonably well simulated as an $S = 1$ species by Dr. Hill (Figure 6.17, red line).

Overall, these data strongly suggest that the LS form of **2** is a diradical. At 15 K, EPR of **4** acquired in a frozen solution of DCM shows a strong, fairly isotropic signal near $g = 2$ (Figure 6.18) consistent with a $S = ½$ species of dominantly organic character. There are no other features

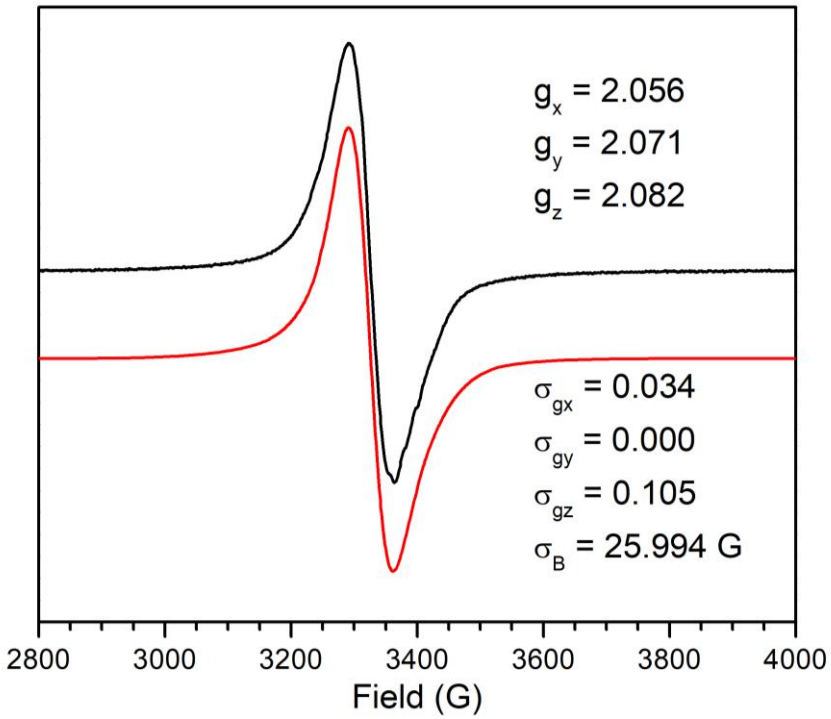

Figure 6.18. EPR spectrum of **4**. Collected at 15 K in DCM at 5 mM with a power of 1.998 mW and frequency of 9.387 GHz. Red lines indicate simulations with the parameters shown. Experimental data is shown in black.

as might be expected for an $S = ½$ Fe(III) center, however the broadness of the signal and deviation in g-value from that for a pure organic radical ($g = 2.0023$) suggest that this species has some Fe character.

6.3.6. Computational Results Given the complex nature of the electronic structure of **2**, we turned towards advanced theoretical techniques to support our assignment of a change in singlet-triplet gap and diradical character. All calculations in this section were performed by Nik Boyn and Professor David Mazziotti. Calculations were performed on **2-LT** using experimental geometries obtained via SXRD and the B3LYP functional with a 6-311G* basis set as implemented in g16/a.01, yielding a triplet ground state with a singlet-triplet gap of $\Delta E(T- S) = -409\ cm^{-1}$. The obtained spin density of the triplet state (**Error! Reference source not found.**a) shows the vast m ajority of the unpaired electron density to be localized on the linker with $\rho Fe = 0.135$ on each FeTPA fragment, and $\rho TTFtt = 1.730$. Given the fact that DFT is not expected to accurately describe the complex open-shell electronic structure of the singlet state we turned towards advanced theoretical techniques to validate the B3LYP results. Variational 2-electron reduced density matrix (V2RDM) calculations were run in Maple 2019 Quantum Chemistry Package (QCP) with a [18,20] active space and a 6-31G basis set, covering the entire spin manifold of singlet, triplet, quintet, septet, and nonet states. The calculations confirm the ground state of **2-LT** to be a singlet ($\Delta E(T- S) = 373\ cm^{-1}$) with strongly correlated, diradical character and frontier natural occupation numbers (NON) of $\lambda_{261} = 1.28$ and $\lambda_{262} = 0.72$ (**Error! Reference source not f ound.**b). Inspection of the frontier NOs reveals the diradical to be localized

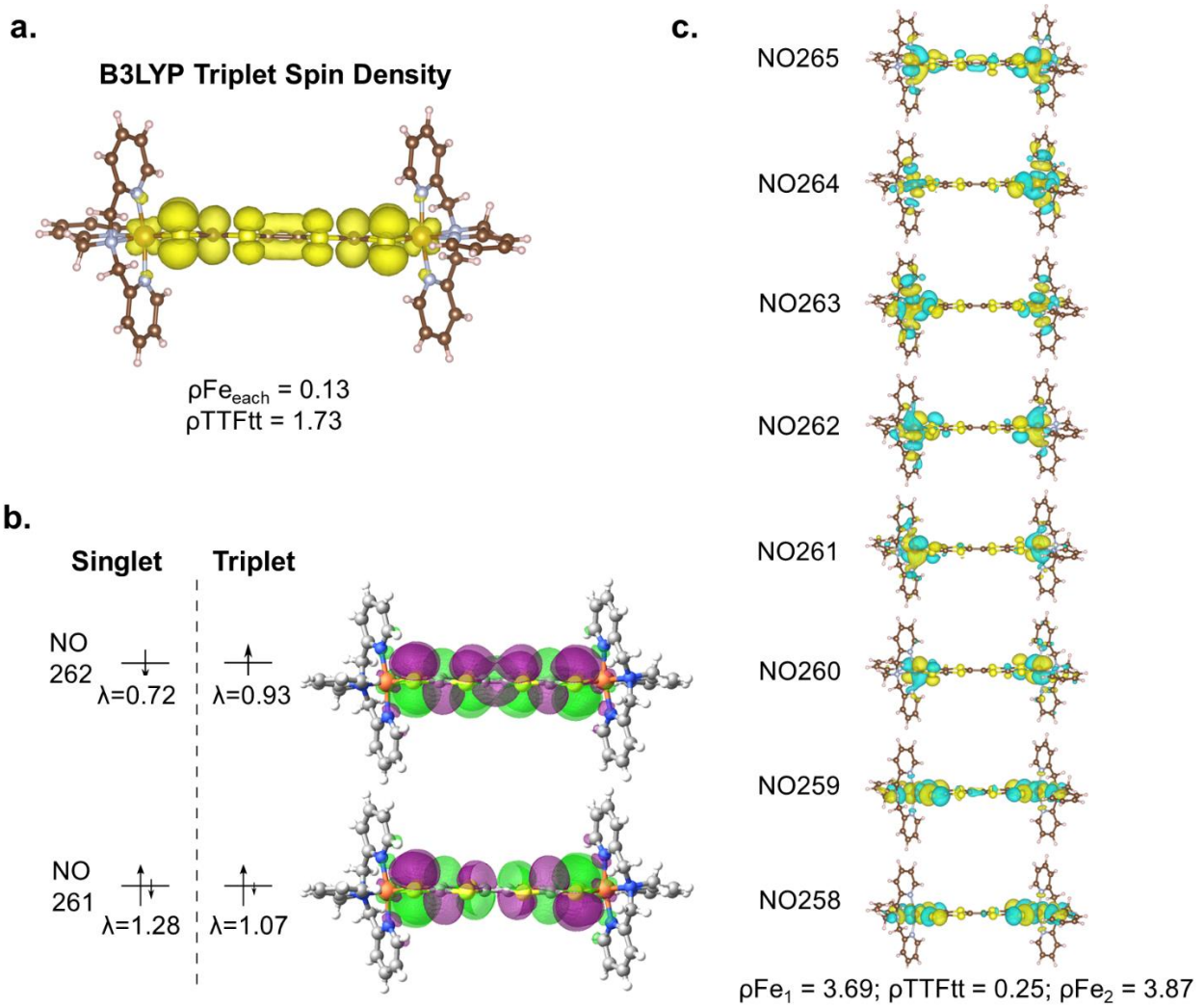

Figure 6.19. (a) Partially occupied frontier NOs and their corresponding NON of the 100 K structure of **2** from a diradical state [18,20] V2RDM calculation with a 6-31G basis set. (b) Spin density (ρ) obtained for the triplet state of **2-LT** in DFT with the B3LYP functional and a 6-311G* basis set as implemented in g16/a.01. The value for "Fe" includes all density on the FeTPA fragment. (c) Spin density obtained for the S = 4 state of **2-RT** in DFT with the B3LYP functional. The values for "Fe" include all density on each FeTPA fragment.

almost exclusively on the TTFtt linker with negligible involvement of the Fe d-orbitals, in good agreement with DFT. Hartree Fock MO coefficients reveal similar distributions. Further calculations were performed to verify that these results were not an artifact of the choice of basis set or orbitals.

Additional calculations were performed on the *S* = 4 ground state of **2-RT** (Figure 6.19c).

In **2-RT** weakening of the interaction between the Fe d-orbitals with the ligand orbitals raises the metal-based orbitals to yield two singly occupied, Fe based, frontier NOs. These results show a significant reduction in diradical character on the organic TTFtt linker in **2-RT**, as compared to **2-LT**. The unpaired electron density previously localized on the TTftt π system in **2-LT** (ρTTFtt = 1.730) is moved into Fe-based NOs in **2-RT**, with ρTTFtt = 0.25.

The computational analysis clearly supports the assignment of a TTFtt based, strongly correlated diradical with close lying singlet and triplet states in **2-LT**. The temperature driven Fe based spin transition gives rise to enhanced diradical character on the $TTFtt^{2-}$ core, that is an increase in the occupancy of the higher-lying NO262 at the expense of decreased occupancy in the lower-lying NO261. The DFT calculations suggest that this arises from the shrinking of the energy gap between the NO261 and NO262 in **2-LT** (19.59 kcal/mol), as compared to the analogous orbitals (NO254 and NO 268, respectively) in **2-HT** (26.01 kcal/mol).

Furthermore, this spin transfer moves electron density from a C–C bonding and C–S antibonding orbital (NO 262 in **2-LT**, NO 268 in **2-RT**) to a C–C antibonding and C–S bonding orbital (NO 261 in **2-LT**, NO 254 in **2-RT**). These changes in orbital populations correlate with the observed changes in bond lengths (Figure 6.2) and suggest that there should be bond length changes of similar trend, but of potentially larger magnitude when TTFtt undergoes a spin transition as compared to an electron transfer. This is indeed the case when comparing the larger bond length changes of **2** versus those for $[(dppeNi)_2TTFtt][BAr^F{}_4]_2$ and $[(dppeNi)_2TTFtt][BAr^F{}_4]$. Taken together, all of the computational analysis is consistent with the experimental data supporting that an Fe based ST shrinks the TTFtt based singlet-triplet gap and increases diradical character.

6.4 Conclusions

We have synthesized and characterized a family of novel Fe-thiolate complexes with intriguing electronic structures. In particular, [(FeTPA)$_2$TTFtt][BAr$^F{}_4$] (**2**), shows temperature dependent spin tautomerism wherein a spin-transition to low-spin Fe(II) decreases the singlet-triplet energy gap on the TTFtt core, generating significant diradical character. Organic diradicals, as seen in **2** at low temperature, are relatively rare in general and are unknown in the well-studied TTF moiety. The reversible and cooperative modulation of spin between this unusual organic radical and the Fe centers in **2** represents a fundamentally new form of spin transition.

6.5 Experimental Methods

General Procedures. Syntheses and general handling were carried out in a nitrogen-filled MBraun glovebox unless otherwise noted. TTFtt-C_2H_4CN, Fe(TPA)$(OTf)_2(ACN)_2$, dmit-(COPh) and [Fc][BAr$^F{}_4$] were prepared according to literature procedures.[14b,21] ^{1}H NMR spectra were acquired on a Bruker DRX 400 at 400 MHz. Elemental analyses were performed by Midwest Microlabs. Electrochemical measurements were made on an Epsilon BAS potentiostat. THF and Et2O were dried and degassed in a Pure Process Technologies solvent system, stirred over NaK amalgam for >24 hours, filtered through alumina, and stored over 4 Å molecular sieves. Methanol was dried with sodium hydroxide overnight, distilled, transferred into the glovebox and stored over 4 Å molecular sieves. 2-Chlorobutane was degassed by the freeze, pump, thaw method and stored over 4 Å molecular sieves. All other solvents were dried and degassed in a Pure Process Technologies solvent system, filtered through activated alumina, and stored over 4 Å molecular sieves. Solvents were tested for O_2 and H_2O with a standard solution of sodium benzophenone ketyl radical. All other reagents were used as purchased without further purification.

$(FeTPA)_2TTFtt$ (**1**). TTFtt-C_2H_4CN (0.1 mmol, 0.054 g) was stirred with sodium tert-butoxide (0.8 mmol, 0.076 g) in THF (6 mL) overnight. The solid material was collected, washed with THF (4 mL x 3), and dried under vacuum to yield a pink powder. The pink solid was then stirred with $Fe(TPA)(OTf)_2(ACN)_2$ (0.2 mmol, 0.152 g) in THF (6 mL) for 2 days. The resulting brick red solid was collected, washed with THF (4 mL x 3), and dried under vacuum. Elemental analysis: expected for $C_{42}H_{30}Fe_2N_8S_8$: % C, 49.41; H, 3.56; N, 10.98. Found: % C, 49.78; H, 3.77; N, 10.88.

$[(FeTPA)_2TTFtt][BAr^F{}_4]_2$ (**2**). $[Fc][BAr^F{}_4]$ (0.075 mmol, 0.102 g) was dissolved in DCM (12 mL) and added in 4 portions to $(FeTPA)_2TTFtt$ (0.05 mmol, 0.065 g) and stirred for 5 minutes after each addition. The mixture was filtered through celite and the filtrate was layered with petroleum ether. After cooling at −38 °C for several days, dark brown crystalline solid formed and was washed with petroleum ether and dried under vacuum (0.0815 g, 59%). Elemental analysis: expected for $C_{106}H_{60}B_2F_{48}Fe_2N_8S_8$: % C, 46.34; H, 2.20; N, 4.08. Found: % C, 46.54; H, 2.26; N, 4.02. EPR (DCM): $g_x = 2.083$, $g_y = 2.041$, $g_z = 2.047$, D = 0.028 cm^{-1}. ^1H NMR (400 mHz, 25 °C, CD_2Cl_2): δ -4.8, 7.53, 56.0, 57.5. UV-Vis-NIR at 20 °C, 2-chlorobutane (ϵ, M^{-1} cm^{-1}): 1025 nm (8 $x10^4$), 280 nm (3 $x10^4$), 300 nm (2 $x10^4$); (-100 °C, 2-chlorobutane): 1615 nm, 325 nm, 396 nm.

$Fe(TPA)(dmit)\cdot 0.5CH_2Cl_2$ (**3**). dmit-(COPh) (0.2 mmol, 0.080 g) was stirred with sodium methoxide (0.4 mmol, 0.022 g) in methanol (6 mL) for 1 hour, then $Fe(TPA)(OTf)_2(ACN)_2$ (0.2 mmol, 0.152 g) was added and stirred overnight. The bright red solid was collected, washed with DCM (4 mL x 3), and dried under vacuum. Elemental analysis: expected for $C_{21.5}H_{21}ClFeN_4S_5$: % C, 44.14; H, 3.27; N, 9.58. Found: % C, 44.65; H, 3.22; N, 9.01. ^1H NMR (400 mHz, 25 °C, $CDCl_3$): δ -3.0, 35.7, 59.8, 59.9, 81.11. UV-Vis-NIR (20 °C, DCM): 310 nm, 498 nm.

[Fe(TPA)(dmit)][BAr$^{F}_{4}$] (**4**). Fe(TPA)(dmit)·0.5CH_2Cl_2 (0.1 mmol, 0.054 g) was stirred with [Fc][BAr$^{F}_{4}$] (0.1 mmol, 0.105 g) in DCM (4 mL) for 10 minutes before filtering through celite. The filtrate was layered with petroleum ether and cooled to -38 °C for several days which yielded green-brown crystals. The solids were washed with petroleum ether and dried under vacuum (0.112 g, 80%). Elemental analysis: expected for $C_{47}H_{32}BF_6FeN_4S_5$: % C, 45.29; H, 2.15; N, 3.99. Found: % C, 45.33; H, 2.32; N, 3.81. EPR – g_x = 2.056, g_y = 2.071, g_z = 2.082, σ_{gx} = 0.034, σ_{gy} = 0.000, σ_{gz} = 0.105, σ_B = 25.994 G. ^{1}H NMR (400 mHz, 25 °C, CD_2Cl_2): δ 7.55, 7.72, 9.1, 17.0. UV-Vis-NIR at 20 °C, DCM (ϵ, M^{-1} cm^{-1}): 417 nm (2 x10^3), 1050 nm (6 x10^3).

Magnetometry. Magnetic measurements were carried out on a Quantum Design MPMS3 performed on bulk powder samples in polycarbonate capsules. The powder samples were suspended in an eicosane matrix to prevent movement and protect the sample from incidental air exposure. Frozen solution samples in PEG-2000 were prepared by dissolving 2 and PEG-2000 in DCM, then removing DCM under reduced pressure. Diamagnetic corrections for the capsule and eicosane were made by measuring temperature vs. moment in triplicate for each to determine a moment per gram correction. The diamagnetic correction for PEG-2000 was made by measuring sample versus moment to determine a moment per gram correction. Pascal's constants were used to correct for the diamagnetic contribution from the complexes.[22]

Single Crystal X-Ray Diffraction (SXRD). The diffraction data for 2-LT and 2-RT were measured at 100 K and 298 K, respectively, on a Bruker D8 VENTURE diffractometer equipped with a microfocus Mo-target X-ray tube (λ = 0.71073 Å) and PHOTON 100 CMOS detector. The diffraction data for 3 was measured at 100 K on a Bruker D8 fixed-chi with PILATUS1M (CdTe) pixel array detector (synchrotron radiation, λ = 0.41328 Å (30 KeV)) at the Chem-MatCARS 15-

ID-B beam-line at the Advanced Photon Source (Argonne National Laboratory). Data reduction and integration were performed with the Bruker APEX3 software package (Bruker AXS, version 2015.5-2, 2015)[23]. Data were scaled and corrected for absorption effects using the multi-scan procedure as implemented in SADABS (Bruker AXS, version 2014/54)[24]. The structures were solved by SHELXT (Version 2014/55)[25] and refined by a full-matrix least-squares procedure using OLEX26 (XL refinement program version 2018/17)[26].

X-Ray Powder Diffraction (XRPD) Diffraction patterns were collected on a SAXSLAB Ganesha diffractometer with a Cu K-α source (λ = 1.54 Å) in wide angle X-ray scattering (WAXS) transmission mode. The samples were contained in a ~1 mm diameter borosilicate capillary tube. A correction was made to subtract the broad peak from the capillary around 16–25° (2θ) from the baseline.

UV-Vis-NIR. Variable temperature UV-Vis-NIR measurements were performed on a Shimadzu UV-3600 Plus dual beam spectrophotometer with a Unisoku CoolSpeK 203-B cryostat. UV-Vis region spectra were collected on Thermo Scientific Evolution 300 spectrometer with the VISIONpro software suite. Samples were stirred during cooling and during measurements colder than room temperature. Background spectra of the cuvette and solvent were collected at maximum and minimum temperatures within the range to account for temperature dependence of the background.

EPR Spectroscopy. EPR spectra were recorded on a Bruker Elexsys E500 spectrometer equipped with an Oxford ESR 900 X-band cryostat and a Bruker Cold-Edge Stinger. Simulation of EPR spectra was performed using a least-squares fitting method with the SpinCount program.

Mössbauer Spectroscopy. Zero-field iron-57 Mössbauer spectra were with a constant acceleration spectrometer and a rhodium embedded cobalt-57 source. Prior to measurements, the spectrometer was calibrated at 295 K with α-iron foil. Samples were prepared in a N2-filled glovebox where powdered samples were placed in a polyethylene cup and frozen in liquid nitrogen prior to handling in air. All spectra were analyzed using the WMOSS Mössbauer Spectral Analysis Software.

TD-DFT. TD-DFT calculations were performed with ORCA software suite[27] using time-dependent density functional theory (TD-DFT). The PBE0 functional was used with a basis set of def2-TZVPP on Fe and def2-TZVP on all other atoms. Furthermore, an effective core potential of SDD was used on Fe. Starting coordinates for all calculations were pulled from crystal structures determined by single crystal X-ray diffraction at 100 K. Simulations of UV-vis spectra were generated using the orca_mapspc function with line broadening of 2000 cm^{-1}. Molecular orbitals were generated using the orca_plot function and visualized in Avogadro with an iso value of 0.3.

To calibrate the calculations, the electronic spectrum of the previously reported reference complex $[(dppeNi)_2TTFtt][BAr^F{}_4]_2$ — which features a doubly oxidized TTF core, as in 2 — was calculated by the same methods using the reported crystal structure. Using the experimental spectral data, a weighted calibration was calculated using the shifts to the primary absorbances (i.e. at 1039 and 516 nm; Figure 6.20). This calibration was then applied to the calculated spectra of 2 in both the $S = 0$ and $S = 1$ forms.

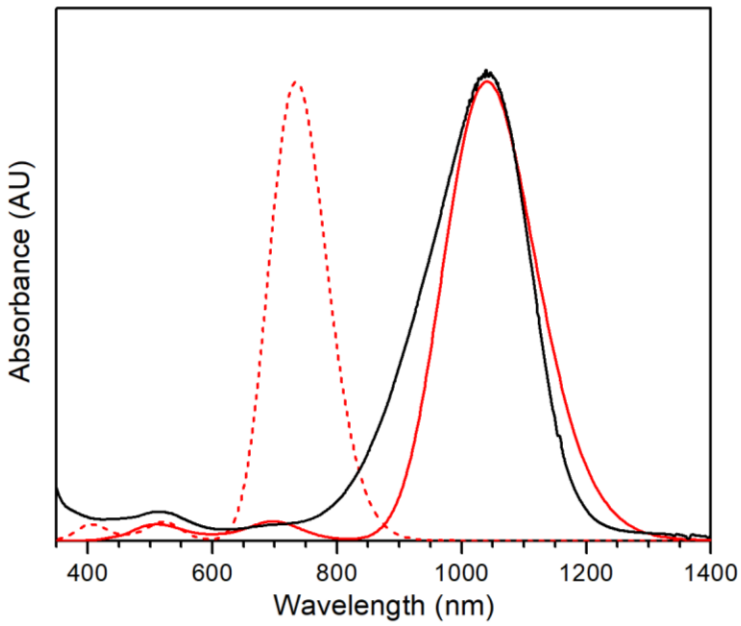

Figure 6.20. Calibration from $[(dppeNi)_2TTFtt][BArF_4]_2$ reference complex**.** The black line shows the experimental data in 50 μM DCM at 20 °C, the dashed red line shows the unadjusted calculated spectrum from TD-DFT, and the solid red line is the calculated spectrum adjusted with the weighted calibration.

At room temperature **2** exhibits a broad absorbance near 1025 nm. The energy of this absorbance shows a slight concentration dependence in the range of 350–50 μM which shifts the position from 975 to 1075 nm. In other TTF containing monocationic species, broad absorbances in this region (873–1092 nm) are sometimes attributed to intermolecular π interactions (e.g. dimerization), however the TD-DFT contradicts this assignment.

Computational Methods and Discussion. Variational 2-electron reduced density matrix (V2RDM) and DFT calculations were carried out to elucidate the electronic structure of **2**. The V2RDM method allows large complete active space self-consistent field (CASSCF) to be carried out with polynomial $O(r^6)$ computational scaling, enabling calculations to be carried out that remain out of reach of traditional wave function based CASSCF methods which scale exponentially.[28] This is achieved by formulating the system energy as a linear functional of the 2RDM:

$$E = Tr[^2K\ ^2D] \quad (1)$$

where ^2K is the 2-electron reduced Hamiltonian, and ^2D is the 2-RDM. Minimization of the energy is subject to a set of constraints on the 2RDM that are termed N-representability constraints and ensure that variationally obtained 2RDM corresponds to a physically feasible system.[29]

$$^2D \geq 0 \quad (2)$$

$$^2Q \geq 0 \quad (3)$$

$$^2G \geq 0 \quad (4)$$

This procedure is carried out using a semi-definite program.[30] The V2RDM method has been demonstrated to recover the vast majority of the correlation energy in strongly correlated systems and has recently been applied to a range of transition metal systems to successfully explain their electronic structure.[4a,31] To ensure that the obtained NO and spin state splitting picture of the LT form of **2** is not an artifact of the choice of active space orbitals and size or basis set further calculations on the singlet and triplet state were carried out using a [16,14] active apace and 6-31G basis sets and a [14,14] active space with a larger 6-31G* basis set, each time forcing iron 3d orbitals into the active space for the initial guess. The data are shown in Table S1. While the [16,14] active space is not large enough to account for the full correlation energy yielding a significantly smaller singlet-triplet gap of $\Delta E(T–S) = 210\ cm^{-1}$, the [14,14]/6-31G* calculation gives an almost identical gap to the larger [18,20] calculation with $\Delta E(T–S) = 379\ cm^{-1}$. In both cases the CASSCF routine rotates the NOs with iron 3d contributions back into the core and virtual orbitals, obtaining identical Nos as those obtained in the [18,20] calculation.

	[16,14] 6-31G		[14,14] 6-31G*	
	Singlet	Triplet	Singlet	Triplet
E_{rel}/cm^{-1}	0	210	0	379
λ_{259}	1.95	1.95	1.92	1.92
λ_{260}	1.95	1.94	1.91	1.91
λ_{261}	1.25	1.04	1.30	1.06
λ_{262}	0.80	1.01	0.71	0.94
λ_{263}	0.06	0.06	0.09	0.09
λ_{264}	0.06	0.06	0.08	0.09

Table 6.1. Energies and NON of **2.** [16,14] active space V2RDM calculations a 6-31G basis set and [14,14] calculations with a 6-31G* basis set

6.6 Supplementary Data

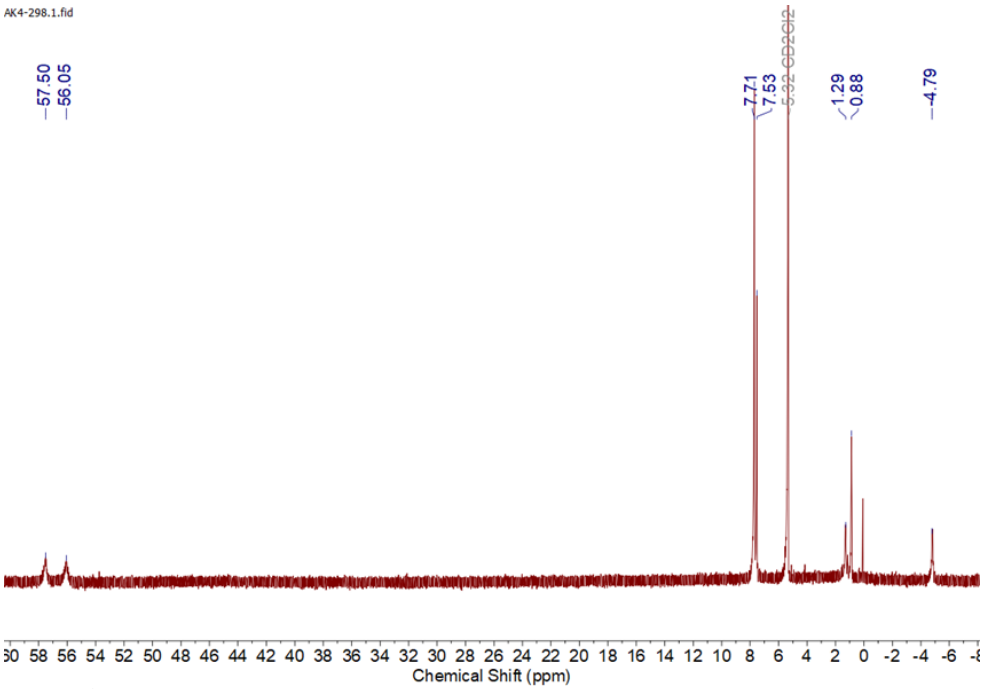

Figure 6.21. ^{1}H NMR spectrum of **2** in d-DCM

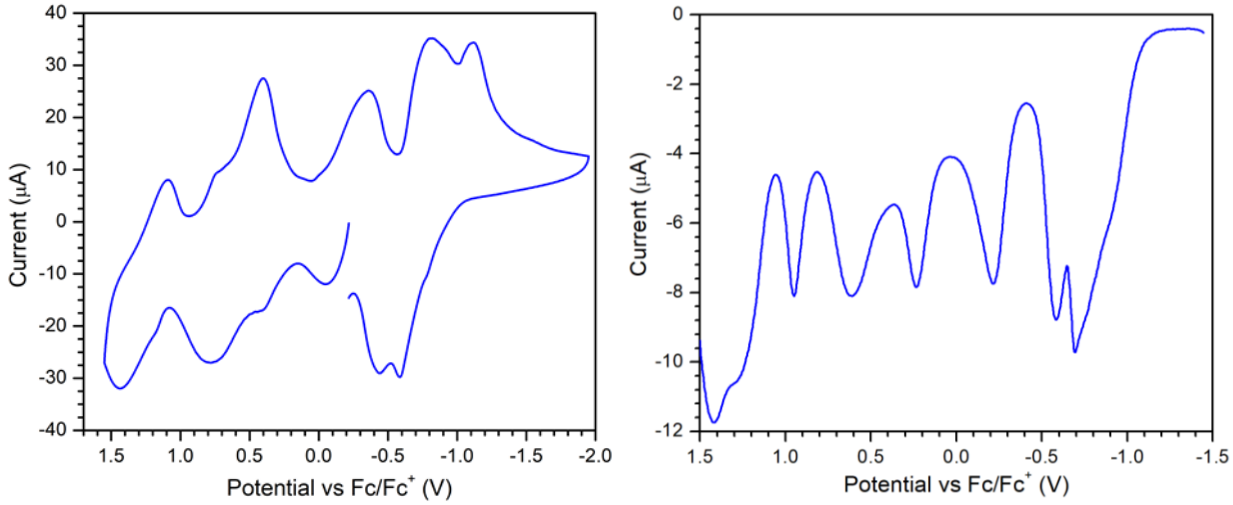

Figure 6.22. Cyclic voltammogram (CV) and differential pulse voltammogram (DPV) of **2** Collected in DCM with 0.1 M [TBA][PF_6]. The CV was collected at a scan rate of 250 mV/s. The DPV was collected with a 4 mV step, 50 mV pulse amplitude, 50 ms pulse width, and 200 ms pulse period.

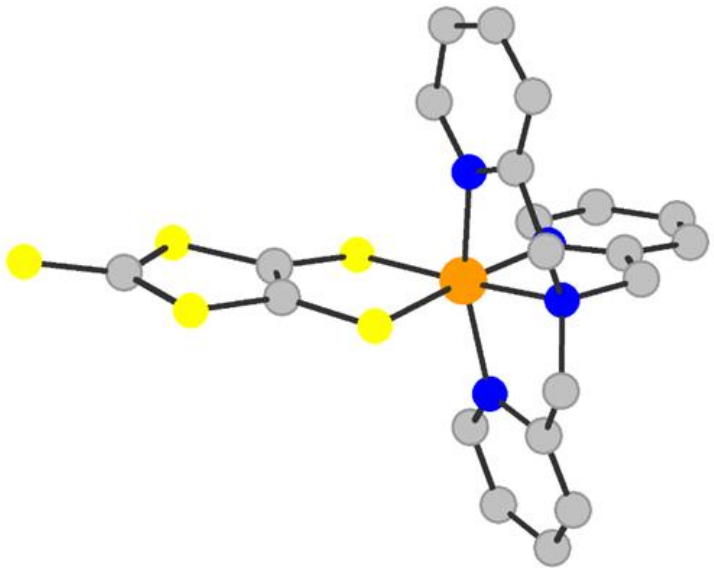

Figure 6.23. Molecular structure of **4** at 100 K. Structure shown in ball-and-stick model for atom connectivity only, due to poor data quality. H-atoms and $BAr^F{}_4$ counter anion omitted for clarity.

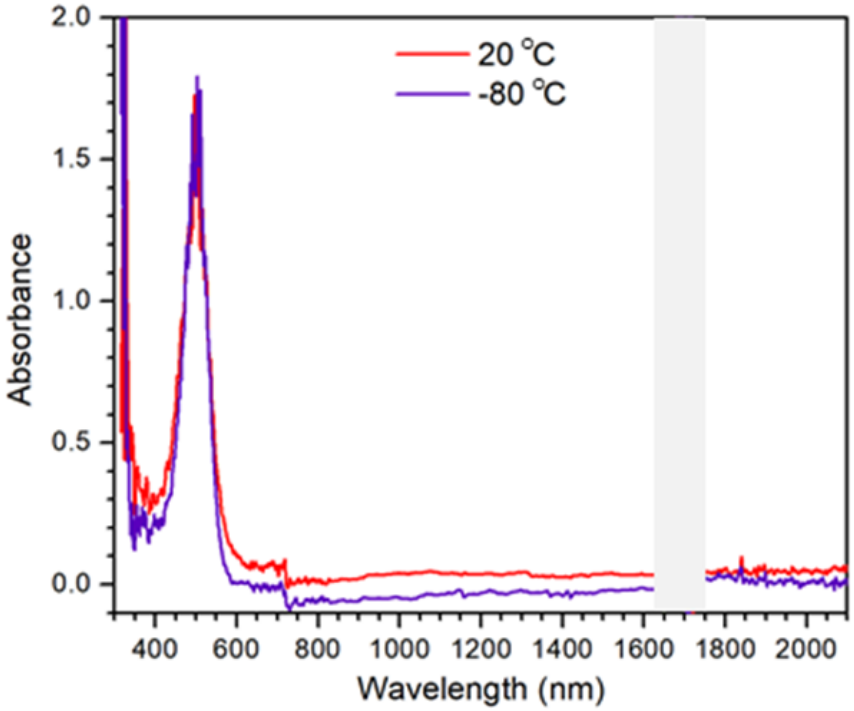

Figure 6.24. Variable temperature electronic spectrum of **3** in DCM. The grey box covers the strong NIR absorptions from the solvent.

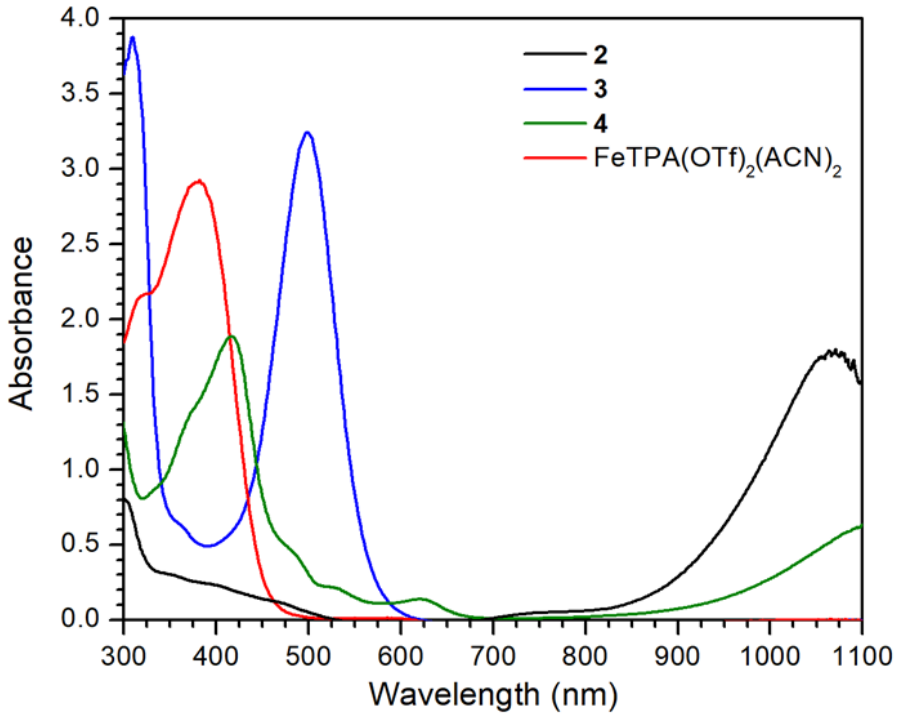

Figure 6.25. Comparison of the UV-Vis spectra of **2**, **3**, **4**, and the starting material

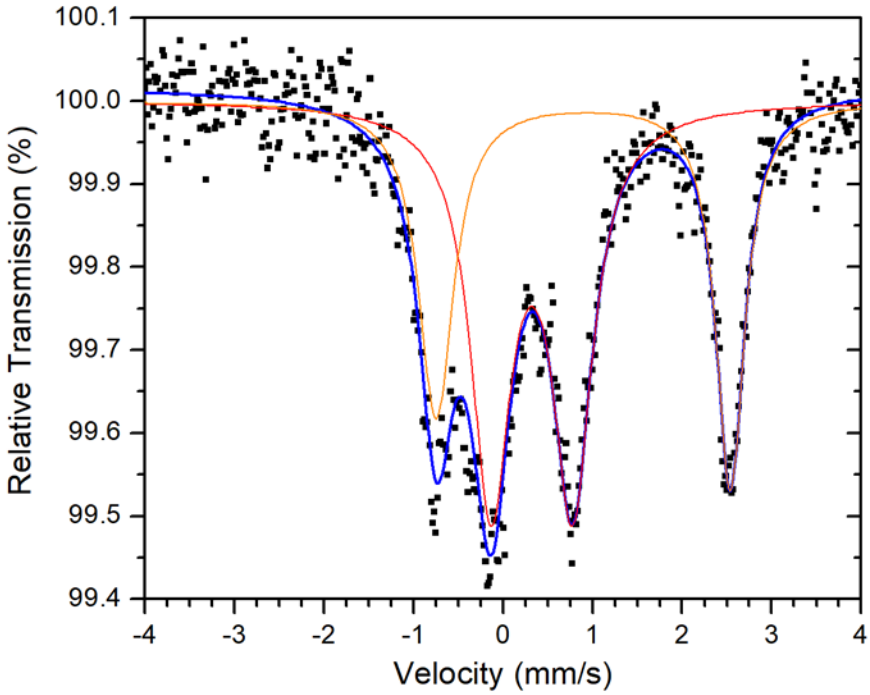

Figure 6.26. Mössbauer spectrum of **2** at in a frozen solution of PEG-2000 at 250 K. Site A (red): δ = 0.32(9) mm/s; ΔE_Q = 0.91(2) mm/s; 64(3)%. Site B (orange): δ = 0.89(5) mm/s; ΔE_Q = 3.29(3) mm/s; 46(5)%. Overall Fit (blue): $R\chi^2$ = 0.565

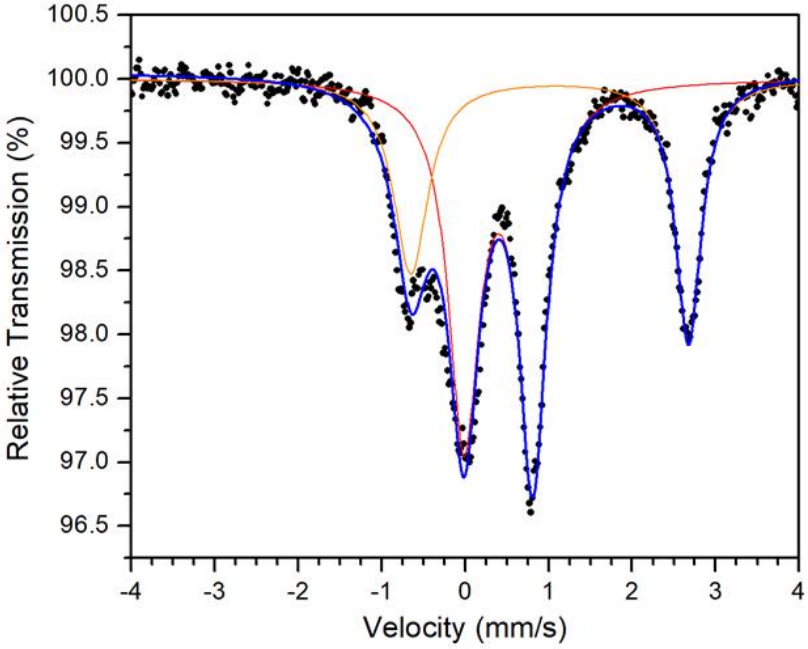

Figure 6.27. Mössbauer spectrum of **2** at in a frozen solution of PEG-2000 at 80 K. Site A (red): δ = 0.398(3) mm/s; ΔE_Q = 0.823(7) mm/s; 67(3)%. Site B (orange): δ = 1.01(1) mm/s; ΔE_Q = 3.32(1) mm/s; 41(3)%. Overall Fit (blue): $R\chi^2$ = 1.632

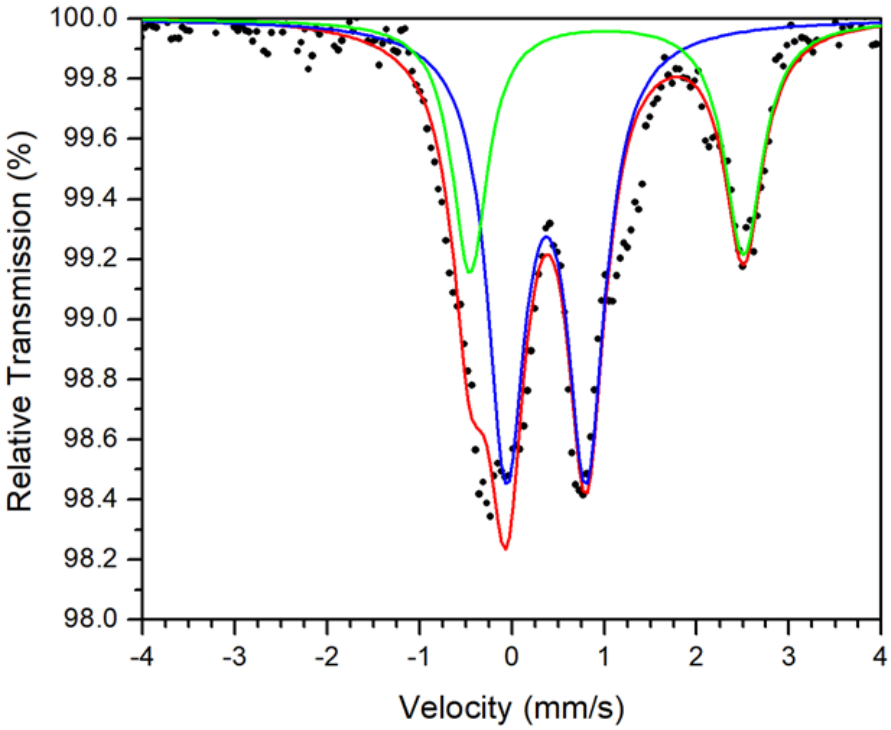

Figure 6.28. Mössbauer spectrum of **2** at 80 K. Site A (blue): δ = 0.37(1) mm/s; ΔE_Q = 0.86(2) mm/s; 70(2)%. Site B (green): δ = 1.02(2) mm/s; ΔE_Q = 2.964(8) mm/s; 38(3)%. Overall Fit (blue): $R\chi^2$ = 1.488

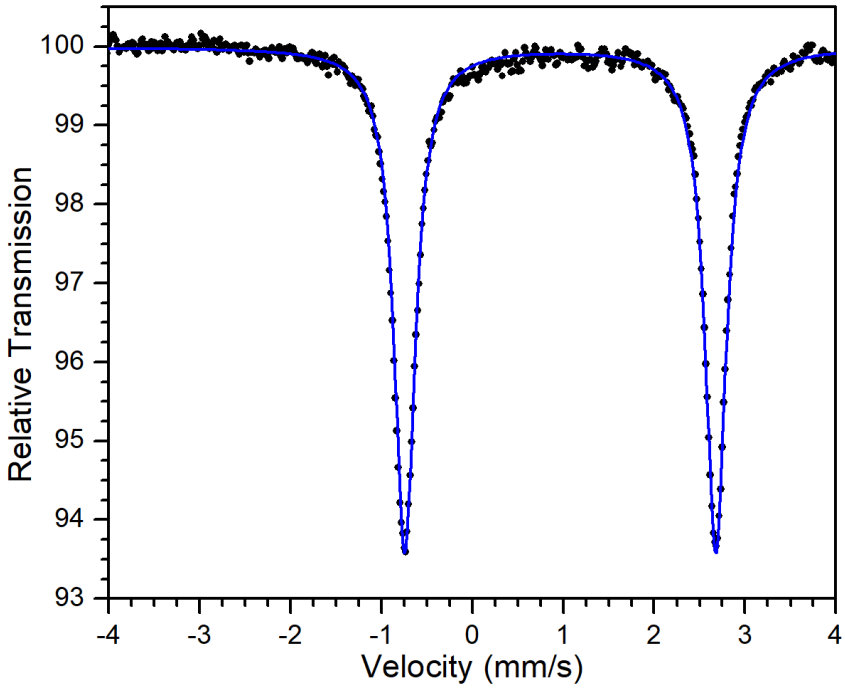

Figure 6.29. Mössbauer spectrum of **3** at 80 K. δ = 0.966(1) mm/s; ΔE_Q = 3.422(3) mm/s. Fit (blue): $R\chi^2$ = 1.08.

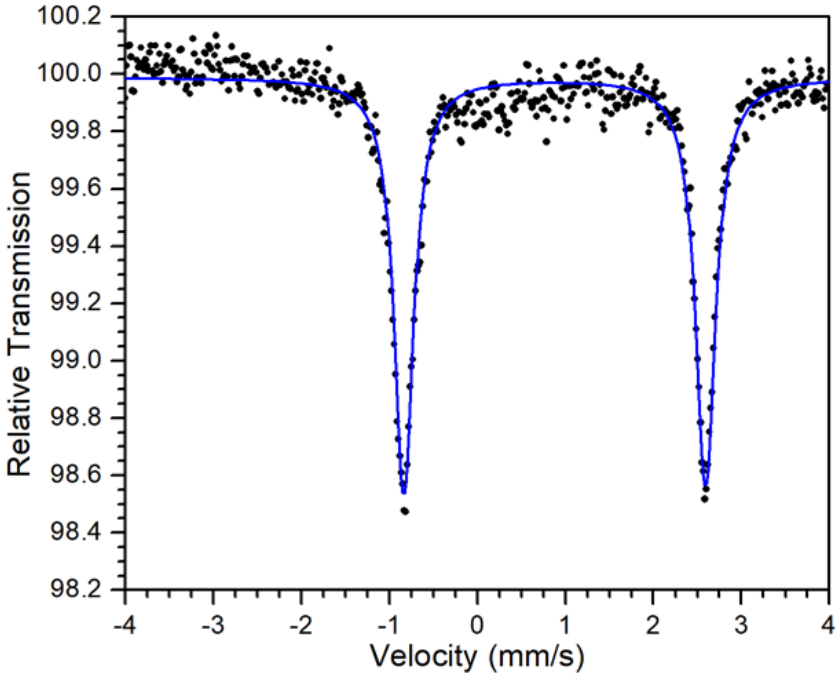

Figure 6.30. Mössbauer spectrum of **3** at 250 K. Parameters: δ = 0.878(5) mm/s; ΔE_Q = 3.43(1) mm/s. Fit (blue): $R\chi^2$ = 0.766.

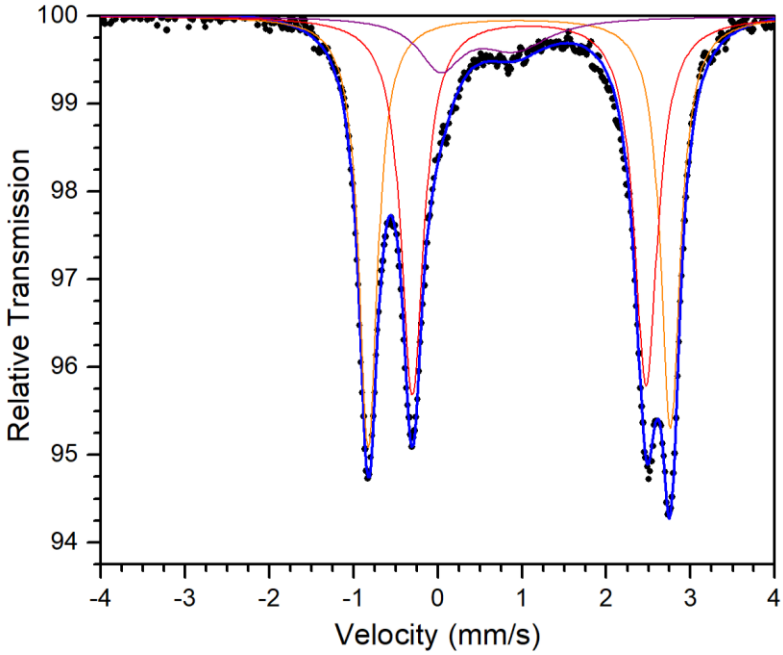

Figure 6.31. Mössbauer spectrum of **1** at 80 K. Batch I. Site A (orange): δ = 0.968(2) mm/s; ΔE_Q = 3.588(5) mm/s; 47(2)%. Site B (red): δ =1.084(2) mm/s; ΔE_Q – 2.773(1) mm/s; 50(2)%. Overall Fit (blue): $R\chi^2$ = 0.839. Note: Overall fit includes minor Fe(III) impurity (purple): δ – 0.45 mm/s; ΔE_Q – 0.90 mm/s.

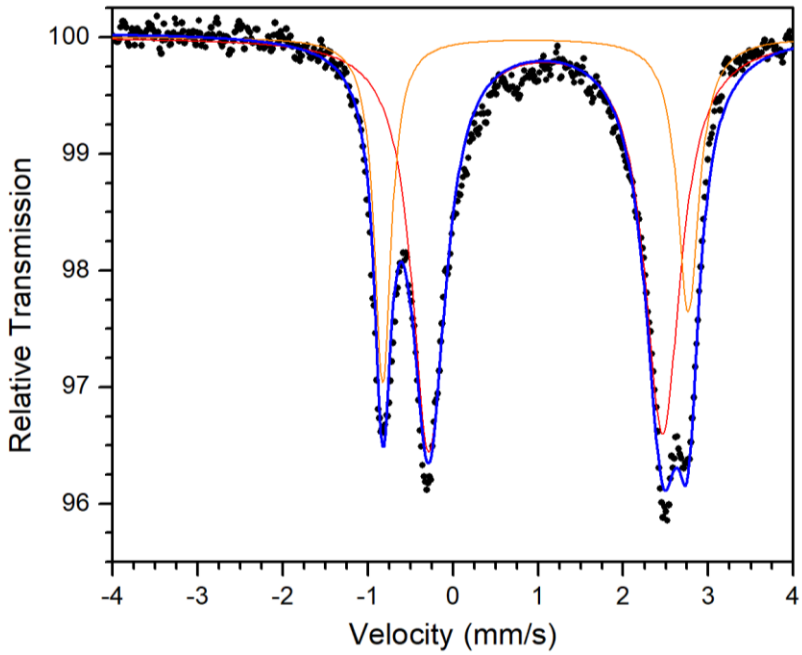

Figure 6.32. Mössbauer spectrum of **1** at 80 K. Batch II. Site A (orange): δ = 0.969(4) mm/s; ΔE_Q = 3.589(9) mm/s; 31(2)%. Site B (red): δ = 1.089(3) mm/s; ΔE_Q = 2.748(8) mm/s; 74(1)%. Overall Fit (blue): $R\chi^2$ = 2.079.

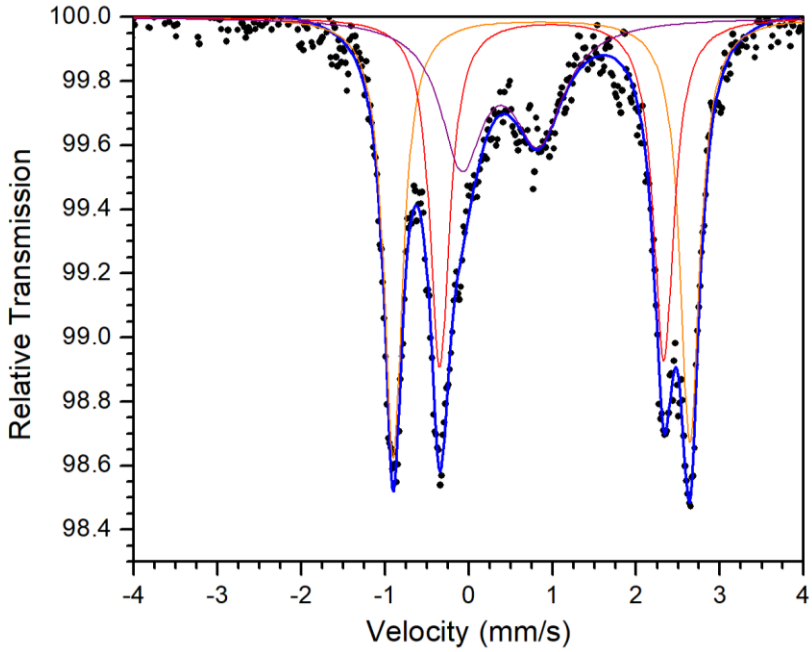

Figure 6.33. Mössbauer spectrum of **1** at 250 K. Batch I. Site A (orange): δ = 0.8700(8) mm/s; ΔE_Q = 3.54(1) mm/s; 44(5)%. Site B (red): δ = 0.991(5) mm/s; ΔE_Q = 2.675(8) mm/s; 37(4)%. Overall Fit (blue): $R\chi^2$ = 0.558. Note: Overall fit includes minor Fe(III) impurity (purple): δ = 0.375 mm/s ; ΔE_Q = 0.915 mm/s.

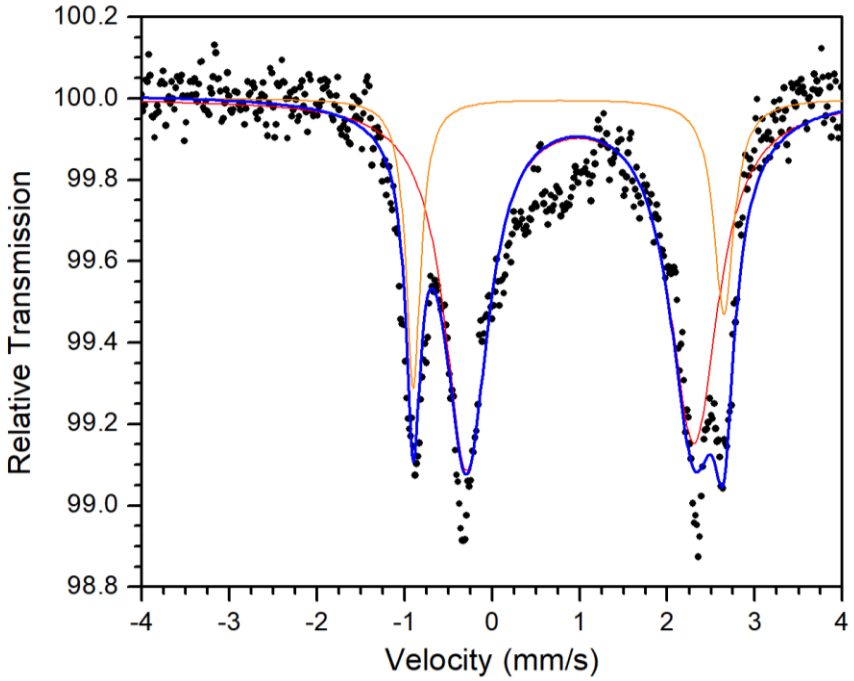

Figure 6.34. Mössbauer spectrum of **1** at 250 K. Batch II. Site A (orange): δ = 0.87(1) mm/s; ΔE_Q = 3.55(2) mm/s; 22(2)%. Site B (red): δ = 1.01(2) mm/s; ΔE_Q – 2.60(3) mm/s; 82(4)%. Overall Fit (blue): $R\chi^2$ = 1.476.

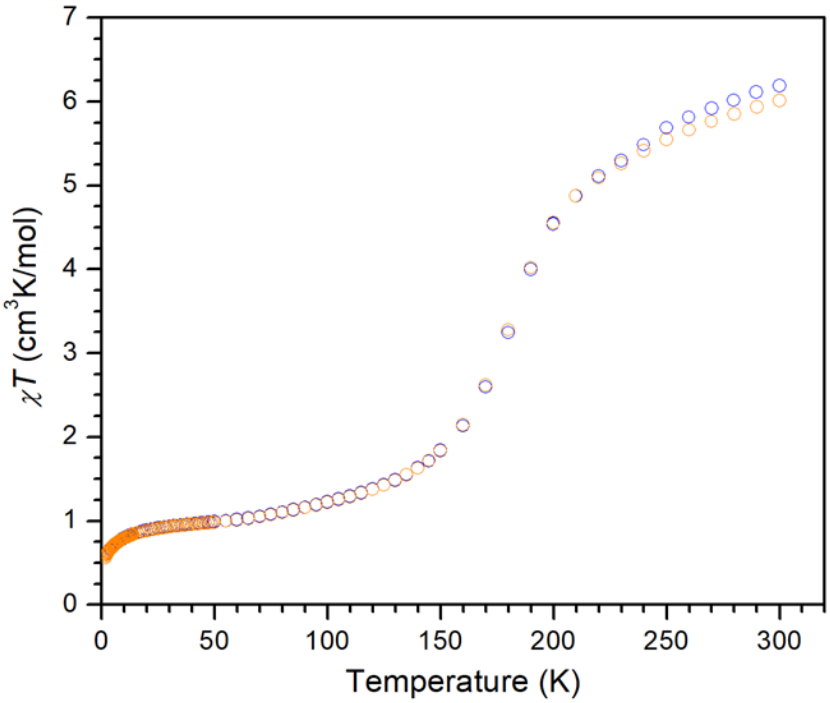

Figure 6.35. Magnetic data for **2** upon cooling and warming. The sample was cooled (blue) then warmed (orange) under a static applied field of 0.1 T.

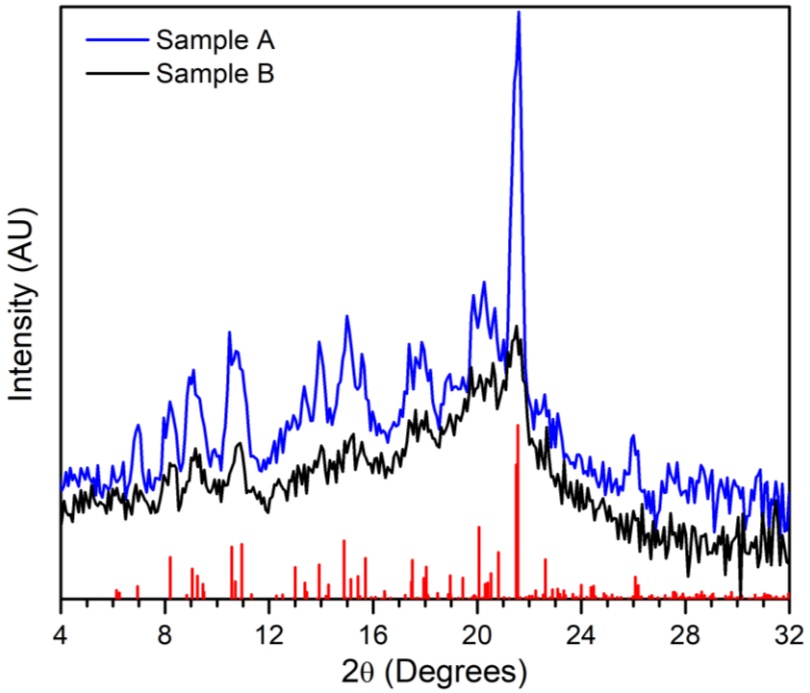

Figure 6.36. XRPD patterns of two samples of **2**. Calculated pattern of **2-RT** from SXRD is shown in red. Both samples were pure and solvent-free by elemental analysis. Temperature dependent χT of samples A and B can be compared in Figure 6.37

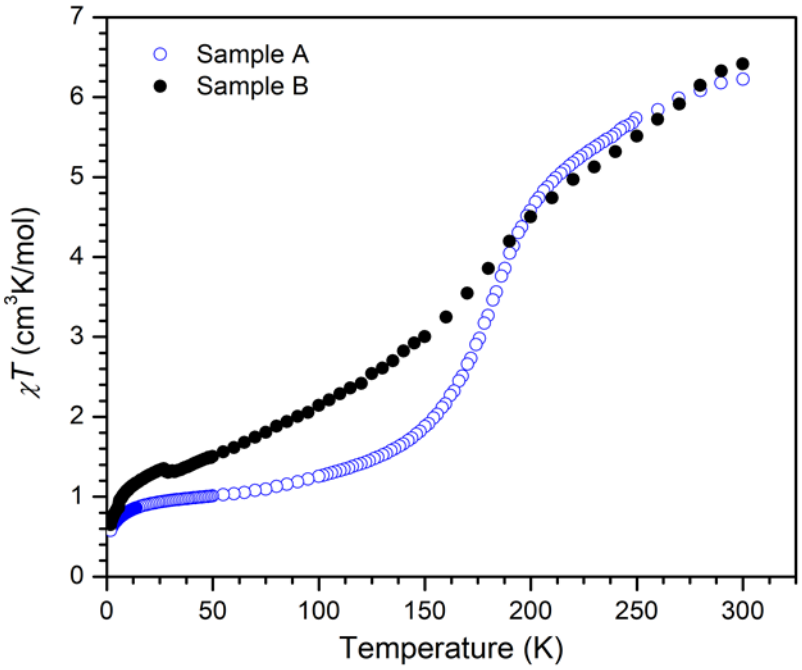

Figure 6.37. Temperature dependent χT of two samples of **2**. Both samples were pure and solvent-free by elemental analysis. XRPD of samples A and B can be compared in Figure 6.36

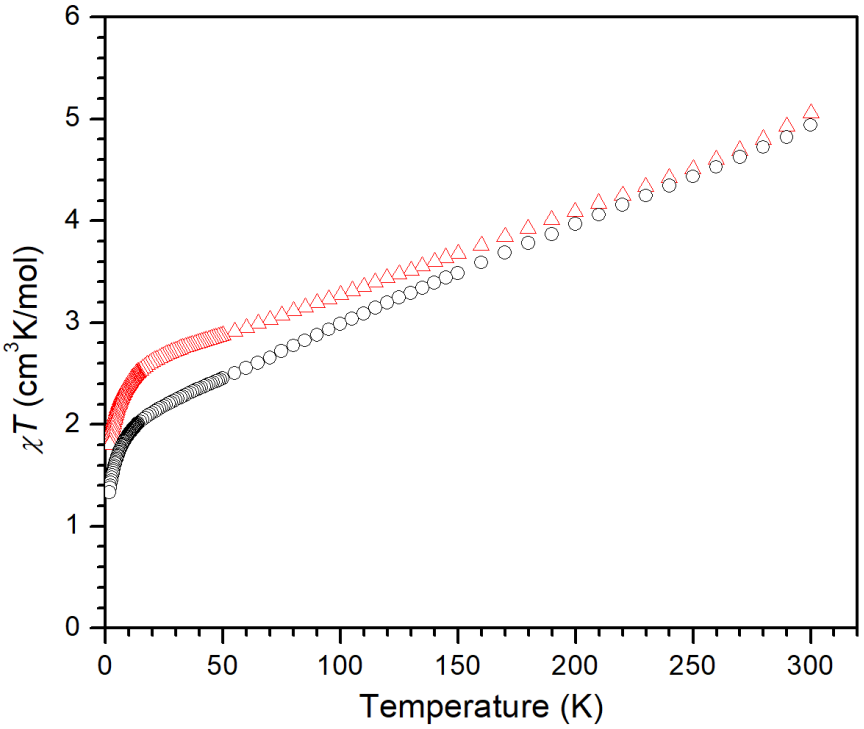

Figure 6.38. Frozen solution magnetic behavior of different samples of **2** in PEG-2000

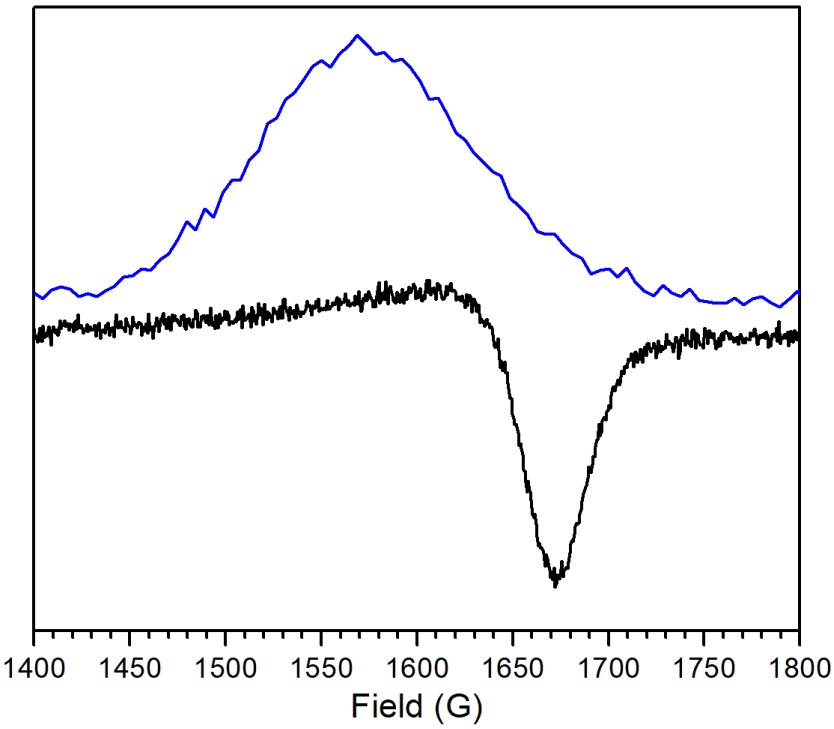

Figure 6.39. EPR spectrum of [Fc][BAr^F] compared to **2**. Both samples were collected in DCM. [Fc][BAr^F] is shown in blue and **2** is shown in black.

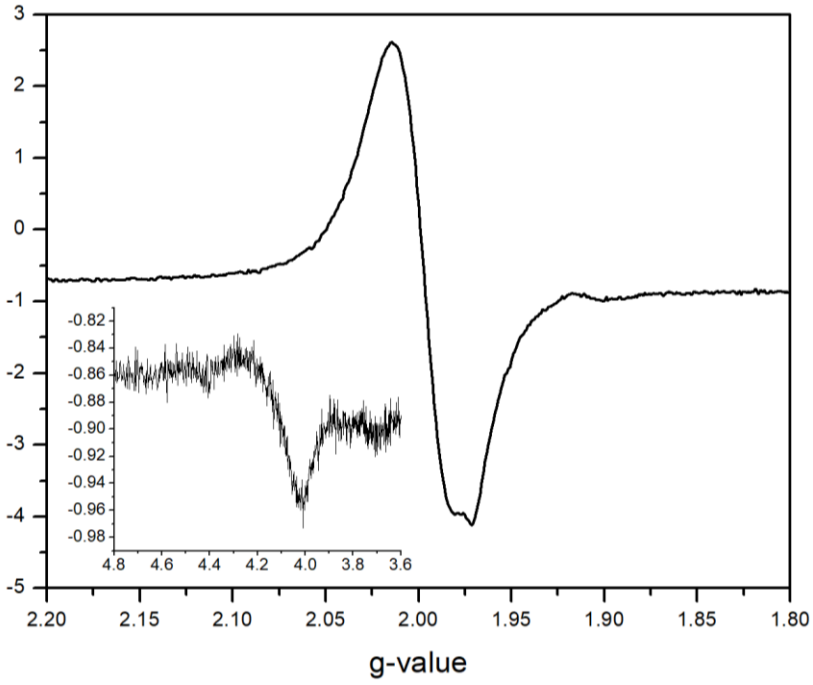

Figure 6.40. Additional EPR spectrum of **2**. Collected in DCM with a power level of 1.998 mW and frequency of 9.632 GHz.

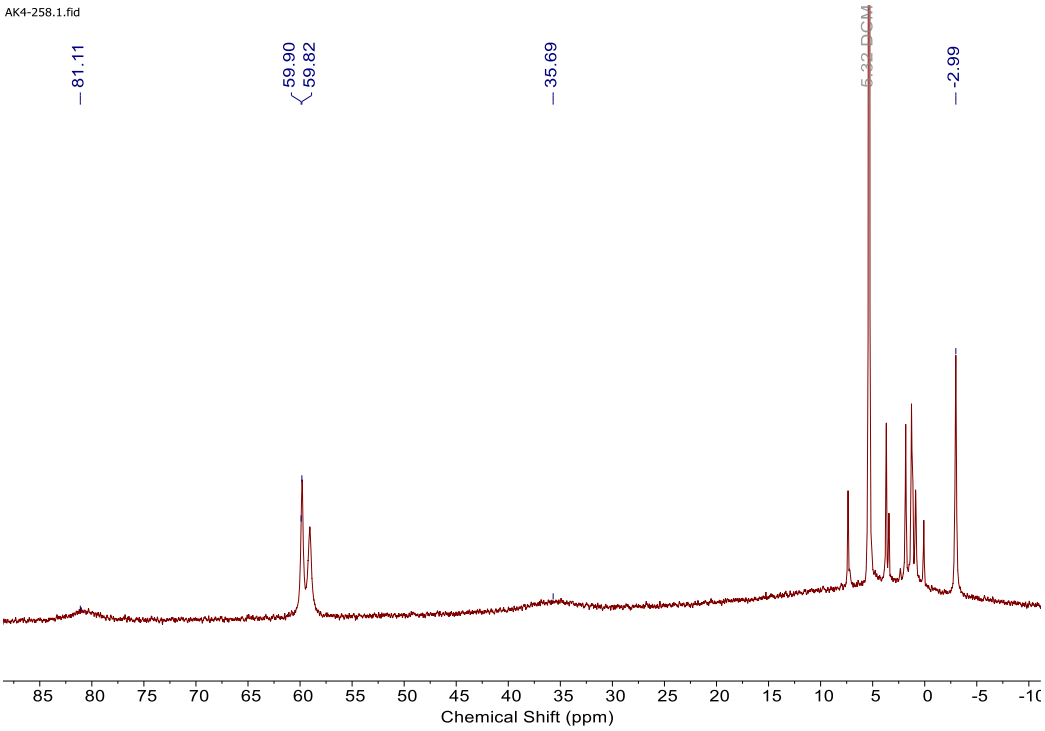

Figure 6.41. ^{1}H NMR spectrum of **3** in DCM. Unmarked peaks are residual solvent.[32]

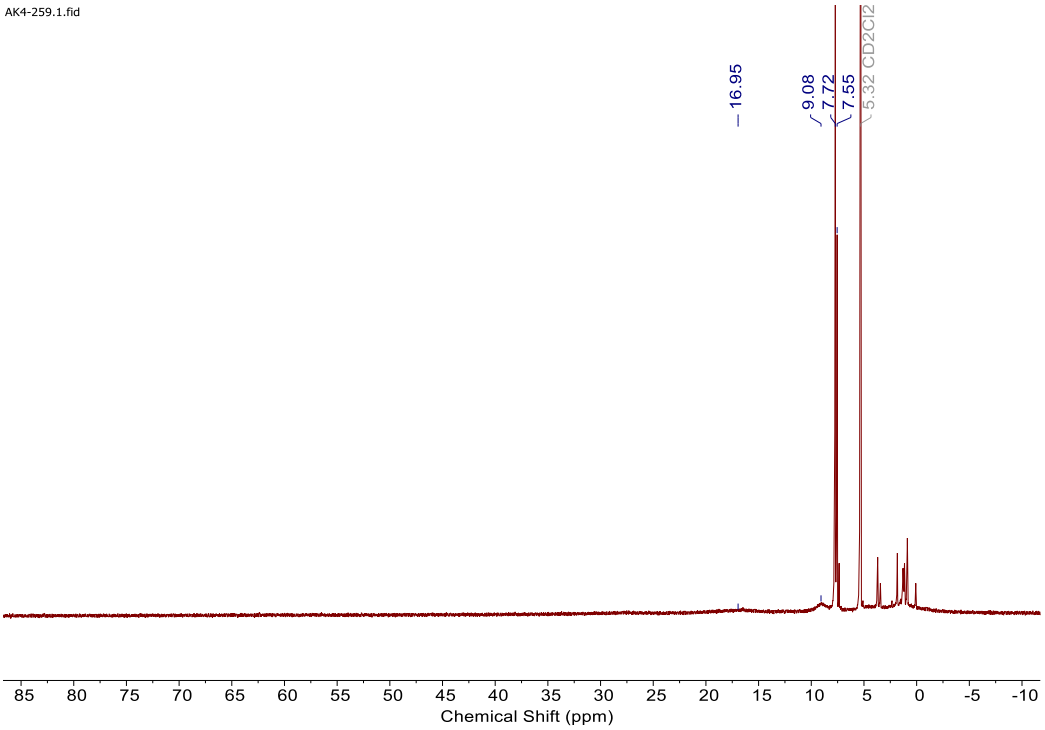

Figure 6.42. ^{1}H NMR spectrum of **4** in CD_2Cl_2. Unmarked peaks are residual solvent.

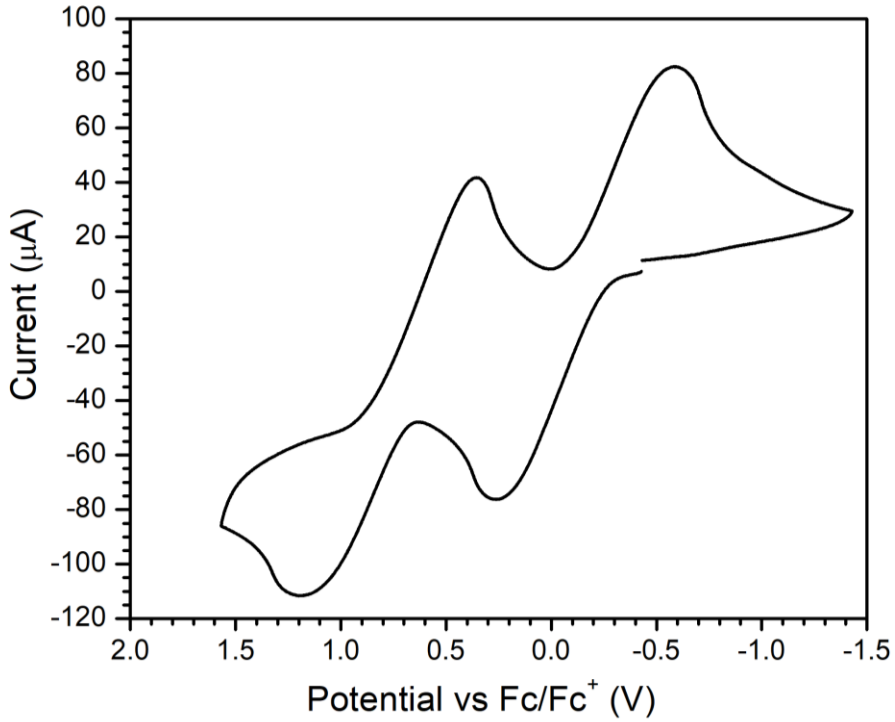

Figure 6.43. CV of **3**. Collected in DCM with 0.1 M of [TBA][PF_6].

Table 6.2. Crystal data and structure refinement for **2-LT**

Identification code	**2-100 K**
Empirical formula	$C_{36}H_{21.33}B_{0.67}Cl_{1.33}F_{16}Fe_{0.67}N_{2.67}S_{2.67}$
Formula weight	972.42
Temperature/K	100(2)
Crystal system	monoclinic
Space group	$P2_1/c$
a/Å	12.6586(12)
b/Å	16.4126(15)
c/Å	32.380(3)
α/°	90
β/°	94.807(2)
γ/°	90
Volume/Å^3	6703.5(11)
Z	6
ρ_{calc}g/cm^3	1.445
μ/mm^{-1}	0.533
F(000)	2916.0
Crystal size/mm^3	0.25 × 0.15 × 0.12
Radiation	MoKα (λ = 0.71073)
2Θ range for data collection/°	4.182 to 44.522
Index ranges	-13 ≤ h ≤ 13, -17 ≤ k ≤ 17, -33 ≤ l ≤ 34
Reflections collected	62339
Independent reflections	8454 [R_{int} = 0.1316, R_{sigma} = 0.0889]
Data/restraints/parameters	8454/0/811
Goodness-of-fit on F^2	1.056
Final R indexes [I>=2σ (I)]	R_1 = 0.0819, wR_2 = 0.1865
Final R indexes [all data]	R_1 = 0.1328, wR_2 = 0.2095
Largest diff. peak/hole / e Å^{-3}	0.72/-0.42

Table 6.3. Fractional Atomic Coordinates ($\times 10^4$) and Equivalent Isotropic Displacement Parameters ($Å^2 \times 10^3$) for **2-LT**.

U_{eq} is defined as 1/3 of of the trace of the orthogonalised U_{IJ} tensor.

Atom	***x***	***y***	***z***	**U(eq)**
Fe1	-752.5(9)	2281.6(7)	1273.7(4)	22.7(3)
S1	-960.4(17)	3635.5(13)	1249.9(7)	26.3(6)
S2	39.8(18)	2332.6(14)	665.4(7)	28.3(6)
S4	-656.5(19)	4883.2(14)	598.6(8)	33.0(6)
S3	328.7(19)	3704.6(14)	75.3(8)	34.5(6)
Cl1	7891(3)	2732(2)	4728.3(11)	73.9(10)
Cl2	7333(3)	1041(2)	4834.1(10)	81.0(11)
F17	323(4)	360(3)	3049.2(18)	49.8(16)
F18	681(4)	452(3)	2422.8(18)	46.7(15)
F12	3380(4)	-442(3)	4178.0(17)	49.4(15)
F16	1713(4)	-209(3)	2861(2)	57.4(18)
F2	7788(5)	4229(3)	3263.5(18)	54.3(17)
F9	7892(4)	-224(4)	3272(2)	59.7(18)
F4	4946(5)	4452(4)	4619.2(18)	57.8(17)
F10	4114(5)	366(4)	4628.4(18)	65.6(19)
F11	4764(5)	-821(4)	4549(2)	68.7(19)
N2	-1351(5)	2188(4)	1817(2)	21.4(17)
N1	651(5)	2239(4)	1576(2)	23.8(17)
F8	8036(5)	-646(4)	3889(2)	76(2)
F5	4506(6)	3211(4)	4707(2)	72(2)
N3	-2117(5)	2017(4)	963(2)	26.7(18)
F3	8429(5)	3198(4)	3591(2)	74(2)
F1	8174(5)	4299(4)	3917(2)	77(2)
F22	5928(6)	482(4)	1495(2)	82(2)
F7	8411(5)	591(4)	3755(3)	86(2)
N4	-658(6)	1057(4)	1308(2)	29.5(19)
F23	6264(6)	-90(4)	2063(2)	82(2)
F24	4690(5)	-13(4)	1819(2)	88(3)
F6	3528(5)	3977(5)	4301(2)	85(2)
C26	5169(6)	2617(5)	2495(3)	23(2)
C24	5247(6)	1177(5)	2488(3)	22(2)
C25	5093(6)	1901(5)	2718(3)	23(2)
C38	3406(6)	1913(5)	3107(2)	16.4(19)
C18	-1659(6)	1256(5)	2364(3)	26(2)
C11	1109(7)	1496(5)	1593(3)	26(2)
C46	5188(6)	2647(5)	3464(3)	22(2)
C32	6155(6)	809(5)	3441(3)	23(2)
C17	-1406(6)	1419(5)	1969(3)	24(2)
C39	2804(6)	1214(5)	3017(3)	25(2)
C27	5385(6)	2640(6)	2086(3)	26(2)
C47	6191(7)	2969(5)	3420(3)	25(2)
C21	-1590(6)	2802(5)	2068(3)	26(2)
C41	1125(7)	463(5)	2816(3)	29(2)
C33	5120(6)	1102(5)	3449(3)	22(2)

Table 6.3. (Continued) Fractional Atomic Coordinates ($\times 10^4$) and Equivalent Isotropic Displacement Parameters ($Å^2 \times 10^3$) for **2-LT**.

Atom	*x*	*y*	*z*	U(eq)
C19	-1897(6)	1902(5)	2617(3)	28(2)
C31	6589(6)	236(5)	3701(3)	27(2)
C23	5458(6)	1193(5)	2080(3)	24(2)
C42	1170(7)	1956(6)	2902(3)	33(2)
C8	-2198(7)	1227(6)	826(3)	31(2)
C20	-1867(6)	2695(6)	2464(3)	27(2)
C40	1721(7)	1225(5)	2916(3)	29(2)
C34	4567(7)	757(5)	3759(3)	25(2)
C43	1741(6)	2663(5)	2989(3)	26(2)
C35	4985(7)	158(5)	4027(3)	30(2)
C15	1204(7)	2859(5)	1768(3)	28(2)
C37	6011(7)	-109(5)	4003(3)	30(2)
C16	-1190(7)	778(5)	1673(3)	28(2)
C9	-1205(7)	746(5)	920(3)	32(2)
C10	495(6)	848(5)	1353(3)	29(2)
C53	4684(7)	2958(5)	3800(3)	27(2)
C28	5526(6)	1918(6)	1870(3)	30(2)
C29	5439(8)	3451(6)	1872(3)	36(3)
C45	2835(7)	2639(6)	3087(3)	29(2)
C13	2665(7)	1994(6)	1991(3)	38(3)
C51	5149(8)	3531(5)	4071(3)	32(2)
C1	-559(6)	3889(5)	785(3)	27(2)
C2	-104(7)	3343(6)	530(3)	30(2)
C12	2095(7)	1350(6)	1801(3)	36(2)
C30	7731(8)	-39(6)	3659(4)	42(3)
C36	4314(8)	-169(6)	4342(3)	37(3)
C44	1184(7)	3467(6)	2986(4)	40(3)
C48	6647(7)	3543(5)	3692(3)	27(2)
C4	-2955(7)	2499(7)	874(3)	41(3)
C22	5584(8)	405(6)	1861(3)	37(3)
C50	6138(8)	3832(5)	4019(3)	36(2)
C5	-3889(7)	2225(7)	664(3)	46(3)
C7	-3085(8)	933(7)	613(3)	47(3)
C14	2212(7)	2757(7)	1970(3)	45(3)
C52	4543(9)	3771(8)	4429(4)	51(3)
C3	-79(7)	4709(5)	145(3)	33(2)
B1	4703(8)	1885(6)	3182(3)	24(2)
C6	-3953(9)	1444(8)	536(3)	57(3)
C54	7161(14)	1888(8)	4547(5)	119(7)
F14	1622(5)	4025(3)	2764.9(19)	56.8(17)
F15	195(5)	3434(4)	2853(3)	120(4)
F19	4607(5)	3905(4)	1917(2)	81(2)
F21	6207(7)	3898(5)	2016(3)	141(5)
F20	5535(10)	3405(4)	1487(3)	140(5)
F13	1201(6)	3788(4)	3366(2)	87(2)

Table 6.4. Anisotropic Displacement Parameters (Å2×103) for **2-LT**

The Anisotropic displacement factor exponent takes the form: $-2\pi^2[h^2a^{*2}U_{11}+2hka^*b^*U_{12}+\ldots]$.

Atom	U_{11}	U_{22}	U_{33}	U_{23}	U_{13}	U_{12}
Fe1	17.4(7)	15.8(7)	35.3(8)	1.9(6)	4.5(6)	1.2(5)
S1	27.4(13)	16.0(12)	36.6(14)	2.3(11)	9.1(11)	2.7(10)
S2	28.7(13)	20.1(12)	37.3(14)	2.1(11)	9.3(11)	2.7(10)
S4	41.0(15)	19.5(13)	40.0(15)	4.7(11)	12.4(12)	3.6(11)
S3	42.4(15)	23.9(13)	39.1(15)	3.2(12)	15.4(12)	3.2(11)
Cl1	69(2)	61(2)	88(2)	12.7(18)	-14.8(18)	1.0(17)
Cl2	79(2)	88(3)	74(2)	17(2)	-8.3(18)	-35(2)
F17	37(3)	35(3)	79(4)	-1(3)	15(3)	-14(3)
F18	53(4)	28(3)	56(4)	3(3)	-10(3)	-12(3)
F12	32(3)	60(4)	56(4)	9(3)	2(3)	-15(3)
F16	32(3)	22(3)	114(5)	2(3)	-16(3)	-2(3)
F2	61(4)	48(4)	56(4)	-1(3)	20(3)	-34(3)
F9	37(4)	64(4)	80(5)	12(4)	16(3)	24(3)
F4	66(4)	51(4)	56(4)	-22(3)	4(3)	3(3)
F10	80(5)	76(5)	44(4)	-7(4)	22(3)	-22(4)
F11	59(4)	72(5)	76(5)	44(4)	9(3)	1(4)
N2	19(4)	4(4)	41(5)	0(4)	1(3)	2(3)
N1	19(4)	18(4)	36(5)	-3(4)	10(3)	-4(3)
F8	45(4)	82(5)	103(5)	37(4)	19(4)	45(4)
F5	95(6)	74(5)	51(4)	-11(4)	34(4)	-20(4)
N3	20(4)	19(4)	41(5)	5(4)	1(3)	1(3)
F3	25(3)	72(5)	125(6)	10(4)	8(4)	-9(3)
F1	76(5)	89(5)	66(5)	-17(4)	10(4)	-61(4)
F22	131(7)	52(4)	71(5)	-18(4)	55(5)	-7(4)
F7	29(4)	65(5)	161(7)	-8(5)	-5(4)	0(3)
N4	41(5)	17(4)	31(5)	-6(4)	3(4)	-3(4)
F23	98(6)	47(4)	95(5)	-28(4)	-19(4)	33(4)
F24	47(4)	75(5)	147(7)	-63(5)	32(4)	-30(4)
F6	47(4)	114(6)	94(5)	-61(5)	6(4)	21(4)
C26	6(4)	19(5)	45(6)	-5(5)	7(4)	4(4)
C24	15(5)	14(5)	38(6)	3(4)	3(4)	1(4)
C25	9(5)	24(5)	36(6)	3(5)	-5(4)	6(4)
C38	9(4)	10(5)	30(5)	3(4)	5(4)	4(4)
C18	15(5)	15(5)	51(7)	4(5)	6(4)	4(4)
C11	19(5)	13(5)	46(6)	3(4)	7(4)	5(4)
C46	17(5)	18(5)	32(5)	9(4)	2(4)	1(4)
C32	13(5)	16(5)	41(6)	-2(4)	7(4)	1(4)
C17	12(5)	26(6)	34(6)	0(5)	3(4)	0(4)
C39	19(5)	17(5)	38(6)	0(4)	7(4)	4(4)
C27	7(4)	34(6)	38(6)	5(5)	1(4)	2(4)
C47	27(5)	17(5)	31(5)	0(4)	2(4)	3(4)
C21	13(5)	15(5)	48(7)	4(5)	1(4)	5(4)
C41	24(6)	19(5)	45(7)	5(5)	3(5)	6(5)
C33	17(5)	15(5)	36(6)	-2(4)	7(4)	0(4)
C19	10(5)	30(6)	44(6)	3(5)	9(4)	-3(4)

Table 6.4. (Continued) Anisotropic Displacement Parameters (Å2×103) for **2-LT**

C31	14(5)	19(5)	48(6)	-4(5)	1(5)	-6(4)
C23	10(5)	27(6)	34(6)	-4(5)	1(4)	3(4)
C42	10(5)	37(6)	53(7)	8(5)	8(4)	4(5)
C8	28(6)	34(6)	32(6)	3(5)	9(5)	-2(5)
C20	15(5)	34(6)	32(6)	-6(5)	9(4)	3(4)
C40	16(5)	26(6)	44(6)	6(5)	4(4)	-3(4)
C34	19(5)	26(5)	31(6)	-5(5)	0(4)	3(4)
C43	10(5)	13(5)	54(6)	2(4)	7(4)	2(4)
C35	39(6)	24(5)	25(5)	2(5)	-3(5)	-12(5)
C15	22(5)	29(6)	36(6)	2(5)	16(4)	7(4)
C37	20(5)	20(5)	48(6)	-2(5)	-8(5)	2(4)
C16	20(5)	18(5)	46(6)	2(5)	5(4)	7(4)
C9	37(6)	16(5)	40(6)	-10(4)	-5(5)	-4(4)
C10	17(5)	21(5)	50(6)	11(5)	8(4)	7(4)
C53	16(5)	25(5)	39(6)	5(5)	2(4)	5(4)
C28	14(5)	45(7)	29(6)	3(5)	2(4)	3(4)
C29	22(6)	35(6)	53(8)	15(6)	15(5)	1(5)
C45	19(5)	30(6)	40(6)	0(5)	7(4)	-8(4)
C13	23(5)	44(7)	46(7)	14(5)	3(5)	7(5)
C51	42(7)	26(6)	26(6)	1(5)	-7(5)	6(5)
C1	18(5)	21(5)	41(6)	-8(4)	1(4)	7(4)
C2	18(5)	35(6)	38(6)	5(5)	1(4)	4(4)
C12	26(6)	36(6)	46(6)	10(5)	7(5)	10(5)
C30	27(6)	21(6)	75(9)	3(6)	-6(6)	5(5)
C36	43(7)	38(6)	31(6)	-2(6)	4(5)	-6(5)
C44	23(6)	26(6)	70(8)	3(6)	4(5)	-5(5)
C48	21(5)	13(5)	46(6)	6(5)	-6(5)	-11(4)
C4	29(6)	59(7)	36(6)	13(5)	11(5)	-2(6)
C22	31(6)	36(6)	46(7)	-10(5)	10(5)	4(5)
C50	47(7)	19(5)	44(7)	-3(5)	2(5)	5(5)
C5	16(6)	71(9)	50(7)	-2(6)	-5(5)	1(5)
C7	44(7)	47(7)	49(7)	-5(6)	-3(6)	-16(6)
C14	20(6)	71(9)	43(7)	2(6)	5(5)	-9(6)
C52	43(7)	61(8)	48(8)	-23(7)	5(6)	-8(6)
C3	30(6)	26(6)	44(6)	10(4)	4(5)	5(5)
C49	60(8)	52(8)	42(7)	-1(6)	-1(6)	-24(7)
B1	20(6)	16(6)	37(7)	-2(5)	5(5)	7(4)
C6	34(7)	83(10)	51(8)	10(7)	-6(5)	-14(7)
C54	169(17)	72(11)	101(12)	-17(9)	-76(12)	31(11)
F14	65(4)	32(4)	77(4)	17(3)	26(4)	27(3)
F15	23(4)	40(4)	289(12)	-27(5)	-27(5)	14(3)
F19	63(5)	58(4)	130(6)	51(4)	43(4)	25(4)
F21	79(6)	94(6)	236(12)	107(7)	-62(7)	-46(5)
F20	311(15)	44(5)	80(6)	30(4)	100(8)	52(6)
F13	140(7)	45(4)	82(5)	6(4)	42(5)	42(4)

Table 6.5. Bond Lengths for **2-LT**

Atom	Atom	Length/Å	Atom	Atom	Length/Å
Fe1	S1	2.238(2)	C18	C19	1.388(12)
Fe1	S2	2.286(3)	C11	C10	1.494(12)
Fe1	N2	1.979(7)	C11	C12	1.389(12)
Fe1	N1	1.957(7)	C46	C47	1.394(11)
Fe1	N3	1.973(7)	C46	C53	1.404(12)
Fe1	N4	2.017(7)	C46	B1	1.637(13)
S1	C1	1.679(9)	C32	C33	1.398(11)
S2	C2	1.721(9)	C32	C31	1.347(12)
S4	C1	1.741(9)	C17	C16	1.464(12)
S4	C3	1.718(10)	C39	C40	1.383(11)
S3	C2	1.720(9)	C27	C28	1.395(12)
S3	C3	1.748(9)	C27	C29	1.505(13)
Cl1	C54	1.739(15)	C47	C48	1.382(12)
Cl2	C54	1.677(14)	C21	C20	1.369(12)
F17	C41	1.325(10)	C41	C40	1.481(12)
F18	C41	1.349(10)	C33	C34	1.391(12)
F12	C36	1.333(11)	C33	B1	1.613(13)
F16	C41	1.332(10)	C19	C20	1.394(12)
F2	C49	1.348(12)	C31	C37	1.390(12)
F9	C30	1.320(12)	C31	C30	1.532(13)
F4	C52	1.355(12)	C23	C28	1.377(12)
F10	C36	1.316(11)	C23	C22	1.490(13)
F11	C36	1.364(11)	C42	C40	1.386(12)
N2	C17	1.357(11)	C42	C43	1.384(12)
N2	C21	1.345(10)	C8	C9	1.493(12)
N1	C11	1.350(10)	C8	C7	1.357(13)
N1	C15	1.356(11)	C34	C35	1.387(12)
F8	C30	1.286(11)	C43	C45	1.396(11)
F5	C52	1.291(13)	C43	C44	1.496(13)
N3	C8	1.371(11)	C35	C37	1.379(12)
N3	C4	1.335(11)	C35	C36	1.480(13)
F3	C49	1.347(13)	C15	C14	1.395(12)
F1	C49	1.308(11)	C53	C51	1.382(12)
F22	C22	1.303(11)	C29	F19	1.307(11)
F7	C30	1.364(11)	C29	F21	1.274(12)
N4	C16	1.480(11)	C29	F20	1.265(12)
N4	C9	1.474(10)	C13	C12	1.393(13)
N4	C10	1.493(10)	C13	C14	1.377(14)
F23	C22	1.319(11)	C51	C50	1.369(13)
F24	C22	1.320(11)	C51	C52	1.496(14)
F6	C52	1.359(12)	C1	C2	1.378(12)
C26	C25	1.386(12)	C44	F14	1.313(11)
C26	C27	1.375(12)	C44	F15	1.289(11)
C24	C25	1.425(12)	C44	F13	1.336(12)
C24	C23	1.369(12)	C48	C50	1.370(13)
C25	B1	1.620(13)	C48	C49	1.504(14)

Table 6.5. (Continued) Bond Lengths for **2-LT**

Atom	Atom	Length/Å	Atom	Atom	Length/Å
C38	C39	1.393(11)	C4	C5	1.389(13)
C38	C45	1.392(11)	C5	C6	1.347(15)
C38	B1	1.641(12)	C7	C6	1.388(15)
C18	C17	1.373(12)	C3	C3[1]	1.366(17)

[1]-X,1-Y,-Z

Table 6.6. Bond Angles for **2-LT**

Atom	Atom	Atom	Angle/˚	Atom	Atom	Atom	Angle/˚
S1	Fe1	S2	89.58(9)	C42	C43	C44	120.1(7)
N2	Fe1	S1	93.16(19)	C45	C43	C44	119.1(8)
N2	Fe1	S2	175.8(2)	C34	C35	C36	118.4(9)
N2	Fe1	N4	84.2(3)	C37	C35	C34	120.1(8)
N1	Fe1	S1	98.7(2)	C37	C35	C36	121.5(9)
N1	Fe1	S2	89.3(2)	N1	C15	C14	122.9(9)
N1	Fe1	N2	87.2(3)	C35	C37	C31	117.7(8)
N1	Fe1	N3	165.2(3)	C17	C16	N4	115.0(7)
N1	Fe1	N4	83.6(3)	N4	C9	C8	108.6(7)
N3	Fe1	S1	96.1(2)	N4	C10	C11	110.4(7)
N3	Fe1	S2	89.8(2)	C51	C53	C46	122.9(8)
N3	Fe1	N2	93.0(3)	C23	C28	C27	118.0(8)
N3	Fe1	N4	81.6(3)	F19	C29	C27	112.7(8)
N4	Fe1	S1	176.4(2)	F21	C29	C27	113.8(9)
N4	Fe1	S2	93.2(2)	F21	C29	F19	103.2(10)
C1	S1	Fe1	103.5(3)	F20	C29	C27	114.4(9)
C2	S2	Fe1	102.1(3)	F20	C29	F19	106.7(9)
C3	S4	C1	96.8(4)	F20	C29	F21	105.1(10)
C2	S3	C3	95.5(4)	C38	C45	C43	122.4(8)
C17	N2	Fe1	115.4(5)	C14	C13	C12	118.1(9)
C21	N2	Fe1	127.0(6)	C53	C51	C52	116.8(9)
C21	N2	C17	117.2(7)	C50	C51	C53	120.9(9)
C11	N1	Fe1	114.9(5)	C50	C51	C52	122.3(9)
C11	N1	C15	117.2(7)	S1	C1	S4	121.7(5)
C15	N1	Fe1	128.0(6)	C2	C1	S1	123.3(7)
C8	N3	Fe1	114.3(6)	C2	C1	S4	115.0(7)
C4	N3	Fe1	128.7(7)	S3	C2	S2	121.1(6)
C4	N3	C8	117.1(8)	C1	C2	S2	121.0(7)
C16	N4	Fe1	108.8(5)	C1	C2	S3	117.9(7)
C16	N4	C10	111.0(7)	C11	C12	C13	119.6(9)
C9	N4	Fe1	106.0(5)	F9	C30	F7	104.3(9)
C9	N4	C16	111.1(7)	F9	C30	C31	112.0(8)
C9	N4	C10	112.9(7)	F8	C30	F9	108.1(8)
C10	N4	Fe1	106.7(5)	F8	C30	F7	107.5(9)
C27	C26	C25	123.6(8)	F8	C30	C31	114.6(9)
C23	C24	C25	122.4(8)	F7	C30	C31	109.8(8)
C26	C25	C24	114.5(8)	F12	C36	F11	104.5(8)
C26	C25	B1	122.5(8)	F12	C36	C35	112.9(8)
C24	C25	B1	122.5(7)	F10	C36	F12	106.8(8)
C39	C38	B1	122.0(7)	F10	C36	F11	105.9(8)
C45	C38	C39	115.0(7)	F10	C36	C35	113.5(8)
C45	C38	B1	122.7(7)	F11	C36	C35	112.5(8)
C17	C18	C19	118.7(8)	F14	C44	C43	113.5(8)
N1	C11	C10	114.8(7)	F14	C44	F13	104.6(8)
N1	C11	C12	122.7(8)	F15	C44	C43	114.1(8)
C12	C11	C10	122.5(8)	F15	C44	F14	106.9(9)

Table 6.6. (Continued) Bond Angles for **2-LT**

Atom	Atom	Atom	Angle/˚	Atom	Atom	Atom	Angle/˚
C47	C46	C53	114.6(8)	F15	C44	F13	105.3(9)
C47	C46	B1	122.4(8)	F13	C44	C43	111.7(9)
C53	C46	B1	122.5(7)	C47	C48	C49	117.3(9)
C31	C32	C33	124.3(8)	C50	C48	C47	121.9(8)
N2	C17	C18	122.8(8)	C50	C48	C49	120.7(9)
N2	C17	C16	114.5(8)	N3	C4	C5	122.8(10)
C18	C17	C16	122.7(8)	F22	C22	F23	104.9(8)
C40	C39	C38	123.6(8)	F22	C22	F24	107.8(9)
C26	C27	C28	120.3(8)	F22	C22	C23	114.0(9)
C26	C27	C29	119.2(9)	F23	C22	F24	104.4(9)
C28	C27	C29	120.5(8)	F23	C22	C23	112.9(8)
C48	C47	C46	122.0(8)	F24	C22	C23	112.1(8)
N2	C21	C20	123.9(8)	C51	C50	C48	117.7(9)
F17	C41	F18	104.9(7)	C6	C5	C4	119.1(10)
F17	C41	F16	106.3(7)	C8	C7	C6	119.0(10)
F17	C41	C40	112.6(8)	C13	C14	C15	119.4(10)
F18	C41	C40	112.4(7)	F4	C52	F6	104.1(9)
F16	C41	F18	106.0(7)	F4	C52	C51	111.8(9)
F16	C41	C40	113.9(7)	F5	C52	F4	107.8(9)
C32	C33	B1	121.9(8)	F5	C52	F6	107.6(10)
C34	C33	C32	113.7(8)	F5	C52	C51	113.8(10)
C34	C33	B1	123.3(7)	F6	C52	C51	111.3(9)
C18	C19	C20	119.4(8)	S4	C3	S3	114.8(5)
C32	C31	C37	120.8(8)	C3[1]	C3	S4	124.7(10)
C32	C31	C30	119.3(9)	C3[1]	C3	S3	120.6(10)
C37	C31	C30	120.0(8)	F2	C49	C48	112.2(9)
C24	C23	C28	121.2(8)	F3	C49	F2	103.9(9)
C24	C23	C22	118.7(8)	F3	C49	C48	112.7(9)
C28	C23	C22	120.1(8)	F1	C49	F2	106.9(9)
C43	C42	C40	117.9(8)	F1	C49	F3	106.7(10)
N3	C8	C9	113.3(7)	F1	C49	C48	113.9(9)
C7	C8	N3	122.5(9)	C25	B1	C38	104.0(7)
C7	C8	C9	124.2(9)	C25	B1	C46	112.0(7)
C21	C20	C19	118.0(8)	C46	B1	C38	112.6(7)
C39	C40	C41	121.2(8)	C33	B1	C25	113.6(7)
C39	C40	C42	120.3(8)	C33	B1	C38	112.3(7)
C42	C40	C41	118.5(8)	C33	B1	C46	102.6(7)
C35	C34	C33	123.4(8)	C5	C6	C7	119.6(10)
C42	C43	C45	120.9(8)	Cl2	C54	Cl1	115.7(7)

[1]-X,1-Y,-Z

Table 6.7. Solvent masks information for **2-LT**

Number	X	Y	Z	Volume	Electron count	Content
1	0.000	0.000	0.000	645.3	190.5	?
2	0.000	0.500	0.500	645.3	190.5	?

Table 6.8. Crystal data and structure refinement for **2-RT**

Identification code	**2-RT**
Empirical formula	$C_{106}H_{60}B_2F_{48}Fe_2N_8S_8$
Formula weight	2747.42
Temperature/K	293(2)
Crystal system	monoclinic
Space group	$P2_1/c$
a/Å	12.7265(13)
b/Å	16.2243(16)
c/Å	28.827(3)
α/°	90
β/°	92.733(2)
γ/°	90
Volume/Å^3	5945.4(10)
Z	2
ρ_{calc}g/cm^3	1.535
μ/mm^{-1}	0.509
F(000)	2748.0
Crystal size/mm^3	0.18 × 0.11 × 0.08
Radiation	MoKα (λ = 0.71073)
2Θ range for data collection/°	4.258 to 41.758
Index ranges	-12 ≤ h ≤ 12, -16 ≤ k ≤ 16, -28 ≤ l ≤ 28
Reflections collected	80374
Independent reflections	6267 [R_{int} = 0.1542, R_{sigma} = 0.0645]
Data/restraints/parameters	6267/1029/784
Goodness-of-fit on F^2	1.023
Final R indexes [I>=2σ (I)]	R_1 = 0.0804, wR_2 = 0.1941
Final R indexes [all data]	R_1 = 0.1501, wR_2 = 0.2351
Largest diff. peak/hole / e Å^{-3}	0.77/-0.43

Table 6.9. Fractional Atomic Coordinates (×104) and Equivalent Isotropic Displacement Parameters (Å2×103) for **2-RT**

U_{eq} is defined as 1/3 of of the trace of the orthogonalised U_{IJ} tensor.

Atom	*x*	*y*	*z*	U(eq)
Fe1	-570.9(11)	3378.5(8)	3931.0(5)	74.2(5)
S1	283(3)	2949.2(18)	4683.1(10)	103.7(10)
S2	-1062(3)	1983.9(17)	3813.3(9)	95.9(10)
S3	-661(2)	484.1(17)	4353.7(10)	95.4(10)
S4	428(3)	1282(2)	5109.5(11)	107.8(11)
N1	-1869(8)	3883(6)	4294(3)	93(3)
N2	-286(7)	4753(5)	3961(3)	83(2)
N3	-1277(6)	3800(5)	3274(3)	67(2)
N4	892(6)	3531(6)	3606(3)	84(2)
C1	-44(8)	380(6)	4883(4)	88(3)
C2	-528(7)	1527(6)	4300(4)	77(3)
C3	21(8)	1938(7)	4666(4)	82(3)
C4	-2749(10)	3487(8)	4360(4)	115(4)

Table 6.9. (Continued) Fractional Atomic Coordinates (×104) and Equivalent Isotropic Displacement Parameters (Å2×103) for **2-RT**

Atom	*x*	*y*	*z*	U(eq)
C5	-3519(14)	3840(11)	4628(6)	174(7)
C6	-3321(17)	4593(13)	4828(7)	191(8)
C7	-2406(15)	4980(10)	4765(5)	158(6)
C8	-1695(12)	4636(8)	4490(4)	101(3)
C9	-675(12)	5016(8)	4398(4)	118(4)
C10	-888(8)	5158(6)	3576(4)	88(3)
C11	-1237(7)	4607(6)	3181(4)	69(3)
C12	-1551(8)	4912(7)	2746(4)	88(3)
C13	-1909(8)	4392(9)	2410(4)	91(3)
C14	-1949(7)	3579(8)	2500(4)	81(3)
C15	-1638(8)	3305(6)	2931(4)	75(3)
C16	864(10)	4862(8)	3941(5)	132(5)
C17	1333(9)	4267(8)	3628(4)	98(3)
C18	2253(10)	4451(10)	3402(6)	140(5)
C19	2663(13)	3833(12)	3139(6)	157(6)
C20	2229(11)	3089(10)	3113(6)	151(6)
C21	1338(9)	2970(8)	3350(4)	107(4)
F1	6850(8)	7804(6)	4918(3)	186(4)
F2	7257(6)	6853(5)	4503(3)	153(3)
F3	6074(6)	6652(6)	4949(3)	192(4)
F4	2708(9)	6517(9)	4108(4)	294(7)
F5	2592(8)	6885(8)	3458(4)	229(5)
F6	2223(8)	7623(10)	3940(7)	310(7)
F7	5313(7)	7013(5)	1917(4)	195(4)
F8	3864(9)	6987(6)	2044(5)	234(5)
F9	4265(13)	7456(5)	1461(4)	276(7)
F10	5079(8)	10871(7)	1699(5)	266(6)
F11	3788(10)	11053(5)	2017(3)	204(4)
F12	3710(9)	10429(5)	1433(3)	201(4)
F13	8256(5)	11275(3)	2720(2)	114(2)
F14	9123(6)	10519(4)	2275(2)	126(2)
F15	9774(5)	10840(4)	2930(3)	124(2)
F16	9329(12)	7403(9)	3529(6)	282(6)
F17	8740(9)	7065(6)	2955(6)	262(6)
F18	10036(8)	7682(6)	2964(6)	316(8)
F19	6846(9)	10511(9)	4855(4)	235(5)
F20	6656(12)	11600(8)	4640(3)	307(7)
F21	5726(7)	11099(8)	5080(3)	213(5)
F22	2379(7)	11446(9)	4109(4)	255(6)
F23	2076(7)	10263(9)	3975(6)	273(6)
F24	2305(6)	11010(6)	3464(3)	185(4)
C22	5324(7)	8346(5)	3627(3)	63(2)
C23	5963(7)	8057(5)	3994(3)	69(2)
C24	5665(9)	7471(6)	4296(3)	79(3)
C25	4682(9)	7144(6)	4257(4)	87(3)

Table 6.9. (Continued) Fractional Atomic Coordinates (×104) and Equivalent Isotropic Displacement Parameters (Å2×103) for **2-RT**

Atom	*x*	*y*	*z*	U(eq)
C26	3991(9)	7411(7)	3901(4)	89(3)
C27	4333(7)	7995(6)	3597(3)	76(3)
C28	6405(12)	7194(9)	4678(5)	116(3)
C29	2964(14)	7074(13)	3864(7)	161(5)
C30	5092(6)	9082(5)	2784(3)	61(2)
C31	4962(7)	8322(6)	2552(3)	69(2)
C32	4616(7)	8275(6)	2098(4)	73(2)
C33	4383(7)	8981(6)	1850(3)	76(3)
C34	4500(7)	9740(6)	2063(3)	70(2)
C35	4845(7)	9773(6)	2520(3)	68(2)
C36	4310(12)	10484(8)	1802(5)	112(4)
C37	4529(13)	7479(8)	1872(5)	116(4)
C38	6912(7)	9145(5)	3211(3)	65(2)
C39	7537(7)	8443(6)	3213(3)	78(3)
C40	8572(8)	8457(7)	3089(4)	96(3)
C41	9007(8)	9173(6)	2942(4)	94(3)
C42	8411(7)	9870(6)	2911(3)	73(2)
C43	7387(7)	9869(6)	3053(3)	72(3)
C44	8858(10)	10628(7)	2714(5)	92(3)
C45	9202(14)	7714(10)	3126(9)	170(6)
C46	5255(7)	9893(5)	3611(3)	59(2)
C47	5874(7)	10218(5)	3979(3)	70(2)
C48	5470(9)	10739(6)	4305(4)	81(3)
C49	4421(9)	10947(6)	4274(4)	86(3)
C50	3792(8)	10643(6)	3911(4)	83(3)
C51	4206(7)	10132(6)	3594(3)	74(3)
C52	2707(12)	10888(12)	3877(6)	143(5)
C53	6089(13)	11033(10)	4691(6)	128(4)
B1	5645(8)	9120(6)	3301(4)	63(2)

Table 6.10. Anisotropic Displacement Parameters ($Å^2 \times 10^3$) for **2-RT**

The Anisotropic displacement factor exponent takes the form: $-2\pi^2[h^2a^{*2}U_{11}+2hka^*b^*U_{12}+\ldots]$.

Atom	U_{11}	U_{22}	U_{33}	U_{23}	U_{13}	U_{12}
Fe1	85.9(10)	67.1(9)	69.3(9)	12.3(7)	-1.8(7)	13.2(8)
S1	132(3)	87(2)	89(2)	14.2(17)	-27.9(18)	10.8(19)
S2	134(3)	72.1(17)	79.8(19)	22.5(15)	-16.6(17)	8.0(17)
S3	101(2)	78.6(19)	106(2)	37.5(17)	-5.7(18)	7.9(16)
S4	123(3)	100(2)	99(2)	39.3(19)	-20.3(19)	5.6(19)
N1	111(7)	102(7)	66(6)	20(5)	8(5)	17(6)
N2	93(7)	77(6)	79(6)	-12(5)	-11(6)	1(5)
N3	71(5)	59(5)	70(6)	10(5)	-1(4)	-1(4)
N4	76(6)	80(6)	96(6)	21(5)	3(5)	13(4)
C1	88(7)	79(7)	99(8)	33(6)	6(6)	11(6)
C2	72(7)	76(7)	85(7)	35(6)	12(6)	19(6)
C3	80(7)	93(8)	73(7)	29(6)	6(6)	16(6)

Table 6.10. (Continued) Anisotropic Displacement Parameters ($Å^2 \times 10^3$) for **2-RT**

Atom	U_{11}	U_{22}	U_{33}	U_{23}	U_{13}	U_{12}
C4	121(9)	114(9)	114(10)	46(8)	30(8)	21(7)
C5	171(13)	166(13)	194(17)	93(12)	100(12)	57(11)
C6	202(16)	172(15)	209(18)	62(13)	121(15)	97(13)
C7	216(16)	128(11)	137(12)	22(9)	76(12)	73(10)
C8	139(10)	97(8)	68(8)	15(6)	14(7)	42(8)
C9	166(14)	96(9)	91(10)	-12(8)	-13(9)	18(9)
C10	100(8)	61(7)	103(9)	9(7)	-5(7)	4(6)
C11	68(7)	62(7)	78(8)	11(6)	12(6)	2(5)
C12	87(8)	81(8)	95(9)	55(8)	8(7)	16(6)
C13	85(8)	121(11)	65(8)	11(8)	-11(6)	2(8)
C14	77(7)	84(9)	82(9)	3(7)	-9(6)	2(6)
C15	85(7)	60(7)	81(8)	13(7)	4(6)	-3(6)
C16	114(11)	122(10)	157(12)	-36(8)	-24(8)	-16(8)
C17	85(8)	100(7)	107(9)	20(6)	-16(6)	-2(6)
C18	80(9)	143(12)	198(15)	48(10)	-1(8)	-7(8)
C19	105(11)	171(13)	199(16)	68(12)	32(10)	23(9)
C20	110(11)	152(11)	195(15)	33(12)	59(10)	46(9)
C21	89(8)	95(8)	139(11)	25(7)	17(7)	30(7)
F1	228(9)	183(8)	139(7)	-13(6)	-82(6)	46(6)
F2	134(6)	174(7)	152(6)	37(5)	7(5)	59(5)
F3	150(7)	253(10)	175(8)	139(7)	23(6)	27(6)
F4	218(10)	365(14)	290(12)	184(12)	-80(9)	-214(10)
F5	160(8)	327(13)	194(9)	30(8)	-49(7)	-143(8)
F6	92(7)	314(14)	530(20)	-84(13)	60(10)	-71(8)
F7	163(7)	118(6)	302(11)	-120(7)	-24(7)	33(5)
F8	239(9)	128(7)	343(12)	-119(8)	109(10)	-88(7)
F9	552(19)	115(7)	149(7)	-62(6)	-111(9)	46(9)
F10	148(7)	256(11)	392(15)	250(11)	9(8)	-31(7)
F11	317(12)	106(6)	188(8)	42(5)	11(8)	79(7)
F12	301(11)	133(6)	158(7)	55(5)	-96(7)	-2(7)
F13	115(5)	57(3)	174(6)	0(4)	34(4)	-5(3)
F14	164(6)	95(5)	124(5)	-11(4)	51(5)	-28(4)
F15	101(4)	102(5)	169(6)	-27(4)	24(4)	-37(4)
F16	308(15)	205(11)	331(14)	84(10)	7(10)	166(11)
F17	210(10)	92(6)	480(18)	-16(9)	-3(11)	70(6)
F18	172(8)	138(7)	660(20)	137(11)	217(11)	100(6)
F19	198(9)	320(12)	178(9)	-84(8)	-75(7)	47(9)
F20	458(16)	285(11)	164(8)	62(8)	-119(9)	-282(12)
F21	160(7)	356(14)	123(6)	-104(8)	-5(5)	-20(7)
F22	139(7)	364(13)	258(10)	-178(10)	-33(7)	141(8)
F23	79(6)	286(11)	459(18)	109(11)	61(9)	45(7)
F24	125(6)	240(10)	187(8)	-53(7)	-33(6)	87(6)
C22	63(5)	52(5)	74(5)	-5(4)	7(4)	-1(4)
C23	62(6)	60(6)	85(6)	1(4)	5(4)	-4(5)
C24	96(6)	65(6)	76(6)	2(4)	11(5)	7(5)
C25	108(7)	65(7)	91(7)	19(6)	23(5)	-9(6)

Table 6.10. (Continued) Anisotropic Displacement Parameters ($Å^2 \times 10^3$) for **2-RT**

Atom	U_{11}	U_{22}	U_{33}	U_{23}	U_{13}	U_{12}
C26	89(6)	87(7)	91(7)	-1(5)	9(5)	-32(5)
C27	71(6)	77(6)	82(7)	2(5)	2(5)	-16(5)
C28	127(9)	116(9)	105(9)	25(6)	6(6)	31(7)
C29	112(9)	200(14)	171(11)	44(10)	-3(9)	-82(8)
C30	48(5)	57(5)	78(5)	0(4)	7(4)	2(4)
C31	62(6)	60(5)	87(6)	-2(5)	11(5)	0(5)
C32	72(6)	66(5)	83(6)	-10(4)	13(5)	3(5)
C33	74(6)	83(5)	74(6)	3(4)	16(5)	-6(5)
C34	60(6)	74(5)	76(5)	11(4)	5(5)	-1(5)
C35	68(6)	58(5)	77(5)	0(4)	3(5)	3(5)
C36	129(10)	94(7)	115(9)	51(7)	2(7)	-4(7)
C37	140(10)	88(7)	119(8)	-44(7)	4(8)	3(6)
C38	56(4)	59(5)	79(6)	-3(5)	-2(4)	3(4)
C39	68(5)	54(5)	112(7)	5(5)	25(6)	6(4)
C40	65(6)	73(5)	151(9)	18(6)	22(6)	18(5)
C41	59(6)	76(6)	149(10)	4(6)	25(6)	8(5)
C42	62(5)	56(5)	101(7)	-9(5)	10(5)	-2(4)
C43	64(5)	54(5)	98(7)	-9(5)	10(5)	6(4)
C44	101(7)	56(5)	122(7)	-16(6)	24(6)	-16(5)
C45	119(10)	88(8)	310(16)	59(10)	71(11)	48(7)
C46	62(5)	52(5)	66(5)	6(4)	16(4)	-5(4)
C47	70(6)	66(6)	73(6)	4(4)	4(4)	-3(5)
C48	90(6)	70(6)	83(6)	-8(5)	12(5)	-20(5)
C49	99(6)	77(7)	85(7)	-8(5)	30(5)	3(6)
C50	74(6)	84(7)	92(7)	-9(5)	20(5)	17(5)
C51	66(5)	77(6)	81(6)	-7(5)	10(5)	13(5)
C52	81(7)	202(13)	148(10)	-41(10)	20(7)	46(8)
C53	129(10)	130(10)	126(9)	-53(8)	1(7)	-47(7)
B1	55(5)	57(5)	77(6)	1(4)	9(5)	8(4)

Table 6.11. Bond Lengths for **2-RT**

Atom	Atom	Length/Å	Atom	Atom	Length/Å
Fe1	S1	2.479(3)	F12	C36	1.282(14)
Fe1	S2	2.368(3)	F13	C44	1.301(12)
Fe1	N1	2.160(9)	F14	C44	1.336(12)
Fe1	N2	2.261(8)	F15	C44	1.340(12)
Fe1	N3	2.168(7)	F16	C45	1.27(2)
Fe1	N4	2.138(8)	F17	C45	1.29(2)
S1	C3	1.675(11)	F18	C45	1.180(16)
S2	C2	1.701(10)	F19	C53	1.351(17)
S3	C1	1.690(10)	F20	C53	1.183(14)
S3	C2	1.708(10)	F21	C53	1.237(15)
S4	C1	1.701(11)	F22	C52	1.211(16)
S4	C3	1.724(9)	F23	C52	1.331(19)
N1	C4	1.313(14)	F24	C52	1.290(17)
N1	C8	1.359(14)	C22	C23	1.386(11)

Table 6.11. (Continued) Bond Lengths for **2-RT**

Atom	Atom	Length/Å	Atom	Atom	Length/Å
N2	C9	1.439(13)	C22	C27	1.383(11)
N2	C10	1.475(11)	C22	B1	1.630(13)
N2	C16	1.478(13)	C23	C24	1.354(12)
N3	C11	1.338(11)	C24	C25	1.359(13)
N3	C15	1.337(11)	C24	C28	1.485(16)
N4	C17	1.320(13)	C25	C26	1.388(13)
N4	C21	1.318(13)	C26	C27	1.376(13)
C1	C1[1]	1.408(18)	C26	C29	1.416(17)
C2	C3	1.404(13)	C30	C31	1.408(11)
C4	C5	1.398(18)	C30	C35	1.383(11)
C5	C6	1.37(3)	C30	B1	1.620(13)
C6	C7	1.34(2)	C31	C32	1.364(12)
C7	C8	1.350(16)	C32	C33	1.373(12)
C8	C9	1.474(16)	C32	C37	1.449(15)
C10	C11	1.498(13)	C33	C34	1.381(12)
C11	C12	1.387(13)	C34	C35	1.370(12)
C12	C13	1.348(14)	C34	C36	1.437(15)
C13	C14	1.345(14)	C38	C39	1.390(11)
C14	C15	1.361(13)	C38	C43	1.407(11)
C16	C17	1.468(16)	C38	B1	1.645(13)
C17	C18	1.398(16)	C39	C40	1.382(12)
C18	C19	1.38(2)	C40	C41	1.363(13)
C19	C20	1.33(2)	C40	C45	1.449(17)
C20	C21	1.365(16)	C41	C42	1.362(12)
F1	C28	1.321(15)	C42	C43	1.384(11)
F2	C28	1.337(14)	C42	C44	1.480(13)
F3	C28	1.262(14)	C46	C47	1.395(11)
F4	C29	1.199(17)	C46	C51	1.389(11)
F5	C29	1.278(18)	C46	B1	1.631(13)
F6	C29	1.32(2)	C47	C48	1.381(12)
F7	C37	1.253(14)	C48	C49	1.376(13)
F8	C37	1.279(15)	C48	C53	1.416(16)
F9	C37	1.218(14)	C49	C50	1.377(13)
F10	C36	1.211(14)	C50	C51	1.359(12)
F11	C36	1.310(15)	C50	C52	1.436(16)

[1]-X,-Y,1-Z

Table 6.12. Bond Angles for **2-RT**

Atom	Atom	Atom	Angle/˚	Atom	Atom	Atom	Angle/˚
S2	Fe1	S1	87.63(10)	F4	C29	F5	105.0(16)
N1	Fe1	S1	89.8(2)	F4	C29	F6	101.2(17)
N1	Fe1	S2	103.2(3)	F4	C29	C26	121.4(17)
N1	Fe1	N2	74.5(4)	F5	C29	F6	94.5(16)
N1	Fe1	N3	90.5(3)	F5	C29	C26	117.5(15)
N2	Fe1	S1	100.4(2)	F6	C29	C26	113.0(17)
N2	Fe1	S2	171.6(2)	C31	C30	B1	120.4(8)
N3	Fe1	S1	177.6(2)	C35	C30	C31	115.6(8)
N3	Fe1	S2	94.6(2)	C35	C30	B1	123.5(8)
N3	Fe1	N2	77.4(3)	C32	C31	C30	122.0(9)
N4	Fe1	S1	93.5(2)	C31	C32	C33	120.3(9)
N4	Fe1	S2	106.1(3)	C31	C32	C37	119.6(10)
N4	Fe1	N1	150.6(4)	C33	C32	C37	120.0(11)
N4	Fe1	N2	76.2(3)	C32	C33	C34	119.8(9)
N4	Fe1	N3	85.1(3)	C33	C34	C36	120.3(10)
C3	S1	Fe1	99.8(4)	C35	C34	C33	119.0(9)
C2	S2	Fe1	101.9(4)	C35	C34	C36	120.6(10)
C1	S3	C2	97.8(5)	C34	C35	C30	123.4(9)
C1	S4	C3	99.1(5)	F10	C36	F11	100.7(14)
C4	N1	Fe1	124.2(9)	F10	C36	F12	106.7(13)
C4	N1	C8	120.2(12)	F10	C36	C34	116.5(13)
C8	N1	Fe1	115.4(9)	F11	C36	C34	114.9(12)
C9	N2	Fe1	105.4(7)	F12	C36	F11	98.3(12)
C9	N2	C10	109.8(9)	F12	C36	C34	117.0(12)
C9	N2	C16	112.4(10)	F7	C37	F8	97.0(13)
C10	N2	Fe1	109.5(6)	F7	C37	C32	116.7(12)
C10	N2	C16	113.5(9)	F8	C37	C32	114.8(12)
C16	N2	Fe1	105.9(7)	F9	C37	F7	105.2(13)
C11	N3	Fe1	117.8(7)	F9	C37	F8	101.6(14)
C15	N3	Fe1	124.7(7)	F9	C37	C32	118.4(13)
C15	N3	C11	117.0(8)	C39	C38	C43	115.5(8)
C17	N4	Fe1	117.4(8)	C39	C38	B1	123.0(8)
C21	N4	Fe1	125.0(8)	C43	C38	B1	120.8(8)
C21	N4	C17	117.3(11)	C40	C39	C38	122.5(9)
S3	C1	S4	113.6(5)	C39	C40	C45	119.9(11)
C1[1]	C1	S3	123.0(12)	C41	C40	C39	120.0(9)
C1[1]	C1	S4	123.4(11)	C41	C40	C45	120.1(11)
S2	C2	S3	117.9(7)	C42	C41	C40	119.7(9)
C3	C2	S2	125.3(8)	C41	C42	C43	120.5(9)
C3	C2	S3	116.8(7)	C41	C42	C44	119.4(9)
S1	C3	S4	122.0(7)	C43	C42	C44	120.0(9)
C2	C3	S1	125.4(7)	C42	C43	C38	121.5(8)
C2	C3	S4	112.6(8)	F13	C44	F14	107.2(11)
N1	C4	C5	120.2(15)	F13	C44	F15	106.6(9)
C6	C5	C4	118.6(18)	F13	C44	C42	115.3(10)
C7	C6	C5	120.2(18)	F14	C44	F15	102.8(10)

Table 6.12. (Continued) Bond Angles for **2-RT**

Atom	Atom	Atom	Angle/˚	Atom	Atom	Atom	Angle/˚
C6	C7	C8	119.6(18)	F14	C44	C42	111.9(9)
N1	C8	C9	115.4(12)	F15	C44	C42	112.1(10)
C7	C8	N1	121.0(15)	F16	C45	F17	93.6(14)
C7	C8	C9	123.6(15)	F16	C45	C40	116.2(18)
N2	C9	C8	112.2(11)	F17	C45	C40	114.2(16)
N2	C10	C11	115.6(8)	F18	C45	F16	105.4(18)
N3	C11	C10	116.3(9)	F18	C45	F17	102.5(18)
N3	C11	C12	121.2(10)	F18	C45	C40	120.8(15)
C12	C11	C10	122.4(10)	C47	C46	B1	122.1(8)
C13	C12	C11	120.0(10)	C51	C46	C47	115.4(8)
C14	C13	C12	119.3(10)	C51	C46	B1	120.9(8)
C13	C14	C15	119.0(10)	C48	C47	C46	122.2(9)
N3	C15	C14	123.6(9)	C47	C48	C53	122.0(12)
C17	C16	N2	112.2(10)	C49	C48	C47	119.9(10)
N4	C17	C16	116.1(12)	C49	C48	C53	118.0(12)
N4	C17	C18	122.3(13)	C48	C49	C50	119.2(10)
C18	C17	C16	121.3(13)	C49	C50	C52	118.3(11)
C19	C18	C17	116.7(16)	C51	C50	C49	120.0(10)
C20	C19	C18	121.8(17)	C51	C50	C52	121.7(12)
C19	C20	C21	117.0(16)	C50	C51	C46	123.4(10)
N4	C21	C20	125.0(13)	F22	C52	F23	103.1(15)
C23	C22	B1	123.1(8)	F22	C52	F24	105.2(15)
C27	C22	C23	114.0(8)	F22	C52	C50	121.6(15)
C27	C22	B1	122.3(8)	F23	C52	C50	111.2(15)
C24	C23	C22	123.8(9)	F24	C52	F23	95.5(15)
C23	C24	C25	120.4(10)	F24	C52	C50	116.3(13)
C23	C24	C28	120.1(11)	F19	C53	C48	115.1(13)
C25	C24	C28	119.4(11)	F20	C53	F19	95.8(15)
C24	C25	C26	119.1(10)	F20	C53	F21	107.6(14)
C25	C26	C29	119.1(12)	F20	C53	C48	118.9(15)
C27	C26	C25	118.5(10)	F21	C53	F19	91.6(14)
C27	C26	C29	122.4(12)	F21	C53	C48	121.6(14)
C26	C27	C22	124.1(10)	C22	B1	C38	112.6(7)
F1	C28	F2	100.0(13)	C22	B1	C46	100.7(7)
F1	C28	C24	113.8(11)	C30	B1	C22	113.0(7)
F2	C28	C24	110.0(11)	C30	B1	C38	104.0(7)
F3	C28	F1	110.1(13)	C30	B1	C46	113.8(7)
F3	C28	F2	104.3(11)	C46	B1	C38	113.2(7)
F3	C28	C24	116.9(13)				

[1]-X,-Y,1-Z

Table 6.13. Crystal data and structure refinement for **3**

Identification code	**3**
Empirical formula	$C_{22}H_{20}Cl_2FeN_4S_5$
Formula weight	627.47
Temperature/K	60
Crystal system	monoclinic
Space group	$P2_1/c$
a/Å	12.277(2)
b/Å	15.270(3)
c/Å	14.049(2)
α/°	90
β/°	95.225(3)
γ/°	90
Volume/Å^3	2622.8(7)
Z	4
ρ_{calc}g/cm^3	1.589
μ/mm^{-1}	0.266
F(000)	1280.0
Crystal size/mm^3	0.1 × 0.1 × 0.05
Radiation	synchrotron (λ = 0.41328)
2Θ range for data collection/°	1.936 to 30.604
Index ranges	-15 ≤ h ≤ 15, -19 ≤ k ≤ 19, -17 ≤ l ≤ 17
Reflections collected	59090
Independent reflections	5561 [R_{int} = 0.0718, R_{sigma} = 0.0291]
Data/restraints/parameters	5561/0/307
Goodness-of-fit on F^2	1.060
Final R indexes [I>=2σ (I)]	R_1 = 0.0309, wR_2 = 0.0823
Final R indexes [all data]	R_1 = 0.0377, wR_2 = 0.0847
Largest diff. peak/hole / e Å^{-3}	0.46/-0.45

Table 6.14. Fractional Atomic Coordinates (×104) and Equivalent Isotropic Displacement Parameters (Å2×103) for **3**

U_{eq} is defined as 1/3 of of the trace of the orthogonalised U_{IJ} tensor

Atom	*x*	*y*	*z*	U(eq)
Fe1	2675.4(2)	6663.5(2)	3772.6(2)	16.32(9)
S1	3705.4(4)	5702.8(3)	2868.5(4)	18.04(12)
S2	1064.0(4)	6440.9(3)	2619.6(4)	18.12(12)
S3	704.8(4)	4980.6(3)	1184.9(4)	18.69(12)
S4	1329.4(4)	3483.5(4)	-34.4(4)	22.39(13)
S5	2935.4(4)	4424.5(3)	1337.0(4)	18.44(12)
N1	2033.0(15)	5797.1(12)	4815.3(13)	19.7(4)
N2	1885.1(14)	7566.1(11)	4776.5(13)	18.9(4)
N3	3011.0(15)	7983.8(11)	3250.5(13)	19.1(4)
N4	4093.5(15)	7030.4(12)	4806.3(13)	19.8(4)
C1	1644.3(17)	4256.8(13)	784.5(15)	19.0(4)
C2	2639.2(17)	5283.0(13)	2093.4(15)	17.6(4)
C3	1577.1(17)	5563.8(13)	2013.9(15)	16.9(4)
C4	2290.9(19)	4943.7(14)	4919.3(16)	23.0(5)
C5	1812(2)	4409.6(16)	5558.3(18)	27.8(5)
C6	1075(2)	4771.0(16)	6133.5(18)	29.3(5)
C7	822.5(18)	5646.9(16)	6045.0(17)	25.5(5)
C8	1299.5(17)	6144.7(14)	5363.0(16)	20.4(4)
C9	968.8(18)	7082.4(14)	5140.5(16)	21.0(4)
C10	1521.3(18)	8337.6(14)	4196.2(17)	22.0(4)
C11	2429.9(18)	8634.5(14)	3613.1(16)	20.8(4)
C12	2648(2)	9512.1(15)	3449.0(18)	26.5(5)
C13	3495(2)	9717.6(16)	2895.8(18)	29.8(5)
C14	4092.6(19)	9057.5(15)	2521.8(17)	26.4(5)
C15	3826.3(18)	8194.3(14)	2718.1(16)	21.3(4)
C16	2697.7(17)	7811.1(15)	5575.7(16)	21.8(4)
C17	3866.8(18)	7734.9(14)	5329.3(15)	19.8(4)
C18	4657.9(18)	8340.4(14)	5648.6(16)	22.0(4)
C19	5725.7(19)	8207.8(15)	5441.4(16)	24.5(5)
C20	5974.1(18)	7468.1(15)	4934.7(16)	24.4(5)
C21	5136.8(18)	6899.4(15)	4626.6(17)	23.3(5)
Cl1	6915.5(5)	7875.0(4)	7678.6(4)	30.39(14)
Cl2	8339.9(5)	6685.5(4)	6745.3(5)	31.62(14)
C22	8290(2)	7609.3(17)	7496(2)	33.3(6)

Table 6.15. Anisotropic Displacement Parameters (Å2×103) for **3**

The Anisotropic displacement factor exponent takes the form: $-2\pi^2[h^2a^{*2}U_{11}+2hka^*b^*U_{12}+\ldots]$.

Atom	U_{11}	U_{22}	U_{33}	U_{23}	U_{13}	U_{12}
Fe1	19.63(16)	13.77(15)	16.21(16)	-0.53(10)	5.19(11)	0.33(11)
S1	19.0(2)	16.5(2)	19.1(3)	-2.66(18)	4.10(19)	0.07(19)
S2	19.8(2)	15.4(2)	19.7(3)	-1.34(18)	4.87(19)	1.51(19)
S3	19.5(3)	15.7(2)	21.2(3)	-1.50(18)	3.76(19)	-0.38(19)
S4	22.7(3)	19.2(3)	25.3(3)	-6.4(2)	2.7(2)	-1.1(2)
S5	19.7(3)	15.2(2)	20.8(3)	-3.13(19)	3.80(19)	0.34(19)
N1	22.1(9)	19.1(9)	18.3(9)	0.4(7)	4.6(7)	1.5(7)
N2	19.9(9)	18.6(9)	18.6(9)	-1.1(7)	3.7(7)	1.0(7)
N3	22.3(9)	16.5(8)	18.8(9)	-2.1(7)	3.3(7)	-2.5(7)
N4	22.0(9)	18.9(9)	18.9(10)	-1.8(7)	3.7(7)	1.7(7)
C1	22.5(10)	14.6(9)	20.3(11)	0.5(8)	4.4(8)	-0.3(8)
C2	22.1(10)	13.2(9)	18.1(11)	0.0(7)	5.1(8)	-0.7(8)
C3	22.1(10)	11.6(9)	17.3(10)	0.6(7)	3.8(8)	-2.0(7)
C4	25.7(11)	19.2(10)	24.7(12)	3.0(8)	5.0(9)	1.7(8)
C5	32.3(12)	21.8(11)	30.0(13)	6.9(9)	6.1(10)	2.4(9)
C6	29.5(12)	29.5(12)	29.9(13)	8.8(10)	8.0(10)	-1.1(10)
C7	22.0(11)	31.3(12)	24.4(12)	3.8(9)	8.7(9)	2.9(9)
C8	19.4(10)	21.8(11)	20.5(11)	-0.3(8)	4.1(8)	2.3(8)
C9	21.8(11)	21.8(11)	20.2(11)	0.2(8)	6.6(8)	1.7(8)
C10	22.6(11)	15.1(10)	28.6(12)	-0.4(8)	4.9(9)	2.7(8)
C11	24.6(11)	17.0(10)	20.5(11)	-0.8(8)	-0.3(8)	0.8(8)
C12	32.5(12)	16.5(10)	30.2(13)	-0.9(9)	1.5(10)	1.0(9)
C13	36.8(13)	18.8(11)	33.1(14)	5.0(9)	-0.1(10)	-5.2(10)
C14	29.3(12)	25.1(12)	25.0(12)	2.5(9)	3.0(9)	-8.8(9)
C15	25.3(11)	19.8(10)	19.1(11)	-1.7(8)	3.8(8)	-3.1(8)
C16	23.4(11)	24.6(11)	17.9(11)	-6.0(8)	3.6(8)	1.9(9)
C17	22.7(10)	21.8(10)	15.3(11)	-0.6(8)	3.4(8)	0.9(8)
C18	27.3(11)	22.6(11)	16.3(11)	-2.7(8)	2.8(8)	2.1(9)
C19	26.1(11)	27.5(12)	20.0(12)	-1.9(9)	2.5(9)	-4.5(9)
C20	22.3(11)	29.8(12)	21.5(12)	-2.5(9)	3.3(8)	1.8(9)
C21	22.5(11)	23.1(11)	24.7(12)	-3.5(9)	4.2(9)	5.3(9)
Cl1	37.5(3)	25.2(3)	28.9(3)	-1.4(2)	5.6(2)	6.5(2)
Cl2	37.7(3)	24.2(3)	34.8(3)	1.5(2)	13.3(3)	4.8(2)
C22	35.1(13)	29.8(13)	35.2(15)	-6.0(10)	4.6(10)	-6.9(10)

Table 6.16. Bond Lengths for **3**

Atom	Atom	Length/Å	Atom	Atom	Length/Å
Fe1	S1	2.3783(6)	N4	C17	1.346(3)
Fe1	S2	2.4637(7)	N4	C21	1.343(3)
Fe1	N1	2.1745(18)	C2	C3	1.368(3)
Fe1	N2	2.2538(18)	C4	C5	1.383(3)
Fe1	N3	2.1971(18)	C5	C6	1.382(3)
Fe1	N4	2.2347(19)	C6	C7	1.376(3)
S1	C2	1.747(2)	C7	C8	1.393(3)
S2	C3	1.736(2)	C8	C9	1.513(3)
S3	C1	1.728(2)	C10	C11	1.512(3)
S3	C3	1.752(2)	C11	C12	1.390(3)
S4	C1	1.669(2)	C12	C13	1.390(4)
S5	C1	1.719(2)	C13	C14	1.378(4)
S5	C2	1.746(2)	C14	C15	1.392(3)
N1	C4	1.346(3)	C16	C17	1.511(3)
N1	C8	1.346(3)	C17	C18	1.386(3)
N2	C9	1.476(3)	C18	C19	1.383(3)
N2	C10	1.478(3)	C19	C20	1.384(3)
N2	C16	1.481(3)	C20	C21	1.385(3)
N3	C11	1.350(3)	Cl1	C22	1.777(3)
N3	C15	1.342(3)	Cl2	C22	1.765(3)

Table 6.17. Bond Angles for **3**

Atom	Atom	Atom	Angle/˚	Atom	Atom	Atom	Angle/˚
S1	Fe1	S2	89.89(2)	S4	C1	S3	123.86(13)
N1	Fe1	S1	103.16(5)	S4	C1	S5	124.24(13)
N1	Fe1	S2	92.30(5)	S5	C1	S3	111.90(12)
N1	Fe1	N2	75.36(7)	S5	C2	S1	117.97(12)
N1	Fe1	N3	150.89(7)	C3	C2	S1	126.21(16)
N1	Fe1	N4	91.36(7)	C3	C2	S5	115.82(16)
N2	Fe1	S1	172.53(5)	S2	C3	S3	119.41(12)
N2	Fe1	S2	97.47(5)	C2	C3	S2	126.01(17)
N3	Fe1	S1	105.23(5)	C2	C3	S3	114.55(16)
N3	Fe1	S2	94.06(5)	N1	C4	C5	122.1(2)
N3	Fe1	N2	75.65(7)	C6	C5	C4	118.9(2)
N3	Fe1	N4	80.10(7)	C7	C6	C5	119.3(2)
N4	Fe1	S1	94.65(5)	C6	C7	C8	119.2(2)
N4	Fe1	S2	173.38(5)	N1	C8	C7	121.5(2)
N4	Fe1	N2	78.13(7)	N1	C8	C9	115.85(18)
C2	S1	Fe1	98.89(7)	C7	C8	C9	122.46(19)
C3	S2	Fe1	97.08(7)	N2	C9	C8	110.27(17)
C1	S3	C3	98.96(10)	N2	C10	C11	109.68(17)
C1	S5	C2	98.74(10)	N3	C11	C10	115.15(18)
C4	N1	Fe1	124.47(15)	N3	C11	C12	122.1(2)
C8	N1	Fe1	116.61(14)	C12	C11	C10	122.8(2)
C8	N1	C4	118.88(19)	C13	C12	C11	118.4(2)
C9	N2	Fe1	107.22(12)	C14	C13	C12	120.0(2)
C9	N2	C10	112.85(17)	C13	C14	C15	118.3(2)
C9	N2	C16	110.24(17)	N3	C15	C14	122.5(2)
C10	N2	Fe1	105.54(13)	N2	C16	C17	113.28(17)
C10	N2	C16	111.45(17)	N4	C17	C16	115.76(19)
C16	N2	Fe1	109.29(12)	N4	C17	C18	122.4(2)
C11	N3	Fe1	115.33(14)	C18	C17	C16	121.79(19)
C15	N3	Fe1	125.30(15)	C19	C18	C17	118.9(2)
C15	N3	C11	118.73(19)	C18	C19	C20	119.0(2)
C17	N4	Fe1	111.56(14)	C19	C20	C21	118.7(2)
C21	N4	Fe1	122.72(15)	N4	C21	C20	122.8(2)
C21	N4	C17	118.03(19)	Cl2	C22	Cl1	110.72(14)

Table 6.18. Crystal data and structure refinement for **4**

Identification code	**4**
Empirical formula	$C_{26.25}H_{15.5}B_{0.5}Cl_{0.33}F_{11.98}Fe_{0.5}N_2S_{2.5}$
Formula weight	711.85
Temperature/K	100.0
Crystal system	triclinic
Space group	P-1
a/Å	11.918(4)
b/Å	15.177(4)
c/Å	18.720(5)
α/°	67.648(6)
β/°	77.670(7)
γ/°	83.106(6)
Volume/Å^3	3056.7(15)
Z	4
ρ_{calc}g/cm^3	1.5467
μ/mm^{-1}	0.559
F(000)	1427.2
Crystal size/mm^3	0.2 × 0.2 × 0.1
Radiation	Mo Kα (λ = 0.71073)
2Θ range for data collection/°	4.46 to 38.06
Index ranges	-10 ≤ h ≤ 10, -13 ≤ k ≤ 13, -17 ≤ l ≤ 17
Reflections collected	21088
Independent reflections	4906 [R_{int} = 0.2612, R_{sigma} = 0.2099]
Data/restraints/parameters	4906/0/385
Goodness-of-fit on F^2	1.126
Final R indexes [I>=2σ (I)]	R_1 = 0.1407, wR_2 = 0.3271
Final R indexes [all data]	R_1 = 0.2397, wR_2 = 0.4108
Largest diff. peak/hole / e Å^{-3}	1.98/-1.27

Table 6.19. Fractional Atomic Coordinates (×10^4) and Equivalent Isotropic Displacement Parameters (Å^2×10^3) for **4**

U_{eq} is defined as 1/3 of of the trace of the orthogonalised U_{IJ} tensor.

Atom	*x*	*y*	*z*	U(eq)
Fe01	1281(3)	7936(2)	1427(2)	27.6(12)
S002	1857(5)	9302(4)	447(4)	27.5(18)
S003	2867(5)	7175(4)	1019(4)	33.5(19)
S004	5084(6)	7923(5)	-103(4)	36(2)
S005	4136(5)	9849(4)	-635(4)	31.8(19)
S006	6548(6)	9445(5)	-1296(4)	47(2)
F007	6221(11)	8608(10)	3005(8)	51(4)
F008	6836(11)	5425(10)	8119(8)	47(4)
F009	-1146(12)	7279(10)	5493(8)	51(4)
F00A	6065(12)	6848(10)	7845(8)	55(4)
F00B	7224(12)	6484(10)	6945(9)	56(4)
F00C	7236(13)	8975(11)	3637(9)	68(5)
F00D	-479(13)	8372(11)	4430(9)	66(5)
N00E	665(14)	6737(12)	2310(10)	16(5)

Table 6.19. (Continued) Fractional Atomic Coordinates ($\times 10^4$) and Equivalent Isotropic Displacement Parameters ($Å^2 \times 10^3$) for **4**

Atom	*x*	*y*	*z*	U(eq)
F00F	2949(13)	11056(11)	4795(9)	64(5)
F00G	6774(14)	7522(12)	4005(10)	78(5)
F00H	-949(13)	7046(11)	4429(9)	72(5)
F00I	2317(13)	10715(10)	3964(9)	62(5)
N00J	-146(15)	8570(12)	1847(10)	26(5)
N00K	226(14)	7710(12)	842(10)	18(5)
F00L	3900(15)	11354(12)	3660(10)	80(5)
F00M	2694(16)	3592(12)	7892(10)	86(6)
F00N	4209(15)	3102(13)	8359(11)	87(6)
N00O	1911(16)	8267(13)	2176(11)	33(5)
C00P	-420(20)	7400(17)	4823(14)	29(7)
F00Q	2929(18)	5589(15)	3569(13)	46(6)
C00R	728(19)	6985(16)	4926(13)	25(6)
C00S	2366(19)	6863(15)	5560(13)	24(6)
C00T	1280(20)	8933(17)	2431(14)	32(7)
C00U	4147(18)	4690(15)	7428(12)	17(6)
F00V	3990(20)	5070(20)	4433(17)	67(8)
F00W	3689(18)	8924(17)	7818(15)	50(7)
C00X	2920(20)	5284(18)	4348(15)	37(7)
C00Y	5070(18)	4913(16)	7666(13)	26(6)
C00Z	2659(18)	8018(14)	7101(12)	16(6)
C010	1301(18)	7240(15)	5387(12)	22(6)
C011	4799(18)	7921(16)	4917(13)	24(6)
C012	2238(18)	7545(15)	6758(12)	20(6)
C013	5321(18)	8630(16)	4254(13)	22(6)
C014	-340(20)	6878(16)	2710(13)	26(6)
C015	-798(18)	8246(15)	840(13)	22(6)
C016	2600(20)	8686(19)	8136(16)	40(7)
C017	3770(19)	8096(16)	5388(13)	28(6)
C018	-1540(20)	7396(16)	210(13)	29(7)
C019	2890(20)	6242(16)	5185(13)	27(6)
C01A	-950(20)	6159(16)	3258(13)	28(7)
C01B	5413(18)	5852(15)	7326(13)	21(6)
C01C	4842(19)	6523(17)	6783(13)	29(7)
C01D	3883(18)	6333(15)	6544(12)	17(6)
C01E	330(20)	7031(17)	556(13)	35(7)
C01F	278(19)	9350(16)	2012(14)	32(7)
C01G	2049(19)	8166(16)	7776(13)	24(6)
C01H	-810(20)	8972(16)	1188(13)	32(7)
C01I	-520(20)	6874(18)	219(14)	39(7)
C01J	3340(20)	9032(16)	5133(13)	27(6)
C01K	2870(20)	7881(18)	2467(14)	43(8)
C01L	3230(18)	8993(15)	100(12)	19(6)
C01M	3840(20)	9750(17)	4485(14)	31(7)
C01N	3250(20)	10732(19)	4227(16)	42(8)

Table 6.19. (Continued) Fractional Atomic Coordinates ($\times 10^4$) and Equivalent Isotropic Displacement Parameters ($Å^2 \times 10^3$) for **4**

Atom	*x*	*y*	*z*	U(eq)
C01O	2360(20)	5989(17)	4693(14)	33(7)
C01P	5304(17)	9111(14)	-722(12)	17(6)
C01Q	1254(18)	6356(15)	4584(13)	24(6)
C01R	1520(20)	9203(17)	2999(14)	36(7)
C01S	4850(20)	9551(17)	4024(14)	36(7)
C01T	-1640(20)	8104(16)	532(13)	29(7)
C01U	3830(30)	3690(20)	7715(19)	66(9)
C01V	3570(19)	5407(16)	6901(13)	25(6)
C01W	1120(20)	5857(17)	2458(14)	33(7)
F01X	2700(20)	8122(17)	8903(14)	67(7)
F01Y	-1297(18)	7294(15)	8519(12)	118(7)
C01Z	6390(20)	6160(20)	7541(17)	52(8)
C020	-861(19)	7885(15)	2543(13)	26(7)
C021	3210(20)	8111(17)	3047(14)	37(7)
C022	6350(20)	8433(19)	3721(16)	44(8)
F023	4128(17)	3298(15)	7173(12)	112(7)
C024	990(20)	7825(19)	8103(17)	57(8)
C025	3660(20)	8102(18)	345(14)	39(7)
C026	1170(20)	7121(19)	7104(16)	53(8)
C027	580(20)	5063(18)	3012(14)	37(7)
C028	-510(20)	5212(17)	3419(14)	35(7)
F029	2070(30)	9430(20)	8220(20)	87(9)
F02A	2360(20)	4498(19)	4604(17)	76(8)
C02B	2510(20)	8778(18)	3289(15)	47(8)
B02C	3080(20)	7190(19)	6060(16)	26(8)
C02D	480(30)	7294(19)	7780(16)	59(9)
F02E	-1140(20)	6830(20)	7683(17)	178(11)
F02F	-590(20)	6170(20)	8590(16)	165(10)
Cl02	6180(40)	5530(30)	120(30)	170(16)
Cl1	7480(60)	4420(50)	660(40)	280(30)
C02L	5500(50)	4780(50)	200(40)	80(20)
F1	3250(30)	4430(20)	4880(20)	23(10)
F6	4050(40)	5570(30)	3900(30)	47(12)
F12	2350(40)	5020(30)	3960(30)	49(12)
F1AA	1800(30)	8780(30)	8800(30)	47(12)
F5	2480(40)	9690(30)	7710(30)	38(12)
F0AA	3590(40)	8410(40)	8300(30)	56(14)

Table 6.20. Bond Lengths for **4**

Atom	Atom	Length/Å	Atom	Atom	Length/Å
Fe01	S002	2.247(7)	C00X	F6	1.44(5)
Fe01	S003	2.240(7)	C00X	F12	1.29(4)
Fe01	N00E	2.024(17)	C00Y	C01B	1.39(3)
Fe01	N00J	2.012(17)	C00Z	C012	1.33(3)
Fe01	N00K	1.969(16)	C00Z	C01G	1.40(3)
Fe01	N00O	1.964(18)	C011	C013	1.38(3)
S002	C01L	1.71(2)	C011	C017	1.41(3)
S003	C025	1.71(3)	C012	C026	1.41(3)
S004	C01P	1.75(2)	C012	B02C	1.69(3)
S004	C025	1.77(3)	C013	C01S	1.38(3)
S005	C01L	1.76(2)	C013	C022	1.49(3)
S005	C01P	1.70(2)	C014	C01A	1.34(3)
S006	C01P	1.64(2)	C014	C020	1.52(3)
F007	C022	1.31(3)	C015	C01H	1.48(3)
F008	C01Z	1.37(3)	C015	C01T	1.34(3)
F009	C00P	1.32(2)	C016	C01G	1.49(3)
F00A	C01Z	1.35(3)	C016	F01X	1.39(3)
F00B	C01Z	1.30(3)	C016	F029	1.27(3)
F00C	C022	1.36(3)	C016	F1AA	1.44(5)
F00D	C00P	1.38(2)	C016	F5	1.43(5)
N00E	C014	1.31(2)	C016	F0AA	1.27(5)
N00E	C01W	1.33(2)	C017	C01J	1.39(3)
F00F	C01N	1.30(3)	C017	B02C	1.63(4)
F00G	C022	1.35(3)	C018	C01I	1.36(3)
F00H	C00P	1.34(2)	C018	C01T	1.40(3)
F00I	C01N	1.32(3)	C019	C01O	1.41(3)
N00J	C01F	1.50(3)	C01A	C028	1.41(3)
N00J	C01H	1.50(3)	C01B	C01C	1.37(3)
N00J	C020	1.49(3)	C01B	C01Z	1.49(3)
N00K	C015	1.38(2)	C01C	C01D	1.41(3)
N00K	C01E	1.31(3)	C01D	C01V	1.37(3)
F00L	C01N	1.30(3)	C01D	B02C	1.61(3)
F00M	C01U	1.33(3)	C01E	C01I	1.39(3)
F00N	C01U	1.33(3)	C01G	C024	1.35(3)
N00O	C00T	1.36(3)	C01J	C01M	1.36(3)
N00O	C01K	1.34(3)	C01K	C021	1.41(3)
C00P	C00R	1.46(3)	C01L	C025	1.33(3)
F00Q	C00X	1.35(3)	C01M	C01N	1.51(3)
F00Q	F6	1.58(4)	C01M	C01S	1.40(3)
F00Q	F12	1.10(5)	C01O	C01Q	1.39(3)
C00R	C010	1.39(3)	C01R	C02B	1.38(3)
C00R	C01Q	1.36(3)	C01U	F023	1.33(3)
C00S	C010	1.38(3)	C01W	C027	1.38(3)
C00S	C019	1.39(3)	F01X	F1AA	1.36(4)
C00S	B02C	1.63(3)	F01X	F0AA	1.34(5)
C00T	C01F	1.51(3)	F01Y	F02F	1.79(3)

Table 6.20. (Continued) Bond Lengths for **4**

Atom	Atom	Length/Å	Atom	Atom	Length/Å
C00T	C01R	1.37(3)	C021	C02B	1.38(3)
C00U	C00Y	1.39(3)	C024	C02D	1.42(3)
C00U	C01U	1.48(3)	C026	C02D	1.45(3)
C00U	C01V	1.39(3)	C027	C028	1.40(3)
F00V	C00X	1.30(3)	F029	F1AA	1.17(4)
F00V	F1	1.30(4)	F029	F5	0.94(4)
F00V	F6	0.99(4)	F02A	F1	1.27(4)
F00W	C016	1.34(3)	F02A	F12	1.16(4)
F00W	F5	1.73(4)	F02E	F02F	1.83(3)
F00W	F0AA	0.94(5)	Cl02	Cl1	2.24(8)
C00X	C01O	1.48(3)	Cl02	C02L	1.42(7)
C00X	F02A	1.32(3)	Cl1	C02L	2.61(9)
C00X	F1	1.38(4)	C02L	C02L[1]	1.50(12)

[1]1-X,1-Y,-Z

Table 6.21. Bond Angles for **4**

Atom	Atom	Atom	Angle/˚	Atom	Atom	Atom	Angle/˚
S003	Fe01	S002	89.6(3)	F0AA	C016	F1AA	111(3)
N00E	Fe01	S002	176.6(5)	F0AA	C016	F5	114(3)
N00E	Fe01	S003	93.4(5)	C01J	C017	C011	115(2)
N00J	Fe01	S002	92.9(5)	B02C	C017	C011	119(2)
N00J	Fe01	S003	177.2(6)	B02C	C017	C01J	126(2)
N00J	Fe01	N00E	84.1(7)	C01T	C018	C01I	116(2)
N00K	Fe01	S002	92.6(5)	C01O	C019	C00S	123(2)
N00K	Fe01	S003	99.2(5)	C028	C01A	C014	119(2)
N00K	Fe01	N00E	85.5(7)	C01C	C01B	C00Y	120(2)
N00K	Fe01	N00J	82.0(7)	C01Z	C01B	C00Y	122(2)
N00O	Fe01	S002	91.6(6)	C01Z	C01B	C01C	118(2)
N00O	Fe01	S003	97.0(6)	C01D	C01C	C01B	124(2)
N00O	Fe01	N00E	89.5(7)	C01V	C01D	C01C	113.8(19)
N00O	Fe01	N00J	81.7(7)	B02C	C01D	C01C	121.0(19)
N00O	Fe01	N00K	163.3(8)	B02C	C01D	C01V	124(2)
C01L	S002	Fe01	101.9(8)	C01I	C01E	N00K	122(2)
C025	S003	Fe01	101.9(9)	C00T	C01F	N00J	107.2(18)
C025	S004	C01P	96.8(11)	C016	C01G	C00Z	119(2)
C01P	S005	C01L	97.8(10)	C024	C01G	C00Z	120(2)
C014	N00E	Fe01	113.2(14)	C024	C01G	C016	121(2)
C01W	N00E	Fe01	126.7(16)	C015	C01H	N00J	108.5(17)
C01W	N00E	C014	120(2)	C01E	C01I	C018	121(2)
C01F	N00J	Fe01	105.0(13)	C01M	C01J	C017	125(2)
C01H	N00J	Fe01	105.1(13)	C021	C01K	N00O	122(2)
C01H	N00J	C01F	110.9(17)	S005	C01L	S002	120.9(13)
C020	N00J	Fe01	112.3(13)	C025	C01L	S002	122.6(19)
C020	N00J	C01F	113.7(17)	C025	C01L	S005	116.5(18)
C020	N00J	C01H	109.5(17)	C01N	C01M	C01J	120(2)
C015	N00K	Fe01	114.6(13)	C01S	C01M	C01J	119(2)

Table 6.21. (Continued) Bond Angles for **4**

Atom	Atom	Atom	Angle/˚	Atom	Atom	Atom	Angle/˚
C01E	N00K	Fe01	126.9(15)	C01S	C01M	C01N	120(2)
C01E	N00K	C015	117.9(18)	F00I	C01N	F00F	107(2)
C00T	N00O	Fe01	115.3(15)	F00L	C01N	F00F	107(2)
C01K	N00O	Fe01	126.3(16)	F00L	C01N	F00I	107(2)
C01K	N00O	C00T	118(2)	C01M	C01N	F00F	113(2)
F00D	C00P	F009	103.1(18)	C01M	C01N	F00I	111(2)
F00H	C00P	F009	104.7(19)	C01M	C01N	F00L	112(2)
F00H	C00P	F00D	104.6(18)	C019	C01O	C00X	121(2)
C00R	C00P	F009	114(2)	C01Q	C01O	C00X	120(2)
C00R	C00P	F00D	115(2)	C01Q	C01O	C019	119(2)
C00R	C00P	F00H	114(2)	S005	C01P	S004	113.2(12)
F6	F00Q	C00X	58(2)	S006	C01P	S004	121.4(12)
F12	F00Q	C00X	62(3)	S006	C01P	S005	125.3(13)
F12	F00Q	F6	113(3)	C01O	C01Q	C00R	120(2)
C010	C00R	C00P	119(2)	C02B	C01R	C00T	115(2)
C01Q	C00R	C00P	122(2)	C01M	C01S	C013	118(2)
C01Q	C00R	C010	119(2)	C018	C01T	C015	121(2)
C019	C00S	C010	115(2)	F00N	C01U	F00M	104(3)
B02C	C00S	C010	125(2)	C00U	C01U	F00M	113(2)
B02C	C00S	C019	120(2)	C00U	C01U	F00N	116(3)
C01F	C00T	N00O	112(2)	F023	C01U	F00M	101(2)
C01R	C00T	N00O	124(2)	F023	C01U	F00N	108(3)
C01R	C00T	C01F	123(2)	F023	C01U	C00U	113(3)
C01U	C00U	C00Y	119(2)	C01D	C01V	C00U	125(2)
C01V	C00U	C00Y	120(2)	C027	C01W	N00E	123(2)
C01V	C00U	C01U	121(2)	F1AA	F01X	C016	63(2)
F1	F00V	C00X	64(2)	F0AA	F01X	C016	55(2)
F6	F00V	C00X	77(3)	F0AA	F01X	F1AA	111(3)
F6	F00V	F1	136(4)	F00A	C01Z	F008	105(2)
F5	F00W	C016	54(2)	F00B	C01Z	F008	108(2)
F0AA	F00W	C016	65(3)	F00B	C01Z	F00A	108(2)
F0AA	F00W	F5	112(4)	C01B	C01Z	F008	111(2)
F00V	C00X	F00Q	106(2)	C01B	C01Z	F00A	112(2)
C01O	C00X	F00Q	112(2)	C01B	C01Z	F00B	112(2)
C01O	C00X	F00V	114(2)	C014	C020	N00J	110.2(18)
F02A	C00X	F00Q	101(2)	C02B	C021	C01K	116(2)
F02A	C00X	F00V	110(3)	F00C	C022	F007	105(2)
F02A	C00X	C01O	113(2)	F00G	C022	F007	107(2)
F1	C00X	F00Q	133(2)	F00G	C022	F00C	105(2)
F1	C00X	F00V	58(2)	C013	C022	F007	116(2)
F1	C00X	C01O	115(2)	C013	C022	F00C	111(2)
F1	C00X	F02A	56(2)	C013	C022	F00G	113(2)
F6	C00X	F00Q	69(2)	C02D	C024	C01G	121(3)
F6	C00X	F00V	42.0(18)	S004	C025	S003	121.8(15)
F6	C00X	C01O	111(3)	C01L	C025	S003	122(2)
F6	C00X	F02A	135(3)	C01L	C025	S004	115.7(19)

Table 6.21. (Continued) Bond Angles for **4**

Atom	Atom	Atom	Angle/˚
F6	C00X	F1	98(3)
F12	C00X	F00Q	49(2)
F12	C00X	F00V	129(3)
F12	C00X	C01O	118(3)
F12	C00X	F02A	53(2)
F12	C00X	F1	103(3)
F12	C00X	F6	111(3)
C01B	C00Y	C00U	118(2)
C01G	C00Z	C012	122(2)
C00S	C010	C00R	124(2)
C017	C011	C013	122(2)
C026	C012	C00Z	119(2)
B02C	C012	C00Z	121(2)
B02C	C012	C026	117(2)
C01S	C013	C011	121(2)
C022	C013	C011	122(2)
C022	C013	C01S	117(2)
C01A	C014	N00E	122(2)
C020	C014	N00E	120(2)
C020	C014	C01A	118(2)
C01H	C015	N00K	112.3(18)
C01T	C015	N00K	121(2)
C01T	C015	C01H	126(2)
C01G	C016	F00W	117(2)
F01X	C016	F00W	101(2)
F01X	C016	C01G	111(2)
F029	C016	F00W	106(3)
F029	C016	C01G	118(2)
F029	C016	F01X	102(3)
F1AA	C016	F00W	134(3)
F1AA	C016	C01G	109(3)
F1AA	C016	F01X	58(2)
F1AA	C016	F029	51(2)
F5	C016	F00W	77(3)
F5	C016	C01G	109(2)
F5	C016	F01X	135(3)
F5	C016	F029	39.9(19)
F5	C016	F1AA	91(3)
F0AA	C016	F00W	42(2)
F0AA	C016	C01G	119(3)
F0AA	C016	F01X	61(3)
F0AA	C016	F029	123(3)
C02D	C026	C012	120(2)
C028	C027	C01W	117(2)
C027	C028	C01A	118(2)
F1AA	F029	C016	72(3)
F5	F029	C016	79(4)
F5	F029	F1AA	151(5)
F1	F02A	C00X	65(2)
F12	F02A	C00X	62(3)
F12	F02A	F1	118(4)
C021	C02B	C01R	124(3)
C012	B02C	C00S	113.7(19)
C017	B02C	C00S	102.7(18)
C017	B02C	C012	109.4(18)
C01D	B02C	C00S	112.6(19)
C01D	B02C	C012	103.7(18)
C01D	B02C	C017	115(2)
C026	C02D	C024	117(3)
F02E	F02F	F01Y	63.7(14)
C02L	Cl02	Cl1	88(4)
C02L	Cl1	Cl02	33.0(19)
Cl1	C02L	Cl02	59(3)
C02L[1]	C02L	Cl02	107(7)
C02L[1]	C02L	Cl1	165(7)
C00X	F1	F00V	58(2)
F02A	F1	F00V	113(3)
F02A	F1	C00X	59(2)
F00V	F6	F00Q	109(4)
C00X	F6	F00Q	52.9(18)
C00X	F6	F00V	61(3)
C00X	F12	F00Q	68(3)
F02A	F12	F00Q	131(5)
F02A	F12	C00X	65(3)
F01X	F1AA	C016	59(2)
F029	F1AA	C016	57(3)
F029	F1AA	F01X	109(4)
C016	F5	F00W	48.9(17)
F029	F5	F00W	98(4)
F029	F5	C016	61(3)
C016	F0AA	F00W	73(4)
F01X	F0AA	F00W	134(5)
F01X	F0AA	C016	64(3)

[1]1-X,1-Y,-Z

Table 6.22. Atomic Occupancy for **4**

Atom	*Occupancy*	Atom	*Occupancy*	Atom	*Occupancy*
F00Q	0.660000	F00V	0.660000	F00W	0.660000
F01X	0.660000	F029	0.660000	F02A	0.660000
Cl02	0.333330	Cl1	0.333330	C02L	0.500000
F1	0.333330	F6	0.333330	F12	0.333330
F1AA	0.333330	F5	0.333330	F0AA	0.333330

6.7 Notes and References

Authorship and publication. This majority of this chapter is in preparation for publication at the time of submission of this thesis. Portions of the work, including all computational work, were completed by coauthors.

1. Senthil Kumar, K.; Ruben, M. *Coord. Chem. Rev.* **2017,** *346*, 176

2. (a) Gallagher, N.*;* Zhang, H.; Junghoefer, T.; Giangrisostomi, E.; Ovsyannikov, R.; Pink, M.; Rajca, S.; Casu, M. B.; Rajca, A., *J. Am. Chem. Soc.* **2019**, *141*, 4764. (b) Su, Y.; Wang, X.; Wang, L.; Zhang, Z.; Wang, X.; Song, Y.; Power, P. P.,. *Chem. Sci.* **2016**, *7*, 6514

3. (a) Abe, M. Diradicals. *Chem. Rev.* **2013**, *113*, 7011. (b) Fukuzumi, S.; Ohkubo, K.; Ishida, M.; Preihs, C.; Chen, B.; Borden, W. T.; Kim, D.; Sessler, J. L., *J. Am. Chem. Soc.* **2015,** *137*, 9780. (c) Suzuki, S.; Furui, T.; Kuratsu, M.; Kozaki, M.; Shiomi, D.; Sato, K.; Takui, T.; Okada, K., J. Am. Chem. Soc. **2010**, 132, 15908. (d) Fukuzaki, E., Nishide, H. J. Am. Chem. Soc. **2006**, 128, 996.

4. (a) Xie, J. Boyn, J.-N.; Filatov, A. S.; McNeece, A. J.; Mazziotti, D. A.; Anderson, J. S., *Chem. Sci.*, **2010**, *11*, 1066. (b) Horwitz, N. E.*;* Xie, J.; Filatov, A. S.; Papoular, R. J.; Shepard, W. E.; Zee, D. Z.; Grahn, M. P.; Gilder, C.; Anderson, J. S., *J. Am. Chem. Soc.* **2019**, *141*, 3940. (c) Kawamura, A., Filatov, A. S., Anderson, J. S. *Eur. J. Inorg. Chem.* **2019**, 2613.

5. (a) Wang, H.-Y.*; Cui, L.; Xie, J.-Z.; Leong, C. F.; D'Alessandro, D. M.; Zuo, J.-L.,Coord. Chem. Rev.* **2017**, *345*, 342. (b) Segura, J. L., Martin, N. *Angew. Chem., Int. Ed.* **2001**, *40*, 1372.

6. Zhou, B.; Ogura, S.; Kato, N.; Idobata, Y.; Kobayashi, A.; Kobayashi, H., *Chem. Lett.* **2013**, *42*, 977

7. (a) Bryce, M. R. *Adv. Mater.* **1999**, *11*, 11. (b) Kobayashi, A., Fujiwara, E. & Kobayashi, H. *Chem. Rev.* **2004**, *104*, 5243. (c) Coronado, E., Galan-Mascaros, J. R., Gomez-Garcia, C. J. & Laukhin, V. *Nature* **2000**, *408*, 447. (d) Canevet, D., Sallé, M., Zhang, G., Zhang, D., Zhu, D. *Chem. Commun.*, **2009**, 2245.

8. (a) García-López, V., Waerenborgh, J. C., Vieira, B. J. C., Clemente-León, M. & Coronado, E. *Dalton Trans.* **2018**, *47*, 9156. (b) Sun, X.-P., Wei, R.-J., Yao, Z.-S., Tao, J. *Cryst. Growth Des.* **2018**, *18*, 6853. (c) Floquet, S.; Simaan, A. J.; Rivière, E.; Nierlich, M.; Thuéry, P.; Ensling, J.; Gütlich, P.; Girerd, J. J.; Boillot, M. L.,*Dalton Trans.*, **2005**, 1734.

9. (a) Tissot, A.; Shepherd, H. J.; Toupet, L.; Collet, E.; Sainton, J.; Molnár, G.; Guionneau, P.; Boillot, M.-L., *Eur. J. Inorg. Chem* **2013**, 1001. (b) Arroyave, A.; Lennartson, A.; Dragulescu-Andrasi, A.; Pedersen, K. S.; Piligkos, S.; Stoian, S. A.; Greer, S. M.; Pak, C.; Hietsoi, O.; Phan, H.; Hill, S.; McKenzie, C. J.; Shatruk, M.,. *Inorg. Chem.* **2016**, *55*, 5904.

10. Gao, F.; Zhu, F.-F.; Wang, X.-Y.; Xu, Y.; Wang, X.-P.; Zuo, J.-L., *Inorg. Chem.* **2014**, *53*, 5321

11. Zadrozny, J. M., Greer, S. M., Hill, S., Freedman, D. E. *Chem. Sci.* **2016**, *7*, 416

12. (a) Bellec, N; Vacher, A.; Barrière, F.; Xu, Z.; Roisnel, T.; Lorcy, D. *Inorg. Chem.* **2015**, *54*, 5013. (b) Xu, C.-H. *et al. Chem. Eur. J.* **2009**, *15*, 8717.

13. (a) Tang, Y., Gan, X., Tan, M., Zheng, X. *Polyhedron* **1998**,*17*, 429. (b) Ferreira, G. B., Hollauer, E., Comerlato, N. M., Wardell, J. L. *Inorganica Chim. Acta* **2006**, *359*, 1239. (c) Mori, H., Nakano, M., Tamura, H., Matsubayashi, G.-E. *J. Organomet. Chem.* **1999**, 574, 77. (d) Nomura, M., Fujii, T., Kajitani, M. *Organometallics* **2009**, 28, 3776.

14. (a) Hitomi, Y., Furukawa, S., Higuchi, M., Shishido, T., Tanaka, T. *J. Mol. Catal. A: Chem.* **2008**, *288*, 83. (b) Diebold, A., Hagen, K. S. *Inorg. Chem.* **1998**, 37, 215.

15. (a) Kawabata, K., Nakano, M., Tamura, H., Matsubayashi, G.-E. *J. Organomet. Chem.* **2004**, *689*, 405. (b) Akasaka, T., Nakano, M., Tamura, H. & Matsubayashi, G.-E. *Bull. Chem. Soc. Jpn.* **2002**, *75*, 2621

16. (a) Min, K. S.; Swierczek, K.; DiPasquale, A. G.; Rheingold, A. L.; Reiff, W. M.; Arif, A. M.; Miller, J. S., *Chem. Commun.*, **2008**, 317. (b) Zheng, C., Xu, J., Wang, F., Tao, J. & Li, D. *Dalton Trans.* **2016**, *45*, 17254. (c) Paulsen, H.; Grünsteudel, H.; Meyer-Klaucke, W.; Gerdan, M.; Grünsteudel, H. F.; Chumakov, A. I.; Rüffer, R.; Winkler, H.; Toftlund, H.; Trautwein, A. X., *Eur. Phys. J. B* **2001**, *23*, 463.

17. (a) Tichnell, C. R., Shultz, D. A., Popescu, C. V., Sokirniy, I., Boyle, P. D. *Inorg. Chem.* **2015**, *54*, 4466. (b) Sreekanth, A. & Kurup, M. R. P. *Polyhedron* **2004**, *23*, 969. (c) Polam, J. R. *et al. J. Am. Chem. Soc.* **1996**, *118*, 5272.

18. Min, K. S., DiPasquale, A., Rheingold, A. L., Miller, J. S. *Inorg. Chem.* **2007**, 46, 1048.

19. (a) Nihei, M., Shiga, T., Maeda, Y.; Oshio, H. *Coord. Chem. Rev.* **2007**, *251*, 2606. (b) Olguín, J.; Brooker, S. *Coord. Chem. Rev.* **2011**, 255, 203.

20. Waterloo Ontario. Maplesoft, a division of Waterloo Maple Inc. Maple. 2019.

21. (a) Hansen, T. K., et al., *Org. Synth.* **1996**, *73*, 270. (b) Svenstrup, N.; Rasmussen, K. M.; Hansen, T. K., Becher, J. *Synthesis.* **1994**, *8*, 809. (c) Chávez, I., et al., *J. Organomet. Chem.* **2000**, *601* (1), 126.

22. Bain, G. A., Berry, J. F. *J. Chem.Ed.* **2008**, *85*, 532.

23. Krause, L., Herbst-Irmer, R.,Sheldrick, G.M., Stalke, D. *J. Appl. Crystallogr.* **2015**, *48* (1), 3

24. Sheldrick, G.M. *Acta Crystallogr., Sect. A: Found. Adv*. **2015**, 71, 3.

25. Dolomanov, O.V., Bourhis, L.J., Gildea, R.J., Howard, J.A.K., Puschmann, H.J. *Appl. Crystallogr*. **2009**, *42*, 339

26. Sheldrick, G.M. *Crystal Acta Crystallogr., Sect. C: Struct. Chem.* **2015**, *71*, 3.

27. (a) Neese, F. Wiley Interdisciplinary Reviews: Computational Molecular Science, **2012**, *2*, 73-78.; (b) H - Kr: Schaefer, A.; Horn, H.; Ahlrichs, R. *J. Chem. Phys.* **1992**, *97*, 2571.; (c) Rb - Xe: Schaefer, A.; Huber,C.; Ahlrichs, R. *J. Chem. Phys.* **1994**, *100*, 5829. (d) Weigend, F.; Ahlrichs, R.; *Phys. Chem. Chem. Phys.* **2005**, 7, 3297.

28. Mazziotti, D. A. *Chem. Rev.* **2012**, 112, 244

29. (a) Mazziotti, D.A. *Phys. Rev. A*, **2002**, *65*, 062511 (b) Mazziotti, D.A. *Phys. Rev. Lett.*, **2012**, 108, 263002.

30. (a) Mazziotti, D.A. *Phys. Rev. Lett.*, **2004**, *93*, 213001. (b) Mazziotti, D.A. *Phys. Rev. Lett.*, **2011**, 106, 083001.

31. (a) McIsaac, A.R., Mazziotti, D.A. *Phys. Chem. Chem. Phys.*, **2017**, *19*, 4656. (b) Montgomery, J.M., Mazziotti, D.A. *J. Phys. Chem. A,* **2018**, **122**(22), 4988.

32. Fulmer, G. R., Miller, A. J. M., Sherden, N. H., Gottlieb, H. E., Nudelman, A., Stoltz, B. M., Bercaw, J. E., Goldberg, K. I., *Organometallics* **2010**, *29* (9), 2176-2179.